



HAL
open science

**Dynamics of inundation events in the
rivers-estuaries-ocean continuum in Bengal delta:
synergy between hydrodynamic modelling and
spaceborne remote sensing**

Md Jamal Uddin Khan

► **To cite this version:**

Md Jamal Uddin Khan. Dynamics of inundation events in the rivers-estuaries-ocean continuum in Bengal delta : synergy between hydrodynamic modelling and spaceborne remote sensing. Hydrology. Université Paul Sabatier - Toulouse III, 2021. English. NNT : 2021TOU30057 . tel-03514722

HAL Id: tel-03514722

<https://theses.hal.science/tel-03514722>

Submitted on 6 Jan 2022

HAL is a multi-disciplinary open access archive for the deposit and dissemination of scientific research documents, whether they are published or not. The documents may come from teaching and research institutions in France or abroad, or from public or private research centers.

L'archive ouverte pluridisciplinaire **HAL**, est destinée au dépôt et à la diffusion de documents scientifiques de niveau recherche, publiés ou non, émanant des établissements d'enseignement et de recherche français ou étrangers, des laboratoires publics ou privés.



THÈSE

En vue de l'obtention du
DOCTORAT DE L'UNIVERSITÉ DE TOULOUSE

Délivré par l'Université Toulouse 3 - Paul Sabatier

Présentée et soutenue par

MD JAMAL UDDIN KHAN

Le 16 février 2021

**Dynamique des inondations dans le continuum rivière-estuaire-océan
littoral du delta du Bengale : synergie de la modélisation
hydrodynamique et de la télédétection spatiale**

École doctorale : **SDU2E - Sciences de l'Univers, de l'Environnement et de
l'Espace**

Spécialité : **Océan, Atmosphère, Climat**

Unité de Recherche :
LEGOS - Laboratoire d'Etudes en Géophysique et Océanographie Spatiales

Thèse dirigée par
Fabien DURAND et Laurent TESTUT

Jury

Mme Marta MARCOS, Rapporteur
Mme Déborah IDIER, Rapporteur
M. AKM Saiful ISLAM, Examinateur
M. Xavier BERTIN, Examinateur
Mme Marine HERRMANN, Examinatrice
Mme Sylvie FANCHETTE, Examinatrice
M. Fabien DURAND, Directeur de thèse
M. Laurent TESTUT, Co-directeur de thèse

ACKNOWLEDGEMENTS

Writing this page brought back so much memory and feelings of gratitude. It was the easiest to keep writing, yet the hardest to finish in a relatively limited count of pages. . .

To begin, I would like to thank CNES and the Embassy of France in Dhaka for the financial support of my PhD. This administrative collaboration was conceived, thanks to the kind efforts of Stephane Calmant. I would like to express my sincere gratitude to him, as well as my appreciation of his great interest in the Indo-Bangla region, his effort to reach out and build collaboration in the quest of seeking knowledge.

I would like to express my most profound appreciation to my PhD supervisors Fabien Durand and Laurent Testut, for their guidance throughout this thesis, their kindness, care and their encouragement during the time of despair. Even with a copious amount of adjectives, it is hard to express my depth of appreciation for them. It has been my great pleasure to spend my crucial formative years as a researcher under their umbrellas. Their contribution to my professional and personal life is enormous, and I am sincerely grateful to them.

Many thanks to Professor Dr. AKM Saiful Islam at IWFm, BUET for supporting me during my Masters, paving the way to a successful and long-lasting Franco-Bangla collaboration which lead to this PhD, providing guidance and hosting during the PhD work. It was a turning point in my journey to be recruited in his lab after my graduation in 2015.

My heartfelt thanks goes to Yann Krien. A substantial portion of this PhD work is built upon his excellent job on the hydrodynamics of the Bengal delta. My initial training on unstructured modelling was smooth, thanks to his guidance. It was a great pleasure to communicate, discuss, and to work with him throughout the PhD.

I would like to thank Dr. Kerry Emanuel at MIT for sharing with us an incredible dataset of cyclonic activity over the Bay of Bengal. The scientific value of this dataset is enormous and surely will keep me looking into it in the coming future.

I thank the Director of LEGOS Alexandre Ganachaud for hosting me at LEGOS. Due to the nature of my PhD, it was required to move around laboratories. I thank him for his continuous support with such collaborations and placements at other labs - particularly in Dhaka and in La Rochelle. I thank Olivier de Viron, Director of LIENSs in La Rochelle for allowing me to work at LIENSs for a substantial part of the thesis.

My sincere thanks go to the members of LEGOS, particularly the OLVAC team, team leader Frederic Marin, for a warm welcome. It was indeed a great pleasure. I particularly like to thanks the current team leader of OLVAC (in the transition to form DYNOTROP) Sophie Cravatte. Being my PhD godmother, I found comfort in talking with her from time to time. Also, thanks to her for providing support to a lot of us during the lockdown of COVID-19. It was invaluable to be in contact with the lifeline at LEGOS during that difficult time. I would also like to extend my thanks to everyone at the LEGOS management. Notably, thanks to Martine Mena, Brigitte Cournou, and Nadine Lacroux, for their backbreaking work to make our life much more manageable.

I express my gratitude to the LIENSs community for their warm welcome too. It was a great pleasure to meet such a diverse group of people working on coastal issues. I would like to thank Olivier de Viron, Mikhail Karpytchev, Guy Wöppelmann, Valerie Ballu, Wayne Crawford for allowing me to attend their classes. Thanks to Mélanie Becker for her support on my work through the DELTA project. Thanks to Etienne Poirier and Denis Dausse for assembling an

excellent low-cost echo-sounding device. Warm thanks to the LIENSs management who had to go extra-miles to manage some missions to Bangladesh.

A big thanks to two of my thesis committee members, Sylvain Ouillon at LEGOS and Xavier Bertin at LIENSs. Their guidance and suggestions were invaluable in the progress of the thesis. Additionally, during my placement at LIENSs, it was a pleasure to interact and collaborate with Xavier Bertin and his group. I express my deep appreciation for his team and their excellent work.

I would like to thank Alvaro Santamaría-Gómez at LEGOS, and Pierre Sakic for their help with GPS processing tools. My thanks to Kevin Martins and Marc Pezerat for their help with WWM modelling. I would like to acknowledge Sara Padilla-Polo and Audrey Delpech with whom I shared offices in LEGOS. Similarly, I would like to acknowledge Yann-Treden Tranchant, Clémence Chupin, Baptiste Mengual, and Marc Pezerat with whom I shared office at LIENSs. I will fondly cherish the memories of my interaction with these excellent people.

I also acknowledge all of my friends, as well as former labmates at IWFm for their kind inspiration. Special thanks to Sazzad Hossain, Abul Bashar, and Faria Fahim at BWDB for providing useful information from time-to-time.

Lots and lots of gratitude for my family, to my parents, who provided endless support in uncountable forms. My two sisters - Mukshatu and Mim - one enjoys architecture, another biochemistry - for being the genius and the loving ones at the same time.

There is not enough words in my vocabulary to express my appreciation to my loving wife, Nushrat Yeasmin. Due to the global pandemic, we got stuck at two different continent. It takes extraordinarily great courage and resilience to push through this challenging time in physical separation. My admiration for her only got more passionate during the past years, even more so during the last few months of the PhD - looking forward to the rest of our life journey.

I would like to express my gratitude to the developer community of SCHISM - the essential tool in the toolbox of this thesis. As well as to the community of python for providing and maintaining such an incredible open-source scientific computing ecosystem. Finally, thanks to the system admins of the computing clusters used throughout this thesis. Without their hard work, thousands of numerical simulations were not possible.

As I said in the beginning, it was hard to stop writing. Although no intentional snubs here, the current list is definitely not exhaustive. To everyone else, even remotely involved in a positive and/or constructive manner... thank you.

DEDICATION

I dedicate my thesis work to my parents. They wanted one of their children to be a doctor, but the other kind. They supported me unconditionally at all stages of life and taught me what can not be learned otherwise.

PUBLICATION RECORD

- Mohammed, K., Islam, A. K. M. S., Islam, G. M. T., Alfieri, L., Bala, S. K., & **Khan, M. J. U.** (2017). Impact of High-End Climate Change on Floods and Low Flows of the Brahmaputra River. *Journal of Hydrologic Engineering*, 22(10), 04017041. [https://doi.org/10.1061/\(asce\)he.1943-5584.0001567](https://doi.org/10.1061/(asce)he.1943-5584.0001567)
- Mohammed, K., Islam, A. S., Islam, G. T., Alfieri, L., Bala, S. K., & **Khan, M. J. U.** (2017). Extreme flows and water availability of the Brahmaputra River under 1.5 and 2 °C global warming scenarios. *Climatic Change*. <https://doi.org/10.1007/s10584-017-2073-2>
- Mohammed, K., Islam, A. K. M. S., Islam, G. M. T., Alfieri, L., **Khan, M. J. U.**, Bala, S. K., & Das, M. K. (2018). Future Floods in Bangladesh under 1.5°C, 2°C, and 4°C Global Warming Scenarios. *Journal of Hydrologic Engineering*, 23(12), 04018050. [https://doi.org/10.1061/\(asce\)he.1943-5584.0001705](https://doi.org/10.1061/(asce)he.1943-5584.0001705)
- Krien, Y., Arnaud, G., Cécé, R., Ruf, C., Belmadani, A., **Khan, J.**, Bernard, D., Islam, A. K. M. S., Durand, F., Testut, L., Palany, P., & Zahibo, N. (2018). Can We Improve Parametric Cyclonic Wind Fields Using Recent Satellite Remote Sensing Data? *Remote Sensing*, 10(12), 1963. <https://doi.org/10.3390/rs10121963>
- Bergmann, M., Durand, F., Krien, Y., **Khan, M. J. U.**, Ishaque, M., Testut, L., Calmant, S., Maisongrande, P., Islam, A. K. M. S., Papa, F., & Ouillon, S. (2018). Topography of the intertidal zone along the shoreline of Chittagong (Bangladesh) using PROBA-V imagery. *International Journal of Remote Sensing*, 1–21. <https://doi.org/10.1080/01431161.2018.1504341>
- Khan, M. J. U.**, Ansary, M. N., Durand, F., Testut, L., Ishaque, M., Calmant, S., Krien, Y., Islam, A. K. M. S., & Papa, F. (2019). High-Resolution Intertidal Topography from Sentinel-2 Multi-Spectral Imagery: Synergy between Remote Sensing and Numerical Modeling. *Remote Sensing*, 11(24), 2888. <https://doi.org/10.3390/rs11242888>
- Khan, M. J. U.**, Islam, A., Das, M. K., Mohammed, K., Bala, S. K., & Islam, G. M. T. (2019). Observed trends in climate extremes over Bangladesh from 1981 to 2010. *Climate Research*, 77(1), 45–61. <https://doi.org/10.3354/cr01539>
- Roy, B., Islam, A. K. M. S., Islam, G. M. T., **Khan, M. J. U.**, Bhattacharya, B., Ali, M. H., Khan, A. S., Hossain, M. S., Sarker, G. C., & Pieu, N. M. (2019). Frequency Analysis of Flash Floods for Establishing New Danger Levels for the Rivers in the Northeast Haor Region of Bangladesh. *Journal of Hydrologic Engineering*, 24(4), 05019004. [https://doi.org/10.1061/\(asce\)he.1943-5584.0001760](https://doi.org/10.1061/(asce)he.1943-5584.0001760)
- Durand, F., Piecuch, C. G., Becker, M., Papa, F., Raju, S. V., **Khan, J. U.**, & Ponte, R. M. (2019). Impact of Continental Freshwater Runoff on Coastal Sea Level. *Surveys in Geophysics*. <https://doi.org/10.1007/s10712-019-09536-w>
- Becker, M., Papa, F., Karpytchev, M., Delebecque, C., Krien, Y., **Khan, J. U.**, Ballu, V., Durand, F., Cozannet, G. L., Islam, A. K. M. S., Calmant, S., & Shum, C. K. (2020). Water level changes, subsidence, and sea level rise in the Ganges–Brahmaputra–Meghna delta. *Proceedings of the National Academy of Sciences*, 201912921. <https://doi.org/10.1073/pnas.1912921117>
- Khan, M. J. U.**, Islam, A. K. M. S., Bala, S. K., & Islam, G. M. T. (2020). Changes in climate extremes over Bangladesh at 1.5 °C, 2 °C, and 4 °C of global warming with high-resolution regional climate modeling. *Theoretical and Applied Climatology*. <https://doi.org/10.1007/s00704-020-02888-8>

[//doi.org/10.1007/s00704-020-03164-w](https://doi.org/10.1007/s00704-020-03164-w)

- Khan, J. U.**, Islam, A. K. M. S., Das, M. K., Mohammed, K., Bala, S. K., & Islam, G. M. T. (2020). Future changes in meteorological drought characteristics over Bangladesh projected by the CMIP5 multi-model ensemble. *Climatic Change*. <https://doi.org/10.1007/s10584-020-02832-0>
- Haque, S., Ali, Md. M., Islam, A. K. M. S., & **Khan, J. U.** (2020). Changes in flow and sediment load of poorly gauged Brahmaputra river basin under an extreme climate scenario. *Journal of Water and Climate Change*, jwc2020219. <https://doi.org/10.2166/wcc.2020.219>
- Das, M. K., Islam, A. K. M. S., Karmakar, S., **Khan, M. J. U.**, Mohammed, K., Islam, G. M. T., Bala, S. K., & Hopson, T. M. (2020). Synoptic flow patterns and large-scale characteristics of flash flood-producing rainstorms over northeast Bangladesh. *Meteorology and Atmospheric Physics*. <https://doi.org/10.1007/s00703-019-00709-1>
- Khan, M. J. U.**, Durand, F., Testut, L., Krien, Y., & Islam, A. K. M. S. (2020). Sea level rise inducing tidal modulation along the coasts of Bengal delta. *Continental Shelf Research*, 211, 104289. <https://doi.org/10.1016/j.csr.2020.104289>

RÉSUMÉ

Le delta du Bengale est le plus vaste au monde. Il est formé par la confluence des trois rivières transfrontalières que sont le Gange, le Brahmapoutre et la Meghna. Des inondations massives frappent régulièrement cette région côtière très densément peuplée, située à seulement quelques mètres au-dessus du niveau moyen de la mer. Elles résultent du puissant cycle saisonnier des débits fluviaux, de la marée océanique très ample, et des cyclones tropicaux fréquents. Au cours des cinquante dernières années, les inondations de la partie littorale du delta ont fait plus de 500'000 victimes. La montée du niveau moyen de la mer ne va faire qu'aggraver la vulnérabilité de cette région où le taux de pauvreté est très élevé. Le long du littoral, les estrans sont les zones alternativement inondées à marée haute et découvertes à marée basse. Leur topographie joue un rôle important dans l'hydrodynamique littorale et dans les submersions qui surviennent lors des événements extrêmes. En mettant en œuvre une synergie entre l'imagerie par télédétection spatiale de la constellation Sentinel-2 et la modélisation numérique de la marée, nous avons cartographié la topographie de l'estran du delta du Bengale sur une superficie de 1134 km², avec une résolution de 10 m. Les marées, qui sont le facteur dominant de la variabilité du niveau de la mer côtier, sont apparues comme sensibles à la montée du niveau de la mer. Dans une hiérarchie de scénarios de montée du niveau de la mer représentatifs de l'évolution attendue au 21^{ème} siècle, nous avons conclu que l'amplitude de marée devrait augmenter significativement avec la montée du niveau de la mer, à la fois dans le Sud-Ouest et dans le Sud-Est du delta. Au contraire, l'extension graduelle et massive de la superficie des estrans dans la partie centrale du delta devrait induire une nette atténuation de la marée, dans ces scénarios futurs. La marée joue par ailleurs un rôle central dans l'évolution des surcotes cycloniques. Un exercice de prévision du dernier super-cyclone ayant frappé le delta du Bengale avec notre plate-forme de modélisation hydrodynamique couplée marée-surcote-vagues a révélé la nécessité du couplage dynamique entre ces trois composantes de la submersion, et nous avons pu confirmer le rôle-clé de la topographie côtière dans le succès des prévisions numériques. Grâce à une approche ensembliste basée sur la simulation numérique hydrodynamique de plusieurs milliers de cyclones synthétiques, cohérents tant du point de vue de la physique que de la statistique, nous avons pu conclure qu'il y a à l'heure actuelle de l'ordre de 10% de la population côtière du delta, soit trois millions de personnes, résidant dans la zone exposée à la submersion cinquantennale. La compréhension et la quantification des mécanismes de l'inondation exposés dans cette thèse constituent une information pertinente pour contribuer à l'ingénierie des infrastructures côtières, à la gestion du risque, ainsi qu'à l'élaboration de l'agenda de la recherche en hydrodynamique côtière sur le delta du Bengale.

ABSTRACT

The Bengal delta is the largest in the world. It is formed by the confluence of three transboundary rivers - Ganges, Brahmaputra, and Meghna. Flooding induced by large seasonal continental discharge, strong tide, and frequent deadly storm surges, regularly strikes this densely populated (density > 1000 person/km²), low-lying coastal region (<5 m above mean sea level). In the last five decades, coastal flooding took more than half a million lives. Ongoing global sea level rise (SLR) will only further aggravate the vulnerability of this impoverished region. Along the shoreline, intertidal zones are the first landmass that gets flooded, periodically between each high- and low-tide. Their topography plays an important role in the coastal hydrodynamics and associated flooding during extremes. A synergy between remote sensing from Sentinel-2 constellation and tidal numerical modelling allowed us to map an intertidal area of 1134 km² and its topography at 10 m resolution. Tides, that prominently drive the variability of coastal sea level, are shown to be sensitive to SLR. In future SLR scenarios in line with the 21st century forecasts, we found that the tidal amplitude will significantly increase with SLR over both the south-western and south-eastern parts of the delta. In contrast, the central part of the delta will potentially experience massive free-flooding of river banks, hereby inducing a decay of the tidal amplitude. Tide plays a vital role in the evolution of storm surges also. Hindcast simulation of a recent super cyclone with our coupled tide-surge-wave model reveals the necessity of the coupling between tide, surge and wave modelling, and confirmed the crucial role played by the coastal topography for effective inundation modelling and forecast. With an ensemble forecast of thousands of physically and statistically consistent synthetic cyclones, we could conclude that about 10% of the coastal population of the Bengal delta, amounting to 3 million people, currently lives exposed to the 50-year return period flooding. The understanding and quantification of the inundation mechanisms extended in this study is expected to help with coastal infrastructure engineering, risk zoning, resource allocation and future adaptation to coastal flood across the Bengal delta.

TABLE OF CONTENTS

Acknowledgements	ii
Dedication	iv
Résumé	vii
Abstract	viii
1 Introduction and Motivation	1
1.1 Introduction	1
1.2 The river deltas	2
1.3 Inundation in the Bengal delta	4
1.3.1 Bengal delta	4
1.3.2 Types of flood in the Bengal delta	5
1.3.3 Storm surge problem in the Bay of Bengal	6
1.4 Bengal delta continuum and knowledge gaps	8
1.5 Scientific questions and study approach	10
1.6 Organization of the thesis	11
2 Hydrodynamic Modeling: Data and Methods	13
2.1 Introduction	13
2.2 Bathymetry assembly	14
2.3 Observations	17
2.4 Modelling framework	17
2.4.1 Hydrodynamic model	17
2.4.2 Discretization	19
2.4.3 Parameterization of bottom friction	20
2.4.4 Coupling with wave model	20
2.5 Model forcings and boundary condition	22
2.5.1 Tidal oceanic boundary	22
2.5.2 River open boundaries	22
2.5.3 Cyclonic wind and pressure	23
2.6 Assessment of tide	25
3 Intertidal Topography: Synergy Between Remote Sensing and Tidal Modelling	27
3.1 Introduction	28
3.2 Shoreline detection with Sentinel-2 imagery	32
3.2.1 Pre-processing of the dataset	32
3.2.2 Coarse water mask	35
3.2.3 Shoreline extraction	36
3.3 Vertical referencing with tidal model	39
3.3.1 Hydrodynamic tidal modelling framework	40

3.3.2	Tidal water level estimation for vertical referencing	42
3.4	Results	43
3.4.1	Intertidal DEM	43
3.4.2	Validation of our DEM	44
3.5	Discussion	45
3.6	Conclusion	47
4	Coastal Tide: From the Present to the Future	49
4.1	Introduction	50
4.2	Observed trend in tidal range: The example of Hiron Point	52
4.3	Tidal model in the Bay of Bengal	54
4.4	Projected changes in tidal range in the Bengal delta	58
4.4.1	Current tidal range	58
4.4.2	+1 m SLR	59
4.4.3	Robustness of the projected changes under other SLR scenarios	60
4.5	Tidal range evolution along the estuaries	62
4.6	Discussion	66
4.7	Conclusions	68
5	Storm Surge Modeling: A Case Study of Recent Super Cyclone Amphan	70
5.1	Introduction	71
5.2	Storm surge and inundation processes in the Bay of Bengal	74
5.3	Atmospheric evolution of cyclone Amphan	76
5.4	Storm surge model and performance	77
5.4.1	Model implementation	77
5.4.2	Model forcings	78
5.4.3	Predictive skills	79
5.5	Near real-time storm surge forecasting	83
5.5.1	Forecast strategy and forcing products	83
5.5.2	Real-time computation and results	84
5.6	Discussion	85
5.6.1	Coupled tide-surge-wave dynamics	85
5.6.2	Performance of storm surge forecasting	86
5.6.3	Inundation	87
5.6.4	Prospects in operational forecasting	89
5.7	Conclusions	89
5.8	Appendix	90
5.8.1	Tide model validation	90
6	Storm Surge Hazard: A Probabilistic-Deterministic Approach	93
6.1	Introduction	94
6.2	Storm surge model	99
6.2.1	Model description	99
6.2.2	Coupling with wave model	100
6.2.3	Wind and pressure field	101
6.2.4	Validation	101
6.3	Probabilistic-deterministic cyclone ensemble	103
6.3.1	Synthetic storm dataset	103
6.3.2	Ensemble surge estimate	104
6.3.3	Statistical analysis methodology	106
6.4	Storm surge hazard	106
6.5	Discussion	110

6.5.1	Synthetic cyclone ensembles statistics	110
6.5.2	Inundation extent and consistency	110
6.5.3	Comparison with previous estimates	111
6.5.4	Return period of previous cyclones	112
6.5.5	Role of embankments	112
6.5.6	Population exposure	112
6.6	Conclusions and perspective	114
7	Conclusions and Perspectives for Future Work	116
7.1	Conclusion	116
7.2	Overview	118
7.3	Summary of conclusions and impacts	119
7.3.1	The synergy between the remote sensing and hydrodynamic modelling . .	119
7.3.2	Impact of sea level rise on the coastal tide	120
7.3.3	Modelling and forecasting of storm surge inundation	121
7.3.4	Mapping the risk of inundation from storm surge under current climate .	122
7.4	Future Research Perspectives	122
7.4.1	Modelling tidal dynamics	122
7.4.2	Salinity and steric sea level	123
7.4.3	Role of embankments and mangroves	124
7.4.4	Storm surge flooding mechanisms	126
7.4.5	Future storm surge hazard	127
7.4.6	Relative sea level rise	128
7.4.7	Other relevant environmental processes	129
7.5	Transferrable lessons and concluding remarks	129
	Bibliography	131

LIST OF FIGURES

1.1	Global distribution of deltaic area (a) and population (b). The total deltaic area and population per 3° lengths of coastline. The colour along the lengths of coastlines shows the percentage of area or population they contain relative to the entire dataset. Black lines are unmapped shorelines. Histograms show the latitudinal distribution (3° bins) of habitable area (c) and population (d). White bars in the histograms show the proportion of area and people in the 100-year storm surge floodplain. (From Edmonds et al. (2020)).	3
1.2	The extent of the Ganges-Brahmaputra-Meghna catchment area and the Bengal delta sitting on its outlet to the Bay of Bengal. The major rivers are shown in blue. Red outlines the extent of each basins catchment area. The topography is from SRTM dataset and bathymetry is taken from GEBCO dataset. Three major cities – Dhaka (star), Chittagong (circle), Calcutta (square) are shown in the map.	4
1.3	Exposure to floods in the Bangladesh part of the Bengal delta based on the classification of Bangladesh Agricultural Research Council (BARC).	5
1.4	Population density over the Bengal delta. The black lines show the storms that made landfall over the region over the last 50 years based on IbTracs dataset (Knapp et al., 2018).	7
2.1	77000 digitized sounding points (in yellow). The coverage of the corresponding individual charts is shown in red outlines.	16
2.2	A schematic for the water level variation described with Equation 2.4 - 2.6. . . .	18
2.3	The model mesh and its extent. The applied boundary conditions are shown with arrows.	20
2.4	Climatological mean annual discharge (in m ³ /s) at the open river boundaries. . .	23
3.1	Location of the study area and the coverage of the Sentinel 2 tiles used in this study. Each tile (showed as a translucent red patch) is annotated with the tile identifier and in bracket the number of images used. The major rivers (showed in aqua color) is overlaid on the Gridded Population of the World (GPWv4) dataset (in grey scale) (Center For International Earth Science Information Network-CIESIN-Columbia University, 2016).	31
3.2	Greyscale display of the four original Sentinel 2 L2A bands obtained for tile #46QCK on 01/02/2017 04:38:25. The band B2, B4, B8 and B11 are respectively being displayed in (a), (b), (c) and, (d). The scale represents the pixel with the lowest value in white to highest in black. For clarity of the image, the pixel value is restricted to lower than the 99.99 th percentile for each band.	33
3.3	Same tile as Figure 3.2 but for the (a) alpha, (b) synthetic red, (c) synthetic green, and (d) synthetic blue band. The grey scale is from the lowest pixel value (black) to highest (white).	34
3.4	Same tile as Figure 3.2 and 3.3 for the (a) hue, and (b) value band converted from the synthetic RGB Band. The grey scale is from the lowest pixel value (black) to the highest (white).	35

3.5	(a) The water mask derived from combined B11 band of tile #46QCK, black being the water and white is the land. (b) Inverse masking of hue band, (c) Masking of value band showed in Figure 3.4.	36
3.6	(a) Binary water (BW) image obtained from the combination of BW_{hue} and BW_{value} for tile #46QCK acquired on 01/02/2017 04:38:25. (b) Same as (a) after applying filling of water pixel group smaller than 10000 pixels and removing land pixel groups smaller 10000 pixels.	37
3.7	The black line is the extracted shoreline for tile #46QCK acquired on 01/02/2017 04:38:25 overlaid on a false colour RGB constructed from B2, B4, and B8 Band presented in Figure 3.2	38
3.8	Flowchart of the shoreline detection procedure.	39
3.9	(a) Model mesh over the domain with indication of the open boundary conditions used. (b) A close-up of the model mesh over the study area. The tidal complex error is shown in colour-scale along the satellite altimetry tracks. The coastal tide gauges used for validation are shown by red stars. The Bengal delta is shown in red translucent patch (c) Bar plot showing the tidal complex error compared to Krien et al. (2016) (denoted as K16) for the 6 tide gauges shown on (b).	41
3.10	(a) The intertidal DEM over the study area. Each colour pixel is according to its elevation above Mean Sea Level (positive upwards). The labelled red rectangles indicate the zones where we have displayed zoom in (b) to (f). The background is a merged raster of B11 bands. The colour scale is the same from (a) through (f).	44
3.11	Validation of Sentinel-2 DEM. (a) Positions of the navy chart sounding points (bullets) overlaid on the Sentinel-2 DEM (blue-brown contours). The bullets colour features the elevation of the navy sounding points (in meters). (b) Positions of the collocated points between the navy sounding points and Sentinel-2 DEM. The colour of the bullets features the difference (in meters) between the two estimates. (c) Scatter plot between Sentinel-2 DEM vs the digitized navy sounding from charts. (d) Trajectory of the shipborne bathymetric survey (red line) overlaid on the Sentinel-2 DEM (blue-brown contours). (e) Positions of the collocated points between the shipborne survey and Sentinel-2 DEM. The bullets colour features the difference (in meters) between the two estimates. (f) Scatter plot between Sentinel-2 DEM vs the shipborne <i>in situ</i> sounding points. ESRI World Imagery is used as background in (b) and (e), whereas for clarity shaded relief from ESRI is used as background in (a) and (d).	46
4.1	Layout of the Bengal delta with country borders. The near-shore bathymetry is mapped associated with the color scale. The cyan lines show the limits of the existing polders. The red stars indicate the location of the main tide gauges stations.	51
4.2	Monthly-mean (28-days) timeseries of observed water level at Hiron Point tide gauge. The red curve shows the mean high water (MHW), the blue curve shows the mean low water (MLW), the green curve shows the mean tidal range (Range), the grey curve shows the mean sea level (MSL). The levels are in meters relative to chart datum (mCD).	53
4.3	(a) Model mesh over the computational domain with indication of the open boundary conditions used. Red box indicates close-up area of frame (b). (b) Spatial distribution of the Manning coefficient n used in the model.	56
4.4	(a) Mean tidal range for the reference simulation, corresponding to present-day conditions. Isobaths 7 m, 10 m and 15 m are displayed. (b) Difference between the mean tidal range in the +1 m SLR and the reference simulation.	58

4.5	Amplitude in the reference simulation and difference between the amplitude with +1 m SLR and reference simulations of M2 tidal constituent (left) and for S2 tidal constituent (right). The bottom row shows the difference between the two simulations, expressed in percentage of the amplitudes in the reference simulation.	61
4.6	Map of the frequency of inundation over the model domain, for the reference simulation (a) as well as for the various SLR scenarios we simulated, from +0.5 m (b) to +2 m (e) with 0.5 m stepping. For the sake of readability, we did not shade the already permanent water bodies.	62
4.7	M2 amplitude modelled at the location of Charchanga (left), Hiron Point (centre) and Chittagong (right), as a function of the magnitude of SLR we imposed in our model, from 0 m (reference simulation) to +2.0 m (most extreme scenario).	63
4.8	Bathymetry of the three estuaries considered – Meghna-Ganges-Brahmaputra (a), Pussur (c), and Hooghly (e). Along-estuary profile of tidal range, normalized by the tidal range of the mouth of the Meghna-Ganges-Brahmaputra (b), Pussur (d), and Hooghly (f). Tidal ranges are shown for the reference simulation (blue) as well as for the SLR scenarios we considered (orange for +0.5 m, green for +1.0 m, red for +1.5 m, violet for +2.0 m). The paths of extraction are displayed in red in the maps.	64
5.1	The path of the super cyclone Amphan of May 2020, overlaid on the population density. The footprint of 34 knots (17.5 m/s), 50 knots (25.7 m/s), 64 knots (32.9 m/s), and 100 knots (51.4 m/s) wind speed area is shown with the red colour bar. Inset shows the location of the study area.	72
5.2	Conceptual diagram of the involved processes that determine the water level evolution and its interaction with the controls determining the inland flooding.	75
5.3	Temporal evolution of the successive forecasts of Amphan cyclone wind and pressure. (a) Forecast track colour-coded with the date (JTWC best track in black) (b) Wind speed forecast with each epoch, (c) Pressure forecast with each epoch. The vertical red dashed line indicates the time of landfall.}	76
5.4	Comparison of simulated (in orange) and observed (in blue) water level, significant wave height (SWH) and mean wave period. (a) The map shows the along-track bias in SWH compared to the one calculated from Sentinel 3B altimeter overpass at 2020-05-18 1603Z. Bottom panel shows the modelled SWH and mean wave period (orange line) compared to buoy observations (blue dots) at BD08 (b-c) and BD11 (d-e) provided by INCOIS. Comparison between observed (blue dots) and modelled (orange line) water level at the station locations – (f) Angtihar, (g) Galachipa, (h) Kuakata, (i) Tajumuddin, (j) Chittagong, and (k) Visakhapatnam. Green dashed lines in (f)-(k) indicates the modelled tidal water level. Location of the buoys and the water level gauges are shown in (a). The vertical red lines in water level plots indicate the time of landfall.	80
5.5	Hindcast of (a) maximum water level, (b) maximum surge (c) wave setup/setdown (d) maximum non-linear interaction between tide and surge. For (a), for the areas above mean sea level, the water level is converted to water level above the topography for consistency. The inset maps show a close-up (75 km × 45 km) of the landfall region.	82
5.6	Temporal combination scheme of the JTWC, GFS, and HWRF forecasts for each 6-hourly storm surge forecast epoch.	84
5.7	Maximum surge (a, c, e) and elevation (b, d, f) evolution for forecast initiated at (a-b) T-60 hours (2020-05-18 0000Z), (c-d) T-36 hours (2020-05-19 0000Z), (e-f) T-12 (2020-05-20 0000Z) hours before landfall.	86

5.8	Digitized location of inundation resulting from embankment breaching (red), flooding of low-lying unembanked area (orange), and embankment overflow (cyan) overlaid on a false-colour image composite derived from B12, B11, and B4 channels of Sentinel-2 during April 2020. The grey patches are the inundated regions predicted by the model, as shown in the hindcast experiment. The polders are shown with cyan outlines.	88
6.1	The population density in the Bengal delta covering Bangladesh and India. A subset of cyclones that made landfall in past decades with the number indicating the associated casualty and the colour indicating the strength of the cyclone. Inset shows the location of the study area. TD and TS correspond to Tropical Depression and Tropical Storm, respectively. The colour-coded lines show the cyclone strength along its track in the Saffir-Simpson scale. For 1970 Bhola cyclone, the wind speed is not available and shown in grey (NA). The associated number at the head of the cyclone tracks refers to the number of casualties. . . .	95
6.2	(a) Model domain with arrows indicating the open boundaries. (b) Distribution of Manning coefficient.	100
6.3	(a) Maximum simulated water level during cyclone Sidr. Comparison of simulated and observed water level during cyclone Sidr at (b) Charchanga, (c) Coxsbazar, (d) Hironpoint, and (e) Khepupara. The station locations are shown in (a). . . .	103
6.4	a) Spatial distribution of the paths of the cyclones that make landfall along the coast of Bengal delta. Each square bin is 20 km wide. A small subset of cyclones trajectories is shown in the inset. (b) Distribution of maximum wind speed of the synthetic cyclones compared to the JTWC dataset, (c) Annual distribution of the occurrence of the synthetic cyclones compared to JTWC dataset.	105
6.5	(a) Inundation extent and corresponding water level at 50-year return period. (b) Water level for the 50-500 years return period expressed as a multiple of the yearly mean tidal high-water level along the nearshore dash-dotted line shown in (a).	107
6.6	Inundation extent and corresponding water level at (a) 5-year, (b) 10-year, (c) 20-year, (d) 50-year, (e) 75-year, (f) 100-year, (g) 250-year, (h) 500-year return period.	108
6.7	Water level as a function of the return period, expressed in multiple of the 50-year return period water level, along the dashed lines shown in red for (a)-(b) Ganges-Brahmaputra-Meghna estuary, (c)-(d) Pussur estuary, (e)-(f) Hooghly estuary. The x-axis is the distance from the mouth of the estuary, in km. The background shading in panels (a), (c) and (e) shows the bathymetry in m.	109
6.8	(a) Spatial coverage of flooding at various n-year return period estimated from the model. Gray colorbar shows the population density per square kilometre. (b) Number of people affected at various n-year water level return period.	113
6.9	(a) Inundation extent and corresponding water level at 50-year return period (REF) computed with coupled tide-surge-wave model and $\alpha = 0.1$. This is same as Figure 6.5. (b) Difference in 50-year return period water level between REF and the ensemble computed with simulations from only tide-surge coupled model including seasonal variability of sea level and without wave coupling (TSS). (c) Difference in 50-year return period water level between TSS and the ensemble computed with simulations from only tide-surge coupled model without seasonal variability of sea level (TS). (d) Difference in 50-year return period water level between REF as shown in (a) and REF but $\alpha = 1$ (typically used value).	115
7.1	Regionally distributed Manning parameter. A constant value of $n = 0.07$ is imposed over land (not shown).	124

7.2	Maximum modelled water level during cyclone Sidr with (a) default wave breaking parameterization ($\alpha=1$), (b) the parameterization used in this study ($\alpha=0.1$), and (c) adaptive parameterization proposed by (Pezerat et al., Accepted). (d) and (e) shows the maximum water level difference between adaptive and $\alpha = 1$ and $\alpha = 0.1$ respectively. (f) shows the maximum water level difference between $\alpha = 0.1$ and $\alpha = 1$	127
7.3	50-year return period water level obtained from the statistical-deterministic analysis of our large ensemble of simulations for (a) current mean sea level conditions and (b) in a 1 m sea level rise scenario (+1m SLR).	128

LIST OF TABLES

2.1	Listing of providers of hydrographic charts.	14
2.2	List of digitized BNHOC charts, scale and year of survey.	15
2.3	In-situ dataset water level dataset.	17
3.1	Spectral characteristics of the Sentinel-2 bands used.	33
4.1	Amplitudes (A) and error (σ_s) are in centimetres, phases (ϕ) is in degrees. Because of their location far upstream in the estuaries, Diamond Harbour and Chandpur are not represented in global tidal models (FES, GOT, and TPXO) .	57
5.1	Data sources for the model forcings. NA stands for Not Applicable.	84
5.2	Computing environment used during the forecast	85
5.3	Performance of tidal model at tide-gauge locations.	91
6.1	Simulated maximum water level for the cyclones shown in Figure 6.1. V_{max} is the maximum wind speed in knots, WL_{max} is the simulated maximum water level range over the delta shoreline in meters. For 1970 Bhola cyclone, the storm surge simulation was not possible thus listed as NA (not available).	102
7.1	Estimated complex error with regionally distributed Manning shown in Figure 7.1 (New Manning) compared to the one presented in this thesis (Current Model).	125

CHAPTER 1

INTRODUCTION AND MOTIVATION

“A journey of thousand miles begins with a single step” – Lao Tzu

1.1 Introduction

Les deltas fluviaux font partie des zones les plus densément peuplées du monde (Ericson et al., 2006). Plus de 4% de la population mondiale vit dans les zones de deltas, qui n’occupent que 0,57% de la surface terrestre (Edmonds et al., 2020). 89% de la population des deltas vit dans la ceinture tropicale, qui est également sujette à l’activité des tempêtes cycloniques (Woodruff, Irish, & Camargo, 2013). On estime que 1,3% de la population mondiale vivant sur le littoral est exposée à une inondation due à une tempête centennale, dont 41% vivent dans les deltas côtiers. De plus, étant des régions de basse altitude chargées de sédiments, les deltas sont très exposés à l’impact de l’élévation du niveau de la mer et de la subsidence (Becker, Karpytchev, & Papa, 2019). L’un de ces deltas densément peuplés et très vulnérables est le delta du Gange-Brahmapoutre, avec une densité de population de plus de 1000 habitants par kilomètre carré (Becker et al., 2020).

Le delta du Bengale, qui est le plus grand delta du monde, est situé au nord de la baie du Bengale. Trois grands bassins fluviaux - le Gange, le Brahmapoutre et la Meghna (GBM) - forment ce méga-delta d’environ 100 millions d’habitants (Brammer, 1990). Environ 30 millions de personnes vivent à 5 m ou moins au-dessus du niveau moyen de la mer (Mean Sea Level, MSL).

Le continuum rivières-estuariers-océan du delta du Bengale est exposé aux ondes de tempête et aux inondations dues aux marées. Le nord du Golfe du Bengale connaît les plus grandes amplitudes de marée de ce bassin océanique. En particulier le long de la côte Sud-Est du delta, l’amplitude de la marée atteint 5 m (Sindhu & Unnikrishnan, 2013). Le niveau moyen de la mer varie également considérablement selon les saisons, le niveau de la mer étant plus élevé d’environ 70 cm pendant la mousson d’été (août) que pendant l’hiver (février) (Tazkia et al., 2017). La région est également soumise à de puissantes tempêtes cycloniques qui sont le facteur déterminant dans l’occurrence des niveaux d’eau les plus extrêmes le long de la côte de la baie du Bengale (Antony, Unnikrishnan, & Woodworth, 2016; Chiu & Small, 2016). En moyenne, un cyclone majeur touche terre dans cette région tous les trois ans. Chaque année, 5 à 6% seulement des cyclones tropicaux mondiaux prennent naissance dans le Golfe du Bengale (Alam & Dominey-Howes, 2014; Ali, 1996). Cependant, plus de 75% des victimes mondiales associées aux cyclones sont enregistrées dans cette région. La situation en terme de mortalité dans le delta du Bengale est encore pire, en effet le Bangladesh représente à lui seul 50% des victimes

mondiales dues aux cyclones alors que seulement 1% des cyclones mondiaux touche terre dans la région du delta du Bengale (Alam & Dominey-Howes, 2014; Ali, 1999).

Un débit fluvial saisonnier important, de fortes marées et les puissants cyclones avec leurs ondes de tempête associées façonnent la dynamique de l'inondation dans le continuum rivières-estuariens-océan du delta du Bengale. Cette région souffre d'un manque criant d'observations in situ des hauteurs d'eau, des événements cycloniques et de l'inondation associée à une échelle de temps pertinente. La bathymétrie et la topographie sont mal cartographiées dans cette région, ce qui complique les activités de modélisation haute-résolution suffisamment précise dans le continuum hydraulique, de même que la compréhension des processus de propagation de la marée (Krien et al., 2016), de la houle et de l'inondation (Krien, Testut, et al., 2017). En outre, le delta du Bengale s'affaisse à un rythme inconnu et potentiellement rapide (Becker, Karpytchev, & Papa, 2019). Cette région est l'une des plus vulnérables au changement climatique et à l'élévation du niveau de la mer (Oppenheimer et al., 2019). La compréhension fine de la dynamique des inondations par la marée, des ondes de tempête sous le climat actuel et futur est une priorité pour la survie de la vaste population vivant dans cette région.

1.2 The river deltas

Deltas are landforms created by the deposition of a large volume of sediments carried by rivers to a relatively calm water body - an ocean, a lake, another river, or even land (Reading, 2009). The formation of world deltas happened over a timescale of thousands of years (Ibáñez et al., 2019). The downstream condition of water body dictates the formation of a delta and the type of delta to be formed (Reading, 2009). These conditions include the stream velocity, mean water level, tide and wave activity. The delta environments are nutrient-rich. The natural supply of food makes deltas ecologically diverse and attractive for human settlement (Ericson et al., 2006).

Deltas have been a focus for human settlement for thousands of years (Kennett & Kennett, 2006). Most world civilisations grew around the rivers and ocean coastlines by exploiting the food resources provided by the sea and fertile soils (Bianchi, 2016). These sediment-laden lands are well suited for the development of agriculture, with an extensive network of water body connectivity to use for transportation. The trade and commerce fuelled by the agricultural production and transportation advantage promoted urbanisation, attracting even more people to settle on these low-lying regions. Indeed, the most densely populated cities around the world are in the deltas (Small & Nicholls, 2003). Figure 1.1 shows the global distribution of deltaic areas and the associated population estimated by (Edmonds et al., 2020). They estimate that in 2017 330 million people were living on the river deltas, which occupies only 0.57% of earth's land surface area. Most large populated deltas are in the mid and low latitudes, especially in Asia (Becker, Karpytchev, & Papa, 2019).

Natural deltas are a balance between the sediment delivery, its deposition and reworking with marine processes like river flow, tide, waves, and subsidence (Swenson, 2005; Syvitski, 2008). The dense population adds the anthropogenic processes to the natural delta systems (Nicholls et al., 2019). The land use is changing rapidly in the river basins, and the development of flood control structures like dams is reducing the sediment supply (Syvitski, 2005). On the other hand, large population accelerated the sediment compaction through groundwater removal,

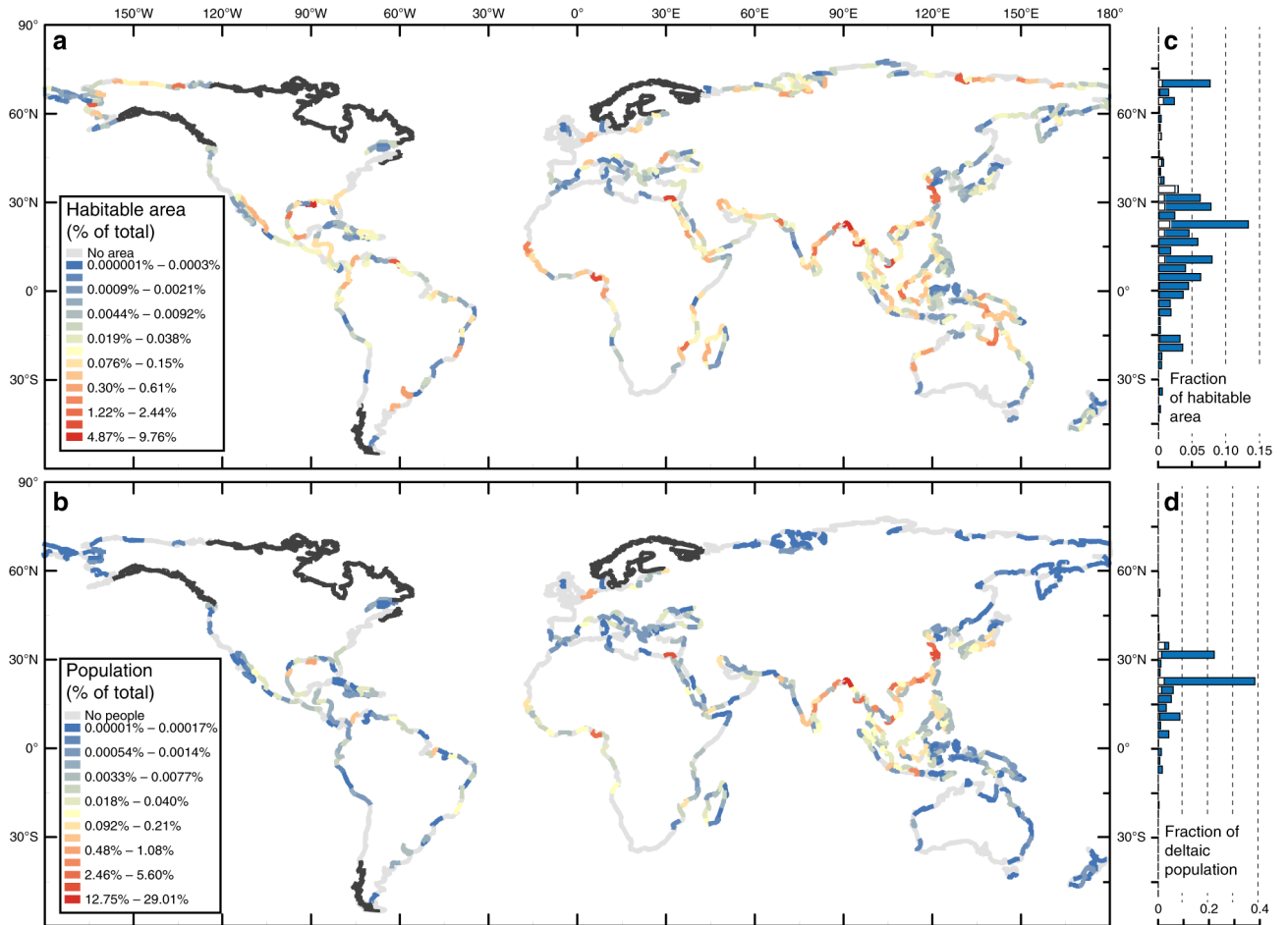


Figure 1.1: Global distribution of deltaic area (a) and population (b). The total deltaic area and population per 3° lengths of coastline. The colour along the lengths of coastlines shows the percentage of area or population they contain relative to the entire dataset. Black lines are unmapped shorelines. Histograms show the latitudinal distribution (3° bins) of habitable area (c) and population (d). White bars in the histograms show the proportion of area and people in the 100-year storm surge floodplain. (From Edmonds et al. (2020)).

flood protections, and urbanisation (Ericson et al., 2006; Syvitski et al., 2009). These factors have increased subsidence, which combined with erosion is causing loss of land in some major deltas (Syvitski et al., 2009), e.g., Nile (Stanley, 1996), and Mekong (Anthony et al., 2015).

Floods, particularly riverine floods, are an integral part of the delta. These landforms typically sit near sea level and are highly exposed to climate-induced sea level rise and subsidence (Becker, Karpytchev, & Papa, 2019). Additionally, as shown by Edmonds et al. (2020), 89% of the deltaic population lives in the tropical belt, which is also prone to cyclonic storm activity (Woodruff, Irish, & Camargo, 2013). An estimated 1.3% of the global population is exposed to 1 in 100-year storm surge flooding around the world coastline, among which 41% lives in the coastal deltas. One of such densely populated and highly vulnerable deltas is the Ganges-Brahmaputra with population density more than 1000 people per square kilometre (Becker et al., 2020).

1.3 Inundation in the Bengal delta

1.3.1 Bengal delta

The Bengal delta, the largest delta in the world, is situated in the head of Northern Bay of Bengal. Three large river basins - Ganges, Brahmaputra, and Meghna (GBM) – forms this mega delta of about 100,000 km² (Brammer, 1990). In this densely populated region, more than 150 million people make their living. Among several megacities, Dhaka, Chittagong, and Calcutta are notable. Bangladesh and India share the administrative jurisdiction over the Bengal delta, with Bangladesh occupying most of the delta land (Figure 1.2).

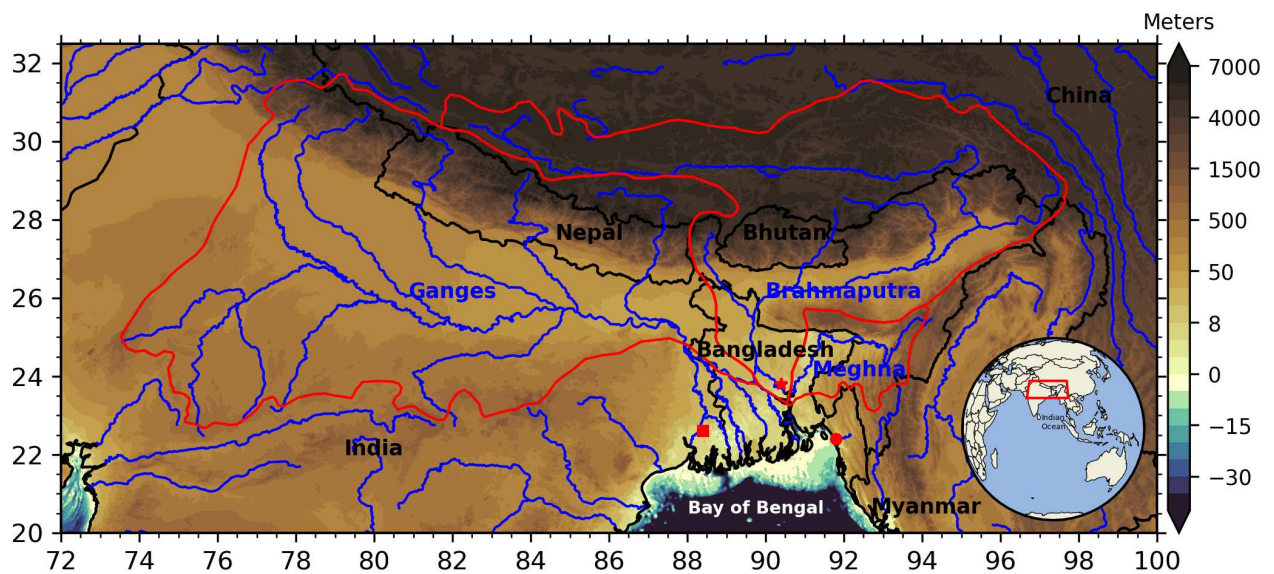


Figure 1.2: The extent of the Ganges-Brahmaputra-Meghna catchment area and the Bengal delta sitting on its outlet to the Bay of Bengal. The major rivers are shown in blue. Red outlines the extent of each basins catchment area. The topography is from SRTM dataset and bathymetry is taken from GEBCO dataset. Three major cities – Dhaka (star), Chittagong (circle), Calcutta (square) are shown in the map.

The combined GBM catchment area consists of about 1.75 million km² covering Bangladesh, India, China, Nepal, and Bhutan. The Ganges river drains the Himalayas in northern India for about 2500 km before entering the delta. This basin receives about 1200 mm of yearly rainfall over about 1 Million km² catchment area producing an average discharge of about 11000 m³/s (Mohammed et al., 2018). The river divides into two main distributaries when entering the delta. The main distributary - the Ganges, locally known as the Padma - flows south-eastward meeting Brahmaputra inside Bangladesh. The other distributary continues southward, flowing through West Bengal in India as the Hooghly river. The Brahmaputra river, on the other hand, originates near the Mount Kailash, located on the northern side of the Himalayas in the Burang County of Tibet. It receives an annual average rainfall of 1900 mm over a catchment area more than half-million km². It flows eastward through southern Tibet, break through the Himalayan mountain range and continues through Arunachal Pradesh of India. Afterwards, it flows southwest through the Assam Valley as the Brahmaputra and enters Bangladesh flowing

southward until merging with the Ganges. Over the catchment area, the water flow creates a complex network of 230 rivers, 57 of these rivers are cross-boundary. Most of the discharge that gets passed through Bengal delta and Bangladesh comes from cross-border runoff. The large volume of discharge generated in the GBM is estimated to inundate one-fifth of Bangladesh every year (Mirza, Warrick, & Ericksen, 2003). Over 1 billion tons of sediment is discharged annually through this extensive river network (Goodbred & Kuehl, 1999).

1.3.2 Types of flood in the Bengal delta

The deltaic region of Bangladesh experiences three types of floods - flash floods, riverine floods, and coastal storm surges (Figure 1.3). The flash flood is a typical feature of the Eastern and Northern part of the delta - around the border of Bangladesh and India (B. Roy et al., 2019). Rivers in these hilly regions are steep. River discharge and water levels show a characteristic sharp rise during heavy rainfall and cause sudden flooding (M. K. Das et al., 2019). The time scale of a flash flood is typically 6-24h. Flash floods mostly occur during the pre-monsoon season (April-May), and typically cause massive damage to the winter crops (B. Roy et al., 2019).

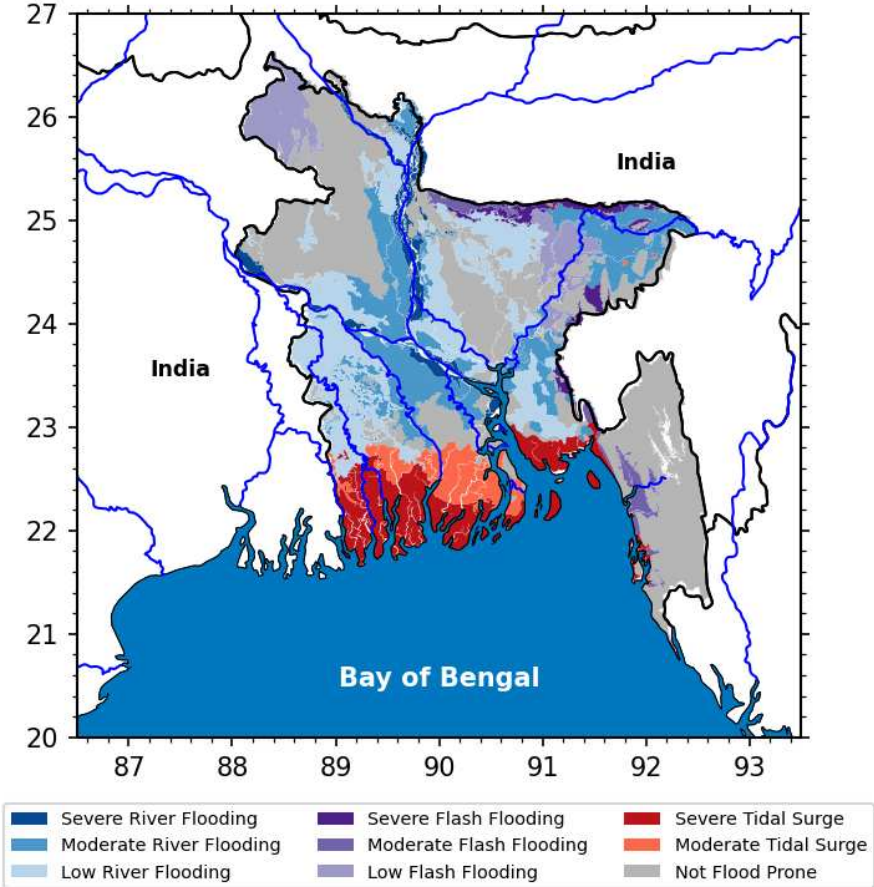


Figure 1.3: Exposure to floods in the Bangladesh part of the Bengal delta based on the classification of Bangladesh Agricultural Research Council (BARC).

Riverine floods (also called monsoon floods) occur when a large volume of basin discharge saturates GBM rivers and their tributaries (Brammer, 1990). As the monsoon onset over the re-

gion takes place around June, these three basins receive monsoonal rainfall in spells. Practically the whole delta population is prone to riverine flood. For example, during the 1998 flood event, more than 75% area of Bangladesh was inundated (Mirza, Warrick, & Ericksen, 2003). These floods typically occur during monsoon, when heavy rainfall from the large watersheds discharges through the GBM river system. The typical timescale of these floods is in weeks (Brammer, 1990). These riverine floods are indeed a bane and a boon in this region (Brammer, 2016). On the one hand, these riverine floods can cause substantial economic and agricultural damage. Floods also cause disruption of the supply of safe drinking water and interruptions of sanitary systems. Consequently, water-borne diseases spread rapidly during flood. On the other hand, they recharge the nutrient contents of the agricultural lands, they enhance fish production, and flush salinity seaward, allowing seasonal agricultural crop production in the southern coastal region (Nowreen, Jalal, & Khan, 2013).

The southern coastal region is also exposed to storm surges and tidal flooding. The northern Bay of Bengal experiences one of the largest tidal range in this ocean basin. Particularly along the Chittagong coast, the tidal range reaches as high as 5 m. In this macro-tidal region, the tide is mostly semi-diurnal (Sindhu & Unnikrishnan, 2013). There is a substantial seasonal variation in the mean sea level too. The sea level sits about 70 cm higher during the summer monsoon (August), compared to the winter (February) (Tazkia et al., 2017). The strong tidal waves penetrate far inland (more than 100 km) and used to flood the low-lying southern delta plain from time to time (Nowreen, Jalal, & Khan, 2013). Government of Bangladesh has established an extensive network of 139 polders (enclosed areas with embankments) during the second half of the 20th century to promote agriculture in this vast region (World Bank, 2005). These embankments, typically earthen, protected inland areas from periodic tidal flooding, they reduced salinity and increased arable farmland. These improvements also induced an increase in the overall population density of the region. However, the embankment system does not cover all the exposed areas in this fluvio-tidally active region. During a strong monsoon, monsoonal depressions combined with spring tides sometimes cause flooding in the unprotected regions. In the embanked area, the earthen embankments can fail from time to time, and the polders get tidally flooded. Lack of maintenance over a long time, illegal water control for aquaculture, and shoddy repair of the damaged embankments induce these failures (Nowreen, Jalal, & Khan, 2013).

1.3.3 Storm surge problem in the Bay of Bengal

Cyclonic storm surges are the reason behind most extreme water level events along the coastal Bay of Bengal (Antony, Unnikrishnan, & Woodworth, 2016; Chiu & Small, 2016). On average, one major cyclone makes landfall in this region every three years. Seasonally, the cyclonic activity shows a distinct bi-modal character - one cyclone-prone period during the pre-monsoon season (March-May), and another during the post-monsoon (September-December) (Alam & Dominey-Howes, 2014). High sea surface temperature over the Bay of Bengal (in excess of 28°C) and low vertical shear in the tropospheric wind creates an ideal situation for a depression to intensify into a cyclone during these two seasons. During monsoon, the vertical shear is typically too high for a cyclone to intensify.

Yearly, a mere 5-6% of the global tropical cyclones originate in the Bay of Bengal (Alam & Dominey-Howes, 2014; Ali, 1996). However, more than 75% of the global casualties associated with cyclones has occurred in the region surrounding this ocean basin. The mortality situation over the Bengal delta is even worse. Among this 6% of global cyclones, only 1% makes landfall in the Bengal delta region (Figure 1.4). Yet, Bangladesh alone accounts for 50% of the global casualties (Alam & Dominey-Howes, 2014; Ali, 1999).

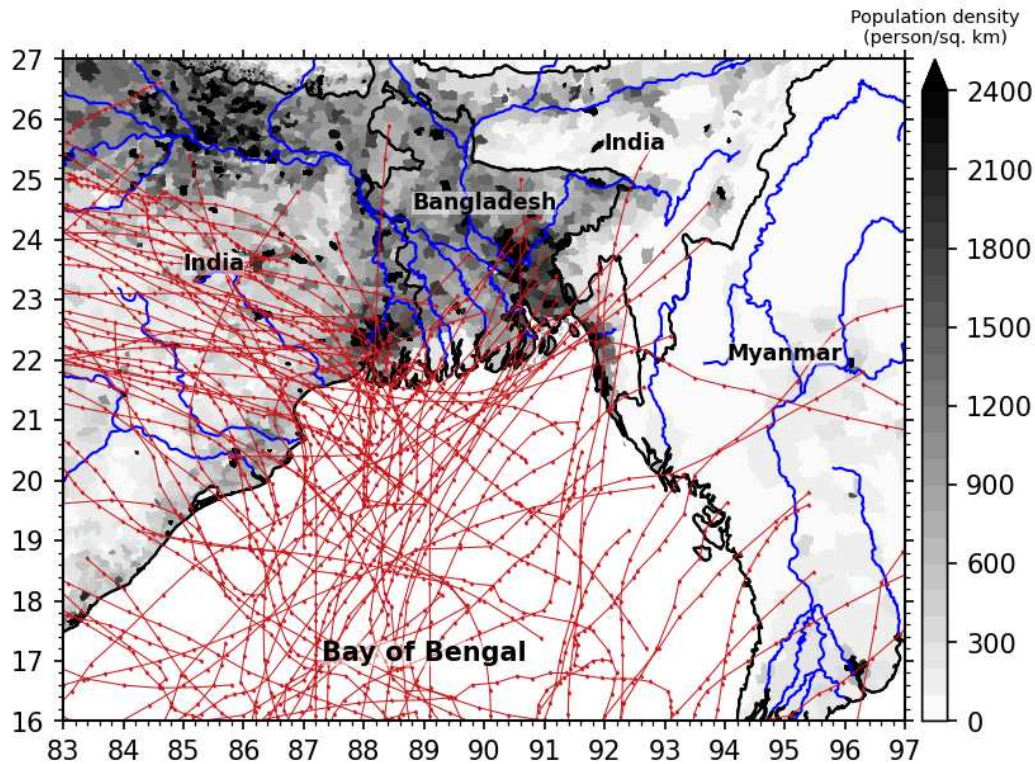


Figure 1.4: Population density over the Bengal delta. The black lines show the storms that made landfall over the region over the last 50 years based on IbTracs dataset (Knapp et al., 2018).

These cyclonic storms cause damage and loss of life along their way. Under certain conditions of tide, these cyclonic storms can bring massive tidal surges, reportedly reaching levels over 5-6 m, and locally as high as 10 m (Frank & Husain, 1971). On a deltaic plain such as the Bengal delta, where most of the land sits below 5 m above mean sea level (MSL), a strong storm surge can induce massive damage. Indeed, the Bengal delta is known for its exposure to large storm surges. One-in-five major storms over this region had surge higher than 5 m (Needham, Keim, & Sathiaraj, 2015).

The known history of landfalling cyclones causing large casualty in the Bengal delta dates back to as far as 1484 AD (Alam & Dominey-Howes, 2014). While a large number of casualties (~200 thousand) is associated with these far historical events, the reliability of the estimates is relatively low. In the recent decades, few of the notable cyclones include the 1970 Bhola cyclone that claimed an estimated 300 thousand lives (Frank & Husain, 1971) and 1991 cyclone Gorky which claimed about 150 thousand lives (Khalil, 1993). Both of these cyclones made landfall around the northern part of the Bengal delta shoreline during high tide. In recent

years, the major cyclones typically made landfall around the central part of the delta (Alam & Dominey-Howes, 2014). The associated death toll has also decreased remarkably over the last two decades. For example, cyclone Sidr, a category five cyclone on the Saffir-Simpson scale that made landfall in 2007, claimed 3406 lives (Paul, 2009). This situation further improved for recent cyclones, e.g., cyclone Aila in 2009 (~200 casualties), cyclone Amphan in 2020 (~100 casualties). This improvement is due to a coordinated effort of the Bangladesh and Indian governments' pre-disaster preparedness through increased shelter infrastructure, coordination of efforts to disseminate available information of any impending storm surge hazard, and evacuation of millions of people to safety at cyclone shelters before the cyclone landfall (Paul & Dutt, 2010). Widespread use of mobile phones greatly complemented this evacuation and dissemination effort. At the same time, the economic damage has increased over time, leading to a slower recovery and a migration pressure from the most vulnerable regions (Penning-Rowsell, Sultana, & Thompson, 2013).

1.4 Bengal delta continuum and knowledge gaps

A robust seasonal river discharge, strong tides, powerful cyclones with their associated storm surges shape the dynamics of the inundation in the rivers-estuaries-ocean continuum of the Bengal delta. It is considerably hard to draw a continuum boundary for a flat region like the Bengal delta. However, from the observed reach of the tide, the delta can be divided into roughly two parts. The upper part of the delta covers the north of the Ganges and the combined Ganges-Brahmaputra. The river distributaries in this part are mostly affected by the riverine floods. Along the Brahmaputra river, the tidal effects can be considered negligible compared to the water level variation from basin discharge. The southern part and its surroundings can be considered as the lower part of the delta. In this region, the inundation events begin to be modulated by the tide. For this study, the term 'continuum' identifies the southern part of the Ganges-Brahmaputra-Meghna river network.

The continuum region of Bengal delta suffers from a lack of consistent in situ measurements of the tide, surge, and associated inundation at the relevant timescale. The datasets are in general, not public. The measurement technique typically consists of a manual recording of water level from manual water level gauges. The records are intermittent, typically once daily to five times in a day. The vertical referencing of these gauges is generally not well known and reported to experience various degrees of unaccounted vertical displacement. These factors together make it rather difficult to study the short period flooding phenomenon (Philip et al., 2018). However, with sophisticated regionalization approaches, it appears to be possible to unveil consistent estimates of the long-term relative sea level rise over this region (Becker et al., 2020).

Estimation of the inundation also suffers from a general lack of topographic knowledge. Bengal delta continuum has a characteristic low topography (less than 5 m above MSL) and a vast network of distributaries. The satellite-derived estimates of the land topography are often erroneous by several meters in this region (Krien et al., 2016), just like in similar deltaic regions (Minderhoud et al., 2019). What is more, the bottom of distributary channels is not at all mapped by satellite observation. The knowledge of the bathymetry of the coastal zone also

suffers from a similar lacking. The global bathymetric datasets are typically too shallow (by several meters), with large-scale artefacts (Krien et al., 2016). As the coastal bathymetry and topography strongly control nearshore water dynamics, to develop a realistic tidal model of the area has been a significant challenge (Krien et al., 2016; Sindhu & Unnikrishnan, 2013). The knowledge of the protective defences along the coastal belt is also lacking. While some information is available regarding the spatial layout of these embankment systems, the height of these embankments is poorly known (Krien, Testut, et al., 2017; Nowreen, Jalal, & Khan, 2013). The available records are mostly of the design heights during their construction in 1960s and 1970s. Anecdotal evidence suggests the designed embankment has been through substantial spatially-variable height changes, mostly degradation from insufficient maintenance. This missing piece of information regarding the embankment height has a paramount importance on the flooding processes, particularly regarding inland inundation (Krien, Testut, et al., 2017). These lacks in the knowledge of topography hinder high-resolution and accurate modelling activity across the hydraulic continuum.

Another significant knowledge gap, in the context of inundation, is the assessment of land subsidence. The Bengal delta is subsiding at an unknown, and potentially diverse rate (Becker, Karpytchev, & Papa, 2019). Aside from the natural sediment compaction (Krien et al., 2019), increased groundwater extraction and general restriction of the sediment deposition are few of the anthropogenic reasons behind the diverse subsidence rate. Large scale tidal channel infilling has occurred over the continuum during the last decades (Wilson et al., 2017). The sediment starvation inside the polder created a situation where the interior of the polders is subsiding through compaction (Auerbach et al., 2015). This process sometimes lowers the topography down to below MSL. Consequently, it is increasing the water logging inside the polder, the soil salinity, and the risk of long-lasting tidal or storm surge inundation.

The impact of climate change on inundation dynamics, being all but certain, is another open-ended question. The scientific consensus considers the Bengal delta as one of the most vulnerable to climate change and sea level rise impacts (Oppenheimer et al., 2019). The riverine floods are expected to be more frequent (Mohammed et al., 2018), as well as with a substantial increase in extreme rainfall events (Khan, Islam, et al., 2020; Khan, Islam, et al., 2019). At the same time, the sea level is rising consistently, with an acceleration during the last decades (Oppenheimer et al., 2019). By the end of the current century, sea level rise could reach about 1 m (Oppenheimer et al., 2019). The impact of sea level rise on river flooding, tide, and bathymetry is expected to be strong. Robust quantitative estimations of these impacts are mostly unknown due to the lack of observations as mentioned earlier and well-suited modelling tools. The inundation and damage from storm surges are also expected to be higher under future sea level condition (S. Rahman et al., 2019). The published modelling exercises on the change of the storm frequency yield also unclear conclusions with conflicting results (Bacmeister et al., 2016; Emanuel, 2013; Gettelman et al., 2017; Vishnu, Sanjay, & Krishnan, 2019). Some sensitivity experiments suggest that with higher sea surface temperature, the storms could potentially get more intense, resulting in higher storm surges (Mittal et al., 2019; Tasnim et al., 2014).

1.5 Scientific questions and study approach

In recent years, our capability to understand the various water level mechanisms at short and long time scale has improved. This improvement is due to two primary sources. First is the improvement in the level of realism of the bathymetric datasets, and second is the improvement in cross-scale hydrodynamic modelling systems. It is well known that the quality of tidal modelling strongly depends on the quality of the bathymetry. Krien et al. (2016) achieved an improved bathymetry by incorporating soundings from a handful of navigational charts. As a follow-up, we assembled a new bathymetry dataset based on Krien et al. (2016) with additional 34 new navigational charts over the coastal part of the Bengal delta. The development of a new hydrodynamic modelling framework followed this new bathymetric dataset.

In this assembled bathymetry, however, the intertidal region of coastal Bangladesh is poorly represented. High-resolution spaceborne optical imagery such as Pleiades, Proba-V, Sentinel-2 is already providing data over the area of interest at moderate to high space-time resolution. One benefit of such satellites consists of the accurate monitoring of the intertidal area. In the Bengal delta continuum, the intertidal area goes through dynamic changes due to erosion and accretion. Intertidal regions are a large modulator of the nearshore tide, surge, and wave, which makes it essential to monitor these regions periodically with enough accuracy for high-resolution nearshore modelling.

The first objective of this study is to explore how the synergy between the remote sensing and hydrodynamic modelling can provide us with relevant information about the topography of the nearshore intertidal zone.

The mapping of intertidal topography provides an estimate of the extent of active tidal influence along the shorelines. It also points out the morphologically active region at seasonal timescales. Indeed, being a macro-tidal region, the tide is the primary source of water level variability in this region. In the context of global sea level rise, which is projected to continue with a high level of confidence, the nearshore coverage of tidal flooding will change, as well as the nearshore depth. Over the past decades, along the world shorelines, the change in tides has been observed. Only a handful of previous studies explored the tidal changes over the Bengal delta region. Given the strong interdependence expected between the tidal high-water level and the probable inundation in this low-lying region, it is essential to understand to what extent the global change in mean sea level will change the characteristics of the tide in the coastal region of Bengal delta.

The second objective of this thesis is to study the sensitivity of tidal parameters to sea level rise over the Bengal delta, from its coastal part to its estuarine network.

The Bengal delta is prone to storm surges which combine with the tide to actuate the extreme spectrum of the water level variability. The modelling of storm surges in this data-poor region is challenging, given the multitude of forcing factors. Notably, one of the hypotheses is that a successful model of storm surge requires a good representation of the wind and atmospheric

pressure as forcing factors to the model while incorporating necessary non-linear physics of tide, surge, waves and their interactions. The inland inundation that occurs during the storm surge events is even harder to predict.

The third objective is to study an observed storm to understand what mechanisms are necessary to model these events, and what are the major challenges to model the inundation process.

Observations related to cyclonic storms and surges are hard to obtain over the Bengal delta to assess the exposure to such storm surges at a relevant temporal and spatial scale. The available storm track, wind intensity, and pressure drop records are also not always available and non-uniform. This lack of reliable storm records makes it challenging to model past storm events. Additionally, the footprint of the extreme storm surge during a given storm is relatively small (a few dozens of km typically) compared to the extent of the Bengal delta shoreline (several hundreds of km). This space scale makes it difficult to reliably estimate the risk of extreme water levels along the Bengal delta shoreline consistently from a small number of recorded cyclones. Over the last decade, cyclone climatology modelling has matured to fill this gap. Sophisticated methods combining the probabilistic nature of the cyclone genesis and the deterministic nature of its evolution has emerged (Emanuel et al., 2006). These methods are providing a high-resolution spatiotemporal representation of the climatic cyclonic activity in the form of a large number of cyclones. These ensembles of synthetically-generated, but statistically and physically consistent cyclones pave the way to tackle the problem of data unavailability in analysing the storm surge inundation hazard along the coast of Bengal delta.

The fourth objective of this study is to make a robust and consistent estimation of the inundation hazard along the shoreline of the Bengal delta.

1.6 Organization of the thesis

This thesis document is structured as an article-based thesis and divided into six chapters. Following the introduction presented in this chapter, Chapter 2 presents the data and the model, which together form the primary means to conduct the studies in the subsequent chapters.

Chapter 3 addresses the first question of this thesis. In this chapter, I develop an automated methodology to extract the shorelines from moderate resolution (10 m) multi-spectral imagery acquired by Sentinel-2 satellite. Combining the spatial information of the extracted shoreline with the temporal evolution of water level estimated from the numerical model, I developed a high-resolution representation of the topography of the intertidal domain.

Chapter 4 tackles the question of the sensitivity of coastal tide to the ongoing sea level rise over the Bengal delta. First, I analyse a long observational record of a tide gauge for insight. Then I pursue numerical modelling in light of global sea level rise projections to understand the sensitivity of tide to sea level rise. I compare the numerical modelling results with an analytical model to understand the controlling factors of the future evolution of tidal water level.

Chapter 5 extends the modelling to a specific storm surge case. With satellite and in situ observations, I look into the contribution of the various components of a storm surge. From a secondary field survey, I explored the main challenges in reproducing an observed storm surge flooding in the Bengal delta.

Chapter 6 combines the storm surge model with a statistical storm model to systematically assess the hazard of cyclonic inundation along the coast of the Bengal delta.

Finally, in Chapter 7, I present the overall conclusions of this thesis and the perspectives for future research. This chapter summarises the thesis with its theoretical contribution, practical impacts, and implications. The chapter ends with an outlook for future research.

CHAPTER 2

HYDRODYNAMIC MODELING: DATA AND METHODS

“All our knowledge begins with the senses, proceeds then to the understanding, and ends with reason. There is nothing higher than reason.” – Immanuel Kant

2.1 Introduction

The hydrodynamic modelling over the northern Bay of Bengal and the continuum of the Bengal delta has been a long-standing challenge (Krien et al., 2016; T. Murty, Flather, & Henry, 1986). This deltaic region is characterized by a macro-tidal regime, with a tidal range reaching up to 5 m in the north-eastern part of the Bay (Sindhu & Unnikrishnan, 2013). Discharges from three major river basins – Ganges, Brahmaputra, and Meghna – pass through the delta (Brammer, 2014). The prevailing Indian summer monsoon broadly defines the flow pattern of these basins (Brammer, 1990; Mirza, 2002). About 1Gt of sediments also gets transported and distributed through the complex riverine network downstream to the Bay of Bengal (Goodbred & Kuehl, 1999). The combination of a sizeable fluvial-sediment discharge and a strong tide gave rise to a complex hydro-morphologic system (Goodbred & Kuehl, 1998). Land subsidence - a process relatively unexplored in this region - enhances the natural complexity even further (Becker et al., 2020). Moreover, the human modifications of the land-use/land-cover and introduction of large-scale coastal structures exacerbate the flooding related issues (Auerbach et al., 2015).

Understanding this complex interaction between tide, river discharge, topography, and anthropogenic factors requires an extensive, well-distributed monitoring network of the relevant environmental parameters - such as water level/currents, topography and bathymetry. However, like many other deltaic regions, the existing monitoring systems are often not well-equipped and well-distributed to de-mystify the plethora of involved physical processes (Antony, Unnikrishnan, & Woodworth, 2016; Chiu & Small, 2016). In such cases, hydrodynamic modelling can provide useful utility (Sindhu & Unnikrishnan, 2013). Numerical modelling provides a mean to understand these complex systems through experimentation, hereby working around the limited amount of available observations (Krien, Testut, et al., 2017; Tazkia et al., 2017).

In the course of this thesis, I have developed a new model setup to study the inundation dynamics over the Bengal delta. In this chapter, I describe the development of the bathymetric dataset that forms the basic input for the development of the hydrodynamic modelling framework (Section 2.2). Then I list the observations that guided the model development (Section 2.3). The description of the dataset is followed by the representation of the hydrodynamic model to simulate the tide and storm surges (Section 2.4 and 2.5). To that extent, the methods and the tools used for the development of the model configuration and the data used for the forcing

of the model are documented. The following section (Section 2.6) documents the approach to calibrate and validate the model for tide. A brief summary is presented in the last section.

2.2 Bathymetry assembly

I built the bathymetry used here based on the work of Krien et al. (2016). The significant improvement of the bathymetry assembled by Krien et al. (2016) is in the nearshore zone of the northern Bay of Bengal. Instead of the publicly available global bathymetric datasets (e.g. GEBCO (Kapoor, 1981), ETOPO), they have relied on the digitization of hydrographic charts published from local and international hydrographic agencies (Table 2.1). Their dataset incorporates six navigational charts comprising 16500 points, covering the coastal part of the submarine delta (20.5°N-22°N). These large-scale navigational charts were published by National Hydrographic Office (NHO) of India, Bangladesh Navy Hydrographic and Oceanographic Center (BNHOC), and Mongla Port Authority (MPA). Along the Hooghly estuary, Krien et al. (2016) incorporated an additional 123000 sounding points from the maps provided by the Inland Waterways Authority of India (IWAI) for Hooghly estuary. They found that the submarine part of the delta is too shallow in GEBCO compared to the navigational charts. On average, this difference amounts to about 3 m. They also found several canyon-like artifacts in the GEBCO, particularly around 89.5°E.

Table 2.1: Listing of providers of hydrographic charts.

Acronym	Full Name	Link	Remark
GEBCO	The General Bathymetric Chart of the Oceans	https://www.gebco.net/	Global
ETOPO	ETOPO1 1 arc-minute global relief model	https://www.ngdc.noaa.gov/mgg/global/global.html	Global
NHO	National Hydrographic Office	https://hydrobharat.gov.in/	India
BNHOC	Bangladesh Navy Hydrographic and Oceanographic Center	http://bnhoc.navy.mil.bd/	Bangladesh
MPA	Mongla Port Authority	http://www.mpa.gov.bd/	Bangladesh
IWAI	Inland Waterways Authority of India	https://iwai.nic.in/	India

As an update to their nearshore digitized sounding dataset, we incorporated a set of 34 new bathymetric charts from BNHOC. The charts are listed in Table 2.2 and their coverage is shown in Figure 2.1. This digitized dataset adds 77000 additional sounding points. Particularly, I obtained a high-resolution bathymetry along the shoreline of Chittagong (91.5°E-92.5°E), and the Bangladesh part of the Sundarbans mangrove forest (89°E-90.5°E). The chart soundings were provided relative to chart datum. Typically, the local level of Lowest Astronomical Tide (LAT) defines the chart datum (CD).

To convert the digitized soundings from the chart datum to the mean sea level, I applied the same procedure as Krien et al. (2016). In this procedure, an estimation of the difference between chart datum (e.g., LAT) and mean sea level (MSL), ΔD_i , at each digitized point is calculated by interpolating a set of control points. These control points are composed of real tide gauge

location, and virtual tidal stations derived from satellite altimetry. A weighted inverse distance interpolation is applied with the following formula –

$$\Delta D_i = \frac{\sum_{j=1}^N \left[\frac{\Delta D_j}{d_{ij}^\alpha} \right]}{\sum_{j=1}^N \left[\frac{1}{d_{ij}^\alpha} \right]} \quad (2.1)$$

Where subscript i, j refers to denote the digitized and control points respectively. N is the total number of control points, d_{ij} refers to the distance between digitized point i and control point j . A value of $\alpha = 3$ is used for the exponent which gave the most realistic interpolation (Krien et al., 2016).

Table 2.2: List of digitized BNHOC charts, scale and year of survey.

Chart	Coverage	Scale	Year	Remark
1002	89.325E–89.675E, 21.333N–22.916N	1:10000	2001-2011	3 Panels
1251	91.771E–91.861E, 22.206N–22.330N	1:12500	2012-2013	
1253	89.410E–89.535E, 22.503N–22.618N	1:12500	2013-2014	2 Panels
1254	92.036E–92.251E, 22.443N–22.511N	1:12500	2014-2015	2 Panels
2501	91.836E–92.072E, 22.317N–22.463N	1:25000	2013-2014	
2502	89.508E–89.592E, 22.516N–22.912N	1:25000	2014-2015	3 Panels
3001	91.667E–91.855E, 22.083N–22.347N	1:30000	2012-2013	
3002	90.240E–90.428E, 21.811N–22.075N	1:30000	2014-2015	
3503	91.883E–92.213E, 20.933N–21.139N	1:35000	2013-2014	
3504	91.883E–92.300E, 21.083N–21.393N	1:35000	2013-2014	
3505	91.800E–92.020E, 21.366N–21.675N	1:35000	2011-2013	
3506	91.703E–91.922E, 21.650N–21.959N	1:35000	2010-2012	
3509	91.371E–91.785E, 22.379N–22.583N	1:35000	2013-2015	
3511	91.338E–91.558E, 22.266N–22.574N	1:35000	2013-2015	
3522	90.000E–90.220E, 21.683N–21.993N	1:35000	2010-2011	
3523	89.786E–90.006E, 21.683N–21.993N	1:35000	2008-2012	
3524	89.778E–90.109E, 21.880N–22.085N	1:35000	2008-2012	
3525	89.583E–89.803E, 21.683N–21.993N	1:35000	2009-2010	
3526	89.416E–89.635E, 21.573N–21.882N	1:35000	2008-2014	
3527	89.445E–89.636E, 21.856N–22.245N	1:35000	2005-2012	2 Panels
3528	89.393E–89.647E, 22.223N–22.568N	1:35000	2011-2012	
7501	89.000E–89.706E, 21.533N–21.971N	1:75000	2002-2011	
7503	89.633E–90.103E, 21.533N–22.193N	1:75000	2008-2012	
7510	91.466E–91.937E, 21.700N–22.360N	1:75000	2010-2014	
7511	91.667E–92.135E, 21.067N–21.729N	1:75000	2011-2014	
7512	92.000E–92.468E, 20.450N–21.115N	1:75000	2003-2015	
7513	89.266E–89.737E, 21.258N–21.922N	1:75000	2002-2014	
25002	91.000E–92.568E, 20.416N–22.628N	1:150000	2002-2015	
35001	89.100E–92.400E, 20.500N–22.550N	1:350000	2002-2010	
40001	88.916E–92.700E, 20.416N–22.766N	1:400000	1999-2008	

In the Bangladesh part of the delta, I incorporated the same river cross-section dataset as Krien et al. (2016) with minor modifications. In their database, the original cross-sections were interpolated through a dedicated 1-D river modelling and interpolation tool (HEC-RAS). This interpolation was done reach-wise, i.e., from one river junction to another, which introduced

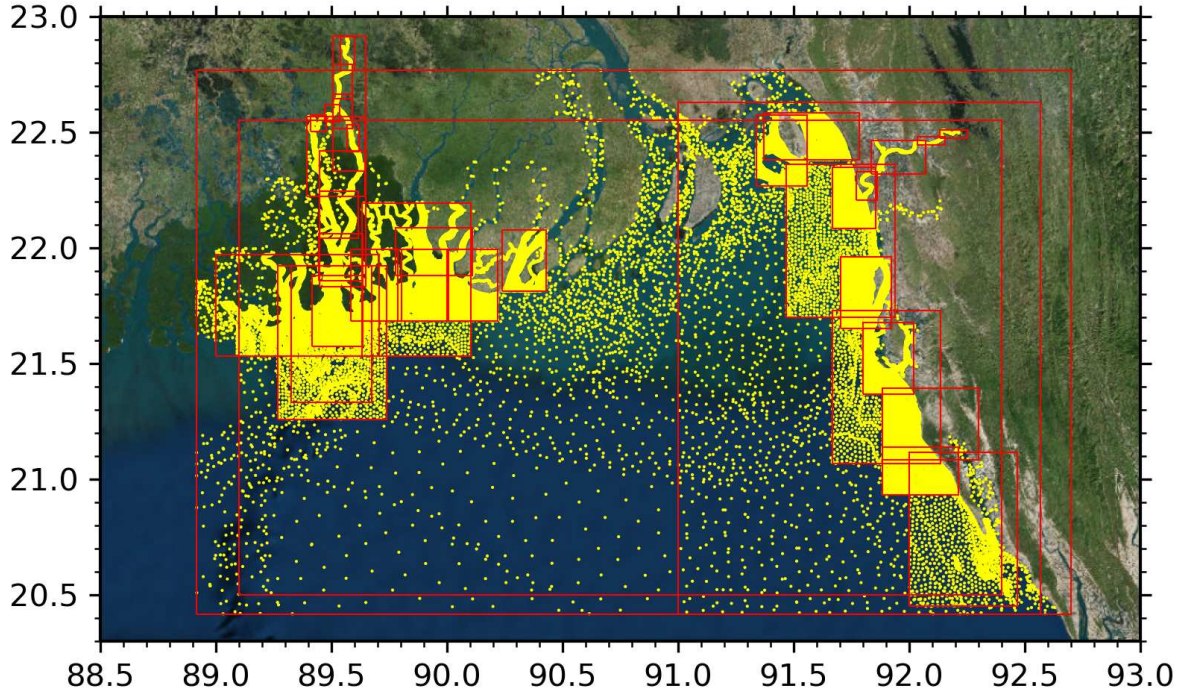


Figure 2.1: 77000 digitized sounding points (in yellow). The coverage of the corresponding individual charts is shown in red outlines.

overlapped cross-sections from rivers at the junctions. I removed these overlapped interpolation points manually to get rid of the noise.

The coastal embankments in the Bengal delta are ubiquitous, and a significant factor in the numerical modelling of the storm surge flooding (Krien, Testut, et al., 2017). There are in total 139 polders (area protected by embankments) in the southern part of Bangladesh which have been built during the second half of 20th century (Nowreen, Jalal, & Khan, 2013). The global bathymetry/topography datasets do not resolve these earthen embankments. Krien et al. (2016) incorporated the outlines of these embankments in their model. However, the unavailability of the real height information forced them to assume an embankment height of 4.54 m above mean sea level (equivalent to 5 m relative to local Public Works Datum). In this new updated bathymetric dataset, I incorporated a more accurate estimate of embankments height in the central part of the delta, based on information provided by Bangladesh Water Development Board.

The rest of the components of the bathymetry dataset used in this study remains essentially the same as Krien et al. (2016). The same digital elevation model of the Bangladesh coastal zone at 50 m resolution provided by the Center for Environmental Geographic Information Services (CEGIS) is used for the delta topography. The rest of the bathymetry is adopted from the GEBCO (2014) dataset. The remaining area without high-resolution topography is complemented from the SRTM dataset (as appear in GEBCO 2014).

2.3 Observations

I used four kinds of hydrodynamic observational datasets throughout this study. These include hourly tide-gauge dataset from Bangladesh Inland Water Transport Authority (BIWTA), water level and discharge over the Ganges-Brahmaputra-Meghna river system from Bangladesh Water Development Board (BWDB), altimetry-derived water level and tidal constituents. We have also used observed tidal constituents at four coastal stations - Sagar Roads, Diamond Harbour, Garden Reach, Dhulasar - provided by the National Institute of Oceanography (NIO) at Goa, India. The list of the in-situ datasets is shown in Table 2.3.

Table 2.3: In-situ dataset water level dataset.

Location	Longitude	Latitude	Type	Source
Sagar Roads	88.0450	21.6470	Harmonic Constituents	NIO
Diamond Harbour	88.1750	22.1930	Harmonic Constituents	NIO
Garden Reach	88.3177	22.5488	Harmonic Constituents	NIO
Hiron Point	89.4650	21.8200	Timeseries (1977-2003)	BIWTA/GLOSS
Dhulasar	90.2700	21.8500	Harmonic Constituents	NIO
Charchanga	91.0500	22.2188	Timeseries (1980-2000)	BIWTA/GLOSS
Chittagong	91.8333	22.323	Timeseries (2007-2012)	BIWTA/GLOSS
Chandpur	90.6516	23.2211	Timeseries (1998-2007)	BIWTA
Hardinge Bridge	89.0255	24.0640	Timeseries (1981-2018)	BWDB
Bahadurabad	89.6802	25.1106	Timeseries (1981-2018)	BWDB
Bhoirabbazar	91.0019	24.0527	Timeseries (1981-2018)	BWDB

The observational network of water level at high temporal resolution with consistent temporal coverage is very scanty around the coastline of Bengal delta. We could rely only on the time series of four observational stations - Hiron Point, Charchanga, Chittagong, Chandpur.

BWDB maintains a daily record of fluvial water level at three key stations for the three major tributaries of the Bengal delta - Hardinge Bridge (over the Ganges), Bahadurabad (over the Brahmaputra), and Bhoirab Bazar (over the Meghna). Additionally, BWDB also maintains an intermittent estimate of discharge at these locations.

2.4 Modelling framework

2.4.1 Hydrodynamic model

I have used a state-of-the-art cross-scale hydrodynamic model named SCHISM (Zhang et al., 2016). It solves the standard Navier-Stokes equations with hydrostatic and Boussinesq approximations. The momentum and continuity equation in 3D read as follows -

$$\frac{D\mathbf{u}}{Dt} = \frac{\partial}{\partial z} \left(v \frac{\partial \mathbf{u}}{\partial z} \right) - g\nabla\eta + f(v, -u) - \frac{g}{\rho_0} \int_z^\eta \nabla\rho d\zeta - \frac{\nabla p_A}{\rho_0} + \alpha g\nabla\psi + \mathbf{F}_m \quad (2.2)$$

$$\nabla \cdot \mathbf{u} + \frac{\partial w}{\partial z} = 0 \quad (2.3)$$

Water level dynamics in the northern Bay of Bengal is very complex due to the multitude of forcing factors, and to the braided river network and complex bathymetry. It is a macro-tidal

region with peak tidal range reaching as high as 5 m at the north-eastern corner. The largest storm surges were also recorded in this area. For this study I have used the model in depth-averaged form (2DH). In a Cartesian coordinate system with the datum fixed at mean sea level (Figure 2.2), the depth-averaged momentum and continuity equation read as follows:

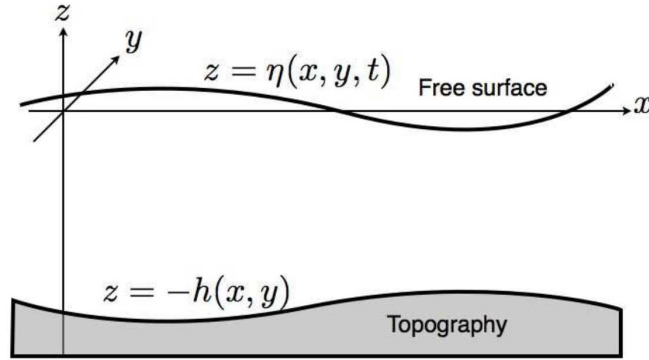


Figure 2.2: A schematic for the water level variation described with Equation 2.4 - 2.6.

$$\frac{\partial u}{\partial t} + u \frac{\partial u}{\partial x} + v \frac{\partial u}{\partial y} = -g \frac{\partial \eta}{\partial x} - \frac{1}{\rho} \frac{\partial p}{\partial x} + \frac{1}{\rho h} (\tau_{sx} - \tau_{bx}) + fv \quad (2.4)$$

$$\frac{\partial v}{\partial t} + u \frac{\partial v}{\partial x} + v \frac{\partial v}{\partial y} = -g \frac{\partial \eta}{\partial y} - \frac{1}{\rho} \frac{\partial p}{\partial y} + \frac{1}{\rho h} (\tau_{sy} - \tau_{by}) - fu \quad (2.5)$$

$$\frac{\partial \eta}{\partial t} + \frac{\partial}{\partial x} (hu) + \frac{\partial}{\partial y} (hv) = 0 \quad (2.6)$$

Where u, v is the components of the depth-average velocity. η is the vertical displacement of free surface according to my reference MSL (hereafter water level). The force imbalance due to the right side of the equation 2.4 and 2.5 coming from hydrostatic pressure p , wind stress $\tau_{sx}\tau_{sy}$ and bottom stress $\tau_{bx}\tau_{by}$ equates to the acceleration of water (left side of the equations), thus changing the water level as expressed in equation 2.6. Here, ρ is the water density which is assumed to be uniform, g is the acceleration due to gravity, f is the Coriolis parameter. Total water depth, h , is the combination of the depth from the mean sea level and the water level η .

Here it is assumed that the vertical component of the velocity is negligible compared to the horizontals. It also assumes the fluid is incompressible. This form of shallow-water equation is found to work quite well for the tide, and storm surge modelling. The depth-averaged modelling strategy has been extensively used in this region to study the tide (Krien et al., 2016; Sindhu & Unnikrishnan, 2013), cyclone surges and tide-surge interactions (Krien, Testut, et al., 2017; P. Murty et al., 2016) (based on SCHISM as well as other numerical models).

From equations 2.4 and 2.5, it is clear that the atmospheric forces that generate the storm surges are pressure p and wind stress τ_s . The pressure acts inversely in the evolution of the water level, i.e., the higher the pressure drop the higher the water level. A rule-of-thumb is that a 1 mb pressure drop will produce a positive surge equivalent of 1 cm. On the other hand, surge induced by wind stress is proportional to the stress itself. Interestingly, the wind stress

component appears divided by the total water depth h , indicating that the wind stress produces high surges in the shallow water where h is small and low surges in the deep water where h is high. Due to sensitivity to the depth change, the evolution of surge becomes contingent upon the evolution of tide and other mechanisms of water level dynamics at longer time-scale.

In a macro-tidal region like the head Bay of Bengal, a large component of the water level is the tide (Antony, Unnikrishnan, & Woodworth, 2016). The tidal range is comparable to a strong surge. Tidal propagation, which is induced at the boundary of this system of equations and as a body force is described by equation 2.4 and 2.5, excluding the atmospheric pressure and wind stress term. For a regional domain, like that of Bay of Bengal, the body force is typically small compared to the boundary forcing. In my case the boundary forcing is applied from global tidal atlas and discussed in a dedicated section later. The propagation of the tidal water level has a very strong dependence on the depth of water and on the bottom friction component - which are essentially the primary sources of error for a tidal model. A good bathymetry is found to be the zeroth-order component to adequately describe the tidal water level evolution, followed by the representation of the bottom friction (Krien et al., 2016). As these remaining terms contain products of the dependent variables η , u , and v the solution is non-linear with an interaction between the components of the fluid motions. These dependent nature of both tide and surge implies that the surge produced by a given meteorological condition can be significantly different at various stages of the tide, particularly in the shallower zone, giving rise to tide-surge interaction (Antony & Unnikrishnan, 2013). It is thus necessary to solve tide and surge coupled together to avoid inducing error in the predicted water level (As-Salek & Yasuda, 2001; Krien, Testut, et al., 2017; P. Murty et al., 2016).

2.4.2 Discretization

In horizontal, the model domain is discretized through an unstructured mesh. In unstructured modelling, the mesh generation is guided by the knowledge of the bathymetry. I used the software Surface water Modeling System (SMS) for this purpose. Similar to Krien et al. (2016), we have first determined the distribution of elements size based on the tidal wavelength (Provost & Vincent, 1986) and a bathymetry gradient criterion (Lyard et al., 2006). For a bathymetric depth of H and smallest considered wave period T , the element size reads as the following -

$$\delta = \min \left(\frac{T\sqrt{gH}}{15}, 0.4 \frac{H}{\|\nabla H\|} \right) \quad (2.7)$$

For this study, the lowest shallow-water wave period selected is 10000s. A smoothing is operated on the obtained size criteria to get an element size estimation ensuring the ratio between two adjacent elements is less than 2.

The final resolution ranges from 250 m in the nearshore zone of the delta, to 15 km in the deeper part of the ocean (Figure 2.3). The final mesh is composed of 600k nodes and 1.1 million elements. After several iterations, I found this resolution of 250 m to be roughly sufficient to represent the riverine network while keeping the node counts to a reasonable number for an efficient large-scale computation. This choice is embraced to achieve the goal of this PhD, which required multi-year integrations of the model, as will be evident in the succeeding chapters.

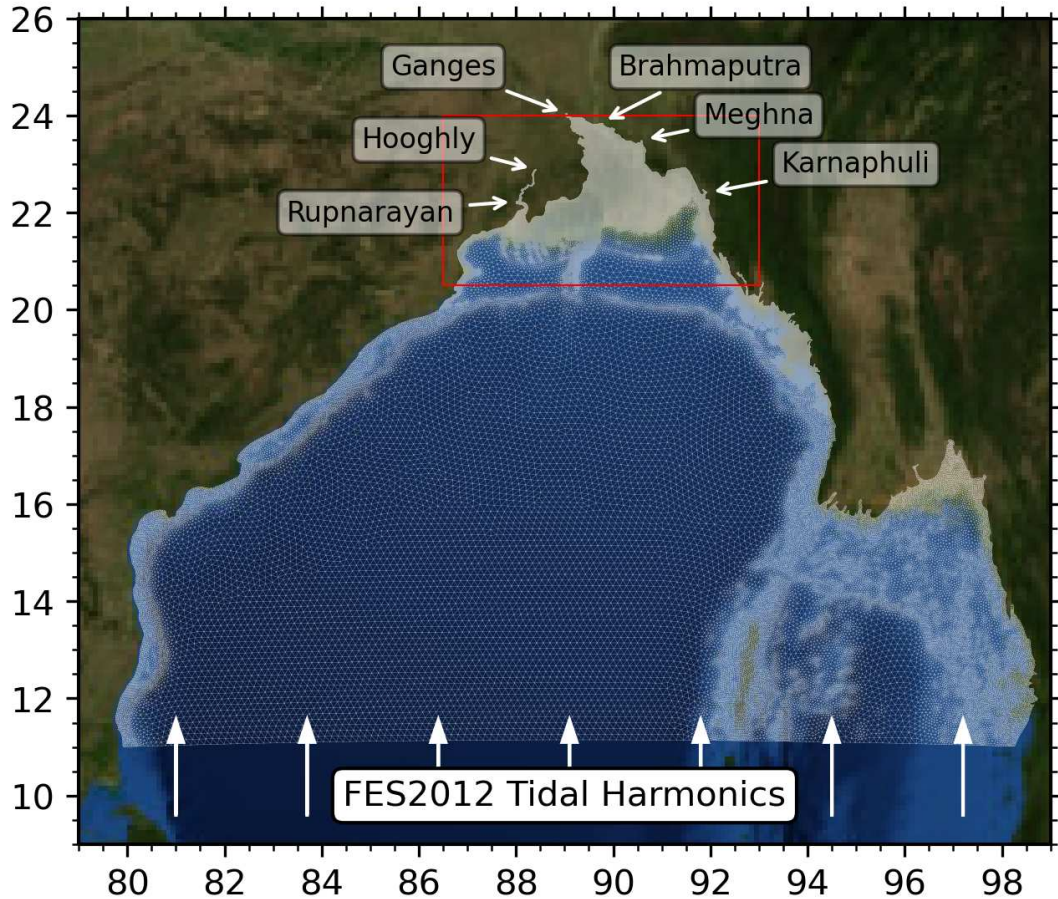


Figure 2.3: The model mesh and its extent. The applied boundary conditions are shown with arrows.

2.4.3 Parameterization of bottom friction

Bottom friction is a sensitive tuning parameter in the application of our model. It is parameterized in our setup through a Manning coefficient n . After sensitivity analysis, a spatially varying distribution of the parameter is adopted, similar to Krien et al. (2016). In the nearshore zone, the friction varies with depth/distance to the shoreline. For the initial tidal modelling, a value of 0.02 is adopted for n , for the deeper part of the ocean (depth > 20 m), and 0.013 for the continental shelves (depth < 20 m). A single value for n (0.01) is adopted for all rivers. For storm surge modelling, however, increased friction of $n=0.07$ is considered for inland areas to account for the vegetation in the inland flooding process (Bunya et al., 2010).

2.4.4 Coupling with wave model

In the nearshore zone, short waves go through various transformations. These transformations include shoaling and dissipation by bottom friction in the shoreface and dissipation by breaking the surf zone. Combinations of short waves also generate higher order harmonics and lower frequency infragravity waves.

Particularly during storms, wave setup along the coast can constitute a significant part of the water level reaching tens of centimetres (Idier et al., 2019; Krien, Testut, et al., 2017; P.

Murty et al., 2014). Wave setup is the increase in the sea level at the near-shore zone with a sloping bottom profile due to radiational stress gradient induced by the dissipation of shorewaves through depth-limited breaking (Longuet-Higgins & Stewart, 1962). To explicitly account for this mechanism, SCHISM is coupled with a third-generation spectral wave model – Wind Wave Model III (WWMIII). It is an updated version of WWMII, which solves the wave action equation on the same unstructured grid as SCHISM (Roland et al., 2012). The wave action equation reads as follows -

$$\frac{\partial N}{\partial t} + \frac{\partial (C_{gx} + u) N}{\partial x} + \frac{\partial (C_{gy} + v) N}{\partial y} + \frac{\partial (C_{\sigma} N)}{\partial \sigma} + \frac{\partial (C_{\theta} N)}{\partial \theta} = \frac{S_{tot}}{\sigma} \quad (2.8)$$

Here N is the wave action, C_{gx} and C_{gy} are the group velocity components in x- and y-direction, σ and θ are the wave relative angular frequency and the wave direction. S_{tot} is the sum of the source terms. These source terms include nonlinear interaction in deep (S. Hasselmann et al., 1985) and shallow waters (Eldeberky, 1996), wave growth and energy dissipation due to whitecapping (Bidlot, 2012; Bidlot et al., 2007), wave breaking (Battjes & Janssen, 1978), and bottom friction (K. Hasselmann et al., 1973). Wind input source term is parameterized as a function of roughness length z_0 . Roughness length is defined here as -

$$z_0 = \frac{\alpha_0}{U_*^2} \sqrt{\frac{\tau_w}{\tau}} \quad (2.9)$$

where U_* is the wind friction velocity, $\tau = U_*^2$, α_0 is the minimum Charnock coefficient, and τ_w is the wave-supported stress. The wind input source term varies proportionally to $e^Z Z^4$ with Z defined as following -

$$Z = \ln \left(\frac{gz_0}{c^2} \right) + \frac{\kappa}{\cos(\theta - \phi) \left(\left(\frac{U_*}{c} \right) + z_{\alpha} \right)} \quad (2.10)$$

Here θ and ϕ represent the discrete wave direction and wind direction at 10 m height. c is the phase velocity, κ is the von Karman constant, and z_{α} is a wave age tuning parameter set to 0.011.

The roughness length z_0 is related to the wind speed at 10 m height (U_{10}) by the following relationship -

$$U_{10} = \frac{U_*}{\kappa} \ln \left(\frac{z_{obs}}{z_0} \right) \quad (2.11)$$

The model can be solved with either an implicit or an explicit scheme. For my model I adopted implicit schemes for integrating both advection and source terms. After sensitivity testing, I discretized the spectrum in 12 directions and 12 frequency bins, with low and high frequency cut-off at 0.04 and 1 Hz respectively. Finer resolution did not made appreciable changes in the results. Water level and current are exchanged between SCHISM and WWM every 30 minutes.

2.5 Model forcings and boundary condition

2.5.1 Tidal oceanic boundary

The model was forced by the astronomical tidal potential over the whole domain for the 12 dominant constituents (2N2, K1, K2, M2, MU2, N2, NU2, O1, P1, Q1, S2, and T2). Along the southern open boundary in our model domain, a tidal water level condition is applied. The water level is generated by the model code from prescribed tidal harmonic constituents. We have used FES2012 (Carrère et al., 2013) for forcing along the boundary for the 26 dominant harmonic constituents (M2, M3, M4, M6, M8, Mf, Mm, MN4, MS4, Msf, MU2, N2, NU2, O1, P1, Q1, R2, S1, S2, S4, SSA, T2, K2, K1, J1, and 2N2). The tidal constituents from FES2012 archive were extracted and interpolated to the nodal points of our model. The coupled amplitude-phase interpolation method of Z. Xu (2017) was used for the interpolation scheme. The interpolation equation for phase (ϕ) and amplitude (A) reads as follows for a given position x -

$$\phi = \arctan\left(\frac{\alpha A_1 \sin \phi_1 + \beta A_2 \sin \phi_2}{\alpha A_1 \cos \phi_1 + \beta A_2 \cos \phi_2}\right) \quad (2.12)$$

$$A = \frac{\alpha A_1 \sin \phi_1 + \beta A_2 \sin \phi_2}{\sin \phi} \quad (2.13)$$

Where subscript 1 and 2 indicates the location of the points from which the interpolation is being done. α and β are the typical linear interpolation weight calculated as $\alpha = (x_2 - x)/(x_2 - x_1)$, $\beta = 1 - \alpha$.

At seasonal scale, the average sea surface in the Northern Bay of Bengal can also show considerable evolution due to the variability of vertical density gradients in the ocean interior (Shankar & Shetye, 2001). In the head Bay of Bengal, the amplitude of this variation can go as high as 40 cm (Tazkia et al., 2017). This is a baroclinic phenomenon, which is not resolvable in the 2DH modelling framework that I use here. Whenever appropriate, this mean sea level variation is parameterized following the approach of Tazkia et al. (2017), by imposing a seasonal barotropic water level signal along the southern open boundary.

2.5.2 River open boundaries

There are six riverine open boundaries in the model - Rupnarayan, Hooghly, Ganges, Brahmaputra, Meghna, and Karnaphuli (Figure 2.3). For Ganges and Brahmaputra, a discharge boundary condition is used. A daily discharge timeseries is generated from a stage-discharge curve developed at the respective locations. For Hooghly and Karnaphuli a monthly climatological discharge timeseries is applied. For Meghna and Rupnarayan, a Flather radiating boundary condition is imposed for all tidal simulations to take into account the general tidal nature of these boundaries. However, for storm surge simulations, a discharge boundary condition is rather imposed for Meghna, considering the heavy rainfall that the region receives during a storm. It is to be noted that the choice of a discharge boundary condition does not appreciably change the tidal nor seasonal water level downstream of this boundary (e.g., at Chandpur station). The climatological discharge for the various stations (except Rupnarayan) is shown in Figure 2.4.

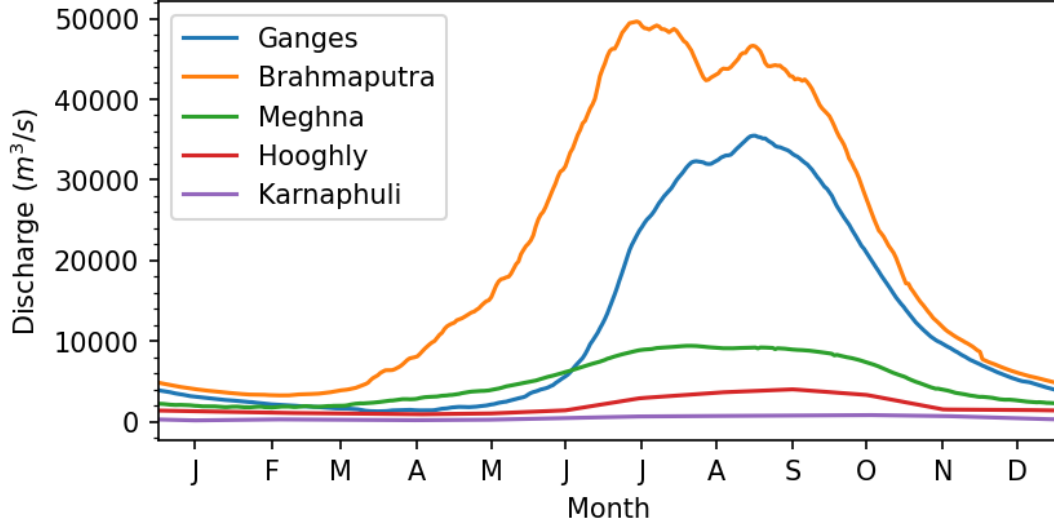


Figure 2.4: Climatological mean annual discharge (in m^3/s) at the open river boundaries.

Evidently the freshwater inflow in the northern Bay of Bengal through the imposed river boundaries is dominated by Brahmaputra (about 50% of total inflow) and Ganges (about 30% of total inflow). All of the rivers show a strong seasonality. During winter period (Dec-Feb), the flow is virtually negligible compared to the summer (Jun-Sep). For Brahmaputra, Ganges, and Meghna, the evolution of freshwater inflow is controlled by the seasonality of monsoon rainfall over these three catchments (Jian, Webster, & Hoyos, 2009). The flow through Hooghly accounts for about 5% of the total freshwater inflow in the model which is mostly regulated through the Farakka barrage located just at the border of Bangladesh and India (Mukhopadhyay et al., 2006). The flow at Karnaphuli is estimated from the discharge at Kaptai hydro-power plant located 20 km upstream of Chittagong (M. A. M. Chowdhury & Al Rahim, 2012). Where no tidal or river open boundary is imposed, a no-slip condition is assumed.

2.5.3 Cyclonic wind and pressure

As discussed in Section 2.4, during a storm event, the water level is forced by wind and pressure on top of the tide. The effect of pressure on water level is much more regional (typically $O(100$ km)) compared to the effect of the wind $O(25$ km), and the numerical modelling of the surge depends strongly on both the pressure and the wind fields. It is found that with observed wind fields, the state-of-the-art numerical storm-surge models can often successfully reproduce the observed surges (Bunya et al., 2010; Westerink et al., 2008). In absence of observed data however, which is the typical case of the Bengal delta, numerical weather prediction can come handy. However, atmospheric numerical modelling of the storm itself is a challenging task. Notably, the error in track position can be of tens of kilometres, inducing large error in the surge estimate. Moreover, the computational domains for such atmospheric numerical models need to be cloud-resolving (resolution of order 1 km) to properly simulate the atmospheric convection processes, which can be very computing-intensive (Lakshmi et al., 2017). An alternative to this approach is the use of parametric wind and pressure models, which are simple, efficient, and widely used in all cyclone-prone basins (Lin & Chavas, 2012). In the parametric approach,

wind and pressure fields are parameterized with storm properties - e.g., central pressure (p_c), maximum wind speed (V_m), and the radii of maximum wind (R_m). These parameters are either estimated from models or from satellite observations (Velden et al., 2006).

The commonly used radial pressure field model is proposed by Holland (1980). In this model, the radial pressure is estimated as following -

$$p = p_c + (p_n - p_c) \exp(-A/r^B) \quad (2.14)$$

where A, and B are the scaling parameters, with $B = \frac{V_m^2 e \rho_{air}}{p_n - p_c}$, and $A = R_m^B$. ρ_{air} denotes the density of air, taken as 1.15 kg/m^3 , p_n is the ambient pressure, and e is the base of natural logarithm.

The effect of error induced by pressure field in storm surge modelling is small, it is typically accepted by the storm surge modelling community. For the rest of the work, all parametric radial pressure fields are estimated using Holland (1980) model.

In the parametric approach, the surface wind field is typically estimated as the combination of an axisymmetric wind field associated with the storm, and a background wind (Lin & Chavas, 2012). Compared to the pressure field, the error in the wind field during a cyclone can induce a large error in the surge estimate (Krien, Testut, et al., 2017; Lin & Chavas, 2012). Among various available axisymmetric wind profiles, few notable models are Holland (1980) (H80), Jelesnianski (1992) (J92), Emanuel et al. (2004) (E04), Emanuel and Rotunno (2011) (E11). From the statistical analysis of a large ensemble of cyclones, Lin and Chavas (2012) showed that the choice of the models induces a prominent difference in the estimation of the surge. From a comparison of storm wind speed for a set of storms during 2017 Atlantic and Eastern Pacific hurricane season derived from satellite-scatterometer Krien et al. (2018) showed that these models perform well for either the inner or the outer core. They have found the best results, by combining two models - E11 for the inner core and H80 for the outer core. Since E11 performs well in reproducing inner core of the storm structure, another way of circumventing this problem is by blending the parametric wind field with the atmospheric reanalysis or forecast products when available (Krien, Testut, et al., 2017). They also showed that the best results are obtained for any wind model when the profile is constrained with wind-speed information at multiple radial distances. For this study, in all subsequent hindcast analyses, I selected the combined E11-H80 model with a blending with the atmospheric model outputs.

The description of the radial wind field in Holland (1980) model is following -

$$V(r) = \sqrt{(R_m/r)^B \frac{B(P_n - P_c) \exp\left(-\left(\frac{R_m}{r}\right)^B\right)}{\rho_{air}} + \frac{r^2 f^2}{4} - \frac{fr}{2}} \quad (2.15)$$

Here, A and B are the same scaling parameters described in Holland (1980) pressure model. The model of Emanuel and Rotunno (2011) describes the radial wind speed as following -

$$V(r) = \frac{2r (R_m V_m + 0.5f R_m^2)}{R_m^2 + r^2} - \frac{fr}{2} \quad (2.16)$$

Whenever available, I used all the radial wind speed information to constrain the estimated wind profile. The E11 model is used in the inner part of the cyclones until the r50 (radius of

50knots wind speed), and H80 is used for the outer region. Where multiple radial information is not available (e.g. for the synthetic storms considered in Chapter 6), I used E11 profile throughout the whole radial structure. When blending with the atmospheric model output fields, I used a smooth linear transition between $3xR_m - 10xR_m$. Additionally, following the findings of Lin and Chavas (2012), a reduction factor $\alpha = 0.56$ (translation speed) and counter-clockwise rotation angle of $\beta = 19.2^\circ$ is applied to consider the effect of translation speed. Irrespective of ocean or land, a surface wind reduction factor of 0.9 is used to convert from the wind speed in the atmospheric boundary layer to the surface wind speed.

2.6 Assessment of tide

The tidal model assessment is done in this study through harmonic analysis of observed water level timeseries. For harmonic analysis, I used the Tidal Toolbox software developed at LEGOS (Allain, 2016).

We have estimated the model error at any location for tidal constituents following the approach of Andersen, Woodworth, and Flather (1995) using the modulus of the complex difference. For any constituent, the complex error for a tidal wave is computed as -

$$|\Delta z| = |A_m e^{i\phi_m} - A_o e^{i\phi_o}| \quad (2.17)$$

Where A and ϕ are the amplitude and phase of the tidal harmonics respectively, for model (m) and the observation (o).

The total error estimate for all constituents is calculated as -

$$\sigma_s = \sqrt{\frac{1}{2} \sum_{N_{harmonics}} |\Delta z|^2} \quad (2.18)$$

For comparison with the results obtained over our area in previous studies, we have calculated the total error for only the four main harmonics – M2, S2, K1, O1 (Krien et al., 2016). These four waves are found to have the most significant contribution to the tidal signal (Sindhu & Unnikrishnan, 2013). Additionally, the other harmonics are often not available for comparisons. Two of the stations, namely Garden Reach and Chandpur are located far inland (typically about 100 km upstream of the delta mouths), where the shallow-water tidal harmonics and seasonal signals have high amplitudes. However, for the sake of consistency, only the error corresponding to the four main harmonics are assessed.

Epilogue

In this chapter the primary data and methods used for our modelling activity were described. A new bathymetric dataset was assembled, based on a new set of high-resolution digitized soundings over the coastal region of Bangladesh for the development of the configuration of the hydrodynamic model. A handful of water level and discharge records form the available dataset, which we assembled to force and validate the performance of our hydrodynamic model. The model formulation, forcing and validation strategy was documented. The validation of the tidal

model is presented in the following chapter compared to tide gauges, and satellite altimetry. The relevance of the data presented here is also illustrated through comparison with other global, and regional tidal solutions.

CHAPTER 3

INTERTIDAL TOPOGRAPHY: SYNERGY BETWEEN REMOTE SENSING AND TIDAL MODELLING

‘ . . . I don’t see the good of the tides. What’s the good of a sea if it’s going to be mud in a few hours.’ ‘It’s like breathing,’ said Titty. ‘Up and down. Up and down. It makes everything alive.’ – Arthur Ransome, Secret Water

Preamble

Accurate and up-to-date knowledge of the topography and bathymetry is a pre-requisite for a realistic hydrodynamic modelling. This requirement is particularly true for unstructured modelling environments such as the one used in this thesis, which can resolve small features efficiently (Zhang et al., 2016). The bathymetric dataset assembled in Chapter 2 based on the work of Krien et al. (2016) gives a good starting point for our hydrodynamic model over the Bengal delta continuum.

A – as thorough as possible – validation of the hydrodynamic model is an essential task before its application to answer any relevant scientific questions. In the open-ocean altimetry, particularly the Topex family has proved to be invaluable for such validation of tide (Carrère et al., 2013). Despite substantial signal contamination at the land-water interface, recent improvement of dedicated processing has extended the altimetry-derived tidal estimations closer to shorelines (~20 km) (Birol et al., 2017). On the other hand, the number of in-situ tide gauges is very limited, hereby providing a limited number of validation points.

Recent satellite optical imaging missions, e.g., Sentinel-2 constellation, periodically monitors the continuum at a decametric resolution, with a moderate frequency (~10days) at multiple spectral bands. Processing of these imageries allows identifying the location of the shoreline at the time of overpass. An interesting test for my model will be to see if the modelled water levels corresponding to the shorelines show a consistent evolution. Shorelines at higher water level will be on the landward side, and lower water level will be on the sea ward side. If the modelled water level associated with a shoreline are consistently ordered, it would indicate that the modelled water level is indeed capturing the state of the sea level. Unsurprisingly, these temporally co-located shorelines with the modelled water levels are the contours of the intertidal topography. This is the so-called "water line method" (Mason et al., 1995).

To explore this satellite-model synergy, in this chapter, an efficient and automated shoreline extraction method is developed by extending a semi-automated method (Bergmann et al., 2018). Then a classical validation of the tidal model is done through comparison with tide-gauge records, and altimetry-derived constituents. Finally, an intertidal bathymetry at decametric resolution

over the coastal Bengal delta is derived from the synergy between the satellite observations and numerical modelling.

Publication: The work of this chapter has been published in Remote Sensing journal on 4 December 2019. The article can be cited as - Khan, M.J.U., Ansary, M.D., Durand, F., Testut, L., Ishaque, M., Calmant, S., Krien, Y., Islam, A.K.M. and Papa, F., 2019. High-resolution intertidal topography from sentinel-2 multi-spectral imagery: Synergy between remote sensing and numerical modeling. Remote Sensing, 11(24), p.2888, [doi:10.3390/rs11242888](https://doi.org/10.3390/rs11242888).

Software: The shoreline extraction toolbox developed during this work can be found at <https://github.com/jamal919/pyIntertidalDEM>

Abstract. The intertidal zones are well recognised for their dynamic nature and role in the near shore hydrodynamics. The intertidal topography is poorly mapped worldwide due to high cost of associated field campaigns. Here we present a combination of remote-sensing and hydrodynamic modelling to overcome the lack of *in situ* measurements. We derive a digital elevation model (DEM) by linking corresponding water level to a sample of shorelines at various stages of tide. Our shoreline detection method is fully automatic and capable of processing high-resolution imagery from state-of-the-art satellite missions, e.g. Sentinel-2. We demonstrate the use of a tidal model to infer the corresponding water level in each shoreline pixels at the sampled timestamp. As a test-case, this methodology is applied to the vast coastal region of the Bengal delta and an intertidal DEM at 10 m resolution covering an area of 1134 km² is developed from Sentinel-2 imagery. We assessed the quality of the DEM with two independent *in situ* datasets and conclude that the accuracy of our DEM amounts to about 1.5 m, which is commensurate with the typical error bar of the validation datasets. This DEM can be useful for high-resolution hydrodynamic and wave modelling of the near shore area. Additionally, being automatic and numerically effective, our methodology is compliant with near-real-time monitoring constraints.

3.1 Introduction

Many coastal regions around the world are facing an increased exposure to flood hazard and related losses because of the growing population and economy. This situation is further exacerbated by the sea level rise and ground subsidence (Hallegatte et al., 2013). The intertidal zone, the tidally flooded area of coastal region, is exposed to a large number of land and oceanic processes. Clearly, the ongoing sea level rise first and foremost impacts the intertidal zone by permanently flooding and changing the hydrodynamics (Murray et al., 2018). Our understanding and modelling of the relevant hydrodynamic processes in the intertidal region require detailed knowledge of its topography, which still remains very poor worldwide due to very high cost associated with necessary field campaign and instrumentation (Eakins & Grothe, 2014).

Spaceborne remote sensing offers a promising alternative for mapping the intertidal topography (Mason, Gurney, & Kennett, 2000; Salameh et al., 2019). Among the various methods, the waterline method is one of the most widely used (Mason et al., 1995; Mason et al., 1997; Tseng et al., 2017; Zhao et al., 2008). In this approach, the horizontal position of the land-water boundary (i.e. shoreline of a coast) is determined from remotely sensed image using image processing techniques. When the horizontal position of this shoreline is combined with the independent knowledge of the water level at this location, at the time of image acquisition, the

relative height of the shoreline can be inferred. Replicating this process over a range of tidal water levels gives an estimation of the topography between highest-water (generally observed at high tide of spring tide) and the lowest-water (generally observed at low tide of spring tide) shorelines. Various applications of this method have been attempted, including the monitoring of coastline changes (Y. Liu et al., 2013), estimation of sediment transport (Mason & Garg, 2001), and data assimilation in a coastal morphodynamic model (Scott & Mason, 2007). At larger scale, Bishop-Taylor et al. (2019) developed an intertidal digital elevation model (DEM) for Australia coast at 25 m resolution using a relative intertidal extent model developed from 30 years of Landsat archive and global tidal modelling (Bishop-Taylor et al., 2019; Sagar et al., 2017).

The use of Synthetic Aperture Radar (SAR) imagery is quite common to infer the shoreline to use with waterline method (e.g. Mason et al., 1995). The reason behind using SAR imagery is its ability to work day or night including under cloudy conditions. Another reason is the ability to automate or semi-automate the shoreline detection from SAR imagery (Heygster, Dannenberg, & Notholt, 2010; Li, Heygster, & Notholt, 2014; Niedermeier, Romaneessen, & Lehner, 2000).

The application of multi-spectral imagery can be similarly useful in waterline method. Typical shoreline detection methods rely on near-infrared (NIR) spectrum since it is absorbed by water and gets reflected by vegetation and dry soil (Work & Gilmer, 1976). The methods based on NIR either use the band directly (e.g. Rundquist et al., 1987) or use indices developed from the conjunction of other bands. For example, the normalized difference vegetation index (NDVI) enhances the water feature with red band (e.g. Tucker and Sellers, 1986), the normalized difference water index (NDWI) uses the green band (e.g. McFeeters, 1996). An updated version of NDWI, known as modified normalized difference index (MNDWI) uses the short-wave infrared (SWIR) to overcome noise issue (H. Xu, 2006). It is generally straightforward, and a common practice, to manually digitize the shorelines from NIR band or aforementioned indices for application of the waterline method. For example, Zhao et al. (2008) mapped the intertidal topography of Yangtze Delta using on-screen digitization of Landsat imagery and Z. Xu et al. (2016) manually digitized Landsat imagery to study the seasonal intertidal topography variation along the coast of South Korea. Using a semi-automated approach based on MNDWI, Tseng et al. (2017) reconstructed the time-varying tidal topography from a 22-year timeseries of Landsat imagery. These semi-automated approaches are typically calibrated for a particular region, or a single tile. Manual digitization or parameter tuning can become overwhelming for large number of tiles over a broad area (Salameh et al., 2019). Thus, the recent high-resolution spectral imagery with short revisit period (e.g., Sentinel-2) or radar missions (e.g. Sentinel 1) which are typically distributed in small tiles is generally not suited for application of manual or semi-automated waterline method over broad areas.

One of the major challenge to automatically identify the shoreline is the need to estimate a threshold (i.e. binary classification) to discriminate water from other. Since the threshold values usually vary with illumination, viewing angle and altitude (S. K. Jain et al., 2005), selecting a threshold can be time-consuming and subjective. Besides, applying a single threshold value for all images can lead to wrong shoreline detection (e.g. Frazier, Page, et al., 2000). Among recent

advancement in shoreline extraction from spectral images, Zhang and Baptista (2008) proposed a dynamic threshold method for the classification of from Landsat-8 OLI water index images, particularly suitable for lakes. Bergmann et al. (2018) proposed a semi-automated processing of multi-spectral imagery from PROBA-V satellite based on the water pixel classification method of Pekel et al. (2014). They also demonstrate the waterline method by combining the water level derived from nearby tide gauges – producing a DEM with typical accuracy of 1 to 2 m, at 100 m resolution using only a handful of PROBA-V acquisitions.

The present paper updates the method presented by Bergmann et al. (2018), with several key advances. First, our method allows the use of high-resolution spaceborne imagery dataset. Here we demonstrate an application using Sentinel 2 imagery at 10 m resolution. This dataset is one order magnitude higher in resolution compared to 100 m in PROBA-V images. To the best of our knowledge, this freely available satellite dataset has never been used for deriving an intertidal DEM. Second, our method is fully automated and generic enough to be applicable to shorelines ranging from sandy to muddy, including the ability to resolve fine estuarine network and narrow creeks. Finally, our method combines the application of remote sensing (used to infer the horizontal position of the waterlines at various phases of the tidal cycle) and high-resolution hydrodynamic modelling (used to vertically reference these waterlines) as suggested by (Mason et al., 1997). Removing the requirement of any ancillary *in situ* data makes our method lightweight. As a test case, we present here an application of our method to infer a DEM of the near-shore intertidal-zone over the whole Bengal delta.

The coast of Bengal delta (Figure 3.1), across Bangladesh and India, is a well known hotspot of coastal vulnerability. About 150 million people live in this region, characterised by a flat topography, with elevation typically inferior to 4 m above mean sea level (MSL) (Krien et al., 2016). The near-shore ocean is characterised by a broad and shallow shelf having a mild slope in order of 1/1000 to 1/5000, and a macro-tidal regime, with a tidal range in excess of 5 m in the North-Eastern part of the coast. The region is also prone to frequent tropical cyclones – on average, one major event in three years (Krien, Testut, et al., 2017). In the recent decades, three particularly devastating cyclones made landfall in this region, notably Gorky (1991), Sidr (2007), and Aila (2009) claiming about 140000, 3400, and 190 lives respectively. Due to the combination of low topography and high population, the coastal districts of Bengal delta are generally very prone to cyclone-induced flooding and associated loss of lives and assets (Ali, 1999).

The modelling of storm surge dynamics over this region is a challenging task for the scientific community. State-of-the-art numerical models are able to reproduce the estimated surge height, but they generally fail to reproduce the spatio-temporal evolution of the flooding (Krien, Testut, et al., 2017). Inaccurate and outdated representation of the near-shore bathymetry and land topography is identified as one of the most important factors that prevent from accurately reproducing the tidal dynamics, the cyclone surges characteristics as well as the coastal inundation patterns (Krien, Testut, et al., 2017; Rose & Bhaskaran, 2017). Using a bathymetry dataset derived from a large ensemble of digitized *in-situ* hydrographic surveys, Krien et al. (2016) significantly improved the representation of tidal hydrodynamics in the Bengal delta region. This dataset, however, essentially consists of point-wise soundings from shipborne surveys, which do

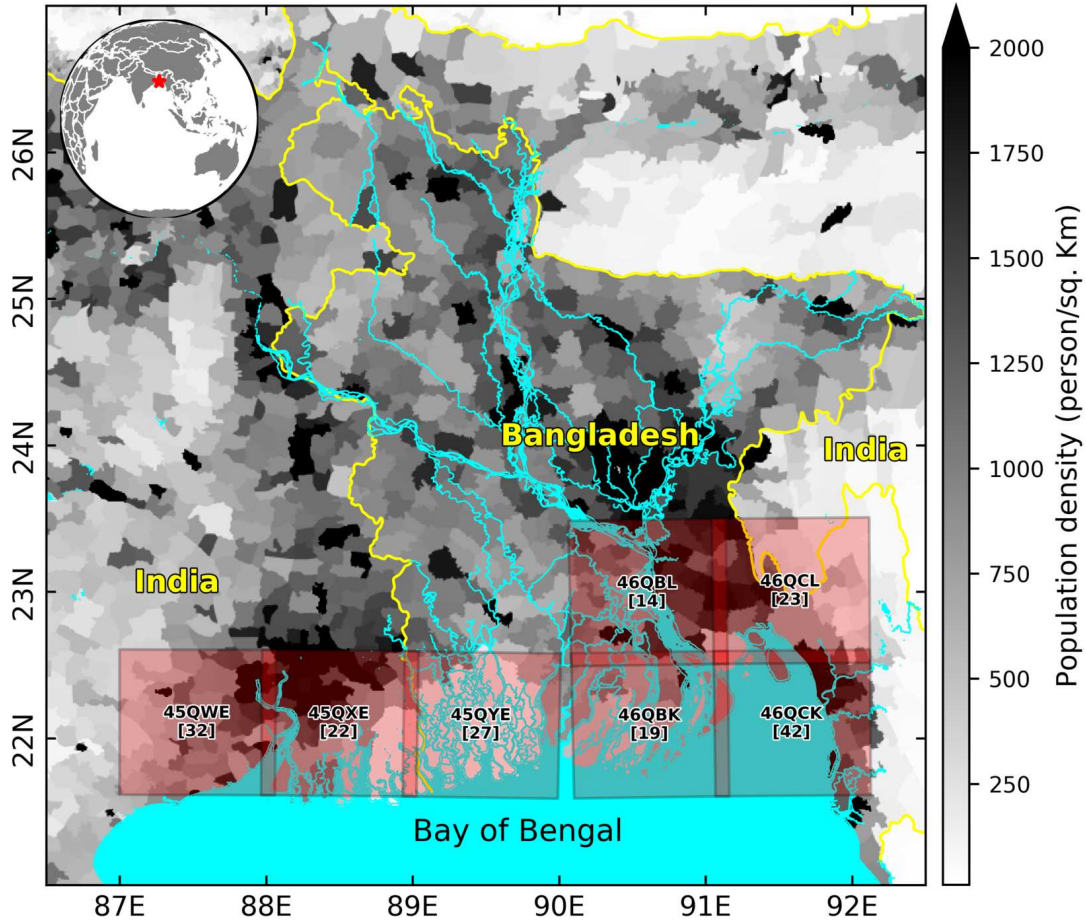


Figure 3.1: Location of the study area and the coverage of the Sentinel 2 tiles used in this study. Each tile (showed as a translucent red patch) is annotated with the tile identifier and in bracket the number of images used. The major rivers (showed in aqua color) is overlaid on the Gridded Population of the World (GPWv4) dataset (in grey scale) (Center For International Earth Science Information Network-CIESIN-Columbia University, 2016).

not cover the very shallow water zones (shallower than 2 m below MSL). This means that the whole intertidal area, which can be quite broad in this very flat region (up to several kilometres wide), are left void of up-to-date topographic data. However, it is well known that the knowledge of the intertidal topography is particularly important to realistically model the effect of wave set-up during storms and cyclones (e.g. Stockdon et al., 2006).

The Bengal coast is also characterised by erosion and accretion of the shoreline, that manifests at various timescales ranging from days to decades (A. F. Rahman, Dragoni, & El-Masri, 2011). These changes are particularly prominent in the mouth of Meghna estuary where the combined flow of Ganges, Brahmaputra, and Meghna is discharged. The large sediment discharge accompanies the runoff during the monsoon and then gets spread by far-reaching tidal currents as well as extreme events such as riverine floods and tropical cyclones (A. F. Rahman, Dragoni, & El-Masri, 2011; Tajima, Hamada, & Hussain, 2015). Because of this dynamic nature, it is not feasible to perform repeated, extensive *in-situ* hydrographic surveys over this extended deltaic region, thus making it a very interesting test case for applying our methodology.

The aim of this study is three-fold. First, we developed an automated procedure to extract waterlines from Sentinel 2 imagery. Second, we vertically referenced those shorelines using a hydrodynamic model of the area. This allows obtaining an intertidal topography. Third, we validated the resulting topography against *in situ* bathymetric observations harvested in a key-region of the Bay of Bengal. We present our algorithm to extract the shoreline in Section 3.2, which is followed by a description of our hydrodynamic modelling framework in Section 3.3. The resulting DEM over Bengal delta and its validation based on two independent *in situ* sounding dataset are presented in Section 3.4. Finally we discuss our results and conclude our work in Section 3.5 and 3.6 respectively.

3.2 Shoreline detection with Sentinel-2 imagery

Sentinel-2 project was launched by European Space Agency to acquire high resolution multi-spectral images with short revisit frequency. It comprises two satellites – Sentinel-2A and Sentinel-2B, successfully launched in 2015 and 2017. The objective of these missions is to provide long-term research-quality acquisition of land surface monitoring products. For the monitoring of water bodies, the use of Sentinel-2 is very appealing due to its open-access nature, high resolution (10 m), and short revisit period (about 10 days). Sentinel-2 satellites acquire data over 13 spectral bands – four bands (blue, green, red, near infra-red - NIR) at 10 m resolution and six other bands (including shortwave infra-red - SWIR) at 20 m resolution. Because of the large dataset size, Sentinel-2 products are distributed as tiles of 1x1 degree. We have used the Copernicus Sentinel-2 data processed at level 2A by CNES at Theia Land data centre (<https://theia.cnes.fr>). The data is provided in separate GeoTIFF arrays for each of the spectral bands. All the individual tiles had been corrected from the atmospheric and adjacency effects, along with the detection of clouds and their shadows using MAJA processing chain (Petrucci et al., 2015).

3.2.1 Pre-processing of the dataset

For detection of shoreline, we have used the B2, B4, B8 and B11 bands, with the spectral properties provided in Table 3.1. We have selected images from the archive avoiding instances with prominent cloud cover (typically less than 10%). The images were already orthorectified and georeferenced. We have considered about three years of archive, from January 2016 to October 2018. This temporal selection encompasses in average 75 individual Sentinel-2 passes. Finally, we have considered seven tiles fully covering the coastal region of the Bengal delta. With 14 to 42 individual frames per tile, this selected dataset encompasses a large fraction of the observable tidal range. The coverage of the selected tiles, and the corresponding number of frames per tile are displayed in Figure 3.1. The corresponding satellite and timestamp information of the images are provided in supplementary Table 1 through 7 of the article.

As mentioned in the previous section, our shoreline analysis approach is essentially an upgrade of the methodology presented in Bergmann et al. (2018). We updated their algorithm to make it compliant with the 10 m resolution of Sentinel-2 imagery, applicable to smaller tiles, and in a fully automated fashion. We consider the surface reflectance products identified by the prefix FRE (Flat Reflectance), corrected from both atmospheric and land slope effects.

Table 3.1: Spectral characteristics of the Sentinel-2 bands used.

Band	Spectrum	Resolution	Central Wavelength	Bandwidth
B2	Blue	10 m	490 nm	65 nm
B4	Red	10 m	665 nm	30 nm
B8	NIR	10 m	842 nm	115 nm
B11	SWIR	20 m	1610 nm	90 nm

Each band data file is coded on 16 bit integer. The original reflectance value is found from dividing this integer dataset with 10000. The pixels which were out of the field-of-view of the satellite pass are coded as -10000. Figure 3.2 shows a sample of the Sentinel-2 bands used in this study.

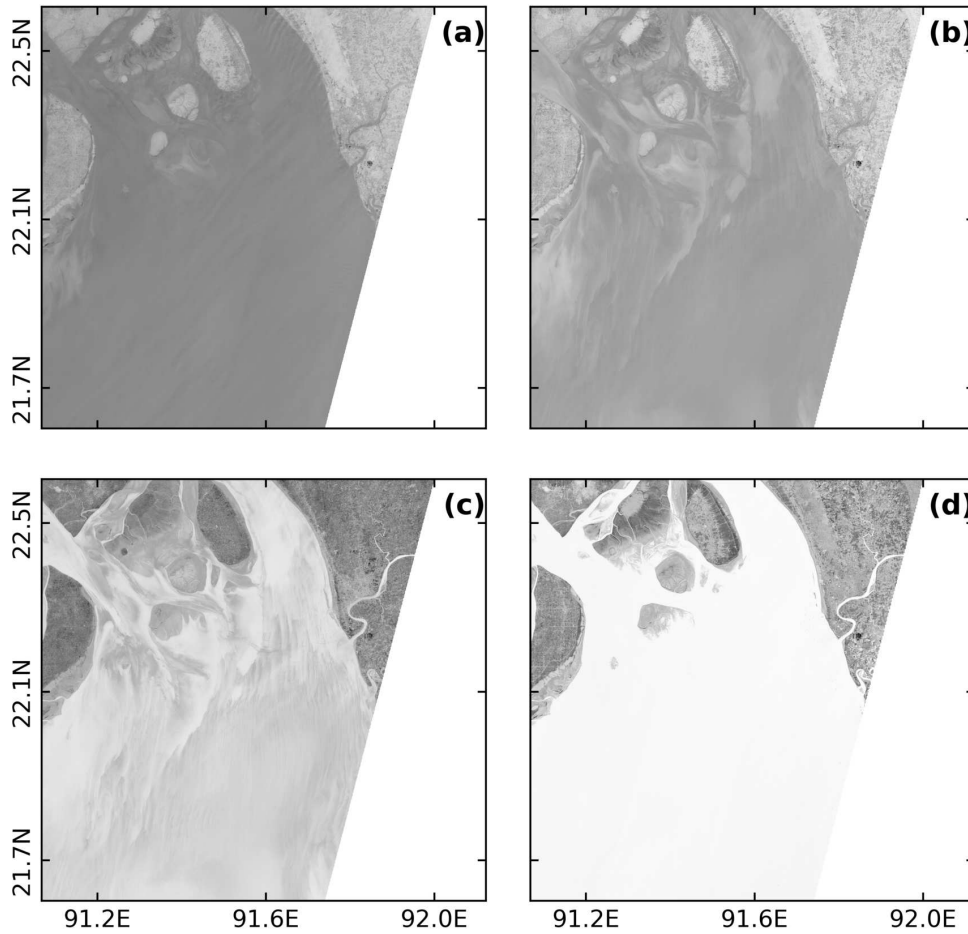


Figure 3.2: Greyscale display of the four original Sentinel 2 L2A bands obtained for tile #46QCK on 01/02/2017 04:38:25. The band B2, B4, B8 and B11 are respectively being displayed in (a), (b), (c) and, (d). The scale represents the pixel with the lowest value in white to highest in black. For clarity of the image, the pixel value is restricted to lower than the 99.99th percentile for each band.

Naturally, the illumination conditions vary from one scene to another for a given tile. On several scenes, we also noticed the presence of few pixels with very high reflectance values. While we could not confirm the reason, at all instances these pixels correspond to some form of slanted roofs that might have induced powerful sun glint. To be consistent along the time series of

the images, and to make our algorithm robust, we applied a pre-processing of the B11 band to remove these artificially bright pixels. We do so by capping the values at mean plus one standard deviation (std) on the upper side, i.e. restricting them within $[0, \text{mean}+1*\text{std}]$. Once the pre-processing of the B11 band is done, we apply a normalisation of the dataset to $[0, 1]$. Finally we use a nearest-neighbour approach to resample B11 band to 10 m from its original 20 m resolution. The B2, B4 and B8 bands are also normalized to $[0, 1]$ for further processing.

In our approach, the B11 band serves as a transparency channel, the so-called alpha band. A synthetic red-green-blue-alpha space is constructed using B2, B4, B8 and B11 bands according to Equation 3.1.

$$\begin{aligned}
 red &= (1 - B11_{norm}) + (B11_{norm} * B4_{norm}) \\
 green &= (1 - B11_{norm}) + (B11_{norm} * B8_{norm}) \\
 blue &= (1 - B11_{norm}) + (B11_{norm} * B2_{norm})
 \end{aligned} \tag{3.1}$$

The subscript *norm* refers to the pre-processed and normalized bands of the previous step. This allows taking the full advantage of land/water contrast captured in the B11 band while retaining the high-resolution information from the other three bands (Figure 3.3).

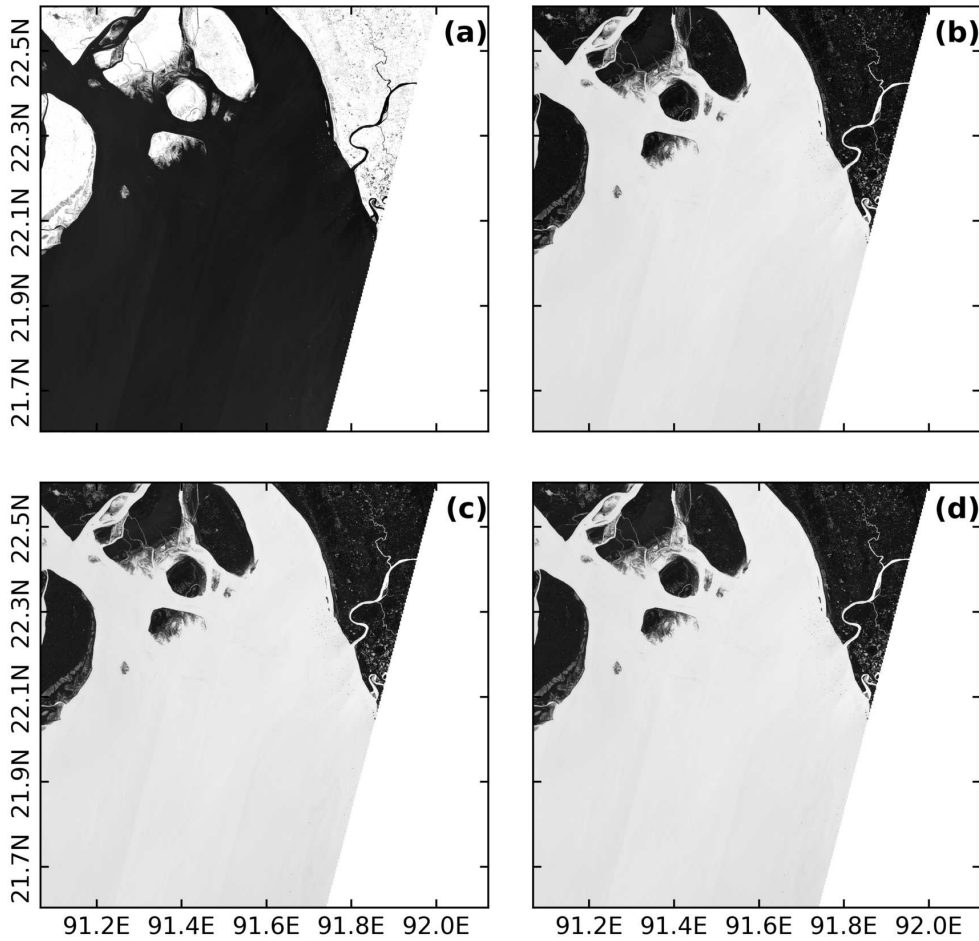


Figure 3.3: Same tile as Figure 3.2 but for the (a) alpha, (b) synthetic red, (c) synthetic green, and (d) synthetic blue band. The grey scale is from the lowest pixel value (black) to highest (white).

This synthetic RGBa (red-green-blue-alpha) bands in Figure 3.3 are converted to hue, saturation and value (HSV) colour space following Pekel et al. (2014). Among these three, we discard the saturation, which is essentially the intensity of the hue. This separation makes our algorithm indifferent to the various illumination conditions which are bound to happen for a multi-year archive. Only value and hue channels presented in Figure 3.4 are retained during the subsequent procedure.

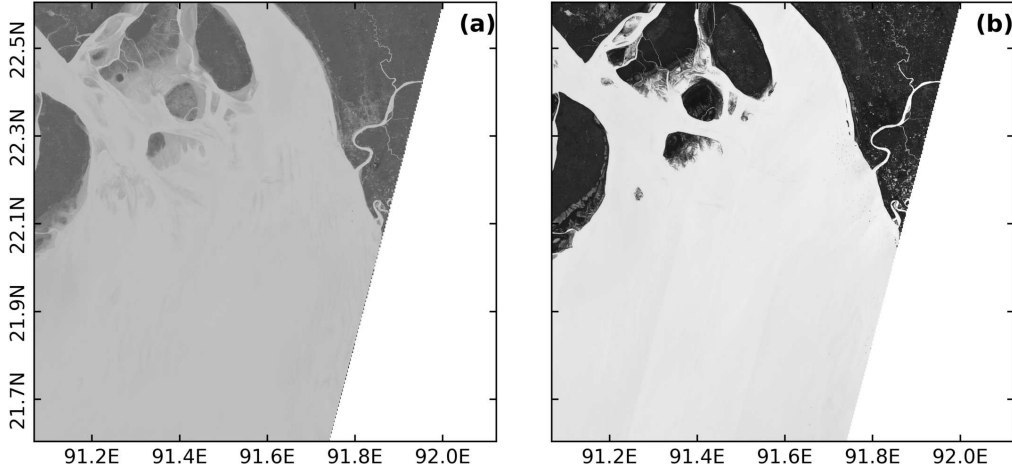


Figure 3.4: Same tile as Figure 3.2 and 3.3 for the (a) hue, and (b) value band converted from the synthetic RGB Band. The grey scale is from the lowest pixel value (black) to the highest (white).

3.2.2 Coarse water mask

One of the essential steps in Bergmann et al. (2018) is the preparation of a coarse water mask – only once for a given region – typically by hand, to roughly separate the water from land areas. This step allows guiding the subsequent accurate discrimination of water and land pixels along the land-water interface area. Preparing such a mask manually for a large area dataset like our test-case could be tedious. To automate the preparation of this mask we used the fact that B11 band consistently shows a very distinct contrast between land and water pixels. First we normalize the multiple acquisitions of B11 band, and merge all images by taking a pixel-by-pixel average. The first advantage of this merging is the filtering of any artefact that may be present in individual B11 band images (typically: localised stripes of under-illuminated pixels), thus retaining a clear separation between land and water with reduced noise. The second advantage is the full coverage of the tile by the accumulation of observed pixels. Each tile is essentially a clipped version of a continuous image along the swath of the satellite, thus yielding individual tiles which are not always fully covered during a pass (i.e., missing values). By combining all the available images, the presence of missing values is avoided.

To generate the water mask itself, we apply a threshold based on the standard deviation of the merged band, using Equation 3.2.

$$Mask = \begin{cases} 0, & \text{where } B11_{merged} \geq n_{mask} * \text{std}(B11_{merged}) \\ 1, & \text{where } B11_{merged} < n_{mask} * \text{std}(B11_{merged}) \end{cases} \quad (3.2)$$

Here $B11_{merged}$ is the normalized and merged B11 band, $\text{std}(B11_{merged})$ is the standard deviation of the $B11_{merged}$ and n_{mask} is a scalar factor. The output of this operation – **Mask** – is a 2D array with water (1) and land (0) coarsely classified. For our application, we found that an n_{mask} of 0.5 is suited for all the tiles. However, we recommend adjusting the value if needed, especially for tiles covering environments where the relative number of water pixels is very low (e.g., inland water body mapping).

The Mask is further refined by application of a blob-removal procedure. For pixels identified as water (mask value of 1), any pixel blob with size smaller than 10000 pixels is replaced by land mask value (0). On the other hand, for the pixels identified as land (0), any blob with size smaller than 50000 pixels is replaced by water mask values (1). This process essentially removes the noise and results in a cleaner coarse segmentation of land and water. Once this final cleaning is done, we obtain the water mask. This process is done only once for a given set of images. One example of such mask for tile #46QCK is presented in Figure 3.5a.

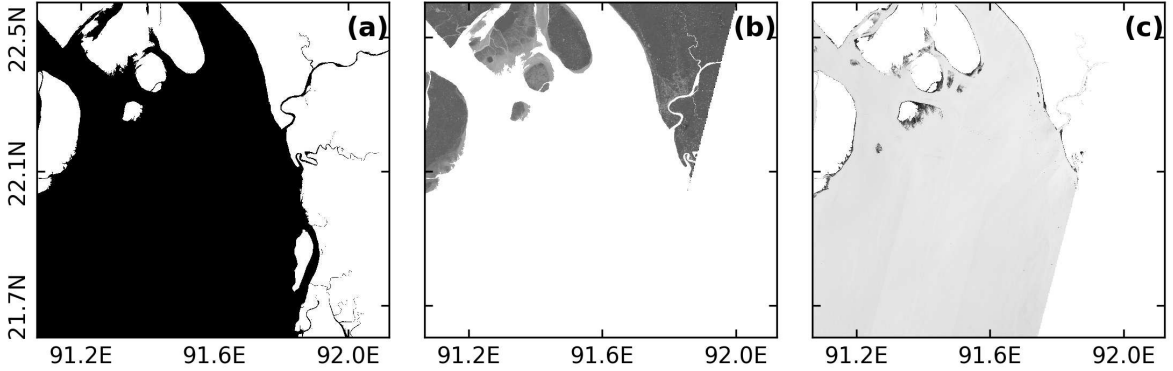


Figure 3.5: (a) The water mask derived from combined B11 band of tile #46QCK, black being the water and white is the land. (b) Inverse masking of hue band, (c) Masking of value band showed in Figure 3.4.

3.2.3 Shoreline extraction

The basic principle of our shoreline extraction algorithm is to discriminate the pixels at the land-water interface guided by the pixel values of land and water zones coarsely separated by the above-defined coarse water mask. To identify the land-water interface, we first apply our water mask presented in Figure 3.5a to the hue and value channels. This mask is applied directly on the value channel (roughly retaining the water pixels, Figure 3.5b) and inversely on the hue channel (roughly retaining the land pixels, Figure 3.5c). For each individual acquisition, median and standard deviation are calculated for these masked channels - which are subsequently used to apply as a threshold on the images as defined by Equations 3.3.

$$\begin{aligned} \mathbf{BW}_{hue} &= \neg(\mathbf{I}_{hue} < T_{hue} + n_{hue} * \sigma_{hue}) \wedge (\mathbf{I}_{hue} > T_{hue} - n_{hue} * \sigma_{hue}) \\ \mathbf{BW}_{value} &= (\mathbf{I}_{value} < T_{value} + n_{value} * \sigma_{value}) \wedge (\mathbf{I}_{value} > T_{value} - n_{value} * \sigma_{value}) \end{aligned} \quad (3.3)$$

Here the *hue* and *value* subscript indicate the channel type, \mathbf{I} is the original value of the channel before masking, \mathbf{BW} (for Black-White) is the resulting binary channel. T and σ are the median and standard deviation respectively. \neg indicates the logical **NOT** operation.

Essentially Equations 3.3 separate land and water pixels at the interface by taking a window around the median of the inversely-masked hue channel and of the masked value channel. The size of the window is controlled by n_{hue} and n_{value} for hue channel and value channel respectively. Lower scaling factor results in a stricter window of threshold, and vice versa. After several trials and visual inspection of the shorelines, we selected 0.5 and 3.0 for n_{hue} and n_{value} respectively. These values are close to the values used by Bergmann et al. (2018) for PROBA-V (0.4 and 5.0 for n_{hue} and n_{value} respectively). The \mathbf{BW}_{hue} and \mathbf{BW}_{value} channels are then AND-connected to obtain the final separation of land-water interface. The result of this operation is presented in Figure 3.6a.

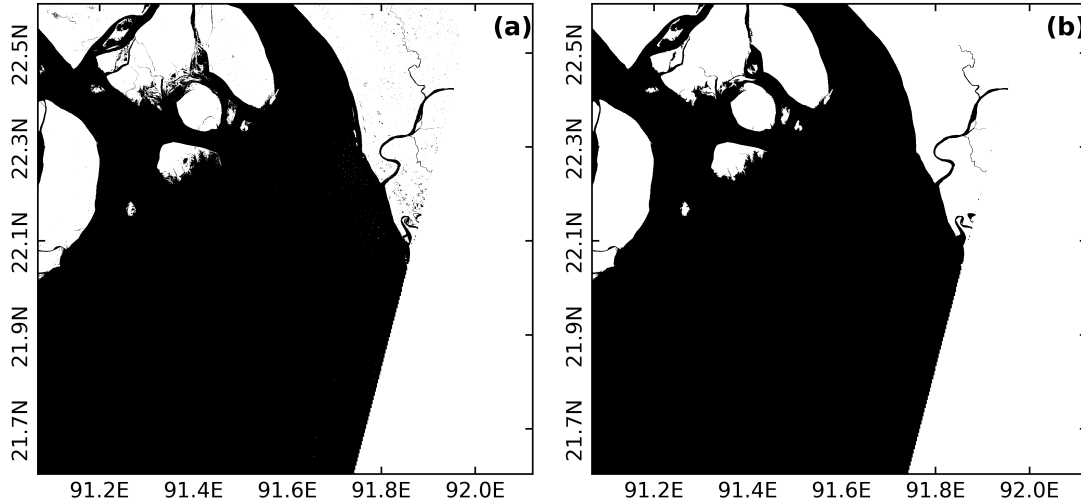


Figure 3.6: (a) Binary water (BW) image obtained from the combination of \mathbf{BW}_{hue} and \mathbf{BW}_{value} for tile #46QCK acquired on 01/02/2017 04:38:25. (b) Same as (a) after applying filling of water pixel group smaller than 10000 pixels and removing land pixel groups smaller 10000 pixels.

At the final step, small-scale features are removed based on their size. We discard all water features smaller than 10000 pixels in size inside land area; similarly we remove all land features smaller than 10000 pixels. These correspond to an area of 1 km². This cleaning essentially removes all ships detected in the ocean as well as the smallest ponds detected inland. As a consequence of this cleaning, certain small-scale features such as coastal sandbars are also removed in our analysis, which are visible during low tide but submerged at high tide. The resulting image after our blob removal procedure is presented in Figure 3.6b.

The final step of identifying the shoreline is applying an edge-detector on the classified land-water binary image. To do this, the blob-removed binary water map obtained in the previous step is convoluted with a 3×3 Laplacian kernel following Equation 3.4.

$$SH(i, j) = \sum_{p=1,2,3} \sum_{q=1,2,3} K(p, q) BW_{clean}(i - p + 1, j - q + 1) \quad (3.4)$$

Here, BW_{clean} is the clean binary water map, SH is the extracted shoreline map and K is the 2D kernel matrix defined as:

$$K = \begin{bmatrix} 0 & -1 & 0 \\ -1 & 4 & -1 \\ 0 & -1 & 0 \end{bmatrix} \quad (3.5)$$

The application of this edge detector in binary 2D space results in a raster image where only the pixels forming the water/land interface are left. The location of the shoreline is then defined at the centre of these pixels and converted to longitude-latitude coordinates from the native UTM projection of the satellite images. An example of the resulting shoreline is shown on Figure 3.7.

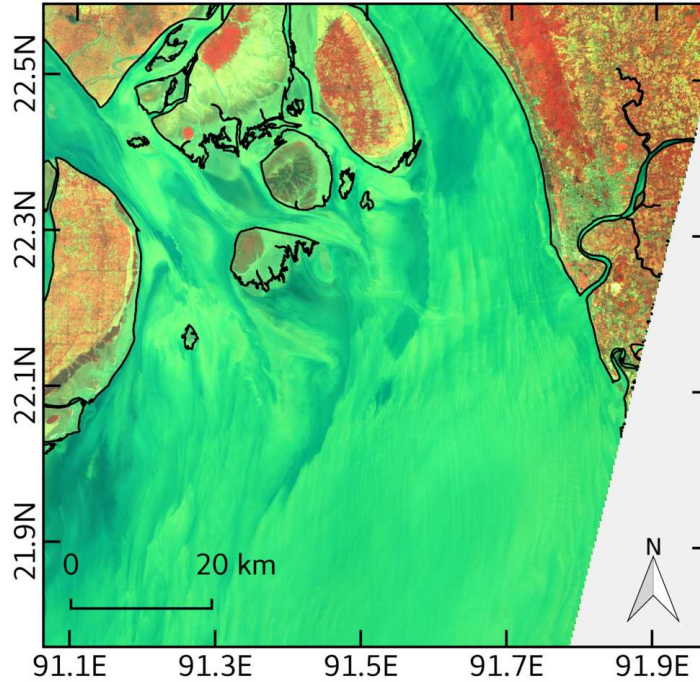


Figure 3.7: The black line is the extracted shoreline for tile #46QCK acquired on 01/02/2017 04:38:25 overlaid on a false colour RGB constructed from B2, B4, and B8 Band presented in Figure 3.2

This aforementioned procedure is summarized in the flowchart shown on Figure 3.8. We apply this algorithm over the time series of selected Sentinel-2 images. Eventually a manual cleaning of the resulting water lines is performed to remove large, disconnected water bodies (particularly for tile #45QXE and tile #45QYE at their northern edge), which were too large to be removed using our blob-removal procedure. In most cases these disconnected water bodies are large shrimp farms. The vertical referencing of this timeseries of shorelines is described in the following section.

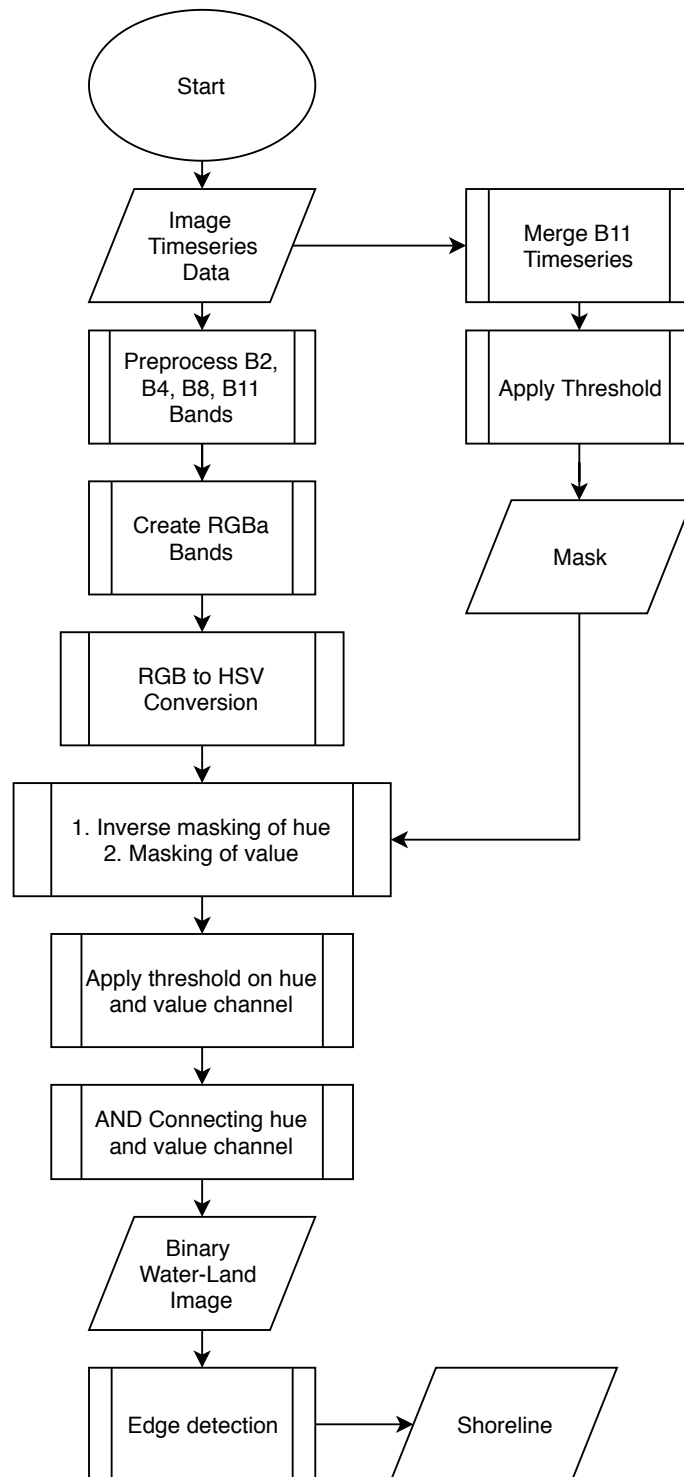


Figure 3.8: Flowchart of the shoreline detection procedure.

3.3 Vertical referencing with tidal model

Applying the method described in the previous subsection over our time series of Sentinel-2 images results in a set of shorelines detected at various tidal phases (between low tide and high tide). Conceptually, assigning a vertical position to each of these shorelines would require the

knowledge of the water level (as observed typically by a tide gauge) at each pixel along the shoreline, at the time of the acquisition of the corresponding image. Such estimates of the water level can be achieved by various means – including using a local tide gauge to estimate the evolution of water level in the time and space, using a publicly available tidal atlas to predict the tidal water evolution, or using a full-fledged hydrodynamic model running over the time span of the acquired image set. For example, Bergmann et al. (2018) used several local tide gauges to estimate the evolution of water level in time and space by spatio-temporal extrapolation. One could also rely on any good-quality tidal atlas available over the area to predict the tidal water evolution at the location and time of observation of the retrieved shorelines. We hereafter follow this latter option, based on a hydrodynamic tidal modelling framework we purposely developed for accurate tidal water level prediction over the Bengal delta.

3.3.1 Hydrodynamic tidal modelling framework

We have used SCHISM (Semi-implicit Cross-scale Hydroscience Integrated System Model (Zhang et al., 2016), a derivative code of SELFE (Semi-Implicit Eulerian-Lagrangian Finite Element) model, originally developed by Zhang and Baptista (2008). This modelling framework solves the 3D shallow-water equations for ocean flow and sea level, using finite-element and finite-volume schemes. It has been designed and used for many geographical areas including our region of interest, covering a broad range of spatial scales ranging from ocean basins (e.g. Krien et al., 2016; Zhang et al., 2016) to very shallow lagoons and estuaries (e.g. Bertin et al., 2014; Guérin et al., 2018) as well as from short temporal scales (e.g. tsunamis, Priest et al., 2014) to seasonal and inter-annual scales (e.g. Tazkia et al., 2017).

The tidal model presented in this study is a major update to the one presented in Krien et al. (2016). Considering the importance of the near-shore bathymetry in the realism of the simulated water level variability, and the successful use of navigational charts in the bathymetric dataset used by Krien et al. (2016) to define the model geometry. We updated the bathymetry described in Krien et al. (2016) with 34 new navigational charts over the northern Bay of Bengal. This process resulted in 77000 manually digitized sounding points. This bathymetry dataset is then used to develop the model mesh showed in Figure 3.9.

The model mesh is triangular, unstructured (viz. with varying spatial resolution) discretized based on the wave propagation criterion and bathymetric gradient (Krien, Testut, et al., 2017). The unstructured grid allows refining considerably the horizontal resolution in the shallow coastal ocean that forms the focus of the present study (Figure 3.9). The model mesh extends from 11° N to 24° N, and comprises about 600000 grid points. The resolution of the elements ranges from 250 m in the inter-tidal area at the lower part of the delta (above 20° N) to 15 km in the deep off-shore ocean. Along the shorelines of India and Myanmar (south-western and south-eastern edges of the model domain), the near-shore resolution ranges from 1.7 km to 3.5 km. The model resolution is found to be sufficient to capture the geometry of the polders and dikes that are ubiquitous in the southern part of the delta. For the temporal integration of the model, a 300 seconds time step was chosen after few sensitivity tests, although in our modelling framework a time step ranging from 200 to 400 seconds was found to be equally performing, thanks to robust numerics of the model formulation.

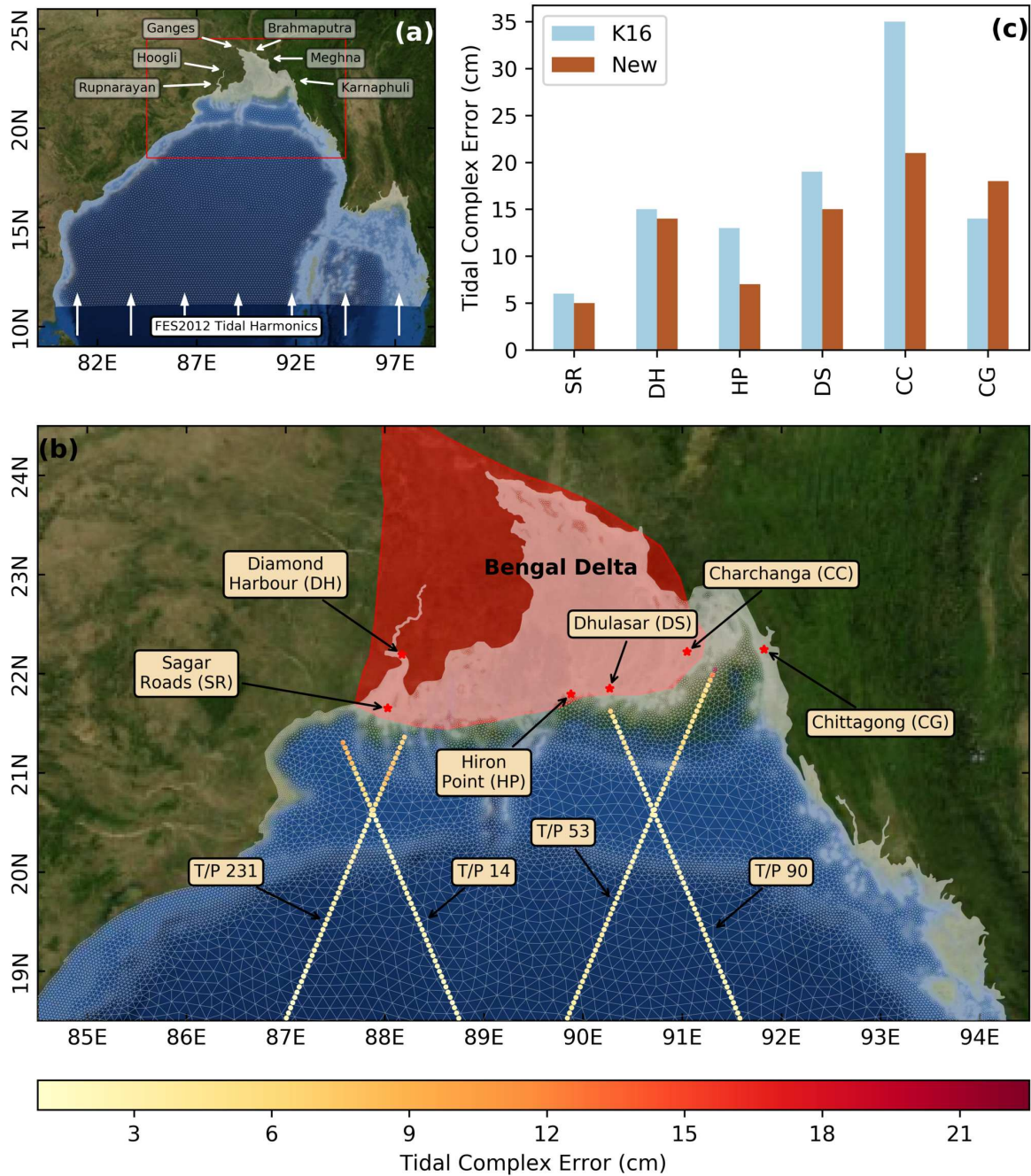


Figure 3.9: (a) Model mesh over the domain with indication of the open boundary conditions used. (b) A close-up of the model mesh over the study area. The tidal complex error is shown in colour-scale along the satellite altimetry tracks. The coastal tide gauges used for validation are shown by red stars. The Bengal delta is shown in red translucent patch (c) Bar plot showing the tidal complex error compared to Krien et al. (2016) (denoted as K16) for the 6 tide gauges shown on (b).

The model is forced with three different forcings – tidal potential for whole domain, tidal elevation at the southern open boundary and river freshwater fluxes at the upstream riverine open boundaries. Figure 3.9a shows the locations of these open boundaries. The choice of tidal

constituents for tidal potential and tidal elevation at the southern boundary is kept essentially the same as in the configuration of Krien et al. (2016) with some addition. The amplitude and phase of the tidal constituents prescribed at the southern boundary are extracted from FES2012 atlas (Carrère et al., 2013). To reproduce the seasonal changes in water level observed in the Northern Bay of Bengal, we have also imposed an annual cycle of 35 cm amplitude along the southern open boundary in the same manner as Tazkia et al. (2017). The river freshwater fluxes - one of the ingredients of coastal water level variability (Durand et al., 2019) - are prescribed in the inland open boundaries. We have prescribed rated daily discharges at the upstream boundaries of Ganges and Brahmaputra rivers with observed data provided by Bangladesh Water Development Board (BWDB) for the year 2014. We have also imposed a monthly climatology of discharge of Hooghly river based on the discharge observed at Farakka (Mukhopadhyay et al., 2006), and a monthly climatology of discharge of Karnaphuli river based on the discharge observed at the Kaptai hydro-electric power plant (M. A. M. Chowdhury & Al Rahim, 2012). We have applied Flather boundary condition (Flather, 1987) at Meghna and Rupnarayan River allowing the tide to propagate freely outside the computational domain. At the remaining coastal boundaries, no normal flow is assumed for the velocity boundary condition. The bottom friction, which is represented through a Manning coefficient n in our modelling framework, is applied in a similar fashion to Krien et al. (2016) based on the bathymetric depth in the ocean ($n=0.013$ for regions shallower than 20 m and $n=0.02$ otherwise). A value of $n=0.01$ is imposed for all the rivers.

3.3.2 Tidal water level estimation for vertical referencing

The tidal analysis on the unstructured grid is performed using COMODO tools developed at LEGOS (Allain, 2016) on simulated hourly water level from December 2013 to January 2015 (14 months). In total, 33 constituents (M2, S2, O1, K1, K2, L2, J1, E2, 2N2, La2, M3, M4, M6, M8, Mf, MKS2, Mm, MN4, MS4, MSf, Mtm, Mu2, N2, N4, Nu2, P1, Q1, R2, S1, S2, S4, T2, Sa, Ssa), as well as the long-term mean (Z0) is extracted. This essentially amounts to a new tidal atlas for the Northern Bay of Bengal. The quality of the tide is assessed using complex error calculated from four dominant tidal constituents – M2, S2, O1, and K1. The assessment is carried out based on two independent datasets: tidal constants obtained from in situ tide gauges, and from spaceborne altimetry. The latter dataset is the CTOH product, available on <http://ctoh.legos.obs-mip.fr/data/coastal-products/coastal-products-1/tidal-constants> (see this website for further details on the altimetric processing). Our tidal atlas appears globally consistent with the spaceborne product, with errors in the offshore domain of order 3 cm, increasing shoreward along all altimetric tracks, but nowhere exceeding 23 cm (Figure 3.9b). Figure 3.9c shows the complex error estimation for the tide gauges shown in Figure 3.9b and its comparison with the results in Krien et al. (2016). At the gauge stations we have found a substantially reduced error estimate, particularly at the central region stations of Charchanga (CC) and Hiron Point (HP). The overall accuracy of our tidal atlas is of order 5 cm to 20 cm, which is unprecedented over our region, and in line with the performance of state-of-the-art tidal atlases along the best-documented shorelines (Stammer et al., 2014).

For vertical referencing of the shorelines extracted in Section 3.2, we used the full set of 33 constituents from our atlas to generate the water level at the timestamps of the image acquisition

by Sentinel-2 using COMODO tools. For each inferred shoreline from the imagery, the water level corresponding to each shoreline pixel is found in the model tidal prediction through a nearest-neighbour interpolation technique. Although most of the shoreline pixels are relatively close to water pixels, there are some instances where the tidal model does not cover the full extent of the tile (particularly the inland rivers in #45QWE). To be consistent, the detected shoreline pixels where the nearest neighbour is more than 6 km were discarded during the referencing process. This distance threshold is selected based on the assumption of relatively low water-level gradient and typical cross-river distance. At the shorelines with high bathymetric gradient, such as cliff shores, where the shoreline change between low tide and high tide is sub-pixel scale (<10 m), the lowest elevation value is registered for the various tidal stages.

3.4 Results

3.4.1 Intertidal DEM

Figure 3.10a presents our DEM over the whole domain overlaid on merged B11 band used in this study. Our DEM maps 1134 km² intertidal area along the coast of Bengal delta at 10 m resolution. The horizontal extent of our DEM is in order of 600000 km². The mapped intertidal topography ranges from -3 m to 3 m with respect to MSL. To the best of our knowledge, The geographical coverage of our product, along with the level of details visible at fine-scale throughout the deltaic river network, is unprecedented over our area. Figure 3.10b–f provides close-up views of several key-locations of the delta, contrasting the eastern active side of the delta (Meghna estuary, Figure 3.10b), the western dead side of the delta (Hooghly estuary, Figure 3.10c), the muddy islands located in the immediate vicinity of the mouth of Meghna (Hatiya Island, Figure 3.10d and Sandwip Island, Figure 3.10e), and the sandy beach region of Chittagong analysed by Bergmann et al. (2018) (Figure 3.10f).

Compared to the Hooghly estuary, Meghna estuary shows a much richer population of islands. The topographic slopes revealed by our dataset along the periphery of the south-eastern sandy islands (Hatiya and Sandwip, Figure 3.10d and 3.10e) are typically much milder than those of the islands located in the Hooghly estuary (Figure 3.10c). The Chittagong close-up in Figure 3.10f can be directly compared with the corresponding map in Figure 13 of Bergmann et al. (2018). It is seen that our waterlines are much smoother compared to Bergmann et al. (2018), despite the ten-fold increased resolution of our dataset. This indicates that our approach has injected appreciable amount of information, even at decametre scales, taking over the small-scale noise and artefacts of our detection procedure to be expected from the higher resolution images. Also, the numerous instances of overlapping and intersecting isolines seen in Bergmann et al. (2018) DEM are mostly unseen in the new DEM, which suggests that our updated procedure and high-resolution dataset altogether yield a physically more consistent retrieval. Given the pivotal role of decametric-scale near-shore bottom slope in the coastal ocean hydrodynamics (e.g. Stockdon et al., 2006), our product thus offers promising perspectives to coastal ocean modellers.

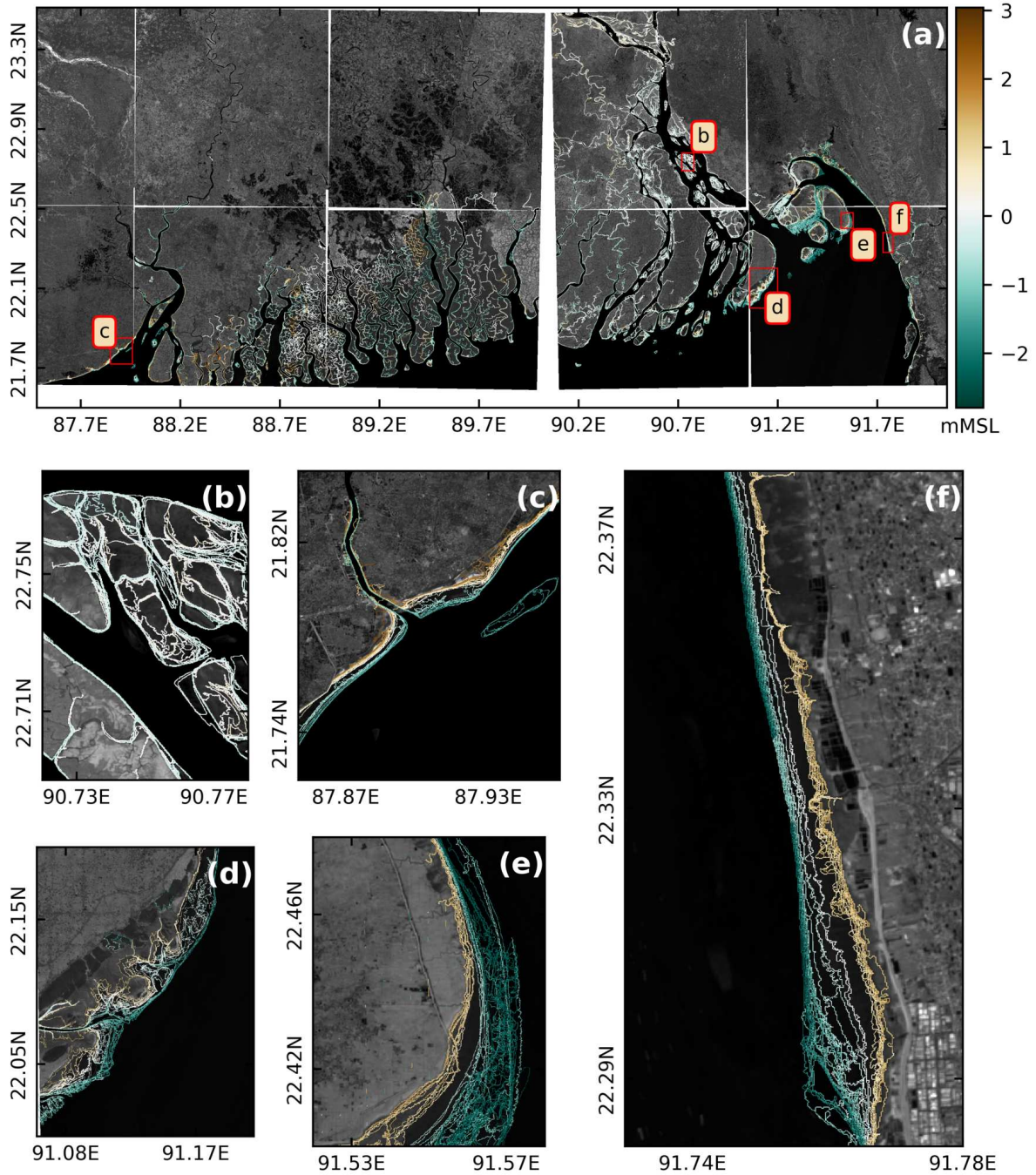


Figure 3.10: (a) The intertidal DEM over the study area. Each colour pixel is according to its elevation above Mean Sea Level (positive upwards). The labelled red rectangles indicate the zones where we have displayed zoom in (b) to (f). The background is a merged raster of B11 bands. The colour scale is the same from (a) through (f).

3.4.2 Validation of our DEM

Beyond the qualitative – though reassuring – features discussed above, it is timely to carry out a quantitative assessment of our DEM against independent *in situ* observations. We did so by relying on the three nautical charts from Bangladesh Navy Hydrographic and Oceanographic

Centre (chart #1251, #3001, and #3509, based on surveys conducted in 2012–2015) . We considered all charts point-wise soundings falling in the intertidal area, and co-located them with our own DEM. This resulted in 145 comparison points, displayed in Figure 3.11a. Figure 3.11b shows the error at individual points. For further visual comparison, a scatter plot between our DEM vs the *in situ* chart observations are shown on Figure 3.11c. The root-mean square difference between our DEM and the *in situ* soundings is close to 1.5 m, which is similar to Bergmann et al. (2018). However, our DEM presents a deep bias with the *in situ* soundings of 0.36 m. This value has the same sign, but is much smaller than the 1.2 m bias observed by Bergmann et al. (2018). This value is also in line with the typical bias of similar approaches in other regions (Salameh et al., 2019).

The aforementioned chart soundings dataset was produced from oceanographic vessels, which essentially leave the shallowest parts of the intertidal region void of observations. Hence we decided to collect a set of primary observations in this near-shore part of the intertidal area. This was done through a ship-borne hydrographic survey conducted on 11-13 February 2018 along the track displayed in Figure 3.11d. The measurements were operated through an acoustic echo-sounder, vertically referenced by an on-board GNSS using precise-point-positioning (PPP) processing. The trajectory usefully complements the spatial coverage of the previous dataset. Indeed, thanks to the small draught of the ship we used, and the high tide conditions during parts of the survey, it was possible to sail shoreward of the 0 m isobath in several occasions. The typical horizontal resolution of the *in situ* dataset is 50 m, which is close to the resolution of our spaceborne DEM. We collocated this dataset with our spaceborne DEM and could find 82 comparison points. It was found that our DEM presents a shallow bias of 1.19 m, and a root-mean square difference of 1.39 m, similar to the value found when considering the navy soundings. All these values of bias and standard error lie within the commonly accepted accuracy of *in situ* soundings (estimated to 1–2 m) (Sciortino et al., 2010). These error estimates and the visibly consistent features mentioned in the previous paragraph (viz. absence of isobaths intersections) give confidence in the overall validity of our new DEM.

3.5 Discussion

Our algorithm essentially builds on a well-known and tested methodology (Bergmann et al., 2018; Mason et al., 1995). However, our method utilizes a new generation of satellites and is computationally lighter and automated. We also demonstrated the utility of a good hydrodynamic modelling framework, instead of depending on ancillary *in-situ* data. The application of our algorithm to the imagery archive of Sentinel-2 over the Bengal delta resulted in a large-scale high-resolution intertidal DEM, encompassing the whole delta. The large area of the region we considered, of order 600000 km², did not induce any computational issue thanks to the lightness of the proposed procedure. Typically, it takes 6 - 7 hours on a laptop computer to process the Sentinel-2 archive and generate the DEM covering such an extended region. Based on both navy soundings and dedicated primary observations, we could conclude that our DEM has an accuracy order of 1 m, which is in line with the state-of-the-art estimates produced in this region or in similar environments (Bergmann et al., 2018; Bishop-Taylor et al., 2019).

There are some assumptions in this approach which should be kept in mind. We assume that

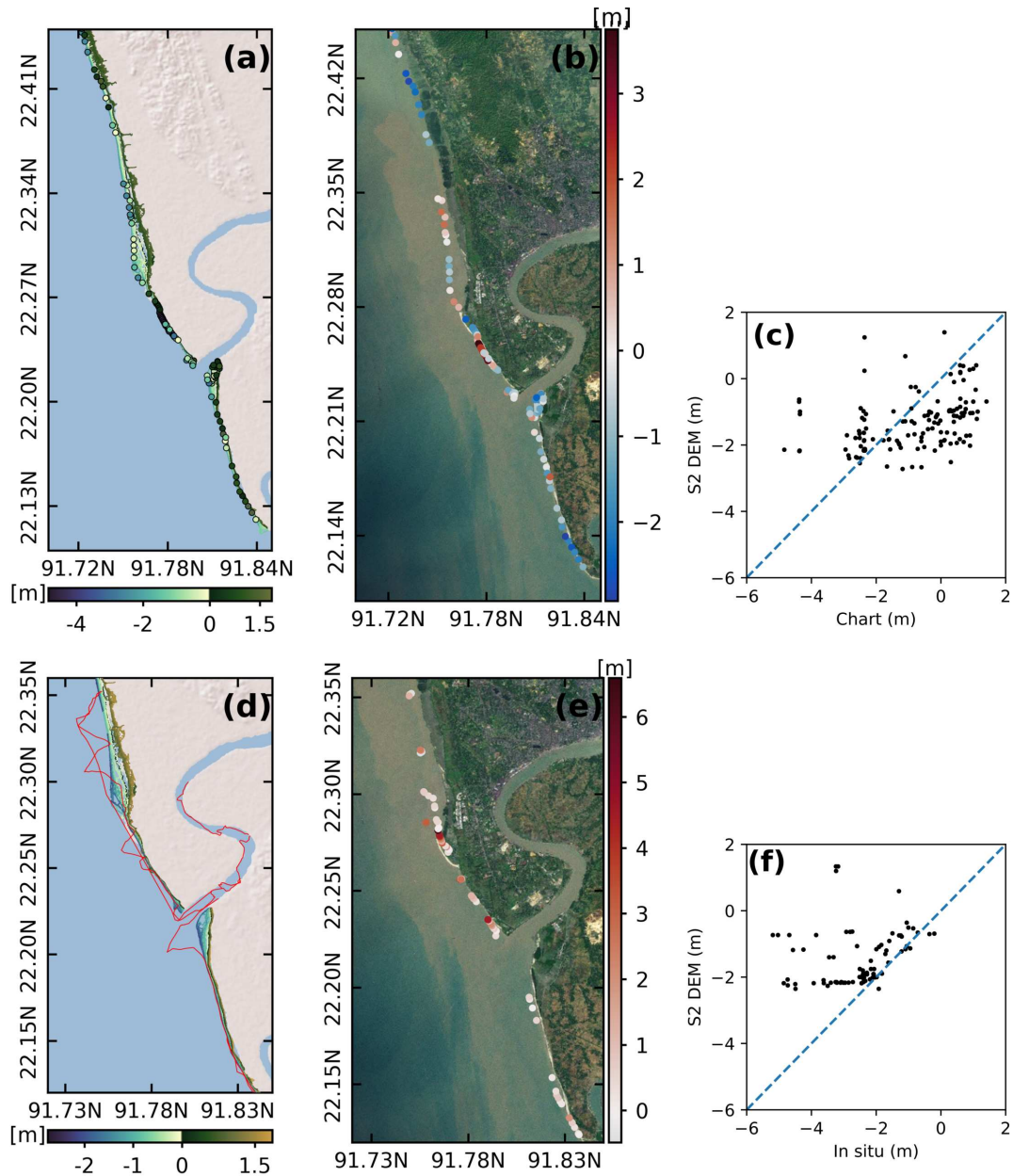


Figure 3.11: Validation of Sentinel-2 DEM. (a) Positions of the navy chart sounding points (bullets) overlaid on the Sentinel-2 DEM (blue-brown contours). The bullets colour features the elevation of the navy sounding points (in meters). (b) Positions of the collocated points between the navy sounding points and Sentinel-2 DEM. The colour of the bullets features the difference (in meters) between the two estimates. (c) Scatter plot between Sentinel-2 DEM vs the digitized navy sounding from charts. (d) Trajectory of the shipborne bathymetric survey (red line) overlaid on the Sentinel-2 DEM (blue-brown contours). (e) Positions of the collocated points between the shipborne survey and Sentinel-2 DEM. The bullets colour features the difference (in meters) between the two estimates. (f) Scatter plot between Sentinel-2 DEM vs the shipborne *in situ* sounding points. ESRI World Imagery is used as background in (b) and (e), whereas for clarity shaded relief from ESRI is used as background in (a) and (d).

the water level changes are driven by oceanic tide only. To validate our assumption, we replaced our tidal atlas by an ocean model hindcast, accounting for the atmospheric forcing (wind speed and air pressure) in addition to the tidal forcing. This did not appreciably change our resulting

DEM, thus not shown here. The reason behind this is that the selection of cloud-free images typically dictates fair weather conditions associated with minor non-tidal sea level variability. However, in other coastal regions of the world ocean, where the tidal range is weaker than in ours and/or where the effects of atmospheric variability on sea level become prominent, it may be required to adopt this kind of more sophisticated approach to make the most of Sentinel-2 and similar imagery products.

For vertical referencing using the model derived tidal water level, we co-located each shoreline pixel to nearest always-wet hydrodynamic model node. This assumes that the water level gradient is negligible in the scale of our hydrodynamic model (typically 300 m).

Additionally, our approach essentially assumes that the bathymetry of the intertidal zone is stationary over the duration of the imagery archive, which is rather small (about 3 years) in our case. However, in the case of coastal zones with prominent erosion/accretion, the long-term morphological changes might significantly distort the resulting DEM, which would result in waterlines artificially stretched, clubbed, and/or intersecting one another. In such circumstances a methodology more refined than ours may be required. Typically a workaround approach could be to segregate the imagery archive in consecutive epochs over which the morphological changes can be neglected, then analysing each of these periods individually following our methodology. This would allow identifying, beyond the intertidal DEM, the regions of marked erosion or accretion.

During the final step of our image processing, we have filtered the images to discard land and water features smaller than a certain size. In our case-study of Bengal delta, we have chosen 10000 pixels (1 km^2) to filter ships and small inland ponds and retaining the ocean-land shorelines. This value is essentially subjective and depends on the objective of the analysis. For example, if the objective of the image-processing is to map the inland water bodies, one may choose to remove this filtering altogether.

Based on the analysis over a broad region and multiple image tiles, we conclude that the n_{hue} and n_{value} parameters used in our study are robust and well suited irrespective of the study area. For any user willing to apply our algorithm on Sentinel-2 imagery, these values should remain as reported in this paper. Our ambition for this algorithm is also to be used for other dataset than Sentinel-2. Thus, we keep open the possibility to tune these parameters for sensors with radiometric characteristics different from Sentinel-2 mission.

3.6 Conclusion

In this work, we present a method to infer an intertidal DEM from Sentinel-2 multi-spectral imagery and hydrodynamic modelling. Our approach, being easy to implement and automate, was designed to be readily usable in any region worldwide.

The nearshore hydrodynamics, particularly during cyclones and storm surges, is an active field of investigation (Krien, Testut, et al., 2017; Rose & Bhaskaran, 2017). While waves play an important role in the flooding, the available topographic information over Bengal delta are generally of inadequate resolution to study the small-scale processes. In future studies, our new DEM could be useful for high-resolution nearshore wave modelling over the Bengal delta. The tools and methodology presented here can be extended to study the morphodynamics of coastal

regions, over broad geographical extent such as the large deltas.

Being computationally light, it paves the way towards the new generation of high-resolution spaceborne imagery. Our methodology is expected to be directly applicable to the meter-scale products already available from SPOT or PLEIADES missions, or to the future CO3D constellation expected in 2022. It also allows reanalysis of past missions in the same automated fashion presented here.

Our approach yields a DEM that can also be used to cross-evaluate other near-shore topography datasets, like the global digital surface model ALOS World 3D (AW3D30, 30 meters of resolution, (Athanasίου et al., 2019)) or newly available topography datasets provided by ICESat-2 (Ice, Cloud, and Land Elevation Satellite-2) altimetry mission carrying the advanced topographic laser altimeter system (ATLAS) instrument, which is very promising for estimating the elevation of coastal and intertidal areas at low tide (Salameh et al., 2019).

Epilogue

The analysis of the Sentinel-2 multi-spectral imagery presented here reveals a synoptic view of the tidally-flooded area across the Bengal delta. The extent of the intertidal zone has a delta-wide diversity, showing the influence of tide along with a rich network of rivers and channels. The analysis of the imagery also clearly illustrates the existence of embankments in the poldered region, with a sharp discontinuity of the inundated and non-inundated area by the tide.

The tidal model developed for this study appears to perform well, compared both to altimetry in the open ocean and to tide gauges at the coasts. Notably, I could achieve an improved tidal representation across the GBM estuary. The improvement is substantial as the water level is strongly influenced by both tide and riverine discharge.

As shown in this chapter, multi-spectral imagery provides an independent mapping of the water extent in the intertidal area in horizontal space-time. The observations of shorelines combined with the water level in vertical space-time simulated from model reveals neatly organized, coherent contours of the intertidal topography height over the delta. The consistency of these two independent datasets – one observed from space, one modelled – indicates that the modelled water level corresponds well with the observed shorelines. The resulting high-resolution intertidal topography fills a gap in the continuum of the assembled topographic dataset. The success of this method serves as a second-order of validation of the tidal model along the vast, intricate and tortuous shoreline of the Bengal delta continuum.

CHAPTER 4

COASTAL TIDE: FROM THE PRESENT TO THE FUTURE

“It is far better to foresee even without certainty than not to foresee at all.” – Henri Poincaré, Foundation of Science

Preamble

Being a macro-tidal region with a low topography, a large portion of the Bengal delta shoreline experiences the tidal inundation twice daily. The multi-spectral shoreline mapping done in Chapter 3 revealed a large extent of these intertidal areas. Evidently, tide plays a major role in the sea level dynamics, and the rise and fall of tide shapes the inundation pattern for the unprotected coastal region. The purpose of the development of the embankments network was to protect the low-lying land from tidal flooding. The spaceborne imagery suggests that the embankment is functioning as expected to restrict tidal flood. It is to be noted that in my analysis, the chosen images were free of cloud, and consequently, the sampled sea level can be considered as primarily tidally-driven (as it excluded stormy conditions).

The tidal model performance with regards to altimetry in the open ocean, and to the available coastal tide gauge stations, indicates the tidal propagation is well captured by my model from the deeper part of the ocean to the coastal creeks. The consistency of the tidal model in vertically referencing the shorelines provides further confidence in the models' reliability in studying the response of the tide.

The response of the tide to the ongoing sea level rise could be of particular importance for the flooding hazard of the Bengal delta shoreline. The low-lying area of Bengal delta continuum is identified as one of the major hotspots of sea level rise induced vulnerability. Any significant change in tidal properties has the potential to modulate the impact of sea level rise. For example, an increase in tidal amplitudes can significantly worsen the flooding hazard. On the other hand, a decrease of tidal amplitudes can help mitigate the effect of the sea level rise. For the Bengal delta region, the trend of estimated sea level rise from tide gauges is slightly higher than the global average. However, the response of tidal behaviour is largely unknown.

This gap of knowledge motivated me to examine the sensitivity of coastal tide to sea level rise using the well-validated tidal model presented in Chapter 3. By imposing a variety of sea level rise scenarios to my model, I did a sensitivity analysis to understand how the modelled tide responds to the sea level rise along the coasts of the Bengal delta.

Publication: The work of this chapter has been published online in Continental Shelf Research on 27 October 2020. The article can be cited as - Khan, M.J.U., Durand, F., Testut, L., Krien, Y. and Islam, A.K.M.S., 2020. Sea level rise inducing tidal modulation along the

Abstract. The Bengal delta, the largest delta on the Earth, is subject to a marked coastal flooding hazard and associated with widespread vulnerability. The situation will expectedly deteriorate in the ongoing context of sea level rise. This sea level rise will not only have a direct effect on the coastal flooding, but will also have indirect effects, through the alteration of the coastal hydrodynamics. In the present study, we investigate the impact of sea level rise on tide, which is the largest source of variability of sea level along the macro-tidal coast of Bengal delta. Through a comprehensive modelling framework comprising the coastal delta, major estuaries, as well as the intricate hydraulic network of the delta, we assess the future changes of tidal properties to be expected for various sea level rise scenarios, representative of the end of the 21st century and beyond. It is found that the effect is large, and regionally dependent. Over both the south-western and south-eastern parts of the delta, the amplitude of the tide is expected to increase when the sea level is higher, which is bound to aggravate the tidal flooding hazard. In contrast, the central part of the delta will potentially experience massive flooding of river banks and adjoining lands in the scenarios exceeding 0.5 m of sea level rise. Consequently, this flooding induces a decay of the tidal amplitude in the central part. Our study shows that the tidal modulation is a significant ingredient that needs to be accounted for in the evolution of the future hydrodynamics of the Bengal delta. The friction-dominated and regionally contrasting damping and amplification mechanism also underscores the potential application of managed realignment strategy for a sustainable delta management in the future.

4.1 Introduction

Based on tide-gauge records, the global sea level has risen at a rate of about 1.1 mm/year on average over the 20th century (Dangendorf et al., 2017). The advent of altimetry revealed a marked acceleration over the last decades, with a sea level rise reaching 3.58 mm/year over the 2006-2015 period (Oppenheimer et al., 2019). According to IPCC, the projected median sea level rise (SLR) to be expected in 2100 ranges from 0.43 m (0.29-0.59 m, likely range; RCP2.6) to 0.84 m (0.61-1.10 m likely range; RCP8.5) above pre-industrial level (Oppenheimer et al., 2019). Recently, several studies projected even more extreme scenarios, suggesting that an increase of order 2 m should be considered as plausible (e.g. Bamber et al., 2019; Dominicis et al., 2020; Sweet et al., 2017). Moreover, SLR is virtually certain to continue beyond 2100 with an estimated rise of 1-3 m for each 1° temperature increase (Church et al., 2013). These numbers are alarming, as the coastal population settled in low-lying areas will exceed 1 billion by 2060 (Neumann et al., 2015).

SLR is of even greater concern for the low-lying subsiding delta areas (Becker et al., 2020; Oppenheimer et al., 2019; Tessler et al., 2015). The Ganges-Brahmaputra-Meghna (GBM) delta is a characteristic example of such subsiding deltas for which coastal flooding can be greatly enhanced by SLR (Becker et al., 2020). It is located at the northern head of the Bay of Bengal, covering an area larger than 100,000 km² (Figure 4.1). The region is densely populated and the delta area sustains more than 150 million people. The typical topography is less than 3 m above mean sea level (Krien et al., 2016) and contains a dense network of rivers and channels. The delta is macrotidal, with a typical tidal range in excess of 4 m (Krien et al., 2016; Krien, Testut, et al., 2017; Tazkia et al., 2017). The climate is dominated by the Indian monsoon. During each summer monsoon season, about 1GT of sediment gets flushed through the river

network (Goodbred & Kuehl, 1999), although in recent years a decreasing trend was reported by M. Rahman et al. (2018). In this sediment-laden fertile area, agriculture is the dominant land-use. To promote agriculture and manage the saline water intrusions, 126 polders (i.e. low-lying areas surrounded by embankments) were built during the period 1960 to 1990 (World Bank, 2005). These polders occupy the southern-central part of the delta (Figure 4.1). These polders, however, restrict sediment distribution over land and infilling of tidal channels (Auerbach et al., 2015). While the regional estimate of the subsidence ranges from 1 to 7 mm/year (Becker et al., 2020; Krien et al., 2019), Auerbach et al. (2015) reports land subsidence as high as 20 mm/year within some polders. This implies that the relative SLR poses a major threat for the ongoing century. In contrast, over the natural part of the GBM delta in the south-central region, the siltation may be able to cope with the effect of SLR (Bomer et al., 2020).

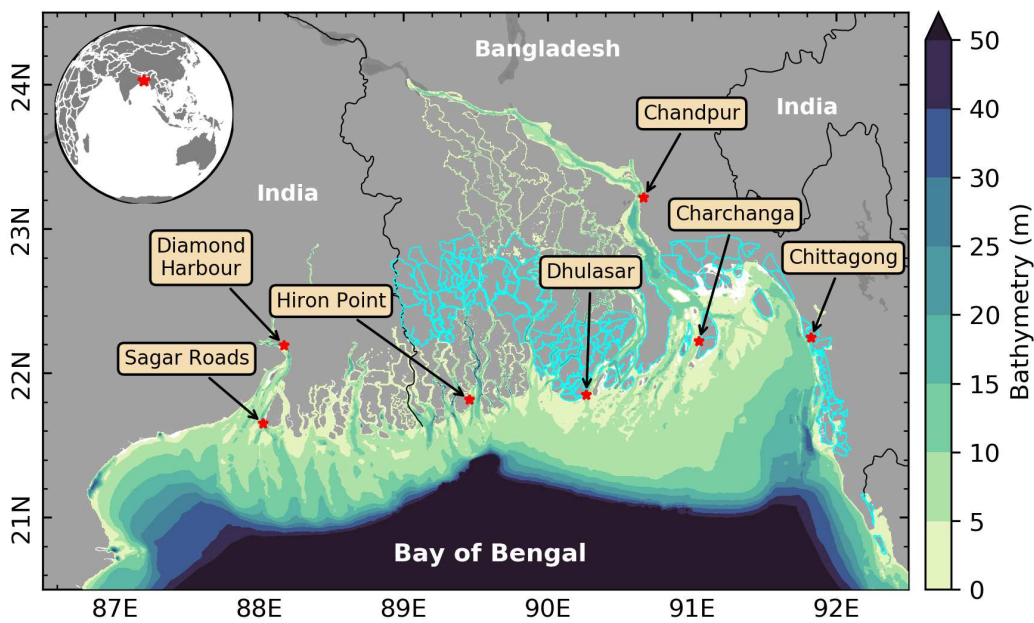


Figure 4.1: Layout of the Bengal delta with country borders. The near-shore bathymetry is mapped associated with the color scale. The cyan lines show the limits of the existing polders. The red stars indicate the location of the main tide gauges stations.

As the tidal sea level is a prominent ingredient of coastal flooding over the GBM delta (Krien et al., 2016; Krien, Testut, et al., 2017), the long-term evolution of the tide deserves specific attention. The objective of the present study is to analyse the long-term evolution of the tide expected in the Bengal delta, as a response to SLR. Indeed, tidal characteristics such as tidal range and tidal phase are known to respond to change in mean sea level (MSL), with strongest impacts in the near-shore ocean (Haigh et al., 2020; Talke & Jay, 2020). From a quasi-global tide-gauge data archive, P. Woodworth (2010) reported significant changes of tidal range in several areas and suggested that the changes are probably already occurring globally. The imprint of SLR on tidal characteristics is largely dependent on the region considered, amplifying tidal range in some locations, and reducing the tidal range in others (Idier et al., 2019; Idier et al., 2017). This is explained by the various mechanisms through which the mean sea level can affect the propagation of the tidal waves, in particular the frictional and non-frictional processes

(Haigh et al., 2020; Talke & Jay, 2020). Pickering et al. (2017) produced a global modelling of the projected tidal range under various SLR scenarios, ranging from +0.5 m to +10 m above current level. Over the northern Bay of Bengal, they suggested that a +2 m SLR would induce a contrasted change, with an increase of the tidal range in the eastern part of the GBM coastline, and a decrease in its central-western part. As the modelling initiative of Pickering et al. (2017) was global, it could not represent the details of the geometry of the GBM delta nor its intricate river network. From a limited set of observational sea level records located along the GBM delta shoreline, Pethick and Orford (2013) concluded that the tidal range has been increasing in the central part of the delta in the recent decades, at rates of order 5 to 30 mm/y, which lies well above the trends of eustatic sea level rise (referring to barystatic sea level, see (Gregory et al., 2019) for their recommendation). Hence it is important to investigate this process regionally, in the current context of SLR and associated increased exposure of the coastal areas to the flooding hazard.

The regional dependency of the impact of SLR on tidal characteristics, combined with the dearth of reliable, long-enough tidal records over the Bengal delta, naturally calls for numerical modelling as an appropriate means to investigate the future evolution of tide over this area. The aim of the present study is to draw firm conclusions on the impact of sea level rise on tides using a regional, high-resolution tidal model of the GBM delta. In Section 4.2, we present the observational dataset and long-term trend of tidal range observed in the central part of the GBM delta. Section 4.3 features our numerical tidal model and its performance analysis. Section 4.4 presents the projected changes modelled under the various scenarios we simulated. We present the analysis of our results in Section 4.5 and we conclude our study in Section 4.6.

4.2 Observed trend in tidal range: The example of Hiron Point

In order to illustrate the current trends over the GBM, we will present the signal observed at Hiron Point (89.47°E, 21.78°N, see Figure 4.1), in the south-central delta. As pointed out by Pethick and Orford (2013), a major hurdle in the GBM delta is the lack of long, consistent in situ tidal records. Although Hiron Point station stands out as the best documented over the GBM, these authors could only analyse 20 years of hourly records there. Here we analyse an updated, enhanced version of Hiron Point record. The Hiron Point tide gauge is situated in a relatively undisturbed region and maintained by Mongla Port Authority. The tide-gauge dataset is maintained and distributed by the Bangladesh Inland Water Transport Authority. Our timeseries is 40 year long (1977-2017), with few missing years in 2004-2005, 2011-2012, 2014-2016. We computed the daily (25 hours) low-water level, daily high-water level and daily tidal range from the hourly water level observations. We then computed monthly (28 days) averages of these quantities to remove the spring-neap cycle. As suggested by P. Woodworth (2012) we refrained from computing and removing the nodal tide from our timeseries.

Figure 4.2 shows the long-term changes and evolution of tidal characteristics in the record of Hiron Point tide gauge. We recall that, being restricted to one unique station, and keeping in mind the regional dependency of the long-term trends of tidal characteristics evidenced by Pickering et al. (2017) along the GBM coastline, this analysis should be considered as a qualitative illustration of the currently observed changes. It may certainly not be considered as

representative of the long-term change of tidal characteristics over the whole GBM delta. What is more, Hiron Point tide gauge is located in a narrow creek, and its vertical land motions have not been monitored.

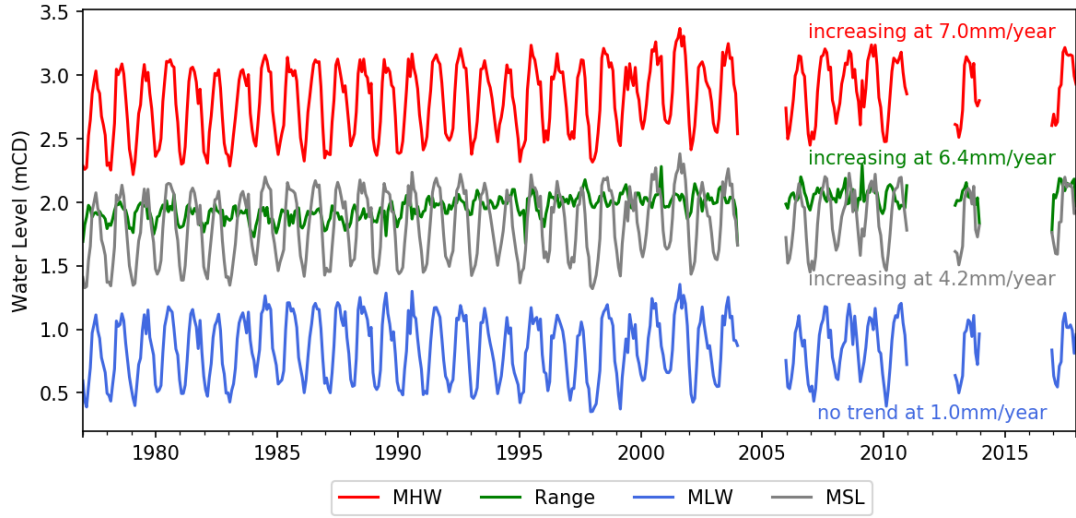


Figure 4.2: Monthly-mean (28-days) timeseries of observed water level at Hiron Point tide gauge. The red curve shows the mean high water (MHW), the blue curve shows the mean low water (MLW), the green curve shows the mean tidal range (Range), the grey curve shows the mean sea level (MSL). The levels are in meters relative to chart datum (mCD).

We have calculated the monotonic trend in various quantities of our timeseries using Sen slope (Sen, 1968). The significance of our trend is estimated using the Mann-Kendall trend test (Kendall, 1975; Mann, 1945). As shown by Tazkia et al. (2017), there exists a strong seasonality of the tidal range along the Bengal shoreline. This seasonality is a response to the seasonal cycle of the Bay of Bengal sea level, which is itself a manifestation of the monsoonal forcing of the thermohaline stratification of the Bay of Bengal (Benshila et al., 2014; McCreary et al., 1996; Shankar et al., 1996). We have applied the technique proposed by Hirsch, Slack, and Smith (1982) to test the significance of our trend for a seasonally varying timeseries. Similarly, the amplitude of the trend is calculated using the modified method suggested by Hipel and McLeod (1994).

From our monthly (28-day) average mean sea level, we found that the relative MSL has increased by 4.2 mm/year. This value, although based on the sole long enough pointwise in situ record we could access, appears representative of the magnitude of SLR observed from spaceborne altimetry over the Northern periphery of the Bay of Bengal during the past three decades (Not shown here, see <https://www.aviso.altimetry.fr/es/data/products/ocean-indicators-products/mean-sea-level.html>).

Similar to the MSL, a daily (25h) maximum and minimum is calculated, and then averaged over a month (28 days) to derive the monthly mean high water (MHW) and mean low water (MLW) timeseries. We have found that the MLW has increased at a much lower rate, at 1.0 mm/year, which is statistically not significant at 95% confidence interval and reported here as “no trend”. In contrast, the MHW has increased at a much faster rate, 7.0 mm/year. As a result, the tidal range has also increased by 6.4 mm/year. Except the MLW, all other quantities

are significant at 95% confidence interval.

These trend estimates essentially confirm and strengthen the findings of Pethick and Orford (2013), that the tidal range in Hiron Point is rising, probably in association with the significant sea level rise observed in the northern Bay of Bengal. The rate we report for the increase in MHW is around twice as large as the one for the MSL. This implies that the long-term changes in tidal characteristics can be a prominent ingredient in the evolution of the flooding hazard in the GBM, in addition to the long-term SLR. Hence the understanding of the underlying processes deserves careful consideration. As there does not exist any other consistent long in situ tidal record over the region, with duration sufficient to address the long-term trends, we hereafter restrict our analysis to numerical modelling, to gain insight on the future evolution of the tidal characteristics at the scale of the whole GBM delta.

4.3 Tidal model in the Bay of Bengal

The numerical model used in this study, SCHISM (Semi-implicit Cross-scale Hydroscience Integrated System Model, Zhang et al. (2016)), is a derivative code of SELFE (Semi-implicit Eulerian-Lagrangian Finite Element) model, originally developed by (Zhang & Baptista, 2008). It solves the 3D shallow-water equations using finite-element and finite-volume schemes, and was designed to model barotropic as well as baroclinic circulation for a broad range of spatial scales, spanning from the open ocean (e.g. Krien et al., 2016) to the very shallow lagoons and estuaries (e.g. Bertin et al., 2014). The model allows for wetting and drying. Our model set-up and the numerical grid are similar to the version used by Krien et al. (2016) and Tazkia et al. (2017), who investigated the tidal characteristics over the GBM delta and their seasonal variability, respectively. In the present study, however, the domain extends throughout the Bay of Bengal, with a southern boundary located along 11°N (Figure 4.3a).

SCHISM is used here in depth-averaged barotropic mode. Our bathymetry is developed over the one published by Krien et al. (2016). Their bathymetry is composed of digitized sounding from navigational charts published by Bangladesh Navy over the nearshore zone, digitized sounding from Inland Waterways Authority of India (IWAI), a high-resolution (50 m) inland topography of the south-central part of the delta from the Center for Environmental and Geographic Information Services (CEGIS), cross-sectional data of the inland rivers from Bangladesh Water Development Board (BWDB). The bathymetry used in this study is updated with digitization of about 77'000 additional points collected from a set of 34 recent nautical charts of the Bangladesh Navy (http://bnhoc.navy.mil.bd/?page_id=165) scattered around the model domain. In the deeper part of the ocean and rest of the inland areas we have complimented with GEBCO2014 (https://www.gebco.net/data_and_products/gridded_bathymetry_data/) and SRTM (<https://www2.jpl.nasa.gov/srtm/cbanddataproducts.html>) digital elevation model (as appear in GEBCO dataset) respectively. The grid resolution varies from 15 km in the central Bay of Bengal to 250 m in the most upstream part of the estuaries, which results in about 600'000 nodes and 1 million elements in total.

The bottom friction in our model is formulated through a regionally varying Manning coefficient n . The spatial distribution of Manning coefficient is similar to Krien et al. (2016) with $n = 0.02$ for the deep ocean (depth ≥ 20 m) and $n=0.013$ over the continental shelf (depth < 20

m). Manning value of 0.01 is set for the rivers, and 0.02 for the inland areas (Figure 4.3b).

The simulations used in the present study were carried out over a 14-month period, from 01/12/2009 to 31/01/2011. We discarded the first 15 days to let the model flow being spun up, and analysed the subsequent period for tidal analysis. A time-varying discharge was imposed for the Ganges and Brahmaputra rivers (Figure 4.3), using observations of the Bangladesh Water Development Board. We have imposed a monthly climatology of discharge for Hooghly river (Mukhopadhyay et al., 2006) and Karnaphuli river (M. A. M. Chowdhury & Al Rahim, 2012). At the upstream limit of Meghna and Rupnarayan rivers, a radiative open boundary was prescribed (Flather, 1987). Tidal elevations from FES2012 global model (Carrère et al., 2013) were prescribed at the southern open ocean boundary from the global model for the 26 dominant harmonic constituents (M2, M3, M4, M6, M8, Mf, Mm, MN4, Msf, MU2, N2, NU2, O1, P1, Q1, R2, S1, S2, S4, SSA, T2, K2, K1, J1, and 2N2). As regards to the tidal boundary conditions, the same modelling strategy was followed both for the current-epoch simulations and for the future-scenarios simulations.

The future scenarios are simply defined by superimposing an offset on the model MSL as regards to the current-epoch. Our choice of forcing the model at its southern open boundary with a present-day tidal solution was motivated by the findings of Pickering et al. (2017), who concluded that in the future SLR scenarios, the tidal amplitude remains practically unchanged in the southern part of the Bay of Bengal. This forcing strategy will be validated in Section 4.4, where we will conclude to a good consistency of our modelled changes and the one reported by Pickering et al. (2017) throughout the coastal part of the northern Bay of Bengal.

As we have significantly upgraded the bathymetry of our model compared to the past studies conducted with it, it is important to assess the realism of the tide simulated. The tidal analysis of the model outputs was achieved through the COMODO software (Allain, 2016). Table 4.1 presents the model performance, expressed in terms of amplitude, phase and complex error of the four dominant tidal constituents (M2, S2, K1 and O1) against observed values. Wherever possible, we also present our model performance against four state-of-the-art global tidal atlases, as follows:

- FES2012, the finite-element model (Carrère et al., 2013) built upon altimetry-derived harmonic constant assimilation;
- FES2012-Hydro, the hydrodynamic version of FES2012 (without data assimilation);
- GOT4.8 (Ray, 1999, 2013) and TPXO7.2 (Egbert & Erofeeva, 2002), two inverse tidal models derived from satellite altimeter data.

We found that, in line with Krien et al. (2016), the tide simulated by our model is far more realistic than the tide of any of the global atlases available. The benefit in terms of mean complex error amounts to an improvement by a factor of 2 to 6. This can largely be explained by our refined resolution and improved regional bathymetry. Moreover, our new model outperforms the representation of the tide compared to our previous study by Krien et al. (2016), by 10 to 50% typically, depending on the station considered. The residual errors we obtain range from 5 cm to 23 cm, for the coastal stations as well as for the estuarine stations located further upstream

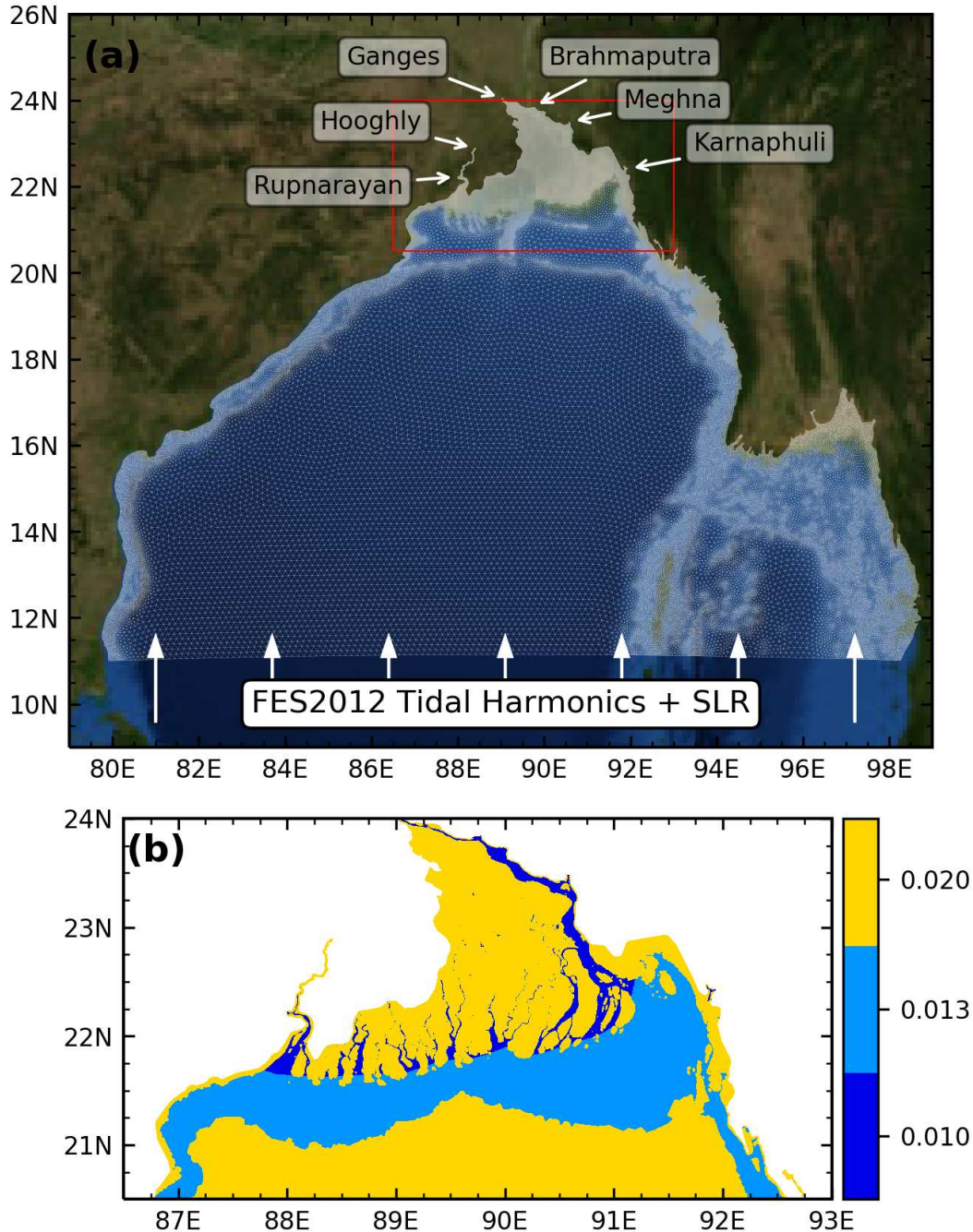


Figure 4.3: (a) Model mesh over the computational domain with indication of the open boundary conditions used. Red box indicates close-up area of frame (b). (b) Spatial distribution of the Manning coefficient n used in the model.

in the GBM delta. This level of realism is unprecedented over our area. Given that we use a similar numerical setup as Krien et al. (2016), with an identical forcing strategy, similar mesh resolution and identical bottom friction coefficient, this means that our improved bathymetry has a prominent impact on the quality of the simulated tide. One exception concerns the Chittagong station, where our model, although far more realistic than the global atlases, does not perform better than the previous version. This could be due to the inclusion of an open boundary in the estuary instead of a closed boundary as in Krien et al. (2016).

Table 4.1: Amplitudes (A) and error (σ_s) are in centimetres, phases (ϕ) is in degrees. Because of their location far upstream in the estuaries, Diamond Harbour and Chandpur are not represented in global tidal models (FES, GOT, and TPXO)

Station	Observation		FES2012-Hydro			FES2012			GOT4.8			TPXO7.2			Krien et al., 2016			This Model			
	A_0	ϕ_0	A_m	ϕ_m	Error	A_m	ϕ_m	Error	A_m	ϕ_m	Error	A_m	ϕ_m	Error	A_m	ϕ_m	Error	A_m	ϕ_m	Error	
Sagar Roads (88.0300°E, 21.6500°N)	M2	140	116	142	99	42	137	104	29	113	113	27	132	104	28	143	116	3	144.5	114.9	5.3
	S2	66	150	73	141	13	62	141	11	40	145	40	48	126	29	62	155	7	62.4	153.3	5.2
	K1	15	262	17	256	2	16	253	3	14	277	14	14	258	1	17	265	2	15.6	265.4	1.1
	O1	5	250	6	251	1	6	243	1	5	270	2	5	252	0.4	6	248	1	5.7	251.6	0.8
	σ_s					31				22			27			29			6		
Diamond Harbour (88.1733°E, 22.1928°N)	M2	157	168												166	161	21	142.3	165.6	15.9	
	S2	68	210												68	207	4	57.6	208.6	10.4	
	K1	15	285												16	284	1	13.2	286.3	1.8	
	O1	7	258												5	253	2	5.4	257.7	1.6	
	σ_s																	15			13.6
Hiron Point (89.4780°E, 21.8169°N)	M2	81	127	86	88	56	87	91	52	80	88	53	104	110	35	81	115	17	99.9	115.0	26.7
	S2	34	159	45	121	28	40	122	24	37	118	25	37	136	14	35	148	7	41.6	150.5	9.3
	K1	13	268	15	250	5	16	252	5	14	248	5	14	261	2	15	265	2	15.0	265.7	1.7
	O1	5	258	6	244	2	6	238	2	5	244	1	5	256	0.3	6	245	1	5.7	255.0	0.7
	σ_s					44				40			42			27			13		20.0
Dhulasar (90.2700°E, 21.8500°N)	M2	73	158	58	114	52	80	117	53	79	117	54	86	121	51	51	156	22	67.6	143.3	18.8
	S2	35	193	39	141	33	39	142	32	39	146	29	35	135	34	20	194	15	28.5	179.6	9.8
	K1	13	286	15	262	6	16	256	8	15	260	6	15	255	8	12	297	3	13.3	287.8	0.5
	O1	4	278	6	256	3	6	243	3	6	256	3	6	250	3	5	280	1	5.6	273.8	1.6
	σ_s					44				44			44			44			19		15.0
Charchanga (91.0500°E, 22.2188°N)	M2	96	234	110	202	57	115	208	50	97	204	49	84	154	103	67	208	46	95.8	216.9	28.5
	S2	37.5	265	38	238	18	30	243	15	34	234	19	36	186	47	27	241	17	36.6	250.3	9.5
	K1	13	304	17	298	4	16	300	4	7	314	6	16	272	8	14	309	2	16.8	308.7	4.0
	O1	8	285	7	289	1	6	284	2	4	303	4	6	267	3	8	289	0	8.1	293.1	1.1
	σ_s					43				37			37			80			35		21.5
Chittagong (91.8274°E, 22.2434°N)	M2	173	196	118	193	56	126	200	49	120	192	54	89	153	123	156	198	18	149.2	194.8	24.1
	S2	64	229	41	230	23	33	236	31	43	227	21	40	160	62	58	235	9	55.0	225.8	9.6
	K1	19	278	17	294	6	17	295	6	9	300	11	16	258	7	20	289	4	19.1	284.9	2.3
	O1	8	263	7	285	3	6	280	3	4	289	5	6	252	2	8	269	1	7.9	267.3	0.6
	σ_s					43				41			42			98			14		18.4
Chandpur (90.6385°E, 23.2344°N)	M2	29.7	31.4																33.6	333.7	30.7
	S2	10.5	62.3																11.2	6.3	10.2
	K1	5.6	18.6																5.4	21.9	0.7
	O1	3.4	12.9																3.6	357.4	1
	σ_s																				

4.4 Projected changes in tidal range in the Bengal delta

4.4.1 Current tidal range

The mean daily tidal range over 2010 simulated by our model over the GBM delta is shown in Figure 4.4. As expected, it is consistent with the known patterns (Krien et al., 2016; Sindhu & Unnikrishnan, 2013; Tazkia et al., 2017). Two maxima of the tidal range are seen in the western part of the delta (Hooghly estuary) and in the eastern part (mouth of Meghna estuary and the north-eastern corner of the Bay of Bengal), with mean tidal ranges reaching 3.2 m and 4.8 m, respectively. In the central part of the coastal GBM from 89°E to 91°E, the mean tidal range is smaller, with values inferior to 2.4 m. On account of the flatness of the delta topography, the tide is seen to propagate far upstream in the various estuaries, beyond 100 km inside Hooghly estuary and inside the various branches of the central delta, and beyond 250 km in the GBM main stream.

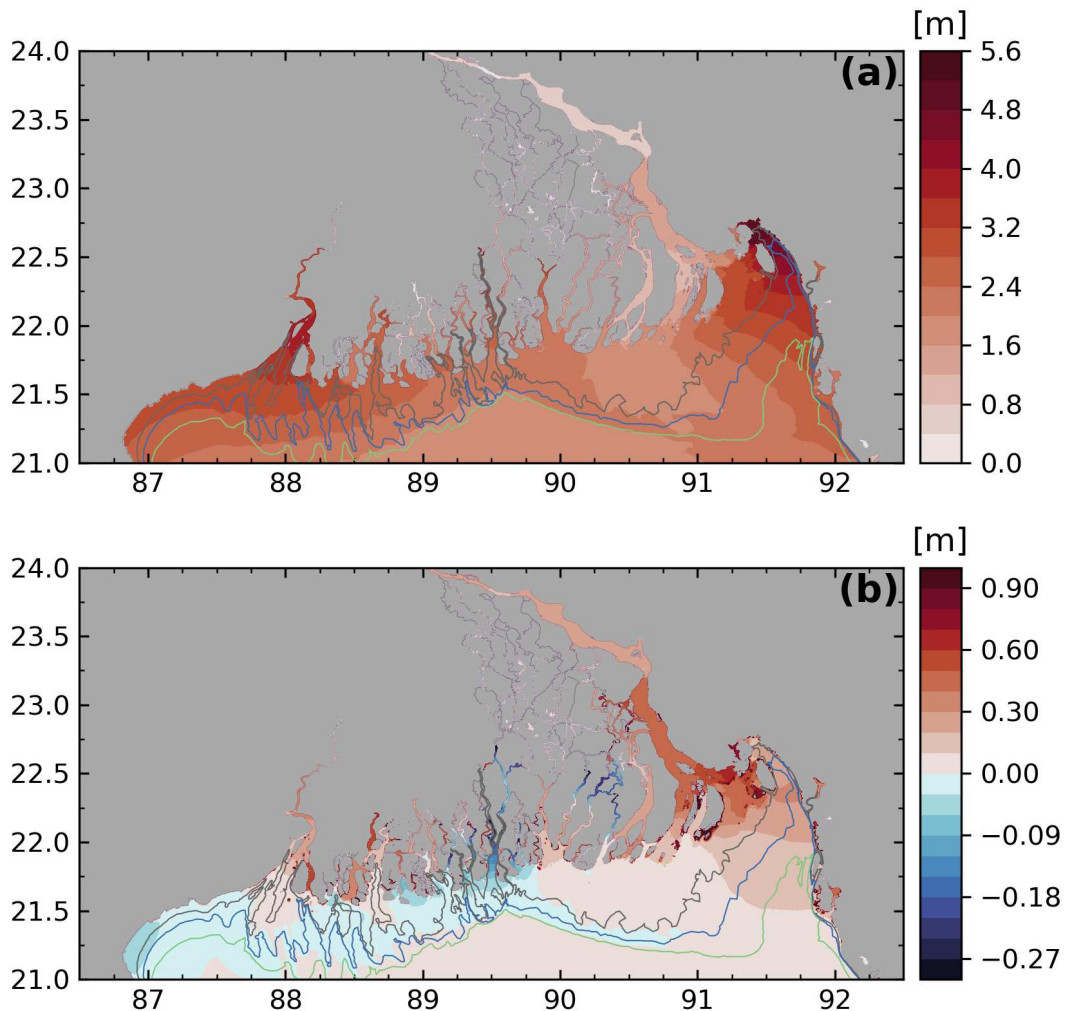


Figure 4.4: (a) Mean tidal range for the reference simulation, corresponding to present-day conditions. Isobaths 7 m, 10 m and 15 m are displayed. (b) Difference between the mean tidal range in the +1 m SLR and the reference simulation.

4.4.2 +1 m SLR

Various approaches have been adopted in the past to model the effect of future SLR on the coastal ocean. Some have assumed an unchanged topography (Krien, Dudon, Roger, Arnaud, et al., 2017; S. Rahman et al., 2019). In this case, whatever continental areas along the coastal strip currently lying below the elevation of imposed SLR plus the tidal amplitude will get flooded. Opposed to this approach, other studies have assumed that the coastline will remain unchanged under SLR scenarios. Numerically, unchanged coastline under SLR scenarios amounts to assuming that high enough structures protecting the shoreline are implemented consistently everywhere in the model domain, along the current coastline (as done for instance in Dominicis et al., 2020). A wide range of intermediate, more refined scenarios can be thought of, so as to take into account the spatial structure of vertical land motions (Pickering et al., 2017), the regionally-dependent erosion/accretion pattern of sedimentary plains (Auerbach et al., 2015; Bomer et al., 2020), or regionally-dependent coastal defence enhancement strategies (Feng et al., 2019). Pickering et al. (2017) evidenced a sensible impact of the approach selected among these, on the long-term evolution of tidal characteristics, in some areas of the world ocean (including in the deep ocean). In the absence of definite knowledge of the future evolution of coastal defences in the GBM, nor of the regional pattern of vertical land motion expected to take place over the GBM, and for the sake of simplicity, we assumed an unchanged topography in the present study. In this sense, our coastline can be seen as a soft shoreline: the low-lying coastal areas are freely inundated when the sea level rises. This choice is, we believe, the most reasonable one can make over our region.

In our first future-scenario numerical simulation, we impose a 1 m SLR by imposing a Z0 tidal constituent of null frequency and 1 m amplitude, along the southern open boundary. Numerically, this is equivalent to offsetting downward the model topography/bathymetry by 1 m. We then run the model in the same fashion as in the reference simulation, starting it on 1/12/2009, spinning it up during 15 days, and retaining the subsequent 13.5 months period for analysis. Figure 4.4b illustrates the change in mean daily tidal range calculated over one-year period simulated by the model in this +1 m SLR scenario, as compared to the reference simulation. It is seen that the effect is sensible over the whole delta, with contrasted values. In both the western and eastern parts of the coastal GBM, from 87.8°E to 88.8°E, and from 89.8°E to 92°E, the coastal mean tidal range increases, by values of order 10-30 cm. This increase extends upstream in the estuaries outflowing in these two regions, with particularly enhanced increase in some of them (for instance up to 40 cm in the Hooghly and up to 70 cm at the mouth of Meghna). In contrast, the central part of the delta, from 88.8°E to 89.8°E, exhibits a decrease of the mean tidal range, with values between -3 cm and -6 cm along the coastline, and stronger values, up to -30 cm, in the upstream part of the estuaries.

To gain further understanding on the modelled changes, we analysed separately the change in tidal amplitude for the two main tidal constituents over the GBM, M2 and S2. This was done by subjecting the 13.5 months of model outputs to the same harmonic analysis, both for the reference simulation and for the +1 m SLR experiment, through COMODO software. The results are displayed on Figure 4.5.

In our reference simulation, M2 and S2 amplitude pattern is in agreement to past studies, showing two local maxima on the east- and the west- corner with a central trough (Sindhu &

Unnikrishnan, 2013) (See their Figure 15 for M2 and Figure 10 for S2). We observe a stronger gradient in amplitude compared to theirs with ranges of spatial scale. It is expected given the high resolution of our model, as well as the inclusion of estuaries.

From Figure 4.5, it is seen that both tidal constituents contribute to the observed change in tidal range in the +1 m SLR scenario, with a decrease of tidal amplitude along the coastal part of the delta between 88.8°E and 89.8°E. The decrease remains weak along the open coastline (less than 5 cm or 5% for M2, less than 2 cm or 5% for S2) but it extends upstream in the estuaries for both constituents. Both to the west as well as to the east of this central region, the model shows an increase of both M2 and S2 amplitudes along the coastline. In the western part, at the mouth of Hooghly, the increase amounts to 5 cm (5%) for M2 and 2 cm (5%) for S2, and is enhanced northward inside the Hooghly estuary, to about 22.5°N, 100 km upstream of the mouth, for both constituents. In the eastern part of the coastal delta, the increase in tidal amplitude rises eastward, up to extreme values of 15 to 20 cm (15 to 20%) at the mouth of Meghna for M2. Similarly, the increase in S2 amplitude also increases eastward, up to values of 10 cm (20%) at the mouth of Meghna. This increase extends northward in the Meghna estuary, and remains in excess of 20 cm for M2 and in excess of 6 cm for S2 up to the bottleneck of Chandpur (23.2°N, 90.6°E).

If we closely look at the central part of the delta shoreline, between 89°E and 90.5°E, what is striking is the contrasted impact of SLR to the west of 89.8°E vs. to the east of 89.8°E, with a decrease of tidal amplitude to the west of this longitude, and an increase to the east of it. However, the tidal range in the reference simulation is fairly homogeneous across this central region. Similarly, the cross-shore variation of bathymetry appears alike, as both sides of this central region sit in the area of narrow submarine delta, with a 15 m isobath located typically not more than 50 km offshore. In this regard, keeping in mind that the delta is both low-lying and very flat in this south-central region, it is relevant to examine the effect of the 1 m SLR on the extent of tidal flooding. Figure 4.6 presents the spatial structure of the frequency of wetting in the current conditions as well as in the +1 m SLR scenario. It is seen that under the +1 m SLR scenario a large fraction of the central delta gets submerged more than 75% of the time, whereas the tidal flooding is minor in the reference conditions. The tidal flooding is widespread in particular in the coastal belt located between 89°E and 89.8°E, where the tidal range is seen to decrease under this SLR scenario. The tidal flooding extends far inland there, up to the edge of the model grid, 75 km upstream or so. A prominent tidal flooding also appears in the inner part of the delta, between 90°E and 90.6°E, to the north of 22.4°N, up to 23°N. To the south of this region, and over the rest of the coastal delta, the currently dry land remains essentially dry in the +1 m SLR scenario, thanks to the embankments present there (Figure 4.1).

4.4.3 Robustness of the projected changes under other SLR scenarios

As the projected SLR by the end of the 21st century has a large uncertainty bound, it is important to get an idea of the linearity of the response of tidal amplitude change to SLR. Beyond the issue of regional dependency of the sign of the expected change in tidal range (positive vs negative) presented in Section 4.4.2, the past modelling studies of Pickering et al. (2017) and Feng et al. (2019) concluded that a significant fraction of the world coastlines exhibit a non-proportional

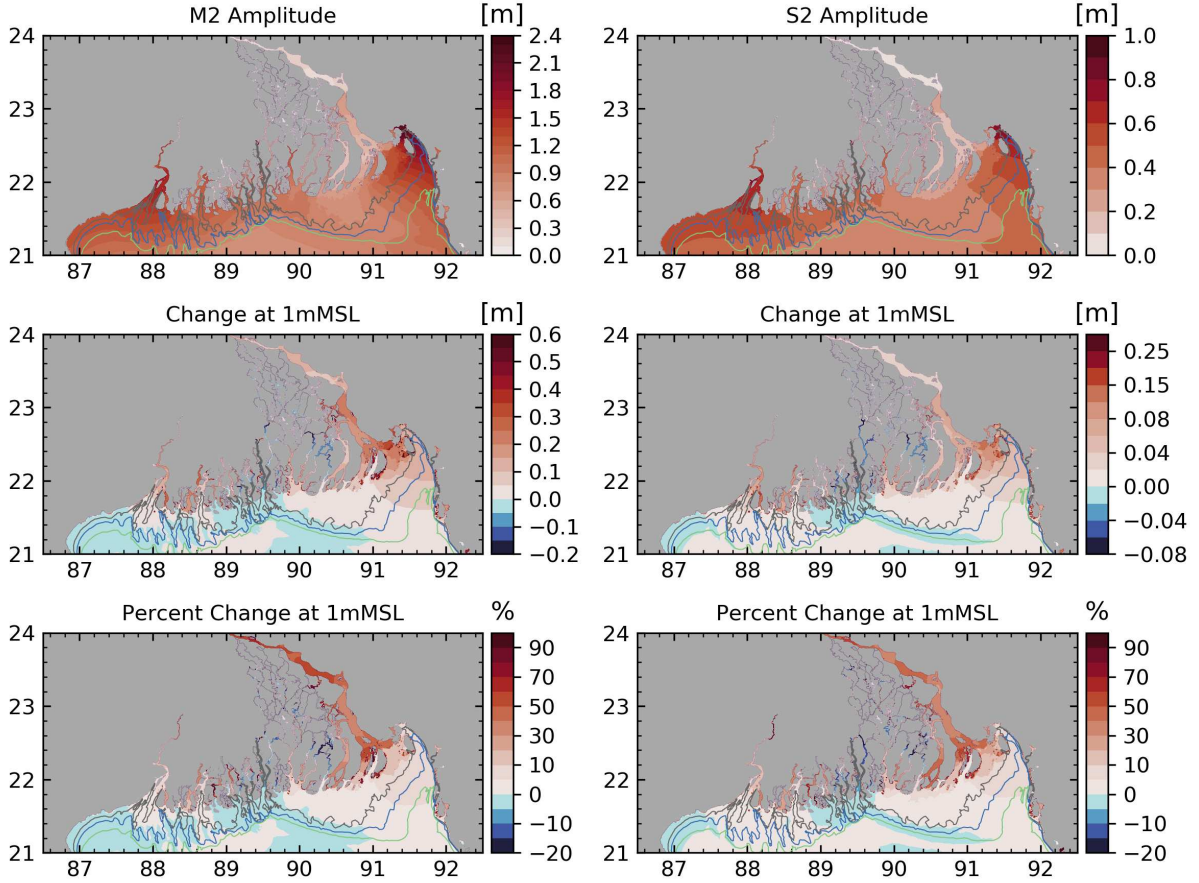


Figure 4.5: Amplitude in the reference simulation and difference between the amplitude with +1 m SLR and reference simulations of M2 tidal constituent (left) and for S2 tidal constituent (right). The bottom row shows the difference between the two simulations, expressed in percentage of the amplitudes in the reference simulation.

response, prominently under severe SLR scenarios (typically +2 m and beyond), with some regions being above proportional and others being below proportional. We simulated two more severe SLR scenarios (+1.5 m and +2 m), as well as one moderate scenario (+0.5 m) to gain insight into this question over the GBM. The same modelling strategy as for the +1 m SLR simulation was followed for these sensitivity experiments, with SLR imposed at the southern open boundary of the model, with 15 days of spin-up and 14 months long simulation. The simulations were similarly subjected to harmonic analysis. We considered the evolution of M2 tidal constituent, as it dominates the tidal signal. Figure 4.7 illustrates the results for three stations located in the eastern part of the GBM, spanning the region of increased tidal range under SLR. Hiron Point is located in the western part of this sub-region as already mentioned in Section 4.2, Charchanga is located in the central part of this sub-region at the mouth of Meghna, and Chittagong is located in the eastern part (Figure 4.1). It is seen that this sub-region shows distinct behaviours from one place to another. The amplitude of M2 appears above-proportional in Charchanga, at the mouth of Meghna, throughout the range of scenarios we tested. While the +0.5 m SLR scenario yields a +1.7 cm amplitude increase (about +2%), the four-fold +2 m SLR scenario shows a +17 cm amplitude increase (20%, or ten-fold the rate of the +0.5 m

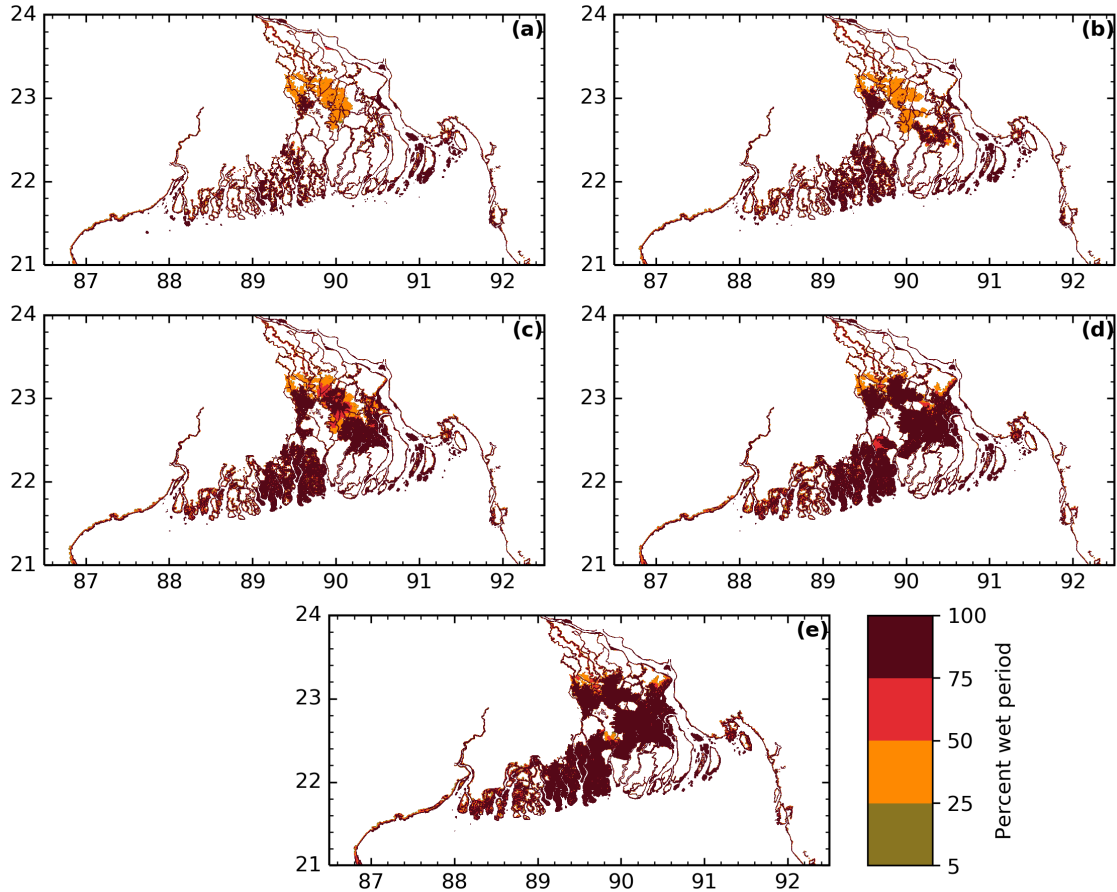


Figure 4.6: Map of the frequency of inundation over the model domain, for the reference simulation (a) as well as for the various SLR scenarios we simulated, from +0.5 m (b) to +2 m (e) with 0.5 m stepping. For the sake of readability, we did not shade the already permanent water bodies.

scenario). In Hiron Point, the change in tidal range shows a nonlinear decreasing behaviour, at a similar rate but of opposite sign of Charchanga. In Chittagong, at the eastern edge of the delta, the response in tidal range increase appears roughly proportional, over the whole range of scenarios we tested.

4.5 Tidal range evolution along the estuaries

As we have seen, the dominant changes in tidal range induced by SLR over the GBM delta, whether positive or negative, are located inside the estuaries. In this section, we examine closely the response predicted by the model in three estuaries, two exhibiting an amplification (Hooghly and Meghna-Brahmaputra-Ganges) and one exhibiting a dampening (Pussur) of tidal range. Figure 4.8 presents the profiles of tidal range extracted along the three estuaries, for the present conditions as well as for the various SLR scenarios we tested, from +0.5 m to +2.0 m. For convenience, the tidal range has been normalized by its value at the mouth of the estuary for all cases.

For the Meghna-Brahmaputra-Ganges (Figure 4.8b), in present conditions, one can see a decay of the tidal range over the first 50 km of the estuary, with a minimal value amounting to

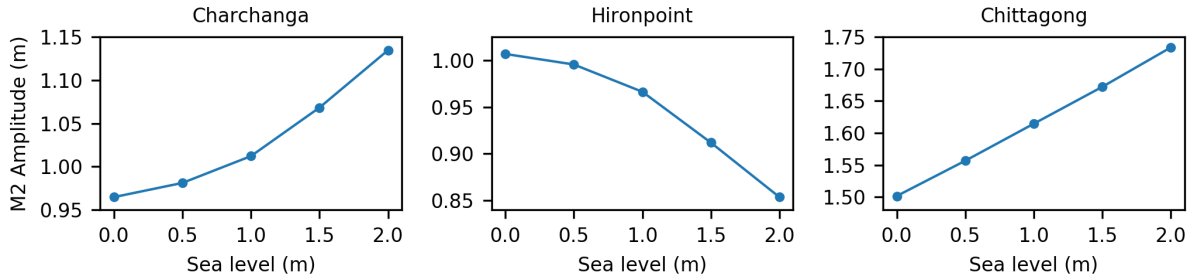


Figure 4.7: M2 amplitude modelled at the location of Charchanga (left), Hiron Point (centre) and Chittagong (right), as a function of the magnitude of SLR we imposed in our model, from 0 m (reference simulation) to +2.0 m (most extreme scenario).

70% of the value at the mouth, located 50 km upstream of the mouth. Then further upstream the range raises mildly up to 90% at 160 km upstream of the mouth. This location corresponds to the choke point of Chandpur, where the width of the channel abruptly decreases from 6 km to 1 km. There the tidal range collapses sharply. Beyond this choke point, further upstream, the tidal range remains around 30% over more than 100 km. The decreasing-then-increasing profile seen in the downstream part is expected in this kind of long estuary (Dronkers, 1964; Du et al., 2018). All SLR scenarios we tested show a similar profile to the present one, though with an upward shift, all along the estuary. The upward shift appears fairly similar for the first three scenarios (+0.5 m, +1.0 m and +1.5 m), with about 10% of excess tidal range for each 0.5 m step of SLR over the lower part (downstream of Chandpur bottleneck) and about 5% of excess tidal range again for each 0.5 m step, upstream of the bottleneck. When considering the most extreme scenarios though (+1.5 m and +2.0 m), the upward shift of tidal range is more modest, around 2% for each 0.5 m step of SLR, from 130 km to 300 km from the mouth. This non-proportionality of the response echoes to the behaviour noted at Hiron Point coastal station (Section 4.4).

In Hooghly estuary (Figure 4.8f), in present conditions we observe a steep increase of tidal range from the mouth up to 60 km upstream, with values 25% higher there than the tidal range at the mouth. Further upstream (60 km to 110 km) the tidal range decreases, but remains superior to the value at the mouth. Upstream of 110 km, the tidal range increases again. Just like for Meghna-Brahmaputra-Ganges, the SLR scenarios show a similar profile to the present-day profile for all cases, with an upward shift. The shift also appears quite proportional to the value of SLR we considered from +0.5 m to +1.5 m, with an additional 5% of tidal range per 0.5 m SLR step. From +1.5 m to +2.0 m SLR, we also note a reduction of the tidal range increase, with values at +2.0 m exceeding the values at +1.5 m by 2%. For this estuary as well, which is notably shorter than the Meghna-Brahmaputra-Ganges, such a profile of consistently higher tidal range inside the estuary compared to the mouth is also consistent with the theoretical cases of Dronkers (1964) or Du et al. (2018). This can be explained by the length of the Hooghly that is closer to its resonant length (amounting to one-fourth of the tidal wavelength), compared to the Meghna-Brahmaputra-Ganges. Indeed, these estuaries have comparable bathymetry (around 10 m throughout, Figure 4.8), which results in similar tidal wavelength (180 km for the Meghna-

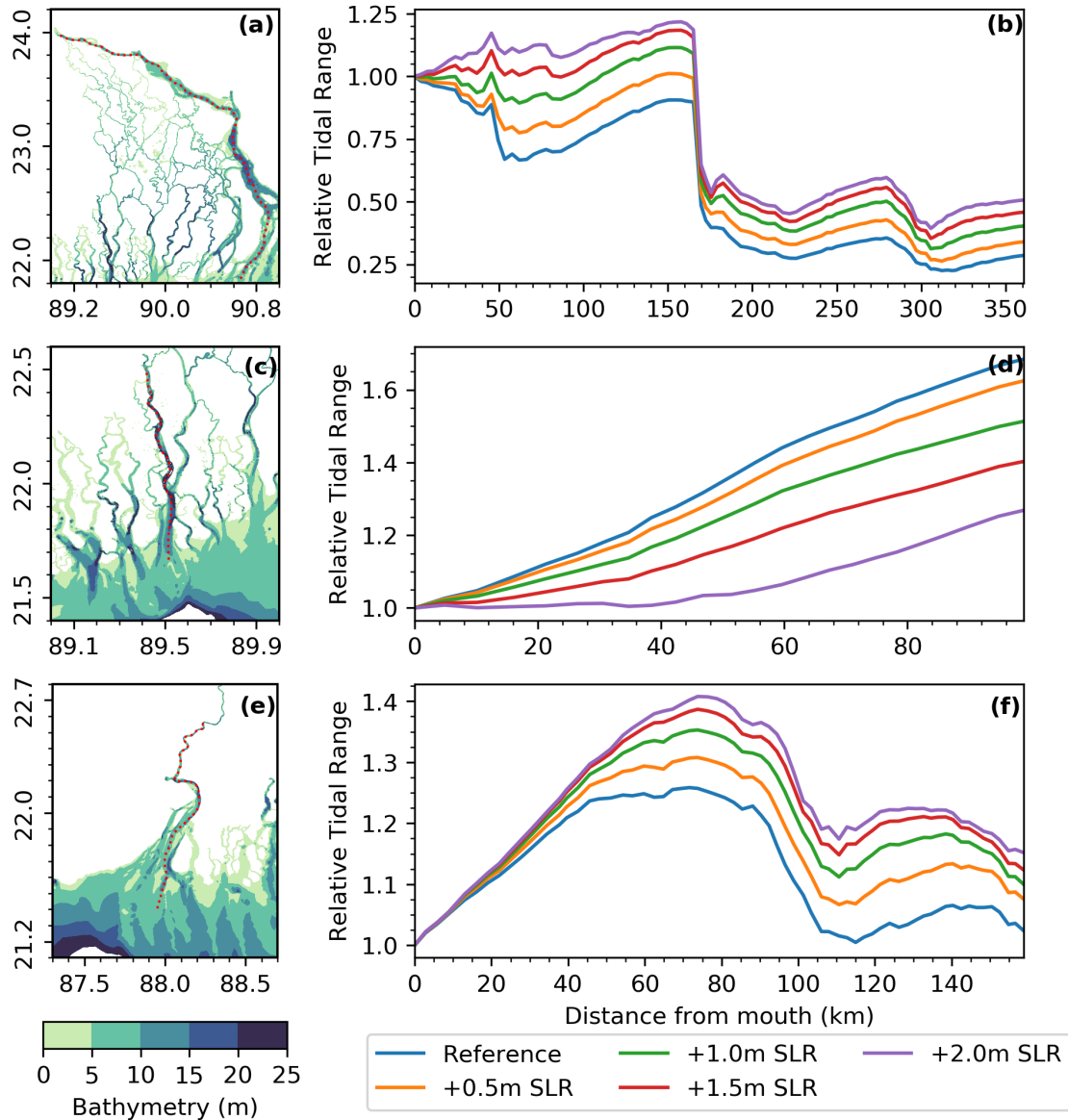


Figure 4.8: Bathymetry of the three estuaries considered – Meghna-Ganges-Brahmaputra (a), Pussur (c), and Hooghly (e). Along-estuary profile of tidal range, normalized by the tidal range of the mouth of the Meghna-Ganges-Brahmaputra (b), Pussur (d), and Hooghly (f). Tidal ranges are shown for the reference simulation (blue) as well as for the SLR scenarios we considered (orange for +0.5 m, green for +1.0 m, red for +1.5 m, violet for +2.0 m). The paths of extraction are displayed in red in the maps.

Brahmaputra-Ganges and 140 km for the Hooghly for the semi-diurnal constituents; not shown). For these estuaries, the resonant length thus amounts to about 35-45 km.

For the Pussur estuary (Figure 4.8d), the profiles markedly differ from the other two. For present conditions first, we can see a regular increase of tidal range throughout the estuary, up to values 60% above the amplitude of the mouth, 100 km upstream of it. This consistent increase is also in line with the past studies (e.g. Du et al., 2018) being an estuary closer to resonance compared to the two others. Indeed, the semi-diurnal tidal wavelength amounts to 160 km there, yielding a resonant length of 40 km. What is also completely different from the

other two estuaries, expectedly, is the decrease of tidal range in all future SLR scenarios, that we had already seen in the +1 m SLR scenario (Section 4.4). Each 0.5 m step of SLR yields a decrease of 2% to 10% of tidal range when considering the region located 60 km upstream of the mouth. The decrease is larger for the upper steps of SLR (from +1.5 m to +2.0 m). The most extreme scenario we considered, +2.0 m of SLR, yields a profile of tidal range that remains close to the range at the mouth throughout the first 60 km, with a moderate increase further upstream up to 25% of the value of the mouth, hereby strongly lowering the effects of estuarine tidal resonance seen in the present conditions.

This contrast between increased tidal range in the Meghna and Hooghly, and decreased tidal range in the Pussur, remains intriguing, as no obvious morphological difference can be seen among these estuaries – all are 3 to 5 times longer than the resonant length, about 10 m deep throughout, weakly convergent, and probably filled with similar sediment, having similar bottom roughness properties. Figure 4.4 already provided a clue about the possible role of new intertidal flats in dissipating the tidal energy in the Pussur, in the future SLR scenarios exceeding +1.0 m. Du et al. (2018) investigated the tidal response to SLR in idealized estuaries, using a numerical model very similar to ours. They considered the cases of solid boundaries along the estuaries, as well as the case of flat floodable banks, that get submerged in SLR scenarios. Our estuaries have geometries that reasonably look like some of their various idealized cases, both in terms of depth and length. Expectedly, it is seen that the behaviour of our three estuaries are in line with theirs, with reduced tidal range for the overflowing Pussur consistent with the response of their "low-lying flat banks" case, and increased tidal range of both Meghna and Hooghly matching their "V-shape channel".

Although our modelling framework, just like that of Du et al. (2018), is dynamically complex (in particular accounting for the non-linearities of the hydrodynamics), and in our case, accounting for the actual geometry of the estuaries at fine scale, it is instructive to interpret our regionally contrasted results in light of the simpler academic cases published in the past studies. The recent review of Talke and Jay (2020) synthesized the idealized framework of constant depth, constant width estuaries, where the tide is subject to linear bottom friction (see their equations 1-2). If we apply this idealized formalism to our three estuaries, we obtain the following. For the Meghna estuary, the semi-diurnal tidal wave (that dominates the tidal signal) has a wavelength of 180 km (not shown). The depth of the estuary lies around 10 m throughout the lower part (south of Chandpur). The length of the estuary, from the mouth to the choke point of Chandpur, amounts to 80 km, that is 40% of the tidal wavelength. Given the Manning coefficient of $0.01\text{s}\cdot\text{m}^{-1/3}$ in the estuaries in our model (Krien et al., 2016), this yields a drag coefficient C_d of 5×10^{-4} . The ratio r/ω introduced by Talke and Jay (2020) in their equation (2d) is the linearized friction coefficient normalized by the angular frequency of the tidal wave. As the amplitude of the tidal current amounts to about $0.6\text{ m}\cdot\text{s}^{-1}$ (not shown), we get a r/ω ratio of about 0.2. These parameters put the estuary in the category of the long (i.e., much longer than the resonant length) and weakly damped channels. The analytical solution of Talke and Jay (2020) indicates that the tidal amplitude would increase by 4% of the SLR magnitude. As we saw in Figure 4.8b, our model predicts a tidal increase amounting to 20% of the SLR in the lower part of the estuary, in qualitative agreement with the theoretical value. If we apply

the same theoretical considerations to the Pussur and Hooghly estuaries, we also find that they fall in the same category of long and weakly damped channels, with predicted increase of the tidal range amounting to 10% for Pussur and 4% for Hooghly. Whereas the value for Hooghly is in line with the 8% increase predicted by our model (Figure 4.8f), the value for Pussur is not, as our model predicted a decrease of the tidal amplitude there, of -15%. This implies that the constant geometry, linear, frictional hydrodynamics of the theoretical model of Talke and Jay (2020) can be invoked to explain the tidal increase for both Meghna and Hooghly estuaries, but it has to be ruled out to explain the tidal decrease in Pussur estuary. One fundamental assumption in the analytical formulation is the constant width, which is certainly not the case in the Pussur at +1 m SLR and beyond, given the massive intertidal flooding seen in Figure 4.7. These additional tidal flats will act as a sink of momentum for the tidal wave, which results in an overall decrease of the tidal amplitude. The contrasted behaviour of Meghna and Hooghly estuaries on one hand, and Pussur estuary on the other hand, appears in line with the findings of Holleman and Stacey (2014). In their modelling of San Francisco Bay, Holleman and Stacey (2014) indeed concluded to a decrease of the tidal amplitude as a response to extended flooding of near-shore diked areas, under future SLR scenarios; however, they modelled an increase of the tidal amplitude if they assumed a rigid shoreline.

4.6 Discussion

The tidal range in the GBM is seen to evolve significantly under future SLR scenarios, but in diverse ways, depending on the location. The contrasted pattern we obtain, with decreased amplitude in the western and central part of the continental shelf and slope, and increased amplitude in the north-eastern part of it, is qualitatively consistent with the findings of (Pickering et al., 2017). We remind that the two forcing strategies are rather different, as they use a global, coarse tidal model, and we use a regional, high-resolution model, with present-day tidal conditions imposed at our open boundary along 11°N. This suggests that the long-term tidal changes to be expected in the Northern Bay of Bengal are prominently generated regionally, in the northern Bay of Bengal itself. This also proves that our southern open boundary, located in the southern Bay of Bengal along 11°N, is far enough from the GBM coast to allow the free development of tidal anomalies in the inner domain of the model, as a response to SLR.

Along the coastline, it is seen that the tidal changes along the open-ocean part of the shore are stronger (positive) both in the eastern and western sides of the delta. This finding is consistent with the seasonal variability of tidal range analysed by Tazkia et al. (2017) using a modelling framework similar to ours. In their study, they concluded that the seasonal changes of M2 amplitude in these two regions were essentially driven by the seasonal variability of the seasonal mean sea level, the wintertime sea level being 0.7 m lower than summertime sea level. They pointed towards the reduced bottom friction as the factor responsible for the stronger tidal amplitude seen at higher water level. As a consequence, one may also point towards the reduced frictional effect of the ocean bottom in the generation of the tidal increase in our SLR scenarios, in these two regions.

In the central part of the delta, in contrast, the widespread negative pattern of tidal trend corresponds closely to the extent of the tidal flooding induced by SLR. This points towards the

increased frictional effect of the tide over these additional extended flooded areas as the process responsible for the decay of tidal amplitude.

Inside the estuaries, our model predicts that the tidal changes will be much larger than along the open ocean shoreline in our SLR scenarios, both in terms of absolute magnitude and in terms of percentage of change with respect to current values. Two factors are apparently competing in the frictional behaviour of the estuaries, under SLR conditions – the decreased bottom friction that tends to enhance the tidal amplitude, and the increased sink of dissipation of newly flooded areas that conversely tends to decrease the tidal amplitude. The latter effect dominates the evolution of the dynamical balance in the south-central part of the GBM delta. In contrast, over the rest of the delta, the former factor takes over. In the south-eastern part of the delta in particular, the ubiquitous dikes protecting the polderized land act as rigid boundaries, across the range of SLR scenarios we considered, resulting in a strong tidal amplification there. Thus, the tide appears as an aggravating factor of SLR over both the western and eastern parts of the GBM delta. In contrast, tide stands as a mitigating factor in the south-central delta. In both cases, we make it clear that future studies aiming towards an assessment of the effects of SLR over the GBM delta and associated vulnerability may not leave apart the intricate relationship between tides and SLR. Under a +1 m SLR scenario, the aggravating effect of tidal range exceeds 0.3 m in the Hooghly estuary around 22.5° N, where the city of Kolkata is located. This mechanically implies that the tide will enhance by about 15% the SLR existing in the ocean, in terms of high-tide water level there. Keeping in mind the socio-economic assets already present in this megacity with 15-million inhabitants (expected to exceed 33 millions by 2050 according to Hoornweg and Pope (2017)), the aggravating effect we report in the present study is worth considering in the design of future adaptation policies. The tide will induce a similar aggravation throughout the lower Meghna, with expectedly similar relevance with regards to the local vulnerability. In contrast, the negative trends seen in the tide in the southern and central parts of the delta, associated with prominent tidal flooding across the area in future scenarios, will act as a mitigating factor of SLR. In some places of the inner delta, this mitigation can reach -0.3 m of tidal range, or -0.15 m of high tide water level, amounting to -15% of the +1.0 m SLR we considered. This amount is considerable, in a context where each centimetre will matter in the evolution of the flooding hazard, and associated vulnerability and risk. This points towards managed re-alignment (Esteves, 2014) as an engineering policy that deserves consideration, in the geographical context of the Bengal delta.

Although the water level extremes are expected to respond in a non-linear way to the superimposition of surges and altered tides in future SLR scenarios, it has to be expected that the increased tidal range will increase the probability of tidal and storm surge flooding in this future scenarios, compared to a situation where one would solely consider the SLR process (Idier et al., 2019). Similarly, the seasonal pluvial and compound flooding can be aggravated in the delta due to an amplified tide, particularly during a synchronized peak of the Ganges and Brahmaputra rivers as seen during 1988 and 1998 monsoon food (Mirza, 2002).

One limitation of our study resides in our assumption of fixed topography in our future scenarios. It is hard to project what will be the policy implemented in the course of the 21st century over the Bengal delta, in terms of coastal defences. But this policy will certainly have a

significant effect on the projections reported here. We also did not account for the vertical land motions nor morphodynamic changes expected to take place over the GBM delta. Although they are not expected to be negligible at centennial timescales, the lack of consistent, synoptic knowledge of the spatial pattern of these vertical motions, precluding a thorough analysis at present, will call for a revisit of our conclusions once such estimates become available.

4.7 Conclusions

In this study we explore the impact of sea level rise on the tidal properties along the shoreline and estuaries of Bengal delta. From an updated long-term observed timeseries we confirmed that the sea level along Bengal coast is increasing at a rate of 4 mm/year. We also show that the tidal range can increase at a faster rate compared to the mean sea level. From a set of comprehensive modelling exercises using a high-resolution tidal model we show that there is a large, and regionally-dependent response in tidal properties to future sea level rise scenarios. Regionally the tidal range increases with increase in sea level over the south-western and south-eastern part of the delta. This amplification can significantly aggravate the tidal flooding over these densely populated embanked regions. The tidal amplification is particularly strong along the upstream parts of the estuaries in these two regions. In contrast, over the central part of the delta with extended mangrove area, our model suggests a decrease in tidal range. Being free from man-made embankments, this area experiences extended inland inundation which induces a tidal decay through dissipation. The results presented here shows the presence of a strong regionally-dependent non-linear relationship between sea level rise and tidal properties. We conclude that tidal modulation is a significant factor that needs to be accounted for in the analysis of future hydrodynamics, flooding hazard assessment, as well as in delta management policies.

Epilogue

In the northern Bay of Bengal, tidal modelling experiments reveal a significant dependence of tidal properties to sea level rise. The sensitivity of tide is large and regionally contrasted. The regional variation is largely controlled by the extent of inland flooding and friction. In this region, wherever the tidal flooding is restricted, the tide amplifies under sea level rise. Vice versa, where the tide is free to flood the coastal land, the tide decays with sea level rise. This mechanism illustrates the importance of the intertidal region mapped in chapter 3, in modulating the coastal sea level variability.

The sensitivity experiments suggest that, if the network of coastal embankments remains as in its current layout, the change in tidal properties can induce an extra 15% of the sea level rise along the coastlines of the major estuaries (Meghna, Hoogly). The mechanisms found here have a direct implication for the delta management policies. The widespread embankment network along the coast of Bengal delta appears to restrict tidal flooding now, with the potential cost of increasing the flooding hazard later. Considering the large population living in a very low-lying subsiding area, this amplification mechanism combined with subsidence can significantly aggravate the impact of sea level rise under a future climate scenario.

Tide is the prominent feature of the sea level variability, and the sensitivity experiments show that tide non-linearly modulates the increase in regional sea level. It is thus necessary to take into account the non-linear response of water level evolution with the water depth in the assessment of flooding at long- (e.g., SLR), intermediate- (e.g., seasonal), and short- (e.g., storm surge) timescales.

CHAPTER 5

STORM SURGE MODELING: A CASE STUDY OF RECENT SUPER CYCLONE AMPHAN

“Forecasting is the art of saying what will happen, and then explaining why it didn’t.”
– *Anonymous.*

Preamble

Besides the tide, the extreme part of the water level statistics over the coastal part of the Bengal delta is typically attributed to storm surges (Krien, Testut, et al., 2017; T. Murty, Flather, & Henry, 1986). The storm surge problem in the Bay of Bengal, particularly in the Bengal delta region, is notorious due to the very high mortality associated with the historic landfalling cyclones. The modelling of the associated storm surges has been a major hurdle due to the magnitude of the tide, and of its interaction with storm surges and waves. This complexity hindered the development of a reliable storm surge modelling system over the Bengal delta.

Aside from the water level boundary conditions used for tidal modelling, storm surge modelling requires the inclusion of momentum transfer from the swirling wind, and the inverse barometric effect of the atmospheric pressure. These two effects are accounted for in the hydrodynamic models through the inclusion of the wind and pressure forcing fields for the storms. Additionally, the breaking of the waves creates a near-shore phenomenon called wave setup, which also contributes to the evolution of the water level during a storm. Accounting for wave setup requires the numerical coupling of a hydrodynamic model with a wave model. Since the tidal model developed in this study is shown to perform well throughout the delta shoreline, it now appears relevant to extend its scope, so as to study the storm surges.

To validate the storm surge model, and to have a close inspection of the contributions from the interactions between tide, surge, and waves, we need observations, i.e., we need to consider a well observed and documented storm surge. Over the Bengal delta, such a well-documented storm event is hard to come by (Krien, Testut, et al., 2017). Incidentally during this thesis, a super-cyclone formed over the Bay of Bengal and made landfall in the Bengal delta. Taking the opportunity of the event, I observed the formation and evolution of the storm from genesis to dissipation. I documented the storm forecasts, their evolutions, and pro-actively forecasted the resulting storm surge at the same pace as the storm forecasts with the extended tide-surge model. In this chapter, I note my observations, illustrate storm surge model performance considering a handful of observed tide gauge records, and finally I present the viability of my model for real-time storm surge forecasting over the northern Bay of Bengal.

Publication: The work of this chapter is currently under review in Natural Hazard and

Earth System Science (NHES) and is published online as a preprint at NHES Discussions. The preprint article can be cited as - Khan, M.J.U., Durand, F., Bertin, X., Testut, L., Krien, Y., Islam, A.K.M., Pezerat, M. and Hossain, S., 2020. Towards an efficient storm surge and inundation forecasting system over the Bengal delta: Chasing the super-cyclone Amphan. *Natural Hazards and Earth System Sciences Discussions*, pp.1-29. doi:10.5194/nhess-2020-340

Abstract. The Bay of Bengal is a well-known breeding ground to some of the deadliest cyclones in history. Despite recent advancements, the complex morphology and hydrodynamics of this large delta and the associated modelling computational costs impede the storm surge forecasting in this highly vulnerable region. Here we present a proof of concept of a physically consistent and computationally efficient storm surge forecasting system tractable in real-time with limited resources. With a state-of-the-art wave-coupled hydrodynamic numerical modelling system, we forecast the recent super cyclone Amphan in real-time. From the available observations, we assessed the quality of our modelling framework. We affirmed the evidence of the key ingredients needed for an efficient, real-time surge and inundation forecast along this active and complex coastal region. This article shows the proof of the maturity of our framework for operational implementation, which can particularly improve the quality of localized forecast for effective decision-making.

5.1 Introduction

Storm surges and associated coastal floodings are one of the most dangerous natural hazards along the world coastlines. Annually, storm surges killed on average, over 8000 people and affected 1.5 million people worldwide over the past century (Bouwer & Jonkman, 2018). Among the storm surge-prone basins, the Bay of Bengal in the northern Indian Ocean is one of the deadliest. This basin has consistently been home to the world's highest surges, experiencing in each decade an average of five surge events exceeding 5 m (Needham, Keim, & Sathiaraj, 2015). On May 18th of 2020, a super-cyclone named Amphan was identified as the most powerful ever recorded in the Bay of Bengal, with highest sustained 3-min wind speed more than 240 km per hour (130 knots) and highest 1-min wind gusts as fast as 260 km/h (<https://www.metoc.navy.mil/jtwc/jtwc.html>). Two days later, on May 20th, Amphan struck the coasts of Bangladesh and India, with a sustained wind speed of 112 km per hour and gusts of 190 km per hour, causing massive damage and claiming hundreds of lives.

The cyclone activity in the Bay of Bengal is very different from the other cyclone-prone oceanic basins (Needham, Keim, & Sathiaraj, 2015). The basin experiences a distinct bi-modal distribution of cyclonic activity - one with a peak in the pre-monsoon (April-May) and another during post-monsoon (October-November) (Bhardwaj & Singh, 2019). The Bay of Bengal is a small semi-enclosed basin (Figure 5.1), which accounts for only 6% of cyclones worldwide. However, more than 70% of global casualties from the cyclones and associated storm surges over the last century occurred there (Ali, 1999). The number of fatalities concentrates in the Bengal delta across Bangladesh and India (Ali, 1999; T. Murty, Flather, & Henry, 1986) where more than 150 million people live below 5 m above mean sea level (MSL) (Alam & Dominey-Howes, 2014). Seo and Bakkensen (2017) noted a statistically significant correlation between storm surge height and the fatality in this region. Two of the notable cyclones that struck this delta include

the 1970 cyclone Bhola and 1991 cyclone Gorky which killed about 300,000 (Frank & Husain, 1971) and 150,000 (Khalil, 1993) people respectively. In recent decades, the death toll has reduced by orders of magnitude. For example, cyclone Sidr, a category five equivalent cyclone on the Saffir-Simpson scale that made landfall in 2007, claimed 3406 lives (Paul, 2009). At the same time, the cost of material damages has significantly increased (Alam & Dominey-Howes, 2014; Emanuel, 2005; Schmidt, Kemfert, & H ppe, 2009). During recent cyclones, government and voluntary agencies of Bangladesh and India took coordinated effort to evacuate millions of people to safety at cyclone shelters before the cyclone landfall (Paul & Dutt, 2010). This kind of informed coordination benefited from improved communication, increased shelter infrastructure, and, most importantly, from the improvement of the numerical prediction of storm track and intensity.

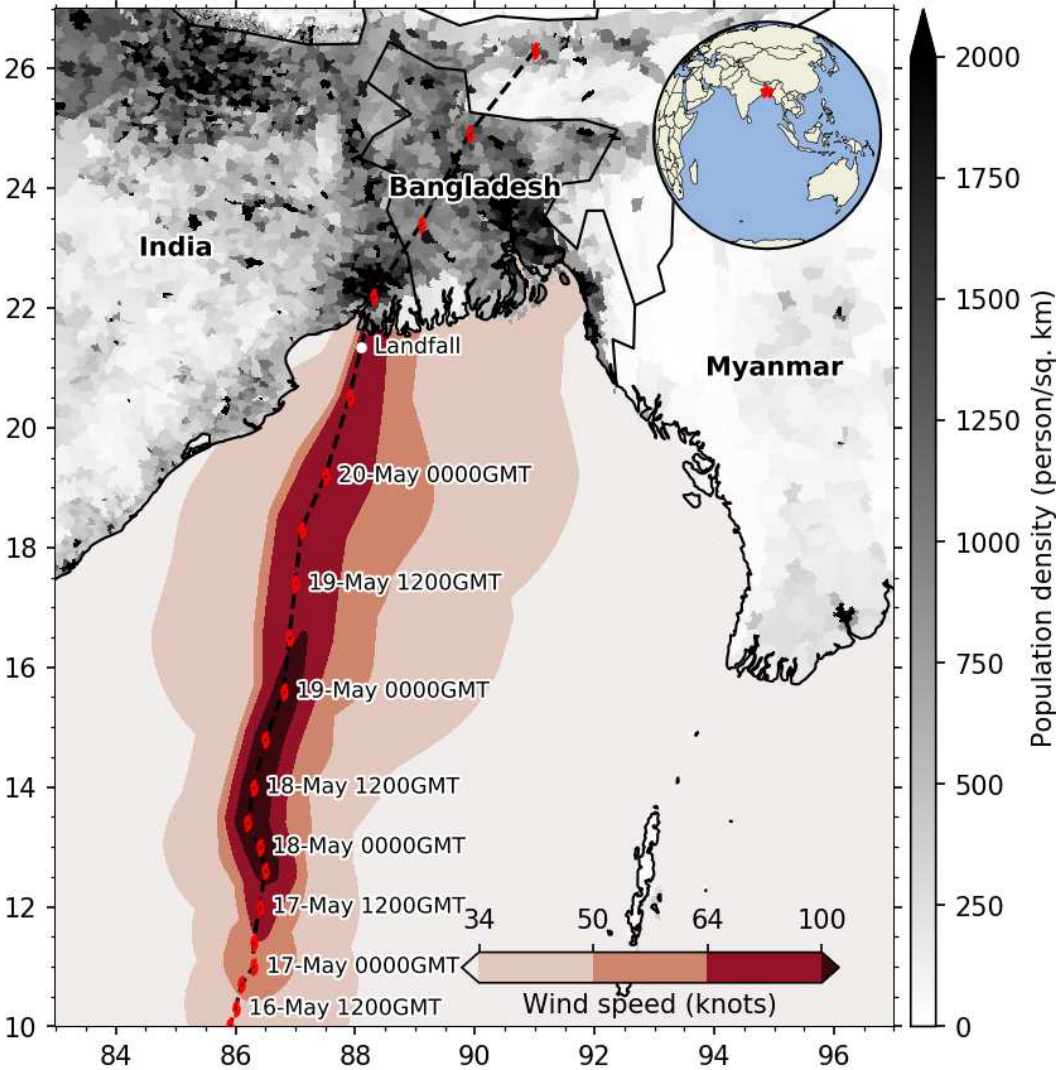


Figure 5.1: The path of the super cyclone Amphan of May 2020, overlaid on the population density. The footprint of 34 knots (17.5 m/s), 50 knots (25.7 m/s), 64 knots (32.9 m/s), and 100 knots (51.4 m/s) wind speed area is shown with the red colour bar. Inset shows the location of the study area.

Over the last decades, global weather and forecasting systems have advanced significantly.

Several global models now run multiple times a day, starting from multiple initial conditions, with horizontal resolution in the order of tens of km, providing forecast with a range of hours to a week. These forecasts have proven useful during weather extremes like tropical storms (Magnusson et al., 2019). Operational hurricane forecasting systems like Hurricane Weather Research and Forecasting (HWRF) have emerged and reached a level of maturity to provide reliable cyclone forecasts several days in advance throughout the tropics (Tallapragada et al., 2014).

Storm surge forecasting has been developed and implemented around the world along with the advancement of the weather and storm forecasting (Bernier & Thompson, 2015; Daniel, Haie, & Aubail, 2009; Flowerdew et al., 2012; Lane et al., 2009; Verlaan et al., 2005). Nowadays, operational surge forecasting systems typically run on high-performance computing systems, either on a scheduled basis or triggered on-demand during an event (Khalid & Ferreira, 2020). In the Bay of Bengal region, the Indian Institute of Technology-Delhi (IIT-D) storm surge model has been running operationally with a horizontal resolution of 3.7 km for one decade (Dube et al., 2009). Under the Tropical Cyclone Program (TCP) of the World Meteorological Organization (WMO), IIT-D model is also implemented to run in Bangladesh Meteorological Department (BMD). Beside the IIT-D model, BMD also experimentally uses MRI storm surge model from Japan Meteorological Agency (JMA) (<http://bmd.gov.bd/p/Storm-Surge>). Storm surge forecasts have shown their potential to better target the evacuation decision, to optimize early-engineering preparations, and to improve the efficiency of the allocation of the resources (Glahn et al., 2009; Lazo & Waldman, 2011). Keeping in mind the cyclonic surge hazards over the densely populated Bengal delta, having a reliable real-time operational forecast system in the region would be extremely valuable.

Storm surge modelling is, however, computationally expensive and proved to be challenging in real-time forecasting mode (Glahn et al., 2009; P. Murty et al., 2017). Several practical solutions exist to curb the real-time constraints of cyclone forecast, such as soft real-time computation based on looking up an extensive database of pre-computed cyclones (Condon, Sheng, & Paramygin, 2013; Yang, Paramygin, & Sheng, 2020), coarse-resolution modelling (Suh et al., 2015), and reduced-physics modelling (P. Murty et al., 2017). In the past decade, unstructured-grid modelling systems are getting more and more popular due to their efficiency in resolving the topographic features and their reduced computational cost compared to structured-grid equivalents (Ji, Aikman, & Lozano, 2009; Lane et al., 2009; Melton et al., 2009).

The published history of storm surge modelling in the northern Bay of Bengal goes hand-to-hand with the land-falling of very severe cyclones (P. K. Das, 1972; Dube et al., 2004; Flather, 1994; Krien, Testut, et al., 2017; P. Murty et al., 2014). From the modelling of the historical storm events, previous studies have identified several ingredients as essential for accurate modelling and forecasting of storm surge induced water level and associated flooding over the Bengal delta. The most important of these ingredients is an accurate bathymetry and topography (Krien et al., 2016; Krien, Testut, et al., 2017; T. Murty, Flather, & Henry, 1986). Second, it is required to have a large-scale modelling domain comprising the whole Ganges-Brahmaputra-Meghna (GBM) estuarine network (Johns & Ali, 1980; Oliveira et al., 2020) at a high-enough model resolution (Krien, Testut, et al., 2017; Kuroda et al., 2010). The modelling framework is

required to simulate tide and surge together to account for the tide-surge interactions As-Salek and Yasuda, 2001; Johns and Ali, 1980; Kuroda et al., 2010; T. Murty, Flather, and Henry, 1986. Furthermore, an online coupling of the hydrodynamics and the short waves is also necessary to account for the wave setup (Deb & Ferreira, 2016; Krien, Testut, et al., 2017). The capability of the model to simulate the wetting and drying is also necessary to model the inundation (Madsen & Jakobsen, 2004). However, due to limited computing resources, storm surge models typically used in the Bay of Bengal region for forecasting purpose are coarse, without any coupling of the hydrodynamics with the waves, and occasionally uncoupled to tide (Dube et al., 2009; P. Murty et al., 2017; T. Murty, Flather, & Henry, 1986; C. Roy et al., 2015). These limitations in operational forecasting systems can significantly impede a proper interpretation during an actual cyclonic storm, as discussed in the next section through a set of hindcast sensitivity experiments of cyclone Amphan.

Cyclone Amphan is not only the latest event on record in the Bay of Bengal but also the costliest event that struck this shoreline, with an estimated bill over 14 billion dollars in West Bengal and Bangladesh (IFRC, 2020; Tribune, 2020). During this cyclone, we have proactively forecast storm surge in real-time with common computational resources using a high-resolution coupled modelling system forced by a combination of freely available atmospheric forecasts. The general goal of this paper is to provide a proof-of-concept of a tractable operational storm surge forecasting system over this key-region of vulnerability, to identify the key ingredients of such a system, and to provide guidance in the near-future initiatives of the operational forecasting community. First, we present the various processes governing the surge dynamics to illustrate the challenges of modelling storm surges in the Bay of Bengal in Section 5.2. Section 5.3 documents the atmospheric forecasts that are required to generate a surge forecast. In Section 5.4, we introduce our numerically-efficient hydrodynamics-waves coupled modelling platform and present its practical real-time computational setup in Section 5.5. Finally, we present the remaining modelling and forecasting issues in Section 5.6. Section 5.7 provides a conclusion to this study.

5.2 Storm surge and inundation processes in the Bay of Bengal

The Bay of Bengal is a macro-tidal region where peak tidal range reaches as high as 5 m over the north-eastern corner of the Bay (Krien et al., 2016; Tazkia et al., 2017). A large geographical extent of the land-sea hydraulic continuum with an intricate estuarine network complicates the water level dynamics in this part of the coastal ocean. During a cyclone, the dynamics get even more complicated due to wave-induced setup and tide-surge interaction. In Figure 5.2, we illustrate a simplified view of water level components – tide, surge, wave setup – and their interactions with the topography in driving inundation during a cyclone.

During a cyclone, the atmospheric pressure drop and the wind stress both generate the water level surge. This atmospheric storm surge is non-linearly dependent on the astronomical tide. The dependent nature of both tide and surge implies that the surge induced by a given meteorological condition differs at different stages of the tide, particularly in the nearshore shallow zone. This departure from linearly-added tide and surge component is known as tide-surge interaction. In a macro-tidal region like the Bengal delta tide-surge interaction typically

amounts to several tens of centimetres (Antony & Unnikrishnan, 2013; Idier et al., 2019). Due to this interaction, the highest surge is obtained for a storm making landfall around 2 hours before the high tide. The strong dependence on tide reinforces the importance of having an accurate tidal model for the region and a reliable network of water level gauge for validation (As-Salek & Yasuda, 2001; Krien, Testut, et al., 2017; P. Murty et al., 2016).

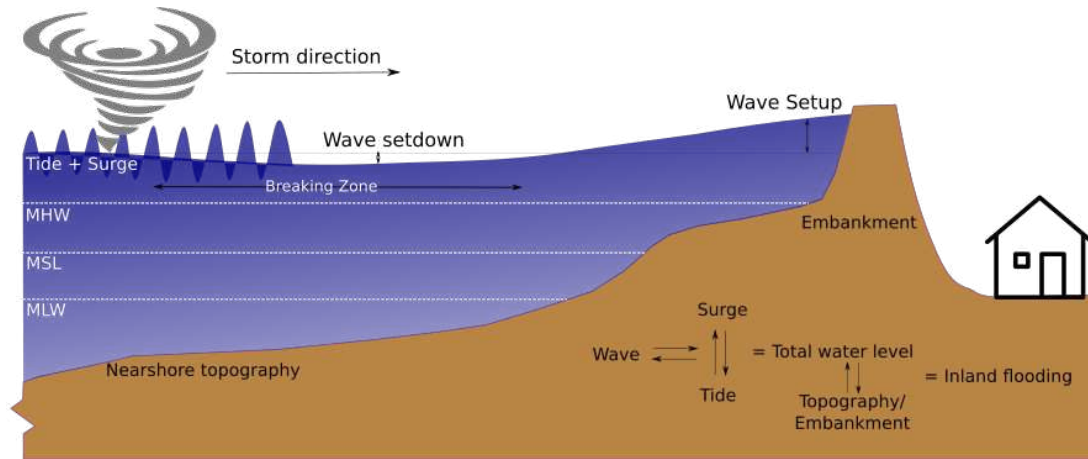


Figure 5.2: Conceptual diagram of the involved processes that determine the water level evolution and its interaction with the controls determining the inland flooding.

Wave setup is another component that has a significant impact on the nearshore sea level (Idier et al., 2019; Krien, Testut, et al., 2017; P. Murty et al., 2014). It manifests as an increase in the sea level occurring in the nearshore zone that accompanies the dissipation of short waves by breaking (Longuet-Higgins & Stewart, 1962). During cyclone Sidr, the modelled wave-setup was around 30 cm (Krien, Testut, et al., 2017). This estimation would be potentially underestimated by up to 100% due to an early dissipation of wave energy by depth-induced breaking arising from usual parameterizations utilized in spectral wave models (Pezerat, Martins, & Bertin, 2020).

At the seasonal scale, the mean sea level around the Bengal delta also shows considerable evolution. The amplitude of this variation can go as high as 40 cm due to freshwater influxes during monsoon from the GBM river system and offshore-ocean steric variability (Durand et al., 2019; Tazkia et al., 2017). During the wintertime cyclone-prone season, this steric variability can induce 10-15 cm variation of mean sea level of the bay.

Except for the Sundarban mangrove forest, coastal Bangladesh is mostly embanked through a network of 139 polders (Nowreen, Jalal, & Khan, 2013). These embanked areas can be flooded in three ways - (a) by overflowing/overtopping, (b) by breaching of the embankments/control structures, and (c) by heavy rainfall inside the embanked area. The height of these embankments plays the most vital role in actuating the inundation from a storm surge (Krien, Testut, et al., 2017). The performance of the embankments during the cyclone is another crucial factor, depending on the composition (typically, earth vs stones/concrete). During a cyclone, the wave action as well as overtopping/overflowing on the embankments can create breaches at a weak point, thus creating local inland flooding (Islam et al., 2011). Particularly for Bangladesh, the consequence can be long-lasting as the topography inside polders is often below the mean sea level due to ground compaction (Auerbach et al., 2015).

5.3 Atmospheric evolution of cyclone Amphan

On May 13th of 2020, a low-pressure area was persisting over northern Bay of Bengal about 300 km east of Sri Lanka. By the end of 15th, the Joint Typhoon Warning Center (JTWC) upgraded the low-pressure system to a tropical depression. Indian Meteorological Department (IMD) also reported the same development on the next day. The tropical depression continued to move northward and intensified into the cyclonic storm Amphan by May 16th 18:00 UTC. During the following 12 hours, the intensification of the system was limited. However, starting from 12:00 UTC on May 17th, Amphan started to intensify very rapidly. In just 6 hours around 18:00 UTC, the maximum wind speed increased from 140 km/h to 215 km/h, making it an extremely severe cyclonic storm (equivalent to Category 4 on the Saffir-Simpson scale). Over the next twelve hours, Amphan continued to intensify reaching a maximum of 260 km/h wind-speed and 907 millibars central pressure, making it the most intense event on record in the Bay of Bengal. During this time, it appeared to form two distinct eye-walls, which is typical of intense cyclones. Over the next 24 hours, Amphan lost most of its strength due to the eye-wall replacement cycle in the presence of moderate vertical wind shear (30-40 km/h). The system continued to decay due to easterly shear and mid-level dry air. The vertical wind shear remained moderate during this period. The cyclone made landfall between 08:00UTC and 10:00UTC around (88.35°N,21.65°E) (Figure 5.1), at mid-tide. At landfall, the reported central pressure amounted to 965 millibars with a maximum wind speed of 150-160 km/h. Afterwards, over its journey inland, the system further eroded and disappeared by May 21st. Figure 5.3 illustrates the evolution of Amphan from JTWC best track.

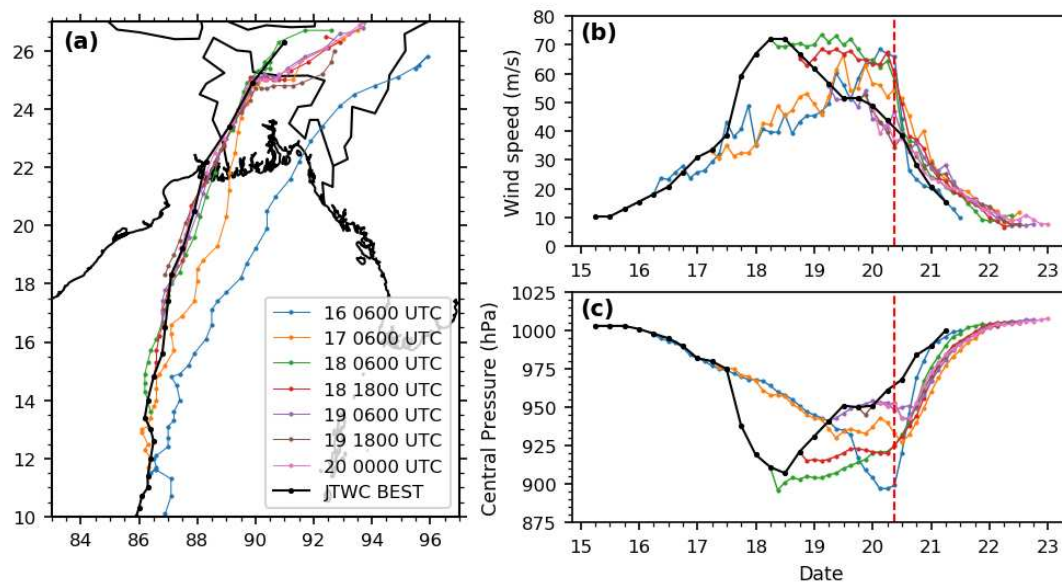


Figure 5.3: Temporal evolution of the successive forecasts of Amphan cyclone wind and pressure. (a) Forecast track colour-coded with the date (JTWC best track in black) (b) Wind speed forecast with each epoch, (c) Pressure forecast with each epoch. The vertical red dashed line indicates the time of landfall.}

The extended range outlook by IMD published on May 7th predicted cyclogenesis to occur during May 8th to May 14th with low probability (RSMC, 2020). Global and regional models

started to predict a significant storm to happen in the Bay of Bengal as early as May 12th, eight days before the cyclone landfall and four days before the actual formation of the tropical depression. The formation of the low-pressure system triggered the operational HWRF system of NOAA (https://www.emc.ncep.noaa.gov/gc_wmb/vxt/HWRF/) on May 14th. Similarly, the operational system of IMD (<https://nwp.imd.gov.in/hwrf/IMDHWRFv3.6>) was also triggered a day later. For the rest of the paper, we confine our analysis to the forecast disseminated by NOAA-HWRF only, relying on the Automated Tropical Cyclone Forecasting System (ATCF) text output (miller1990). Figure 5.3 illustrates a few of the selected forecast cyclone tracks sequentially issued from NOAA-HWRF.

The forecasts illustrate the convergence of the location of the landfall. As early as May 17th, three days before the landfall, the forecast tracks had converged towards the observed track. One day later, on May 18th, the forecast error on the storm track location had reduced to around 50 km. The forecast wind speed and central pressure did not show as much accuracy as the forecast trajectory. The initial forecasts captured the magnitude of the intensification. However, they failed to forecast the rapid intensification that occurred during the 17-18th of May. On the other hand, the subsequent forecasts initiated during May 17th and May 18th failed to capture the rapid weakening of the system that occurred over May 19th-20th, before landfall. Overall, in terms of wind speed, the forecast evolution was accurate (within 1 m/s) only at 24 hours range.

5.4 Storm surge model and performance

We have developed our tide-storm surge model based on the community and open-source modelling platform SCHISM (Semi-implicit Cross-scale Hydroscience Integrated System Model) developed by Zhang et al. (2016) - a derivative code of SELFE (Semi-implicit Eulerian-Lagrangian Finite Element) model, originally developed by Zhang and Baptista (2008). This model solves the shallow-water equations using finite-element and finite-volume schemes in an unstructured grid that can combine tri- and quad- elements. The model is applicable in baroclinic as well as barotropic ocean circulation problems, for a broad range of spatial scales from the creek scale to the ocean basins (Ye et al., 2020; Zhang, Stanev, & Grashorn, 2016; Zhang et al., 2020). It has already been shown to have an excellent performance in reproducing shallow water processes over the Bengal shoreline and elsewhere, including the coastal tide (Krien et al., 2016), wave setup (Guérin et al., 2018) and storm surge flooding (Bertin et al., 2014; Fernández-Montblanc et al., 2019; Krien, Dudon, Roger, Arnaud, et al., 2017).

5.4.1 Model implementation

We have implemented our model on an updated bathymetry of Krien et al. (2016) with the additional inclusion of 77,000 digitized sounding points from a set of 34 nautical charts published by Bangladesh Navy (Khan, Ansary, et al., 2019). Our bathymetric dataset is a blend of two digitized sounding datasets in the nearshore zone – one from navigational charts produced by Bangladesh Navy, and another being a bathymetry of the Hooghly estuary provided by IWAI (Inland Waterways Authority of India). The river bathymetry is composed of a set of cross-sections obtained from the Bangladesh Water Development Board (BWDB). The south-central

part of the delta is composed of a high-resolution (50 m) inland topography. We considered GEBCO 2014 bathymetry to complement in the deeper part of the ocean (https://www.gebco.net/data_and_products/gridded_bathymetry_data/), and SRTM digital elevation model for the rest of the inland topography as appearing in the GEBCO 2014 dataset (<https://www2.jpl.nasa.gov/srtm/cbanddataproducts.html>). Our unstructured model mesh was developed based on this blended bathymetry, covering the whole Bay of Bengal (11°N to 24°N) with a variable resolution based on the shallow water wave propagation and bottom slope criteria. Our model grid consists of about 600,000 nodes and 1 million elements in total. The resulting grid resolution ranges from 250 m in the estuaries and the delta, to 15 km in the deeper part of the central Bay of Bengal. The model domain and mesh are identical to those presented in Khan, Ansary, et al. (2019) (see their Figure 9).

To account for the effect of short waves on the mean circulation, Wind Wave Model III (WWMIII), a third-generation spectral wave model, is coupled online with SCHISM in our modelling framework (Roland et al., 2012). In our configuration, WWMIII solves wave action equation on the native SCHISM grid, using a fully implicit scheme. The source terms in our model comprise the energy input due to wind (Ardhuin et al., 2010), the non-linear interaction in deep and shallow water, energy dissipation in deep and shallow water due to white capping and wave breaking, and energy dissipation due to bottom friction. We run WWMIII with a 12 directional and 12 frequency bins. Water level and current are exchanged among the two models every 30 minutes. Wave breaking is modelled, according to Battjes and Janssen (1978). As the nearshore region of Bengal delta has a very mild slope, the value for the breaking coefficient α , which controls the rate of dissipation, was reduced from 1 to 0.1 to avoid over-dissipation (Pezerat, Martins, & Bertin, 2020). WWMIII was also forced along the model southern open boundary by time series of directional spectra, computed from a large-scale application of the WaveWatch3 (hereafter WW3) model (WW3DG, 2019). WW3 was implemented at the scale of the whole Indian Ocean with a spatial resolution of 0.5° and forced by the FNL reanalysis wind data at 3-hour time step (National Centers for Environmental Prediction, National Weather Service, NOAA, U.S. Department of Commerce, 2015).

5.4.2 Model forcings

Our model is forced over the whole domain by the astronomical tidal potential for the 12 main constituents (2N2, K1, K2, M2, Mu2, N2, Nu2, O1, P1, Q1, S2, T2). At the southern boundary, we have prescribed a boundary tidal water level from 26 harmonic constituents (M2, M3, M4, M6, M8, Mf, Mm, MN4, MS4, Msf, Mu2, N2, Nu2, O1, P1, Q1, R2, S1, S2, S4, Ssa, T2, K2, K1, J1, and 2N2) extracted from FES2012 global tide model (Carrère et al., 2013). At each of the upstream river open boundaries of Ganges, Brahmaputra, Hooghly, and Karnaphuli, we implemented a discharge boundary condition. At Meghna and Rupnarayan river open boundaries, we implemented a radiating Flather boundary condition. From a year-long tidal simulation, we found that the updated version of the bathymetry performs 2-4 times better compared to the global tidal models – which includes FES (Carrère et al., 2013), GOT (Ray, 1999), and TPXO (Egbert & Erofeeva, 2002) (see Table A1).

We derived the atmospheric wind and pressure fields for SCHISM from a blending of analyti-

cal wind field inferred from a parametric wind model (close to the cyclone track) and background atmospheric field from the Global Forecast System (GFS, <https://www.ncdc.noaa.gov/data-access/model-data/model-datasets/global-forecast-system-gfs>) reanalysis (further away), following Krien, Testut, et al. (2017) and Krien et al. (2018). We used the best-track data of JTWC provided at 6-hour time step as input for the analytical wind and pressure field. Here we choose the analytical wind profile of Emanuel and Rotunno (2011) and the analytical pressure field profile of Holland (1980). To be consistent with our forecast described in Section 5.5, the background wind field was generated incrementally from an accumulative merging of GFS forecasts for each 6-hour forecast window, with a 1-hour time step. The analytical and background wind fields were first temporally interpolated every 15 minutes and overlaid on the background GFS fields using a distance-varying weighting coefficient to the cyclone centre to ensure a smooth transition. We took into account the asymmetry of the wind field following Lin and Chavas (2012).

5.4.3 Predictive skills

With the above-described model setup, we ran our model to calculate the water level and sea state evolution during Amphan. The simulation was done a-posteriori, once the cyclone had passed, and JTWC and GFS hindcasts being already available throughout the cyclone lifetime. Figure 5.4 shows comparisons between observed and modelled significant wave heights (SWH), peak wave period and water level. First, we compare the significant wave height derived from the altimetric estimate of Sentinel-3B processed by the Wave Thematic Assembly Center from Copernicus Marine Environment Monitoring Service (<https://scihub.copernicus.eu/>), which overpass on May 18th 2020 at 16:03GMT. For each altimetric data point inside our domain, we interpolated the model output using a nearest-neighbour approach, both spatially and temporally. This comparison shows that SWH is reasonably reproduced, with RMSE typically within 1 m (within 18% of the mean value). However, we observed an overestimation of SWH of about 2.5 m near the cyclone centre. One of the reasons for such difference is a limitation of analytical wind field models, as explained by Krien, Testut, et al. (2017).

We present an in situ observed time-series of SWH and mean wave period during the life cycle of Amphan in Figure 5.4 for BD08 (Figure 5.4, b-c) and BD11 (Figure 5.4, d-e) oceanographic buoys (the dataset is available online at <https://incois.gov.in/portal/datainfo/mb.jsp>). The two buoys are located on either side of Amphan track, 250 km to its east / 230 km to its west, respectively. We can see that at both locations, the model reproduces the SWH well. The match is particularly good at BD11, consistently within 1 m of the observed evolution. At BD08, SWH is found to be overestimated by about 2 m at its peak, with a 12-h lead shift in time. Such difference can come from positional and timing uncertainties in JTWC best track data, from our assumption of a constant translational velocity in-between each 6-hourly JTWC time step, and finally from the intrinsic uncertainty of the analytical wind field itself, as shown on Figure 5.3b. Despite multiple sources of potential errors and uncertainties, our model appears capable of capturing the general features of the sea state, both significant wave height (SWH) and period, relatively well. The overall predictive skills of the model in terms of short waves are only slightly below those from hindcast exercises typically conducted over other ocean basins using similar

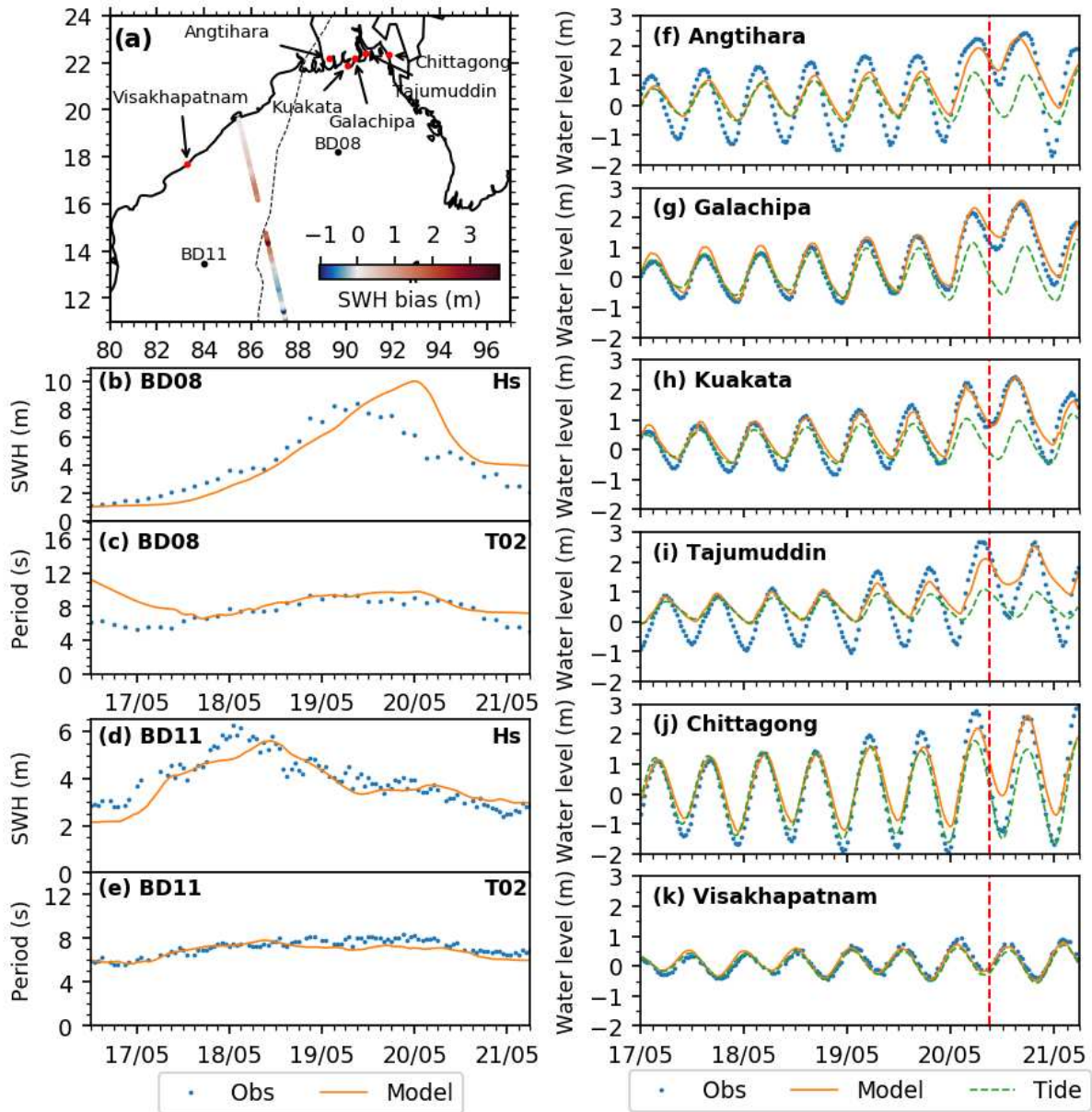


Figure 5.4: Comparison of simulated (in orange) and observed (in blue) water level, significant wave height (SWH) and mean wave period. (a) The map shows the along-track bias in SWH compared to the one calculated from Sentinel 3B altimeter overpass at 2020-05-18 1603Z. Bottom panel shows the modelled SWH and mean wave period (orange line) compared to buoy observations (blue dots) at BD08 (b-c) and BD11 (d-e) provided by INCOIS. Comparison between observed (blue dots) and modelled (orange line) water level at the station locations – (f) Angtihara, (g) Galachipa, (h) Kuakata, (i) Tajumuddin, (j) Chittagong, and (k) Visakhapatnam. Green dashed lines in (f)-(k) indicates the modelled tidal water level. Location of the buoys and the water level gauges are shown in (a). The vertical red lines in water level plots indicate the time of landfall.

modelling strategies (Bertin et al., 2014; Krien et al., 2018).

The real-time availability of observed water level time series in this region is relatively scanty. We were able to access only a handful of coastal water level records, most of them located eastward of the landfall location. The right panels of Figure 5.4(f-k) illustrated the comparison of the recorded water level and modelled storm surge. Among these tide-gauges, Chittagong (Figure 5.4j) and Visakhapatnam (Figure 5.4k) time series are retrieved from the UNESCO IOC Sea Level Monitoring service (<http://www.ioc-sealevelmonitoring.org/map.php>) and the rest are provided by Bangladesh Inland Water Transport Authority (BIWTA, <http://www.biwta.gov.bd/>). The datum for water level timeseries at Chittagong and Visakhapatnam is changed from in-situ datum to MSL by removing long-term mean. The timeseries provided by BIWTA are already referenced to MSL, thus kept unchanged. We also plotted the reconstructed tidal water level from the tidal atlas derived from our model. The overall tidal propagation is well simulated in Galachipa and Kuakata, while at Angtihar and Tajumuddin the simulation tidal range is found to be underestimated. The local bathymetric error and friction parameterization might be the source of the discrepancy. The tide gauge at Angtihar is located in a data-scarce location inside Sundarbans mangrove forest. Tide gauge at Tajumuddin is situated at the mouth of Meghna, where bathymetry is rapidly changing (Khan, Ansary, et al., 2019). However, our model correctly reproduces the peak of the water level at all locations. Depending on the site, the landfall occurred 2-4 h after high tide. The maximum recorded water level at these stations is around 2-2.5 m above mean sea level, with a storm surge (water level – tide) of the same order of magnitude.

To spatially assess the storm surge generated by cyclone Amphan, we first take a look into the temporal maximum water level in Figure 5.5(a). We can see that the whole coastal region experienced a high-water level ranging from 2-5 m for Amphan. To quantify the contribution of the cyclone, we have looked in the surge component, defined as the difference between the total modelled water level and a tide-only simulation. Figure 5.5(b) illustrates the temporal maximum of surge over the delta region. The highest surge level is 5 m around the location of the landfall (88.3°E, 21.6°N). The maximum non-linear interaction between tide and surge amounts to about 30 cm in the nearshore domain (Figure 5.5d).

To quantify the contribution of the wave setup, we re-calculated the storm surge without the coupling with the wave model. Figure 5.5(c) shows the maximum of the difference between the two simulated water levels. In general, wave setup contributes to the Amphan storm surge by about 20 cm all along the Bengal shoreline, and locally over 30 cm close to the cyclone landfall. Nevertheless, the spatial resolution at the nearshore region employed in this study (250 m) is still too coarse for capturing the maximum wave setup that develops along the shoreline, where a resolution of a few tens of m should be employed (Guérin et al., 2018). Nonetheless, this comparison shows that wave setup is not only developed along the shoreline exposed to waves but affects the whole delta up to far upstream, a process already observed over large estuaries (Bertin et al., 2015; Fortunato et al., 2017).

Our findings reaffirm the necessity of a proper coupling between tide, surge and wave to forecast the water level evolution. For Amphan, the magnitude of tide-surge interaction amounts to about 10% of the maximum total water level with spatial variation. Similarly, the magnitude

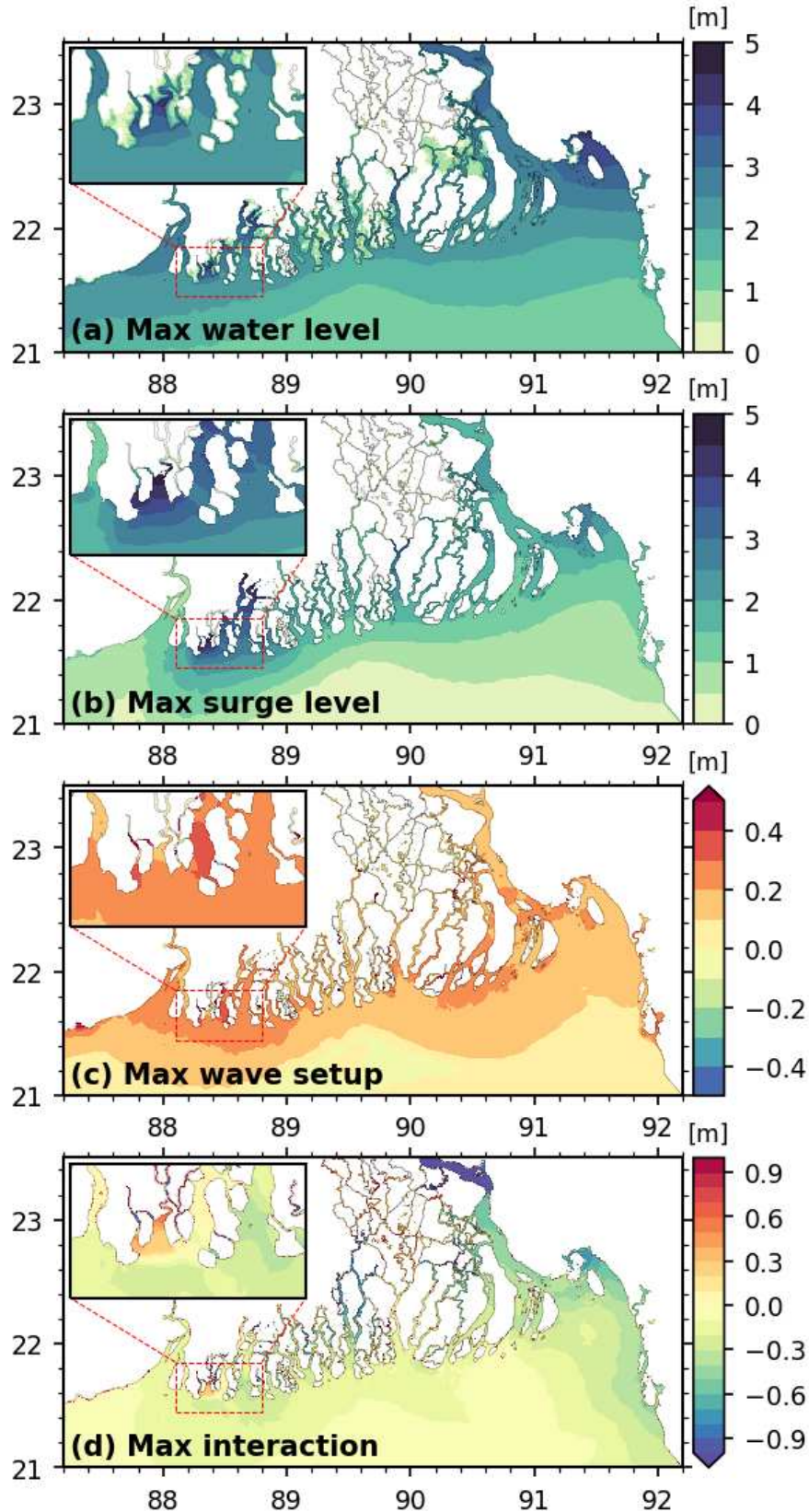


Figure 5.5: Hindcast of (a) maximum water level, (b) maximum surge (c) wave setup/setdown (d) maximum non-linear interaction between tide and surge. For (a), for the areas above mean sea level, the water level is converted to water level above the topography for consistency. The inset maps show a close-up (75 km × 45 km) of the landfall region.

of wave-setup is also spatially varying with a typical amplitude of 10-15% of the maximum total water level. This non-negligible non-linear dependency shows the importance of a fully coupled hydrodynamic-wave modelling system for a successful forecast of the water levels in the hydrodynamic setting of the Bengal delta. Our modelling framework showed reasonable accuracy in reproducing observed storm surge water level along the Bengal coastline. The accuracy is in line with the typical level of performance of similar systems applied elsewhere in the world ocean (Bertin et al., 2015; Fernández-Montblanc et al., 2019; Suh et al., 2015). The hindcast experiment thus shows the viability of our model for a proof-of-concept of real-time forecasting exercise.

5.5 Near real-time storm surge forecasting

The current state of maturity of atmospheric real-time cyclone forecast products allows their application to real-time surge forecasting, as discussed in Section 5.3. As explained in Section 5.2, the storm surge generated from cyclones depends on the atmospheric pressure, wind, and background (typically: tidal) water level. A realistic surge forecast issued three, or even two days before landfall can usefully predict the order of magnitude of the expected maximum water level. Particularly a spatial prediction of expected maximum water level could be of utmost utility to determine the locations of impact and associated damages. This two to three-day timeframe can help to prepare the embankments or critical systems over the vulnerable areas, and prepare for the evacuation of the population living in low-lying coastal zones. Storm surge and water level evolution estimated 24 hours to 12 hours before landfall, once the cyclone forecasts from the operational agencies have converged, can further help to elaborate location-specific evacuation orders.

5.5.1 Forecast strategy and forcing products

During cyclone Amphan, we performed near-realtime storm surge forecasts based on our model. We communicated the results to Bangladesh local government authority through personal communications, as well as to the scientific community through social media. In our forecasts, we relied on the outputs of global models (GFS, and HWRF) and advisories (JTWC) for the estimates of the atmospheric forcing. These advisories and global models are updated every 6 hours. Similar to the GFS forecast cycle, we updated our forecasts at every 00:00, 06:00, 12:00, 18:00 UTC.

For each forecast, we derived the atmospheric forcing from a blend of JTWC, HWRF, and GFS data (Table 5.1). JTWC publishes storm advisories at 03:00, 09:00, 15:00, 21:00 UTC. The advisory includes an analysis of the storm intensity and position from a satellite fix 3-hours prior, followed by a forecast for the following 72 hours, with 6 to 12 hours time-steps. NOAA published their HWRF model advisory for each GFS forecast cycle at 3-hour time steps. GFS provides the wind and pressure fields in hourly timesteps at 0.25° regular spatial grid. The GFS model is initialized 6-hourly at 00:00, 06:00, 12:00, 18:00 UTC, and the data is available 3 hours after the initialized period.

The wind and pressure fields around the centre of the storm are derived analytically from a concatenated JTWC and HWRF. We used GFS data as the background wind and pressure on

Table 5.1: Data sources for the model forcings. NA stands for Not Applicable.

Name	Datatype	Timestep	Resolution	Source
JTWC advisory	Text	Variable (6-24 hours)	NA	https://www.metoc.navy.mil/jtwc/jtwc.html
HWRP forecast	Text	3 hours	NA	https://www.emc.ncep.noaa.gov/gc_wmb/vxt/HWRP/index.php
GFS	DAP	1 hours	0.25°	https://nomads.ncep.noaa.gov/dods/gfs_0p25_1hr
FNL	netCDF	3 hours	0.25°	https://rda.ucar.edu/datasets/ds083.3/

the outer region of the analytical fields.

We initiated our forecast cycles on March 16th 2020 at 06:00 UTC - utilizing the first advisory from JTWC published at 03:00 UTC, merged with the forecast from HWRP issued at 18:00 UTC of the preceding day. We took the background wind and pressure field from GFS forecast published at 00:00 UTC. In the subsequent forecast cycles, we updated the previous track file by first replacing the past time-steps with the analysis from the latest JTWC advisory, then appending the forecasts from HWRP again. For the background wind and pressure fields from GFS, we retained the first 6 hours of forecasts from the previous cycles and updated the remainder of the time series from the latest forecast with new initialization. For each forecast cycle, we kept the starting time of our model the same, on May 16th at 00:00 UTC, and ran till one-day after the landfall for a consistent initial condition. This approach is feasible as the storms in the Bay of Bengal typically form, grow and dissipate in about a week. A graphical representation of our strategy to temporally concatenate JTWC, GFS, and HWRP forecasts over a forecast cycle is shown in Figure 5.6.

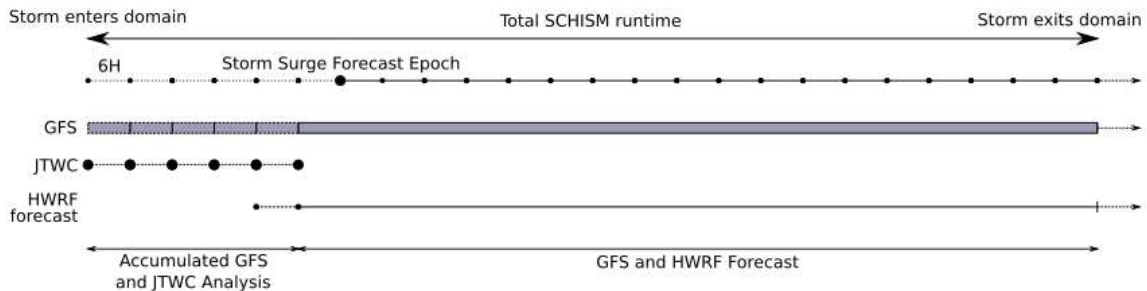


Figure 5.6: Temporal combination scheme of the JTWC, GFS, and HWRP forecasts for each 6-hourly storm surge forecast epoch.

5.5.2 Real-time computation and results

Since our forecast is contingent to the JTWC advisory of three hours before, we had only a three-hour-long window to achieve the pre-processing of the forcing files, to run the model, and to complete the necessary post-processing of the model outputs. The numerical efficiency of our model made it possible to cope with this time constraint of the forecast, using a modest computing resource. The computing environment we used is detailed in Table 5.2, which essentially

amounts to a single desktop computer fitted with a high-end consumer-grade processor.

Table 5.2: Computing environment used during the forecast

Model simulation duration	5.5 days
Model timestep	5 min
WWM Coupling Timestamp	30 min
Processor clock speed	2.8 GHz
Number of MPI processes	20
Wall clock time (pre-processing)	10 min
Wall clock time (model integration)	1 h 45 min
Wall clock time (post-processing)	5 min
Disk storage (each simulation)	8 GB
Memory usage	18 GB

Figure 5.7 illustrates the evolution of the maximum total water level and surge for the corresponding forecasts issued at T-60 hours, T-36 hours, and T-12 hours, where T is the time of landfall (May 20th 2020 at 08:00 to 10:00 UTC). For the forecast issued at T-60 hours, the cyclone landfall is located near 90°E, associated with the strong surge simulated over the surrounding area. As the atmospheric cyclone forecasts gradually converge towards the actual landfall location more than 100 km westward, so do our storm surge forecasts at T-36 hours and T-12 hours. The dependency of the timing of the landfall to the forecast range is notable here. At T-36 hours, the maximum water level pattern is similar to the hindcast shown in Figure 5.5. By T-12 hours, the magnitude of the forecast maximum water level corresponds well with the hindcast estimate.

5.6 Discussion

5.6.1 Coupled tide-surge-wave dynamics

The water level dynamics over the Bay of Bengal and particularly around the Bengal delta is complex, and the various components of water level have different relative contributions depending on the location. Due to tide-surge interaction, the maximum water level can be lower or higher depending on the tidal phase in a fully non-linear tide-surge coupled simulation, compared to its linear counterpart. During Amphan the tide-surge interaction was mostly negative, except within about 10 km of the landfall location. The positive interaction near the landfall location means that the coupled tide-surge estimate was higher than the linearly added tide and surge. In this case, the typical magnitude of tide-surge interaction ranged from -30 cm to +30 cm. The contribution from the wave-induced setup along the shoreline increases the maximum water level estimation throughout the coast by about 10-15% during Amphan.

Fully coupled tide-surge-wave models have been recommended for operational forecasting in the Bay of Bengal for years (As-Salek & Yasuda, 2001; Deb & Ferreira, 2016; Johns & Ali, 1980; Krien, Testut, et al., 2017; T. Murty, Flather, & Henry, 1986). Besides the development of the wave-ocean coupled hydrodynamic modelling tool itself, the main challenge in implementing such a system sums up to the high computational requirements for the proposed modelling systems (P. Murty et al., 2016; P. Murty et al., 2014). Due to this constraints, operational systems are

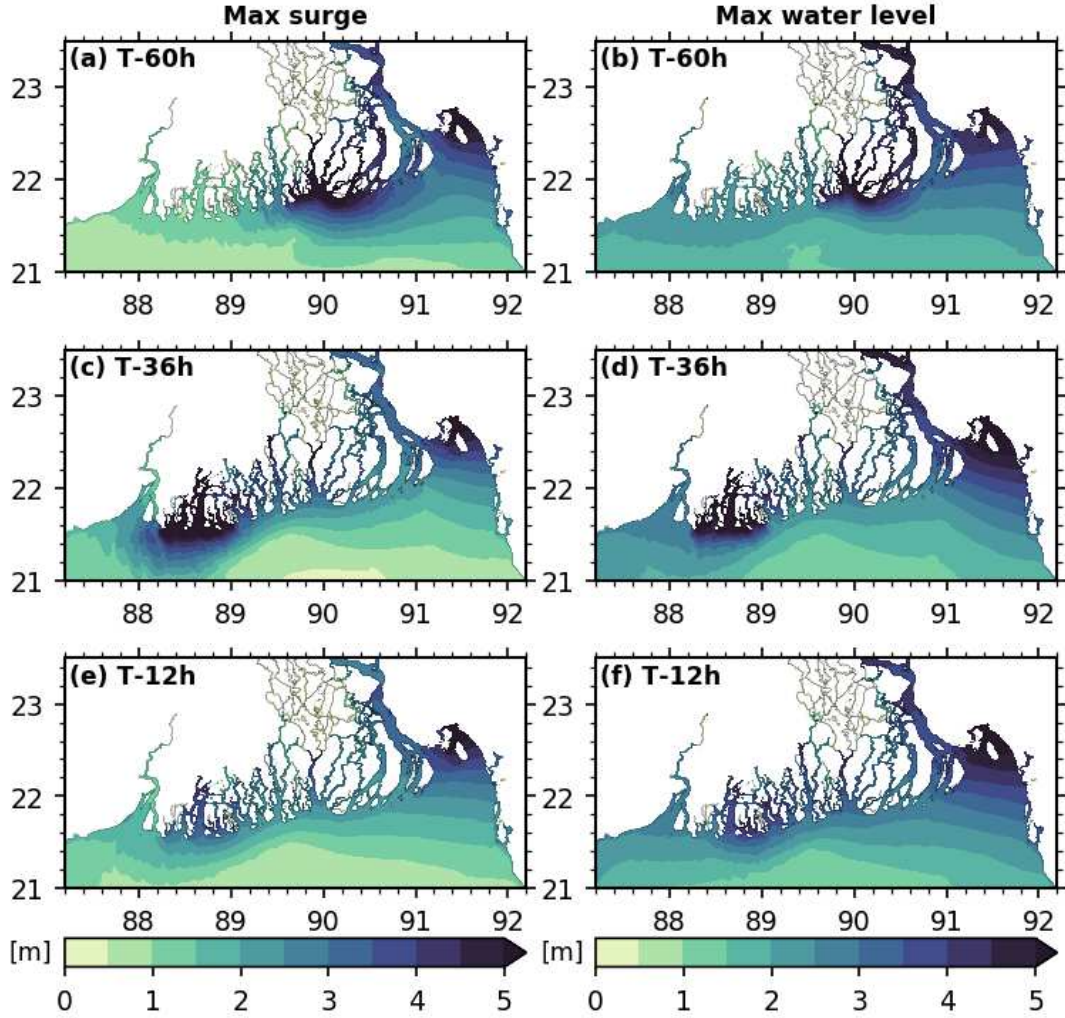


Figure 5.7: Maximum surge (a, c, e) and elevation (b, d, f) evolution for forecast initiated at (a-b) T-60 hours (2020-05-18 0000Z), (c-d) T-36 hours (2020-05-19 0000Z), (e-f) T-12 (2020-05-20 0000Z) hours before landfall.

commonly run with either only surge, or only coupled tide-surge model, but without waves (P. Murty et al., 2017) and with a much coarser spatial resolution.

5.6.2 Performance of storm surge forecasting

Aside from the necessary inclusion of relevant physical processes – tide, surge, waves and their non-linear interactions – the performance of storm surge forecasting depends on the wind and pressure forcings. The errors in the wind forcing and in the atmospheric pressure forcing are typically the most important ones among the various sources of error in storm surge modelling (Krien, Testut, et al., 2017). In our forecast environment, the source of this error is two-fold – the analytical model used to synthesize the fields from the storm parameters, and the numerical weather model used to forecast the storm wind and pressure fields to derive the storm parameters themselves. There have been attempts to find a more accurate formulation from recent satellite scatterometer missions (Krien et al., 2018). However, not one formulation works best in all radial distances from the storm centre. Despite the well-known error associated

with the parametric wind field, they are widely used in applications due to their computational simplicity and lightweight data requirements (Lin & Chavas, 2012). The best way to avoid the error from the analytical wind field might be not using these formulations and rely on the full-fledged atmospheric forecasts. However, atmospheric models are costly in terms of computation. It is particularly true for cyclonic storms where high spatial resolution (typically kilometric) is required (Tallapragada et al., 2014).

From the validation of water level at a few tide gauge locations for our hindcast simulation, it appears that the modelling framework proposed here could capture the maximum surge level successfully throughout the coast. Our tide-gauge sites were limited to the eastern side of Amphan landfall location and were operational throughout the life cycle of the cyclone. However, it was not possible to confirm the ability of the model to reproduce the water level on the western side of the landfall location due to data unavailability. The proper reproduction of the maximum water level by the model gives strong confidence in the formulation as well as in the coupling strategy of our modelling framework.

5.6.3 Inundation

One of the potential, but challenging, outcomes of storm surge forecasting is the prediction of inundation. Particularly in the northern Bay of Bengal, the existing modelling studies do not generally consider the inundation process (Dube et al., 2004; P. Murty et al., 2014). Some modelling systems take advantage of simplified inundation modelling schemes to tackle this problem (Lewis et al., 2013). While the recent improvements in models bathymetry and the detailed accounting of dikes and coastal defences improved the overall modelling of the inundation, the associated error remains large (Krien, Testut, et al., 2017). As an update to Krien, Testut, et al. (2017), in our model we have incorporated a novel dike heights dataset, bearing varying dike crests heights, for the numerous polders scattered around the Bengal delta. The assessment of the impact of the updated embankment heights is, however, hard to quantify and validate.

In the absence of any operational network of inundation monitoring, to understand and better characterize the inundation dynamics, we systematically skimmed the Bengal delta local newspapers on the day of Amphan landfall and on the few subsequent days, to achieve an as-comprehensive-as-possible mapping of the inundation extent observed *in situ*. We digitized the reported flooded locations through Google Earth and categorized the inundation mechanism. We digitized 88 such locations over the Bangladeshi part of Bengal delta, as shown in Figure 5.8. Over the Indian side of the delta, the news reporting of inland flooding from dike breaching was not accurate enough for us to be able to geotag the locations. We overlaid the inundated locations over the inundation predicted by the model on a false-colour image derived from Sentinel-2 satellite using Google Earth Engine (<https://earthengine.google.com>).

Three categories of inundation mechanism are typically observed – inundation by breaching of the dikes (labelled as "Embankment breach"), inundation of unprotected low land by increased water level ("Unembanked lowland"), and flooding by overflowing of the dikes ("Embankment overflow"). From the reported news, it is clear that the major part of the inundation results from the breaching of dikes. We also note two breaching instances in the south-eastern corner of our domain, very far from the cyclone landfall. On the other hand, the flooding from merely

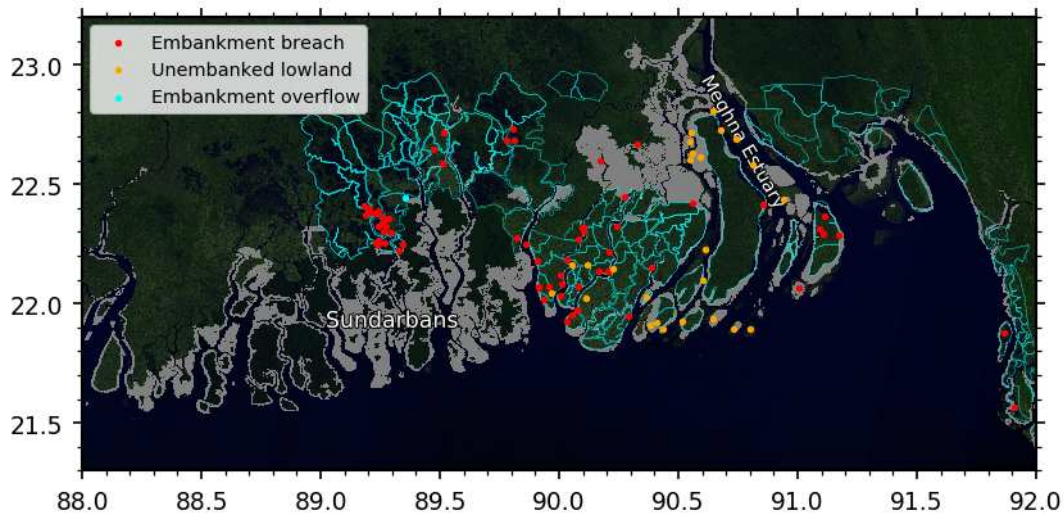


Figure 5.8: Digitized location of inundation resulting from embankment breaching (red), flooding of low-lying unembanked area (orange), and embankment overflow (cyan) overlaid on a false-colour image composite derived from B12, B11, and B4 channels of Sentinel-2 during April 2020. The grey patches are the inundated regions predicted by the model, as shown in the hindcast experiment. The polders are shown with cyan outlines.

increased water level in non-diked areas is mostly concentrated along the Meghna estuary. Along the estuary, designed embankments probably do not exist to protect many populated low-lying char areas (land/island formed through accretion). We could find only one report of the occurrence of overflowing of an embankment, in Maheshwaripur of Koyra upazila (89.30°E, 22.45°N). Around (90.1°E-90.5°E, 22.4°N-22.6°N), in Barisal district, our model predicted an extended inundated area, which is known not to be polderized. While we could find some reports of flooding around that region from our newspaper survey, the widespread inundation predicted by our model in this region probably did not occur in reality due to the presence of levees and city protection embankments. Indeed, this kind of small-scale geographic information, to the best of our knowledge, is not systematically available publicly and thus could not be incorporated in our model topography, despite being of utmost importance for localized inundation forecast. The forecast flooded vs non-flooded areas show a wealth of spatial scales, demonstrating that our unstructured modelling framework has the intrinsic capability to model the small-scale hydrodynamic gradients. In our modelled forecasts, the contrast between the well-predicted water level temporal evolution, and the comparatively limited predictive skills of inundated locations points out the necessity of accurate knowledge and incorporation of reliable topographic and embankment information, at the local scale. Our modelling system has the ability and appropriate resolution to ingest such topographic information efficiently due to its unstructured nature.

The coastal polder management has long been a boon and a bane (Warner, van Staveren, & van Tatenhove, 2018). On one side, the polders have protected the fertile areas from daily tidal flooding of brackish waters, which favoured agricultural production by reducing the soil salinity (Nowreen, Jalal, & Khan, 2013). On the other hand, these embankments have restricted freshwater and sediment supply, causing significant subsidence inside the embanked areas due to sediment compaction (Auerbach et al., 2015). Over time, the land use inside these polders

has also changed from agriculture to aquaculture (namely shrimp and crab farming). Although the embankments were not built to protect from the cyclonic surges, in many instances they functioned as such. The presence of these protective structures also contributed to a false sense of security in the residents living inside (Paul & Dutt, 2010). Embankments have become part and parcel of survival in this low-lying region. It has now become essential to monitor the condition and topography of the embankments for efficient management and maintenance. From a forecasting point of view, embankment breaching is extremely hard to model in the state-of-the-art hydrodynamic modelling frameworks. However, consistent periodic monitoring of the embankment conditions can improve the forecast by providing a more objective view of the associated inundation hazard.

5.6.4 Prospects in operational forecasting

Throughout our forecast and hindcast experiments, we have relied on freely available forecast products as the forcing for our storm surge model. These forecasts data are publicly available within 3 hours of their initialization time through online portals. The primary input to generate the forcing is the forecast storm track, which is distributed as a text file and which is very lightweight even for a limited internet connection. We have implemented our storm surge model on a freely available open-source framework. The model code is already operationally used in regional forecasting systems and services (Fortunato et al., 2017; Oliveira et al., 2020).

As we have demonstrated, the modelling setup presented here is tractable in an operational, real-time forecasting scenario. Thanks to advanced and efficient numerics, one can deploy such a system in a consumer-grade computing environment. The computing setup we have deliberately used (see Table 5.2) essentially amounts to a high-end x86-64 desktop personal computer (e.g. Intel® Core™ i9-10900 or similar). This computing requirement takes only a portion of the available computing capacity of an institute such as the BMD (15x4 cores@2.8GHz) (C. Roy et al., 2015). Furthermore, the model is easily deployable in cloud computing infrastructure ([oliveira2020](#)), which could provide additional reliability and cost-savings for an event-driven operational forecasting system of the Northern Bay of Bengal.

5.7 Conclusions

In this study, we present a retrospective evaluation of storm surge prediction during super-cyclone Amphan using an efficient, state-of-the-art coupled hydrodynamic-wave numerical model. During cyclone Amphan, the predicted maximum water level ranges from 2 to 5 m along the coastline. Comparison with in-situ measurements revealed that the water level could be modelled with high accuracy on condition that all the relevant mechanisms are considered. Notably, we demonstrated the necessity of considering a coupled hydrodynamic tide-surge-wave modelling framework for the head Bay of Bengal, for effective forecasting. For Amphan, the contribution from tide-surge interaction, and wave-setup typically amounts to 10% and 10-15% of the total water level, respectively.

From our proactive forecast initiative during cyclone Amphan, we showed that with publicly available storm forecast products and easily accessible computing resources, it is feasible to

forecast the evolution of water level throughout the vast coastline of the Bengal delta in real-time. During Amphan, a sufficiently skilful storm surge forecast was achieved as early as 36-48 hours before landfall. The forecast water level with 36-hour lead time seemed quite similar to our best (hindcast) simulation, in terms of maximum water level as well as the spatial pattern.

From a secondary post-disaster news-survey, we have identified the limiting factors for location-specific inundation forecasts. The main limiting factor is due to limited and outdated topographic information of the existing coastal defences. Also, dike-breaching, which was the prevalent process of inland inundation during Amphan, is not explicitly modelled in our hydrodynamic framework. These two factors call for routine monitoring of embankment topography and condition.

Cyclone and storm surge warning has always been a communication and trust issue in the Bay of Bengal (Paul & Dutt, 2010; C. Roy et al., 2015). It is thus necessary to communicate well-grounded storm and surge forecast to the community for coordinated and informed decision-making during a storm surge (Morss et al., 2018). The forecasting system we implemented and assessed in the present case study provides the proof-of-feasibility and opens short-term operational prospects to fill a gap in the existing disaster management tools in this part of the world.

5.8 Appendix

5.8.1 Tide model validation

Our tidal model is validated at 7 tide gauge locations, around the Bengal delta. We have used complex error as the performance indicator (Mayet et al., 2013). The harmonic analysis is done using the Tidal toolbox developed at LEGOS (Allain, 2016). The modulus of the complex difference defines the complex error for a tidal constituent.

$$|\Delta z| = |A_m e^{i\phi_m} - A_o e^{i\phi_o}| \quad (5.1)$$

Where A and ϕ are the amplitude and phase (in radians) respectively, of the tidal harmonics. The subscript denotes the model (m) and observation (o). The total error of all the constituent at one location is calculated as the squared root of half of the squared sum.

$$\sigma_s = \sqrt{\frac{1}{2} \sum_N |\Delta z|^2} \quad (5.2)$$

Along the coast of Bengal delta, only four of the constituents - M2, S2, K1, and O1 are found to contribute significantly to the tidal energy (Sindhu & Unnikrishnan, 2013). As in many cases, information for other tidal harmonics is not available, only these four constituents are considered for calculating the total complex error at a location.

A comparison of the complex error between the global models and the model presented here is shown in Table 5.8.1. Amplitudes (A) and errors are in centimeter, phase (ϕ) is in degrees. Hooghly River, Diamond Harbour, Garden Reach and Chandpur are not represented in global tidal models (FES, GOT, and TPXO) due to their location in far upstream.

Table 5.3: Performance of tidal model at tide-gauge locations.

Station	Observation		FES2012-Hydro			FES2012			GOT4.8			TPX07.2			(Krien et al., 2016)			This Model			
	A_0	ϕ_0	A_m	ϕ_m	Error	A_m	ϕ_m	Error	A_m	ϕ_m	Error	A_m	ϕ_m	Error	A_m	ϕ_m	Error	A_m	ϕ_m	Error	
Sagar Roads (88.0300°E, 21.6500°N)	M2	140	116	142	99	42	137	104	29	113	113	27	132	104	28	143	116	3	144.5	114.9	5.3
	S2	66	150	73	141	13	62	141	11	40	145	40	48	126	29	62	155	7	62.4	153.3	5.2
	K1	15	262	17	256	2	16	253	3	14	277	14	14	258	1	17	265	2	15.6	265.4	1.1
	O1	5	250	6	251	1	6	243	1	5	270	2	5	252	0.4	6	248	1	5.7	251.6	0.8
	σ_s					31				22			27			29			6		
Diamond Harbour (88.1733°E, 22.1928°N)	M2	157	168												166	161	21	142.3	165.6	15.9	
	S2	68	210												68	207	4	57.6	208.6	10.4	
	K1	15	285												16	284	1	13.2	286.3	1.8	
	O1	7	258												5	253	2	5.4	257.7	1.6	
	σ_s																	15			13.6
Hiron Point (89.4780°E, 21.8169°N)	M2	81	127	86	88	56	87	91	52	80	88	53	104	110	35	81	115	17	99.9	115.0	26.7
	S2	34	159	45	121	28	40	122	24	37	118	25	37	136	14	35	148	7	41.6	150.5	9.3
	K1	13	268	15	250	5	16	252	5	14	248	5	14	261	2	15	265	2	15.0	265.7	1.7
	O1	5	258	6	244	2	6	238	2	5	244	1	5	256	0.3	6	245	1	5.7	255.0	0.7
	σ_s					44			40			42			27			13			20.0
Dhulasar (90.2700°E, 21.8500°N)	M2	73	158	58	114	52	80	117	53	79	117	54	86	121	51	51	156	22	67.6	143.3	18.8
	S2	35	193	39	141	33	39	142	32	39	146	29	35	135	34	20	194	15	28.5	179.6	9.8
	K1	13	286	15	262	6	16	256	8	15	260	6	15	255	8	12	297	3	13.3	287.8	0.5
	O1	4	278	6	256	3	6	243	3	6	256	3	6	250	3	5	280	1	5.6	273.8	1.6
	σ_s					44			44			44			44			19			15.0
Charchanga (91.0500°E, 22.2188°N)	M2	96	234	110	202	57	115	208	50	97	204	49	84	154	103	67	208	46	95.8	216.9	28.5
	S2	37.5	265	38	238	18	30	243	15	34	234	19	36	186	47	27	241	17	36.6	250.3	9.5
	K1	13	304	17	298	4	16	300	4	7	314	6	16	272	8	14	309	2	16.8	308.7	4.0
	O1	8	285	7	289	1	6	284	2	4	303	4	6	267	3	8	289	0	8.1	293.1	1.1
	σ_s					43			37			37			80			35			21.5
Chittagong (91.8274 °E, 22.2434°N)	M2	173	196	118	193	56	126	200	49	120	192	54	89	153	123	156	198	18	149.2	194.8	24.1
	S2	64	229	41	230	23	33	236	31	43	227	21	40	160	62	58	235	9	55.0	225.8	9.6
	K1	19	278	17	294	6	17	295	6	9	300	11	16	258	7	20	289	4	19.1	284.9	2.3
	O1	8	263	7	285	3	6	280	3	4	289	5	6	252	2	8	269	1	7.9	267.3	0.6
	σ_s					43			41			42			98			14			18.4
Chandpur (90.6385°E, 23.2344°N)	M2	29.7	31.4																33.6	333.7	30.7
	S2	10.5	62.3																11.2	6.3	10.2
	K1	5.6	18.6																5.4	21.9	0.7
	O1	3.4	12.9																3.6	357.4	1
	σ_s																				22.9

Epilogue

Building on the development of the tidal model in Chapter 3 and knowing its applicability to study current and future sea level variability in Chapter 4, the model was extended for storm surge events in this chapter. The storm surge phenomenon is hydrodynamically complex and calls for an equally complex modelling environment. The modelling strategy requires to force the model with a reliable wind and pressure forcing to realistically simulate the surge. Additionally, including the contribution from the short waves breaking demands a coupling of the hydrodynamic model with a wind-wave model. This coupling significantly increases the computing complexity and computational requirements. Thanks to the efficiency of the modelling framework, it is shown to be feasible to meet the computational needs with moderate computing power.

Cyclonic storm surge poses a significant threat to the communities residing in the coastal part of the Bengal delta. From this case study of cyclone Amphan, the tide, surge, waves and their interactions altogether constitute the necessary ingredients for storm surge modelling and forecasting. Similar to the tide, storm surge-induced inundation is controlled by the embankments topography and their performance during a storm event. This case study also confirmed that the storm surge is highly dependent on the storm parameters and the evolution of storm surge is regionally variable for the cyclones making landfall along the coast of Bengal delta.

CHAPTER 6

STORM SURGE HAZARD: A PROBABILISTIC-DETERMINISTIC APPROACH

“Religion considers the universe deterministic and science considers it probabilistic – an important distinction.” – Issac Asimov

Preamble

Combined with the strong tide, storm surges make up the potent inundation hazard over the Bengal delta. The hindcast experiments with the model illustrate that there is a marked regional diversity of maximum water level patterns during a cyclonic storm. The water level depends on the intensity and spatial location of the storm, the phase of the tide, and the wave activity. The inundation extent is strongly controlled by the presence of coastal embankments and their performance during the storm event.

The hindcast experiment during cyclone Amphan and subsequent survey of flooding reports suggest that there is a delta-wide exposure to storm surge flooding. Mapping of this flooding hazard is, however, hindered by the lack of a well-distributed network of tide gauges and long-enough reliable observed water level records. Storm surge modelling could fill the gaps of tide gauge records to some extent. However, the observational records of the track and intensity of cyclones suffer from homogeneity issues. For most of the storms that occurred before 1998, precise information about the cyclone intensity does not exist (Kossin, Olander, & Knapp, 2013; Singh, Panda, & Mohapatra, 2020). Beyond the inhomogeneity of the cyclones records, the population size of the known past cyclones is not enough to cover the 700 km long shoreline of the Bengal Delta and extract reliable extreme water level statistics. Large tidal range, which is typically as large as surges, further complicates the statistics as the phase of the tide at the cyclone landfall strongly modulates the extreme water level reached during a given cyclonic event.

With the recent advancement of the understanding of cyclones dynamics, various methods have been proposed to study the cyclonic activity through statistical approaches. These statistical models are now providing a consistent and synoptic view into the statistical properties of the cyclonic activity, based on very large ensembles of synthetic cyclones. Combining such cyclones ensembles with the hydrodynamic model we developed could be an elegant way to curb the lack of observations and understand the storm surge hazard over the Bengal delta region.

Abstract. Storm-surge induced coastal inundation constitutes a substantial threat to lives and properties along the vast coastline of the Bengal delta. Some of the deadliest cyclones in history made landfall in this region claiming more than half a million lives over the last decades. Complex hydrodynamics and observational constraints have hindered the understanding of the storm surge flooding hazard of this low-lying (less than 5 m above mean sea level), densely populated (>150 million) mega-delta. Here, we generated and analysed a storm surge database from a large ensemble of 3600 statistically and physically consistent synthetic storm events and a high-resolution storm surge modelling system. From this dataset, we performed a robust probabilistic estimate of the storm surge extremes. Our ensemble estimate shows that there is a diverse range of water level extremes along the coast and the estuaries of the Bengal delta, with well-defined regional patterns. We confirm that the risk of inland storm surge flooding at a given return period is firmly controlled by the presence of coastal embankments and their heights. We conclude that about 10% of the coastal population is living under the exposure of a 50-year return period inundation. We expect our flood maps to provide relevant information for coastal infrastructure engineering, risk zoning, resource allocation, as well as future research planning.

6.1 Introduction

Among global coastlines exposed to storm surges, the countries along the Indian Ocean are among the most severely impacted places by deadly cyclones (Needham, Keim, & Sathiaraj, 2015). Particularly the northern Bay of Bengal is one of the deadliest regions in terms of cyclones mortality (Ali, 1999). Although a tiny percentage (~6%) of cyclones forms and makes landfall around this region, the total death toll is more than 50% of the global total (Alam & Dominey-Howes, 2014). The Bay of Bengal experiences, on average, five surge events per decade exceeding a surge level (water level – tide prediction) of 5 m (Needham, Keim, & Sathiaraj, 2015). Surge level height has a significant correlation with the number of casualties in this region (Seo & Bakkensen, 2017). More than 100 million people live below 10 m elevation in this mega-delta region (Becker et al., 2020).

Figure 6.1 illustrates a representative subset of the deadly cyclones that occurred in the last five decades. Table 1 lists the illustrated cyclones and associated surges. For a comprehensive historical catalogue of cyclones over the Bengal delta region see Alam and Dominey-Howes (2014). This small sample of cyclones and their associated surge indicates that cyclones can induce strong storm surge along this macro-tidal region of the world, depending on the tidal condition on their landfall (Krien, Testut, et al., 2017). Tide is pre-dominantly semi-diurnal in this region (Sindhu & Unnikrishnan, 2013). The tidal range is high, reaching about 5 m along the north-east coast (Khan, Durand, et al., 2020; Krien et al., 2016). A sizeable continental river flow discharges through the distributaries of Ganges-Brahmaputra-Meghna. The shallow coastal submarine delta with an average width of 50 km provides the conditions for large surges and a strong interaction with tide (Krien, Testut, et al., 2017). Combination of all these properties can give rise to high water levels during a storm that have the potential to inundate the low-lying delta region and to cause thousands of casualties (T. Murty, Flather, & Henry, 1986). Considering the tidal range and strong tide-surge interaction, the term “water level” is hereafter used to refer to the water level derived from the dynamic interaction of tide, surges and waves.

The number of casualties from storm surge has been reduced drastically over the last decades (Paul, 2009). This improvement is partly due to the government effort to build cyclone shelters

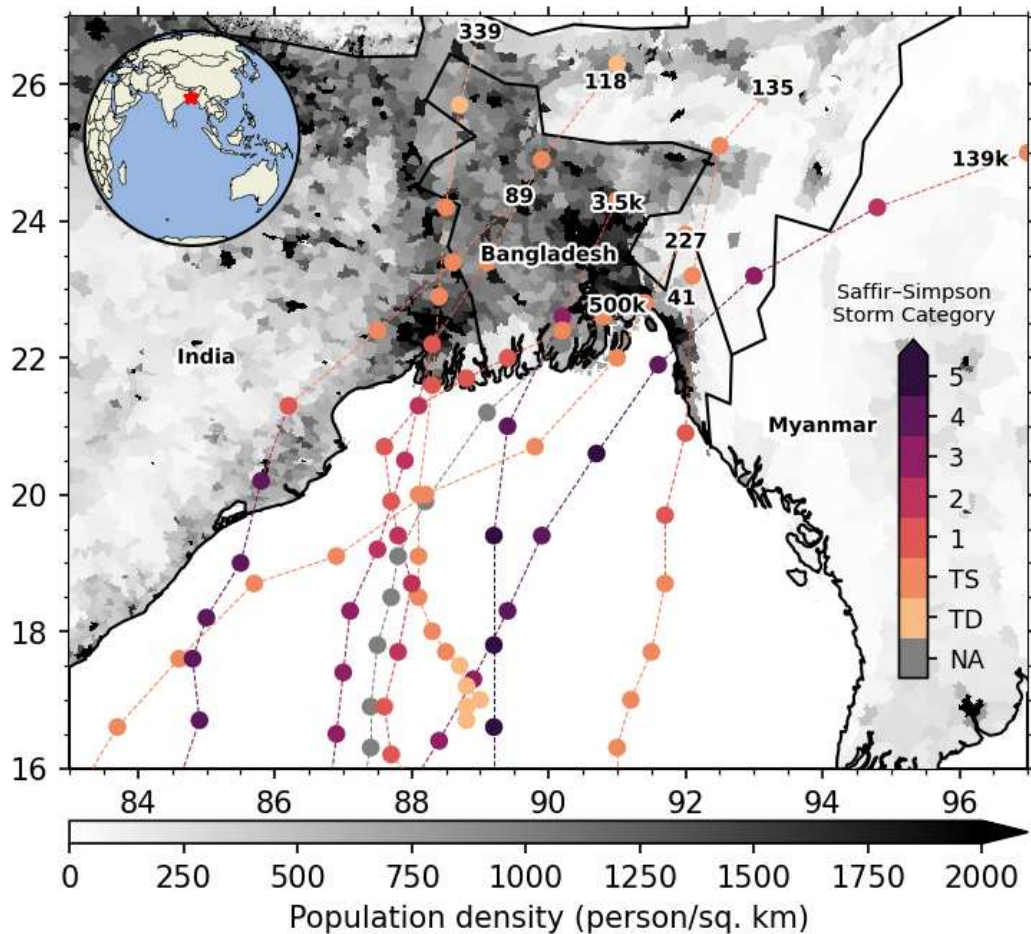


Figure 6.1: The population density in the Bengal delta covering Bangladesh and India. A subset of cyclones that made landfall in past decades with the number indicating the associated casualty and the colour indicating the strength of the cyclone. Inset shows the location of the study area. TD and TS correspond to Tropical Depression and Tropical Storm, respectively. The colour-coded lines show the cyclone strength along its track in the Saffir-Simpson scale. For 1970 Bhola cyclone, the wind speed is not available and shown in grey (NA). The associated number at the head of the cyclone tracks refers to the number of casualties.

and pre-storm preparedness. The local governments and communities put their efforts to implement timely evacuations during storms. Consistent development in the communications system (e.g. mobile phone network) and improvement in the numerical storm and surge forecasting further facilitated the evacuation effort. Engineering structures like embankments (Nowreen, Jalal, & Khan, 2013) also provided a level of protection (Adnan, Haque, & Hall, 2019). Proper engineering design of these structures, however, depends on the understanding of the variability of sea level, particularly the extreme water levels (J. U. Chowdhury et al., 1998).

The variability of water level along this intricate coastline is poorly observed. The available limited set of water level observations reveals regionally-varying water level dynamics at long as well as short time scales (Antony, Unnikrishnan, & Woodworth, 2016; Becker et al., 2020; Tazkia et al., 2017). Antony, Unnikrishnan, and Woodworth (2016) found a robust amplification of extreme high-water level from south to north along the east coast of India. In their analysis, the tide appears as the largest contributor to extreme high-water events. Tazkia et al. (2017)

showed a summer-winter variability of mean sea level along the Bengal delta coastlines reaching up to 70 cm in range. From an extensive database of daily water level records, Becker et al. (2020) showed a consistent increase in relative sea level over the delta.

Nevertheless, due to the limited availability of uniform water level records, consistent estimation of water level hazard from storm surges from in situ observations over the delta is not yet possible in this region (Chiu & Small, 2016; Lee, 2013). The main challenge is to secure long-enough hourly (or higher temporal resolution) tide gauge records for reliable statistical analysis (Unnikrishnan & Sundar, 2004). The separation of short timescale (driven by meteorological effects, among which surges) from longer timescale (driven by tidal effects) on water level variability poses another challenge. The failure of the tide gauges during a cyclonic event is also commonplace, causing bias in the record of extreme water levels (Antony, Unnikrishnan, & Woodworth, 2016; Chiu & Small, 2016; Krien, Testut, et al., 2017).

Hydrodynamic modelling of the storm surges has been used with varying degree of complexity to curb these problems, both along the east coast of India (Chittibabu et al., 2004; I. Jain et al., 2010; Sindhu & Unnikrishnan, 2011) and the coast of Bangladesh (J. U. Chowdhury et al., 1998; Jakobsen et al., 2006). The approach of Chittibabu et al. (2004) and that of I. Jain et al. (2010) are similar. Their estimation of 50-year return period water level involved determining a 50-year return level of the atmospheric pressure drop (ΔP), from the observed cyclone records. Afterwards, they used the pressure drop estimate in conjunction with artificial cyclone tracks to spatially cover their area of interest. In their approach, the tide is added linearly to the cyclone surge. Chittibabu et al. (2004) estimated the 50-year return period tidal water level and added it with the 50-year surge water level to compute the 50-year return period water level.

On the other hand, I. Jain et al. (2010) added the total tidal amplitude for M2, S2, K1 from FES2004 (see Lyard et al. (2006)) tidal atlas. Both I. Jain et al. (2010) and Chittibabu et al. (2004) considered an additional constant water level of 50 cm to account for the wave setup. This approach assumes that tide and surge do not have any interdependence and that 50-year return level tide and 50-year return level surge adds up to 50-year return level tide-surge. Moreover, the wave setup is assumed to be the same for all return periods, in the sense that the linear addition of the wave-setup does not change the return period of an estimated water level. For the Orissa coast in India (19°N-21°N), they both obtained a similar pattern of combined total water level (combining surge, tide, and wave set-up) at 50-year return period with an increase from 4.3 m in the south to 8.5 m in the north. The numbers reported in I. Jain et al. (2010) (see their Figure 10) seem to be the same as those of Chittibabu et al. (2004) (see their Figure8b). Along the coastline of West Bengal (21°N-20°N), the estimated 50-year return level ranges from 5 to 10 m.

Sindhu and Unnikrishnan (2011) addressed the non-linear dependence of tide and surge with a coupled tide-surge model. In their analysis, they simulated 136 events spanning 1974 to 2000 to estimate maximum water levels during those storms. They applied an extreme value analysis on the estimated water levels using an r-largest annual maxima approach to determine the return period of extreme water level. Similar to Chittibabu et al. (2004) and I. Jain et al. (2010), they also found an increasing amplitude of 50-year return level of total sea level from south to north along the east coast of India. The highest 50-year return period water level was estimated in the

northern edge – Sagar Island (88.11°E, 21.72°N) (8.7 m) and Chandipur (87.01°E, 21.43°N) (6.9 m). Compared to the 50-year return water level estimates of Chittibabu et al. (2004) and I. Jain et al. (2010), the estimates by Sindhu and Unnikrishnan (2011) are inferior in water level by about 50% throughout the coast of Orissa. One notable issue with the approach of Sindhu and Unnikrishnan (2011) is, however, the limited number of available storm events. They derived the extreme water level along the 1200 km shoreline from 136 storm events, i.e., three events per 30 kilometres (typical footprint of storm surges). This spatial sampling is potentially not adequate to capture the storm surge water level at various phases of the tide. Additionally, the storm parameters are collected over a long period, and the homogeneity of the storm records are not well defined (Singh, Panda, & Mohapatra, 2020). Finally, these studies focused on the east coast of India do not cover the Bangladesh part of the delta, where a larger tide and a stronger tide-surge interaction is observed (Antony & Unnikrishnan, 2013).

In the Bangladesh part of the delta, J. U. Chowdhury et al. (1998) estimated the water levels inside the estuaries with a 1-D model at 10 to 50-year return period to plan the construction of cyclone shelters. In their approach, they used an empirical formulation to estimate the surge level for a given wind speed. To estimate the surge level at a given return period, they assumed that the surge height corresponds to the wind speed of the approaching cyclone to that location at half the return period. This relatively simple approximate solution appears to hold on this macro-tidal regime. Statistically, the tidal water level is relatively high for about half of the cyclones, those making landfall during the high-tide part of the tidal cycle. Their estimated 50-year return period surge level ranges from 3 to 4 m along the central part of the delta from west to east. However, in the final estimate for the design water level for the cyclone shelters in their study, they added the spring tide level linearly. They did not, however, provide an estimate of total water level at 50-year return period.

The study by Jakobsen et al. (2006) took a similar approach as Sindhu and Unnikrishnan (2011). For the Bengal delta coastline (of about 300 km length) they selected 17 historic cyclones which produced significant surges during 1960-2000 period. The simulated 17 water level records at each model grid point are then fitted to an exponential distribution to estimate the associated distribution parameters. According to their estimate, the 100-year return period water level goes as high as 10 m at the north-eastern corner of the estuary. They also noted a rapid evolution of water level with return period along the shoreline of the lower part of the Meghna estuary.

Past studies to understand the storm surge hazard over the Bengal delta relied on the evolution of a single storm. In these studies, the storm is manually translated in space to achieve full spatial coverage (Hussain et al., 2017). The temporal coverage is also obtained similarly, mainly to study the impact of the tide and tide-surge interaction along the delta coastline (Hussain et al., 2017; Krien, Testut, et al., 2017). While these sensitivity experiments give a general idea about the hydrodynamic response, they do not reveal the statistics of the flooding hazard.

From the literature review, it is clear that the unavailability of data hindered the previous attempts to map the storm surge hazard using numerical models. This lack of data includes both the storm track records and associated storm parameters – e.g., pressure drop (ΔP), maximum wind speed (V_{max}), and radius of maximum wind (R_m). The recorded storm parameters also

have inherent inhomogeneity due to gradual changes in observational techniques (Singh, Panda, & Mohapatra, 2020). Finally, the spatial and temporal coverage of the recorded storms are sparse relative to the size of the shoreline and sampling of tidal phases. Indeed, the past studies reported sensitivity of the surge level estimates to storm parameters around the Bengal delta region, both for the maximum water level ($\sim O(\text{m})$) and the inundation extent ($\sim O(\text{km})$) Hussain et al., 2017; Lewis, Horsburgh, and Bates, 2014. Additionally, the modelling approach used in the past studies often did not consider the tide-surge interactions or wave set-up dynamically, e.g. Chittibabu et al. (2004) and I. Jain et al. (2010).

Over the last decade, hydrodynamic modelling in this region saw significant progress. Thanks to the improvement of bathymetry and topography tidal characteristics are now comparatively well reproduced (Chapter 2; Krien et al. (2016)). On top of it, the implementation of coupled hydrodynamic-wave modelling for cyclones has improved the realism of the extreme water level dynamics during storms (Chapter 5; Krien, Testut, et al. (2017)). These improvements in modelling naturally call for revisiting the prospect of understanding the flooding hazard from cyclone-induced storm surges. Last important piece in this hazard assessment is the climatology of the storms.

Our understanding of the dynamics of the cyclones has also progressed over the last decades. Recent advancement in this field enabled translating climatic properties to large ensembles of statistically consistent storm events. Examples of such methods include distribution sampling (Rumpf et al., 2007), Joint Probability Method with Optimal Sampling (JPM-OS) (Toro et al., 2010) or statistical-deterministic approach (Emanuel et al., 2006). Among these approaches, the statistical-deterministic approach is perhaps the most advanced. This modelling approach combines the statistical generation of the storms with a deterministic evolution and intensity estimation. The result is an ensemble of physically consistent cyclones representing the cyclonic activity of a basin climate. The statistical-deterministic approach has been successfully used to estimate the storm surge hazard at a local scale (Krien et al., 2015; Krien, Dudon, Roger, Arnaud, et al., 2017; Lin et al., 2010), as well as, at continental scale (Haigh et al., 2013).

The objective of this chapter is to estimate the storm surge and associated flooding hazard across the Bengal delta using an efficient and well-validated regional coupled storm-surge model (see Chapter 5). To this extent, we integrated the model for a large ensemble (several thousand) of synthetic cyclones generated through the statistical-deterministic method, covering the whole range of natural variability of storm frequency, size, intensity and track location, with a dense spatial distribution. The interactions among the tide, surge, and waves are modelled explicitly at high spatial resolution. We then used the ensemble modelling results to study the storm surge-induced water level at various return periods, up to 500 years. In Section 6.2, we describe our modelling framework, boundary conditions, and forcing generation strategy, along with validation for recent cyclones. In Section 6.3, discussion continues with the probabilistic-deterministic cyclone ensemble. We show the results of the modelled storm surge-induced inundation mapping in Section 6.4. A discussion is presented in Section 6.5, followed by a conclusion in Section 6.6.

6.2 Storm surge model

6.2.1 Model description

We developed our modelling framework based on SCHISM (Semi-implicit Cross-scale Hydro-science Integrated System Model). SCHISM is a derivative product built from the original SELFE (v3.1dc; Zhang and Baptista (2008)) and distributed with an open-source Apache v2 license, with many enhancements and upgrades including an extension to the large-scale eddying regime and a seamless cross-scale capability from the creek to ocean (Zhang et al., 2016). The model uses unstructured triangular-quad mesh for spatial discretisation, and a combination of s -, z -, sz -, or fully unstructured LSC² for vertical discretisation. SCHISM also includes a wetting and drying algorithm in the shallow areas.

One of the consequential inputs in hydrodynamic models is accurate topography and bathymetry data. Over the Bengal delta, the publicly available datasets do not provide enough data for accurate modelling. We built our bathymetry dataset on top of the work done by Krien et al. (2016). Their dataset is composed of a digitised nearshore bathymetry over the coastal region of Bangladesh and India, a dedicated river bathymetry from Bangladesh Water Development Board (BWDB), and a high-resolution topography dataset over the Bangladesh part of the delta. We updated the bathymetry dataset of Krien et al. (2016) with an additional set of 34 new hydrographic charts obtained from the Bangladesh Navy (see Chapter 2).

We built our model mesh based on this bathymetry and topography dataset. The model domain covers the Bay of Bengal from 11°N to 24°N, comprising the whole delta and its surroundings (Figure 6.2). We have used variable model resolution based on the topography and wave propagation criterion. The final mesh resolution ranges from 15 km over the deep parts of the ocean to 250 m over the delta, amounting to about 0.6 Million mesh nodes, and 1.1 Million triangular elements. A time step of 300 seconds was suitable for the resolution of our model (Chapter 3).

Hydrodynamically, our model is bounded on the ocean and the riverfronts with open-boundary conditions, with the no-slip condition along the closed boundaries. Along the ocean boundary, we have implemented a tidal water level derived from the 26 dominant tidal constituents. These are - M2, M3, M4, M6, M8, Mf, Mm, MN4, MS4, Msf, Mu2, N2, Nu2, O1, P1, Q1, R2, S1, S2, S4, Ssa, T2, K2, K1, J1, and 2N2. In total, we implemented six open riverine boundaries. For the rivers Ganges, Brahmaputra, Meghna, Hooghly, Karnaphuli, we have prescribed a discharge boundary condition. We have implemented a radiating boundary condition for the Rupnarayan river. To mimic the seasonal pattern of sea level reported by Tazkia et al. (2017), we have implemented a seasonally-varying sea level along the southern boundary with an amplitude of 35 cm. Over the whole domain of the model, the astronomical tidal potential is also forced for 12 constituents (2N2, K1, K2, M2, Mu2, N2, Nu2, O1, P1, Q1, S2, T2).

Our model is set up in depth-averaged mode (2DH). The frictional parameter is set using Manning n formulation. We adopted an approach for the spatial distribution of the Manning coefficient similar to Krien et al. (2016) and the one used in the previous chapters (Figure 6.2). For the deeper part of the ocean (depth \geq 20), we used a Manning coefficient value of 0.02. In the nearshore zone, the Manning coefficient is set to 0.013. In the rivers, a Manning coefficient

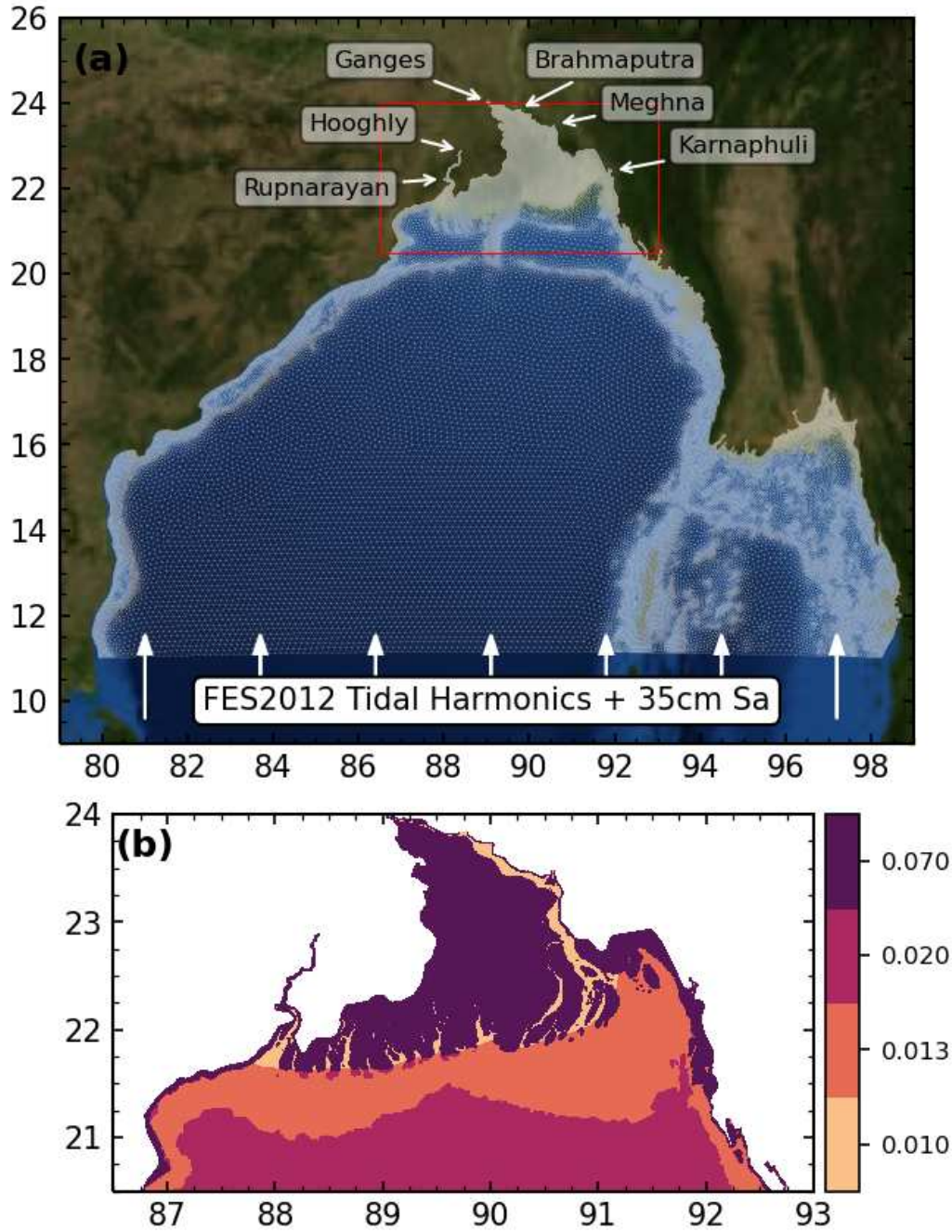


Figure 6.2: (a) Model domain with arrows indicating the open boundaries. (b) Distribution of Manning coefficient.

value of 0.01 is set. Unlike in Krien et al. (2016) and Chapter 3 and 4, for the inland area, we adopted a Manning coefficient value of 0.07, which is more reasonable for a vegetated land like the Bengal delta (Bunya et al., 2010).

6.2.2 Coupling with wave model

Our modelling framework is online coupled with the spectral Wind Wave Model III (WWMIII) at source code level. WWMIII solves the wave action equation over the same unstructured

grid as the hydrodynamic core (Roland et al., 2012). It considers source terms for the energy input from wind (Ardhuin et al., 2010), non-linear interaction in deep and shallow water, energy dissipation due to white-capping, wave breaking, and bottom friction. We modelled the wave breaking using the formulation of Battjes and Janssen (1978). A low value of coefficient of breaking, $\alpha = 0.1$ (instead of $\alpha = 1$), is adopted to avoid over-dissipation over a mild slope region like Bengal delta (Pezerat, Martins, & Bertin, 2020). We have discretised our modelled wave spectra into 12 directional and 12 frequency bins. The model is solved with an implicit scheme with an exchange of water level and current between SCHISM and WWMIII every 30 minutes.

6.2.3 Wind and pressure field

During a cyclone, the momentum transfer from the wind to the water column, and the inverse barometric effect of the pressure drop are the primary forcings of the storm surge. Thus, an accurate enough representation of the wind and pressure field in a numerical modelling framework is of high importance. In some well-monitored basins, there are extensive networks of observational data which can provide relatively accurate wind and pressure field during a storm. However, the observations of these variables over the Bay of Bengal are virtually non-existent. As such, the wind and pressure field during a cyclonic storm has to be estimated from either numerical weather models or satellite observations. Due to the high error associated with the commonly available numerical weather models, it is a fairly common practice in storm surge modelling to infer the wind and pressure fields from parametric cyclone models (Lin & Chavas, 2012). As the computation of parametric wind and pressure fields is comparatively light, this approach is also useful for sensitivity studies based on various configurations of a single storm (e.g. Hussain et al., 2017) or from a large ensemble of synthetic cyclones (e.g. Krien, Dudon, Roger, Arnaud, et al., 2017).

The associated error with these parametric cyclone models is diverse with distance from the centre of the storms (Krien et al., 2018). The most considerable uncertainties in estimating wind and storm are from the surface wind reduction factor (SWRF) and the choice of gradient wind profile (Lin & Chavas, 2012). From a comprehensive comparison of parametric cyclonic wind fields with scatterometer observations for 16 storms, Krien et al. (2018) showed that the relative error in the wind field is minimal with a combination of parametric wind fields. Following their findings, we have used a combination of Emanuel and Rotunno (2011) and Holland (1980) to derive the parametric wind profile. We have applied a SWRF of 0.9 (Krien, Testut, et al., 2017; Lin & Chavas, 2012). The effect of storm translational speed is accounted for through a surface background wind reduction factor of 0.55 and a counter-clockwise rotation angle of 20° as suggested by Lin and Chavas (2012). In all cases, we used the Holland (1980) model to derive the pressure field.

6.2.4 Validation

The performance of our model in simulating the tide was documented in previous studies (Chapter 3 and 4; Khan, Ansary, et al. (2019) and Khan, Durand, et al. (2020)). We found that our model has a 2 to 4 times better reproduction of tidal water level compared to global tidal models,

and comparable performance with the state-of-the-art models in this region (Krien et al., 2016). The total complex error calculated over four major tidal constituents – M2, S2, K1, O1 – ranges from 5 to 20 cm, which is comparable to other well-documented shorelines around the world. Notably, the current model shows better performance around the mouth of Meghna estuary – a critical region with complex hydro-morpho-dynamics.

The observational network of tide gauges is sparsely distributed, and typically non-functional during an intense cyclone Krien, Testut, et al., 2017. It is thus relatively difficult to achieve a thorough assessment of the model realism for most of the historic cyclones. The quality of the tide gives a preliminary assessment of the potential skills of our model in simulating storm surges. Given that the wind and pressure fields are adequately prescribed, and necessary physics – particularly the wave coupling – is incorporated, the model is expected to simulate a storm surge appropriately.

The performance of the model in simulating storm surges is demonstrated through a recent cyclone – Amphan – that made landfall in this region (Chapter 5). From a set of in-situ observations, it was found that the model performs well in reproducing the maximum water level at multiple tide-gauge locations distributed throughout the Bengal shorelines.

Similar to (Krien, Testut, et al., 2017), we also performed a hindcast of the water level generated by cyclone SIDR – another comparatively well documented historic cyclone. Figure 6.3 shows the water level evolution at four tide gauge stations around the landfall location. The modelled water level is shown in black lines, and the observed water level records are shown in dots. As noted by Krien, Testut, et al. (2017), the tide gauge stopped working at Khepupara at the time of very high water.

The results of these experiments – cyclone Amphan (Chapter 5) and Sidr (this section) – suggest that our model can successfully reproduce water level evolution, as well as maximum water level, during cyclones along the shoreline of northern Bay of Bengal.

Additionally, for the cyclones shown in Figure 6.1, the estimated maximum water level from our model is listed in Table 6.1. We adopted JTWC Best track dataset for the cyclone track and intensity information. For 1970 Bhola cyclone, the intensity of the cyclone was not available in the JTWC dataset.

Table 6.1: Simulated maximum water level for the cyclones shown in Figure 6.1. V_{max} is the maximum wind speed in knots, WL_{max} is the simulated maximum water level range over the delta shoreline in meters. For 1970 Bhola cyclone, the storm surge simulation was not possible thus listed as NA (not available).

No	Cyclone	Year	Casualty	V_{max}	WL_{max} (Sim)
1	Bhola	1970	200-500k	100	NA
2	Gorky	1991	64-139k	140	5-8
3	Sidr	2007	3.5k	140	4-5
4	Aila	2009	339	65	3-4
5	Ruanu	2016	227	60	4-6
6	Mora	2017	135	80	2.5-3.5
7	Fani	2019	89	135	2.5-4.0
8	Bulbul	2019	41	85	3.5-4.5
9	Amphan	2020	118	140	3-5

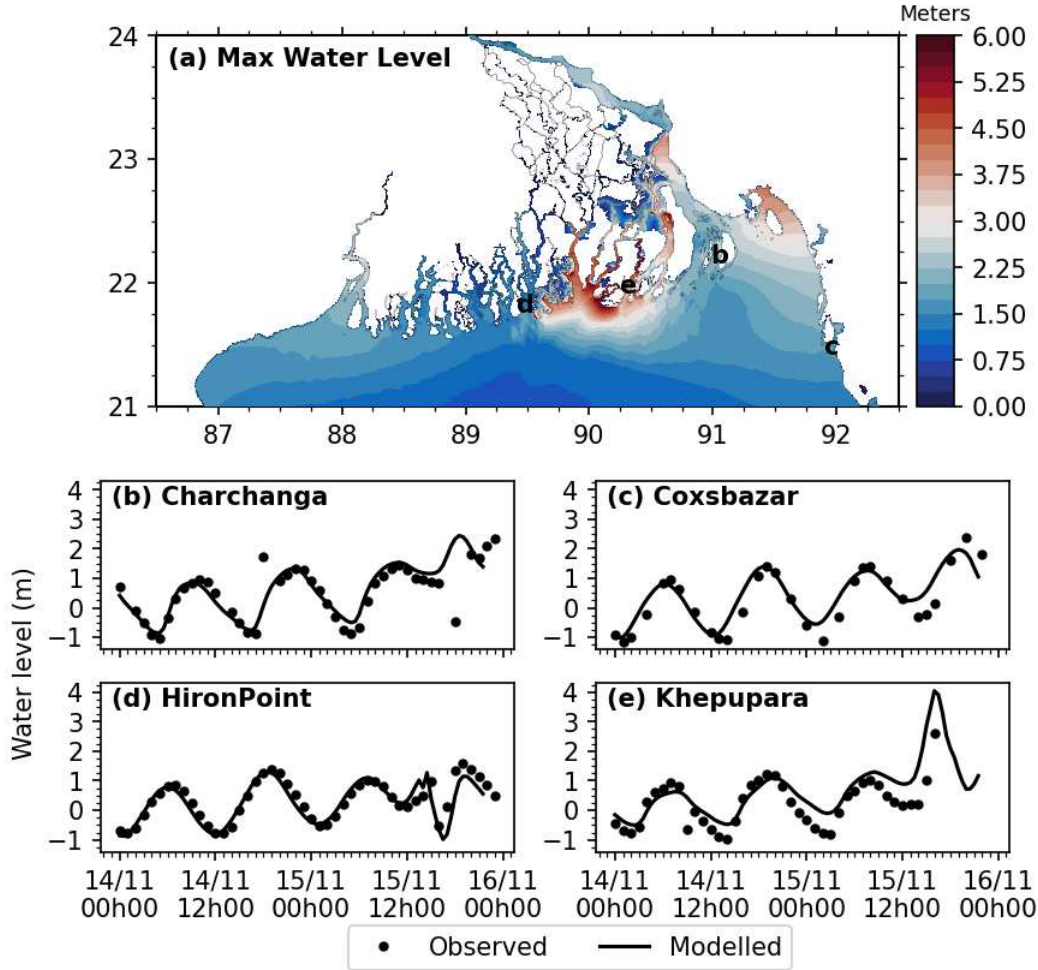


Figure 6.3: (a) Maximum simulated water level during cyclone Sidr. Comparison of simulated and observed water level during cyclone Sidr at (b) Charchanga, (c) Coxsbazar, (d) Hironpoint, and (e) Khepupara. The station locations are shown in (a).

6.3 Probabilistic-deterministic cyclone ensemble

6.3.1 Synthetic storm dataset

We use here a large ensemble of 3600 synthetic storms passing by the lower part of the Bengal delta. These synthetic storms were generated by Kerry Emanuel, through his statistical-deterministic approach (Emanuel et al., 2006) based on the climatic conditions of the 1981-2015 period. The forcing background climate is derived from the National Center for Environmental Prediction/National Center for Atmospheric Research (NCEP/NCAR) reanalysis (Kalnay et al., 1996). In this method, synthetic storms are generated in three steps. First, a synthetic environmental wind field is derived from a long-term dataset which conforms to the mean climatology. For the dataset we used, the environmental wind field is derived from NCEP/NCAR reanalysis dataset for the zonal and meridional wind components at 250 and 850 hPa. During this step, the observed monthly means and variances are respected, as well as most covariances. In the second step, a set of tracks are generated from a random field of genesis points and a weighted mean of 250 and 850 hPa flow plus a correction for beta drift (Emanuel et al., 2006).

The generation of cyclones is tuned by the weight factor and beta-drift so that the frequency of the storms is consistent with the observed displacement statistics. Finally, the storm intensity is estimated along the tracks using a coupled ocean-atmosphere one-dimensional axisymmetric model (Emanuel et al., 2004). The wind shear is given by the synthetic time series of winds determined previously. Previous application of this model includes calculating storm surge hazard in Guadeloupe (Krien et al., 2015) and Martinique (Krien, Dudon, Roger, Arnaud, et al., 2017), storm surge return period in New York City (Lin et al., 2010), wind return period in Boston and Miami (Emanuel et al., 2006).

In the cyclone ensemble for Bengal delta, only the cyclones that pass through a 300 km radius centred on the delta (89.57°E, 21.71°N) are retained. With an average annual frequency of 0.70314 cyclones, the ensemble of 3600 cyclones considered here represents more than 5000 years of cyclonic activity over the northern Bay of Bengal under present climate conditions. The landfalling cyclone frequency along the shoreline (for each 20x20 km pixel) is shown in Figure 6.4(a). The inset of Figure 6.4(a) shows a subset of the cyclone tracks in the ensemble.

These synthetic ensemble of storms are fundamentally different from hypothetical storms. Hypothetical storms are typically generated from a known storm by modifying its track or strength or both, which could render some storms as unrealistic. On the other hand, the storms in our ensemble are physically meaningful and statistically consistent. The consistency of the cyclone ensemble is illustrated in Figure 6.4 (b) and (c). The distribution of the simulated maximum wind speed (V_{max}) shows a good agreement with the observations from JTWC (Figure 6.4b).

Similarly, the seasonal distribution of the cyclone ensemble and observed from JTWC, both show a well matching pattern with a bimodal seasonality (Figure 6.4c) (Alam & Dominey-Howes, 2014). In the Bay of Bengal, low-pressure systems typically cannot intensify into a storm due to strong vertical wind shear present during monsoon (June-August). During the pre- (March-May) and post-monsoon (September-November), low vertical wind shear, and high sea surface temperature provides a suitable condition for low-pressure systems to intensify. The simulated bimodal temporal distribution of the synthetic cyclones indicates that the statistics captured by the statistical-deterministic method correspond well with the seasonal climatological characteristics.

6.3.2 Ensemble surge estimate

Estimation of storm surge associated with the storms in the ensemble is done in two steps. First, for each synthetic storm, the wind and pressure field are derived, as explained in Section 6.2.3. Here, for the inner core of the cyclones ($r < r_{50}$), the wind field is estimated using the model of Emanuel and Rotunno (2011). On the outer core ($r \geq r_{50}$), we used Holland (1980) model. The pressure field is estimated from the formulation of Holland (1980) for all radial distances. The wind and pressure fields are updated every 15 minutes with a linear interpolation of the associated variables.

With wind and pressure fields, we then calculate the ensemble of water level estimate using the same ocean-wave coupled model set-up described in the previous section. We achieved this ensemble of water level estimate through individual simulation of 3600 storms – which amounts

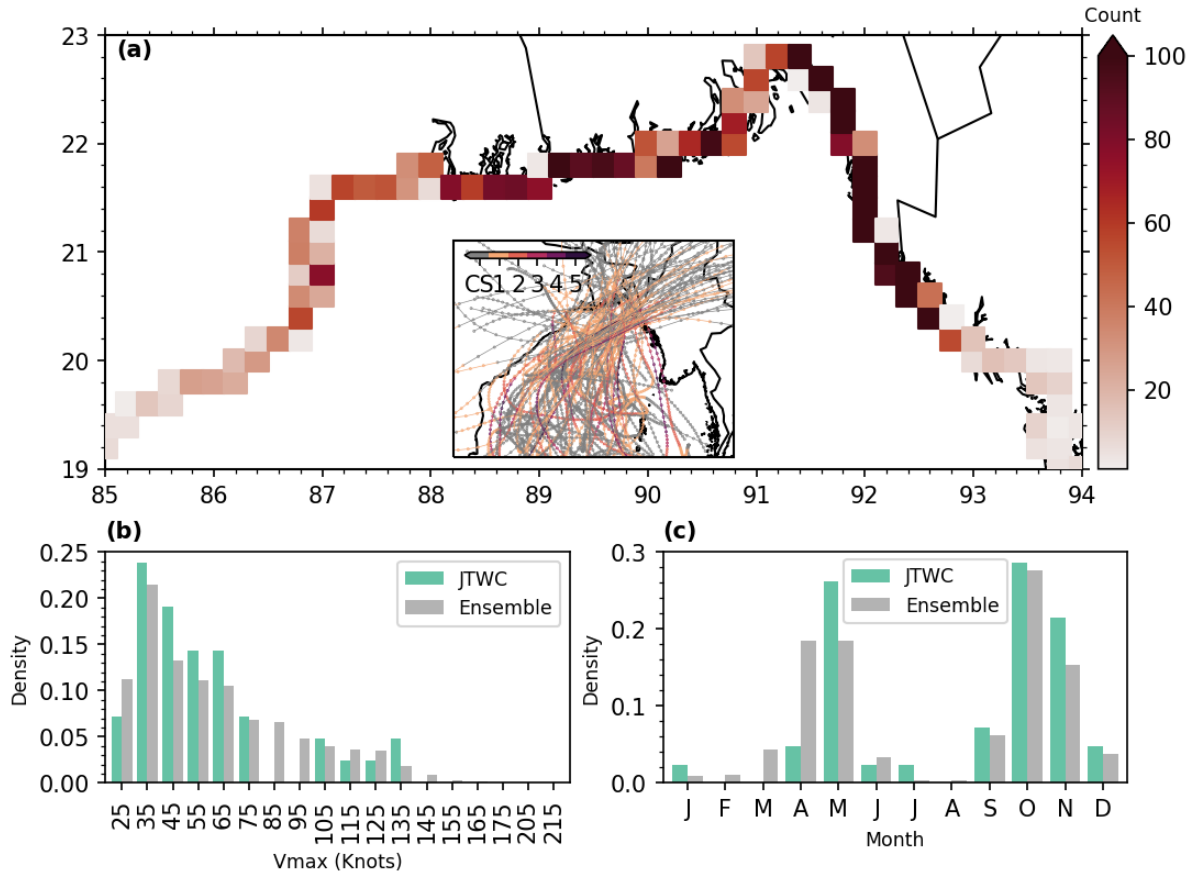


Figure 6.4: a) Spatial distribution of the paths of the cyclones that make landfall along the coast of Bengal delta. Each square bin is 20 km wide. A small subset of cyclones trajectories is shown in the inset. (b) Distribution of maximum wind speed of the synthetic cyclones compared to the JTWC dataset, (c) Annual distribution of the occurrence of the synthetic cyclones compared to JTWC dataset.

to 14 years of model simulation. Along the open boundaries of the rivers Ganges, Brahmaputra, and Meghna, we have prescribed time series of observed discharge at the fictional timestamp of the cyclones, which ranges from 1980 to 2015. We have applied a discharge climatology as the boundary condition for Hooghly (Mukhopadhyay et al., 2006), and Karnaphuli (M. A. M. Chowdhury & Al Rahim, 2012). Similar to the model set-up used for the hindcast experiments, we have also taken into account the seasonal mean sea level variation of the Bay of Bengal by applying an annual harmonic on the water level along the oceanic open boundary with a period of 1 year peaking in August with an amplitude of 35 cm. The coupling between SCHISM and WWMIII allows accounting for the wave set-up induced by radiational stress gradient of the waves (Longuet-Higgins & Stewart, 1962). Similar to the model set-up for cyclone Amphan hindcast in Chapter 5 and the Sidr hindcast in this chapter, the breaking coefficient is set to 0.1 (instead of the default parameter $\alpha = 1$) to avoid over-dissipation of the waves over the submarine part of the delta with mild slopes (Pezerat, Martins, & Bertin, 2020). We also invoked the wetting and drying algorithm in SCHISM with a threshold of 10 cm depth of water for an element to be registered as wet.

6.3.3 Statistical analysis methodology

We have applied ranking-based statistical analysis to infer the quantities at a given return period. To do so, at each node the quantity of interest (e.g., maximum water level, maximum surge level) is first sorted sequentially among the 3600 members, from the smallest value to the largest one. Since our dataset consists of 3600 cyclones with a yearly frequency of 0.70314 cyclones, it corresponds to 5120 years of cyclonic activity. Once sorted in ascending order at each point of the model grid, each water level present in the sorted ensemble corresponds to a return period ranging from $5120/3600$ viz. 1.42 years (for the smallest return period) to 5120 years (for the largest return period). Estimated quantities at return periods between 5 years and 500 years (at 5-year steps) are considered trustworthy in our subsequent analysis, to make sure that our ensemble contains a large enough sample for each return level. At 500 years level, the number of cyclones that contributes amounts to about 50 cyclones (on average three cyclones per 20 km of shoreline). Above 500 years, the sample size for cyclones that contributes to the return period is smaller, which is potentially too small to capture the extreme value statistics. We linearly interpolated the water level at individual integer return level from the sorted dataset.

6.4 Storm surge hazard

The outcome of the statistical analysis consists of water level maps at various return periods, spatially distributed on our model grid. Figure 6.5a shows the water level at the 50-year return period over the northern Bay of Bengal. The meaning of the colour bar is twofold. At all grid points located below mean sea level, including the estuaries the colour indicates the water level above MSL. For the grid points located above mean sea level (e.g., inland), the colour indicates the inundation depth above topography. The 50-year return period water level shows a similar spatial pattern as the tidal range (Chapter 4). We see that a dipolar pattern arises, with a very high water level in the north-eastern (around 88°E) and the north-western (around 91.5°E) corners of the bay. In contrast, in the central region (between 88.5°E and 91°E), there is a local minimum in the estimated 50-year return period water level. However, among these two maxima, the 50-year water level in the north-eastern part reaches about 6 m, twice as much as the 50-year water level in the north-western part of the delta (barely 3 m).

Inland, at 50-year return period, a contrasting flooding pattern is observed. Two specific regions are found to be flooded by a storm surge at 50-year return period - one around $89-90^{\circ}\text{E}$ $21.5-22.5^{\circ}\text{N}$, and another around $90-91^{\circ}\text{E}$ $22.5-23.5^{\circ}\text{N}$. The first inundated region is the Sundarbans mangrove forest, which spans across the border between Bangladesh and India. The region is a sanctuary and legally protected region, and thus undisturbed from engineering intervention, like embankments. The second inundated region along the GBM estuary is densely populated. According to the polder embankments dataset used in our modelling, the region is not protected by the coastal polder network and thus exposed to the risk of flooding. Other than these two regions, the sea-facing inland areas are primarily found to be not flooded at a 50-year return level. These regions are protected by polder embankments (typically earthen), hence creating this contrast in the pattern of the flooded area.

Along the delta coastline facing the open ocean, the return period water level evolves signif-

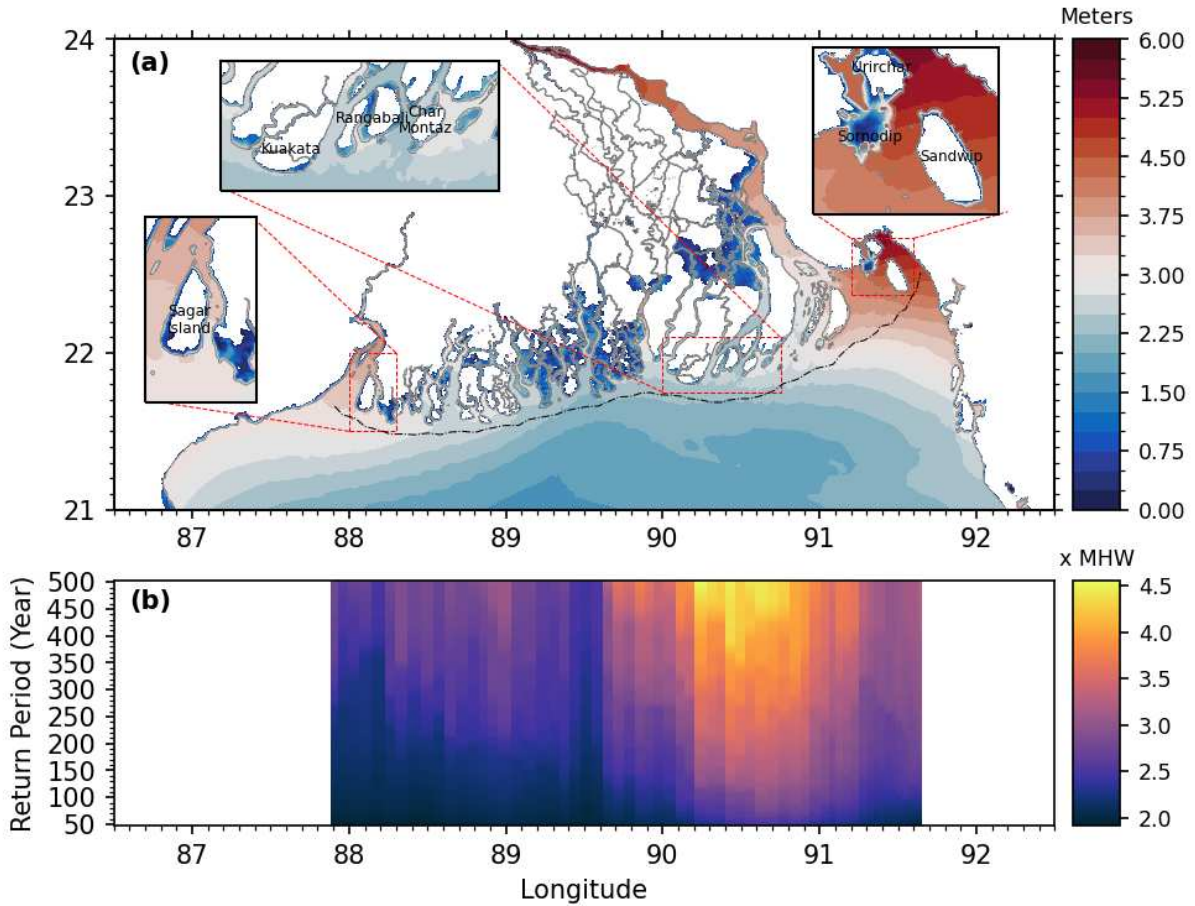


Figure 6.5: (a) Inundation extent and corresponding water level at 50-year return period. (b) Water level for the 50-500 years return period expressed as a multiple of the yearly mean tidal high-water level along the nearshore dash-dotted line shown in (a).

icantly differently. To illustrate this, we extracted the water level at the various return periods along the black line shown in Figure 6.5a, and display it as a multiple of mean high-water level (MHW) along the line (Figure 6.5b). The MHW level is calculated from a 1-year long tidal simulation, and taking the mean of daily (25-hour) tidal high-water estimate. We got this motivation from the contrasting range of MHW along the shoreline – two poles in the north-western and north-eastern corners reaching around 2 m (at 88°E) to 3 m (at 91.6°E) and a dip of 1 – 1.25 m around 90°E to 91°E. From Figure 6.5b, it can be seen that throughout the cross-section, the 50-year return period water level is around twice as much as MHW or higher. The increase in water level with the return periods along this nearshore cross-section shows regional sensitivity. From the mouth of Hooghly estuary to the region of the Sundarbans mangrove forest (88°E-89.5°E) the water level evolves moderately with return period showing only 50% increase from 50-year return period to 500-year return period. On the other hand, when approaching the mouths of the Meghna estuary, between 90.5°E and 91°E, the pluri-centennial water level increases sharply with the return period, to reach more than twice the 50-year return period water level for the 500-year return period. The spatial structure of water level at various return periods keeps showing the same bi-polar pattern throughout the return periods investigated

here, from 5-year to 500-year return periods (Figure 6.6).

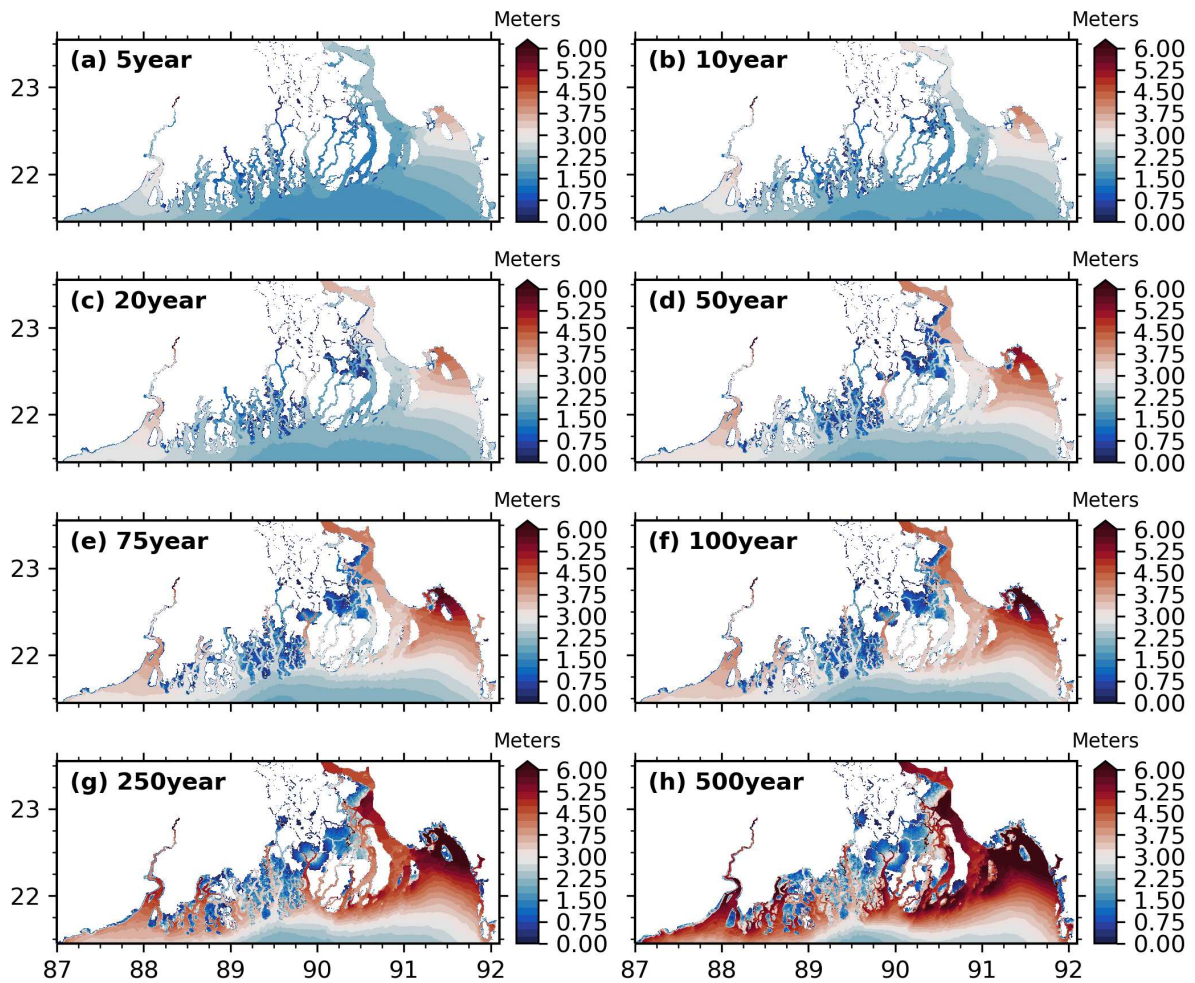


Figure 6.6: Inundation extent and corresponding water level at (a) 5-year, (b) 10-year, (c) 20-year, (d) 50-year, (e) 75-year, (f) 100-year, (g) 250-year, (h) 500-year return period.

The inundations in the mangrove region seem to have a large saturation effect on the evolution of the return water level around 89.5°E . There the water level remains practically the same for the various return periods (slightly rising from 2.50 m at 50-year return period to 3 m at 500-year return period). We also observe this evolution in Figure 6.6.

A varying degree of the N-year return period water level along the estuaries is observed from Figure 6.6. Similarly, the flooding extent in the adjoining areas also changes significantly from the short return periods to the longest ones. We choose three estuaries to take a closer look at the evolution of water level with the return periods. These are Ganges-Brahmaputra-Meghna (GBM) on the eastern side (Figure 6.7a-b), Hooghly estuary on the western side (Figure 6.7c-d), and Pussur estuary in the central mangrove region (Figure 6.7e-f). The water level at the various return periods is extracted along the line shown in Figure 6.7a,c,e and shown as a multiple of the 50-year return period water level in Figure 6.7b,d,f.

In the GBM estuary, the water level increases sharply with increasing return period, as shown in Figure 6.7a-b along the whole cross-section considered here. During the first 50 km,

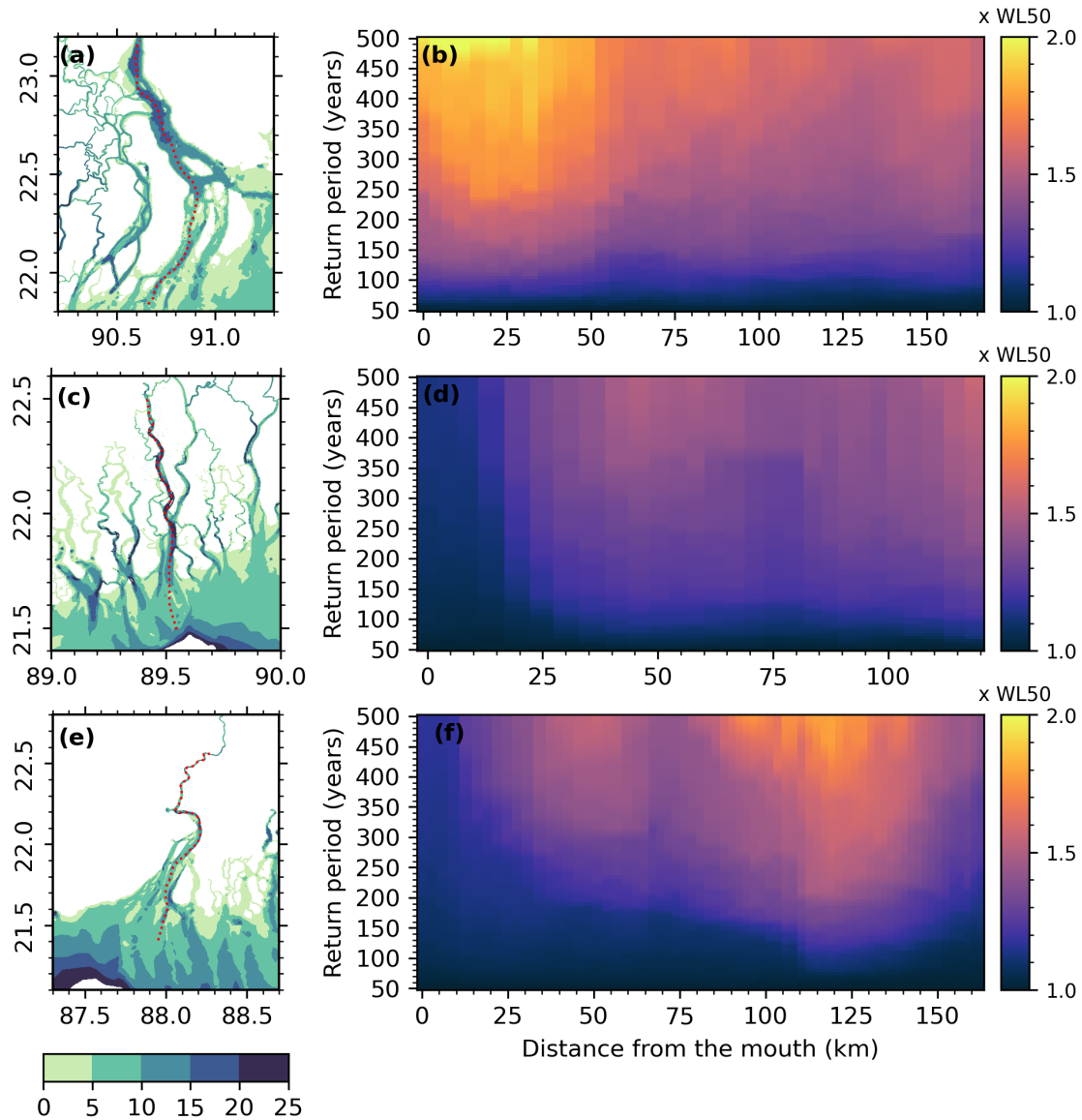


Figure 6.7: Water level as a function of the return period, expressed in multiple of the 50-year return period water level, along the dashed lines shown in red for (a)-(b) Ganges-Brahmaputra-Meghna estuary, (c)-(d) Pussur estuary, (e)-(f) Hooghly estuary. The x-axis is the distance from the mouth of the estuary, in km. The background shading in panels (a), (c) and (e) shows the bathymetry in m.

the 500-year return level reaches more than twice the 50-year return level. Further upstream, up to the estuarine bottleneck of Chandpur (24°N), the sensitivity of the water level to the return period is more moderate, with around 50% higher water level at 500-year return period compared to the 50-year return level.

In the Hooghly and Pussur estuaries, a contrasting scenario is observed compared to GBM. Along the Hooghly estuary, the sensitivity of the water level to the return period is moderate for the first 100 km but amplifies considerably afterwards. Along the Pussur estuary, intense saturation of the water level is seen over the first 25 km and then shows a moderate evolution.

6.5 Discussion

6.5.1 Synthetic cyclone ensembles statistics

The synthetic cyclone dataset used in this study makes our estimation inherently different from the previous attempts to map the storm surge hazard along the shoreline of the Bengal delta. The underlying statistical-deterministic approach of our storm database provides three significant improvements over the previous approaches. First, the random genesis of the storms adds a probabilistic nature to the population of the storms. Second, the deterministic evolution of the storms makes sure that the resulting population of tracks are physically valid, consistent with the ocean-atmosphere coupling to a reasonable extent. The resulting statistical distribution of maximum wind speed of the storms shown in Figure 6.4b gives confidence in the capability of the statistical-deterministic approach to capture the actual behaviour of the ocean-atmosphere system over the Bay of Bengal. Third, a large enough population of storms allows both an appropriate spatial coverage of the coastline and appropriate temporal coverage of the pluri-annual to pluri-centennial return periods of interest here (Figure 6.4a,c).

The distribution of the cyclones along the shoreline shown in Figure 6.4a illustrates a dense population of cyclone making landfall along the convex delta front (88°E-91°E). An affluent population of storms is also observed along the eastern coast of Bangladesh. This landfall pattern corresponds to previous observations that the landfalling cyclones in the Bangladesh coastline tend to move north-eastward (Ali, 1996).

6.5.2 Inundation extent and consistency

The storm surge inundation hazard has significant spatial variability across the Bengal delta region (Figure 6.5). Our underlying statistical analysis is an empirical rank-based return period estimation, which requires a large enough size of the ensemble to achieve a smooth spatial and temporal resolution. Visibly, the water level estimation at the 50-year return period showed in Figure 6.5 evolves smoothly over the Bengal delta region. In our estimate, about 600 and 400 unique cyclones contribute to the 50- and 100-year return period water level. In other words, the associated return period water level is pulled-in from a large number of individual cyclones, which in turns sampled cyclones with a range of intensity landfalling at various phases of the tide. Indeed, this spatial consistency of water level is observed for all the return periods we analysed from 5-500 years (Figure 6.6), indicating a robust estimate of the storm surge water level.

It appears that the water level has a similar regional distribution as tidal amplitude with two maxima in the north-eastern and north-western corners, and a relative minimum in-between (Figure 6.5a). At the mouth of Hooghly, in the north-western corner of the delta, the 50-year return period water level is about 3.5 m. The 50-year water level reduces to about 2 m moving eastward at the mouth of the Pussur river. Further eastward the water level increases again to reach more than 5 m along the shoreline of Sandwip Island (91.6°E, 22.5°N) and Chittagong. This estimated water level is on average twice as much as the mean high water level (Figure 6.5b). We found the highest 50-year return period water level at the mouth of Meghna estuary (90°E-91°E). There the 50-year return period water level reaches thrice as much as the mean

high water.

6.5.3 Comparison with previous estimates

As mentioned previously, a reliable estimate of the return period of storm surge water level over the Bengal delta has not emerged due to the gap in data as well as modelling. A comparison is presented here with the previous estimates by Lee (2013) and Jakobsen et al. (2006). Lee (2013) did an extreme value analysis of the observed time series over 1977-2009 (33 years), at Hiron Point tide gauge located in the central Bengal shoreline (89.5°E, 21.8°N). For this purpose, he decomposed the time series using the Ensemble Empirical Mode Decomposition approach. He reconstructed the water level by only keeping the very high-frequency (~3 hours) and very low-frequency modes. This process essentially removed the tide from the water level and retained the detided residual (i.e., surge). Using a yearly-maximum method, in his extreme value analysis, he obtained a 1.66 m surge level at 50-year return period. In the previous section, our analysis was focused on the water level rather than surge level. To compare with the estimate of Lee (2013), we reprocessed the whole ensemble of storm event simulation results. We have first extracted the tidal water level from the 3600 cyclones that we simulated. Then, for each cyclone, we extracted the maximum surge level. Finally, on this maximum surge estimate, we applied the same ranking-based return period estimate. At 50-year return period, the surge amounts to 1.8 m at Hiron point. With a difference of only 14 cm, this value is comparable to the estimated value by Lee (2013) from the observation time series. To be noted that, the estimated 50-year return period water level from our ensemble is about 3 m at Hiron point.

The evolution pattern of 50-year return period water level is consistent with the previous estimates but with various degree of agreement on the amplitude (Jakobsen et al., 2006; Sindhu & Unnikrishnan, 2011). From an ensemble of 17 historic cyclones, Jakobsen et al. (2006) estimate that the 100-year return period water level reaches about 5 m at the mouth of Meghna, and about 8-10 m around Sandwip (See their Figure 5). A similar pattern has emerged in our analysis but with a much different water level estimate. We estimate that the 100-year return period water level is about 4 m at the mouth of Meghna, reaching about 6 m around Sandwip. In general, the water level estimates of Jakobsen et al. (2006) consistently overestimates compared to the one presented here. It is noteworthy that the modelling framework of Jakobsen et al. (2006) does not take into account the wave set-up. However, the limited and potentially biased sampling of the “strongest” cyclones (17 in total, over 40 years) leads to an overestimation of the storm surge level.

Along the eastern part of West Bengal shoreline (87°E-88°E), Sindhu and Unnikrishnan (2011) found an increase in water level when moving northward. The pattern of water level is similar to ours, but the values are overestimated. At Sagar Island, their estimated 5- and 50-year return period water level is 6.92 m, and 8.74 m respectively. In our estimation, the 5- and 50-year return period water level is 2.75 m and 3.5 m above MSL respectively. It is not clear if their estimate of water level is relative to MSL. It is noted that the mean estimated high water at Sagar Island is about 1.75 m above MSL.

6.5.4 Return period of previous cyclones

The maximum water level estimate from our hindcast of the Sidr cyclone (see Figure 6.3.) shows a strong surge near the landfall location where it reaches 6 m along the shoreline of Kuakata and remain strong in the connected tributaries. This water level amounts a return period of about 500 years. At the same time, the maximum water level hindcast along the coast of Chittagong and Sandwip (91.5°E, 22.4°N) is about 4.5 m, which corresponds to roughly 50-year return period water level at that location (Figure 6.6).

Compared to Sidr, the regional variation of maximum water level is much less pronounced for cyclone Amphan (Chapter 5, see Figure 5.5). The maximum modelled water level reached about 5 m around (88.4°E), which corresponds to a 250-year return period. At the landfall location of Sidr (around Kuakata - 89.7°E, 21.8°N), about 100 km eastward, the maximum water level is estimated to be 2.5 m, corresponding to 50-year return level. Similar to Sidr, the water level along the Sandwip coast during Amphan reached about 4.5 m, i.e., 50-year return level.

6.5.5 Role of embankments

From the various maps of n-year return period inundation extent and water level shown in Figure 6.6, it is clear that the embankments play a vital role in the storm surge flooding. Although these embankments were established for controlling tidal intrusion to promote agricultural activity, the initial designed heights appear to be well-designed providing considerable protection during extreme events. Our estimate shows that, under current climate cyclonic activity, for the embankment heights implemented in our model, the embankments start overflowing at 75 to 100-year return period water level (Figure 6.6).

The level of embankment protection estimated here must be taken with caution as we are limited by the availability of the embankment information and up-to-date status. These earthen embankments are poorly maintained (Islam et al., 2011). The information of embankment height used in the model of this study is more than a decade old. The current height of these embankments is unknown. Additionally, in our embankment height dataset, only one value of height is provided along the embankment. In reality, we expect a spatial variation of embankment heights. Considering all these factors, the estimated return period when the embankments start overflowing could be overestimated.

6.5.6 Population exposure

Storm surge is a significant hazard for the large population that lives in the Bengal delta. Figure 6.8 shows the population density per square kilometre in the delta area with a grey colour bar based on GPWv4 dataset (Center For International Earth Science Information Network-CIESIN-Columbia University, 2016). The contours of the return period of water level starting from 5-year to 500-year are shown in colour.

The estimation of the population living under a given return period of water level is not straightforward. The GPW dataset typically resolves the population at the second administrative level (Upazila), which typically covers hundreds of square kilometres of area. However, the data itself is provided at a regular longitude-latitude grid. For the pixels that cover the adminis-

trative area, a constant density is assigned for all the pixels that falls within the administrative boundary. On the other hand, the model grid is unstructured, and the resolution of our model output is sub-kilometric. Hence it is first necessary to map the inundation over the population dataset. We took the following steps for mapping :

1. We interpolated the modelled return period water levels to the same regular lat-lon grid as the population dataset (30" resolution, about 1 km at the equator). As the model grid is triangular, we used a linear triangulation interpolation method. We also interpolated the bathymetry to the population grid in a similar fashion. After the water level interpolation, we considered a pixel inundated if the inundation level is 10 cm above the topography.
2. We set the pixels in population dataset associated with topography below MSL in the model to null. The pixels outside the model boundary are also set to a null value.
3. For each return period, we counted the exposed population if the pixel is registered as inundated in step 1.

The estimated population living in our model domain over the Bengal delta extent shown in Figure 6.8a amounts to 30 Million. This count amounts to the number of population living at an

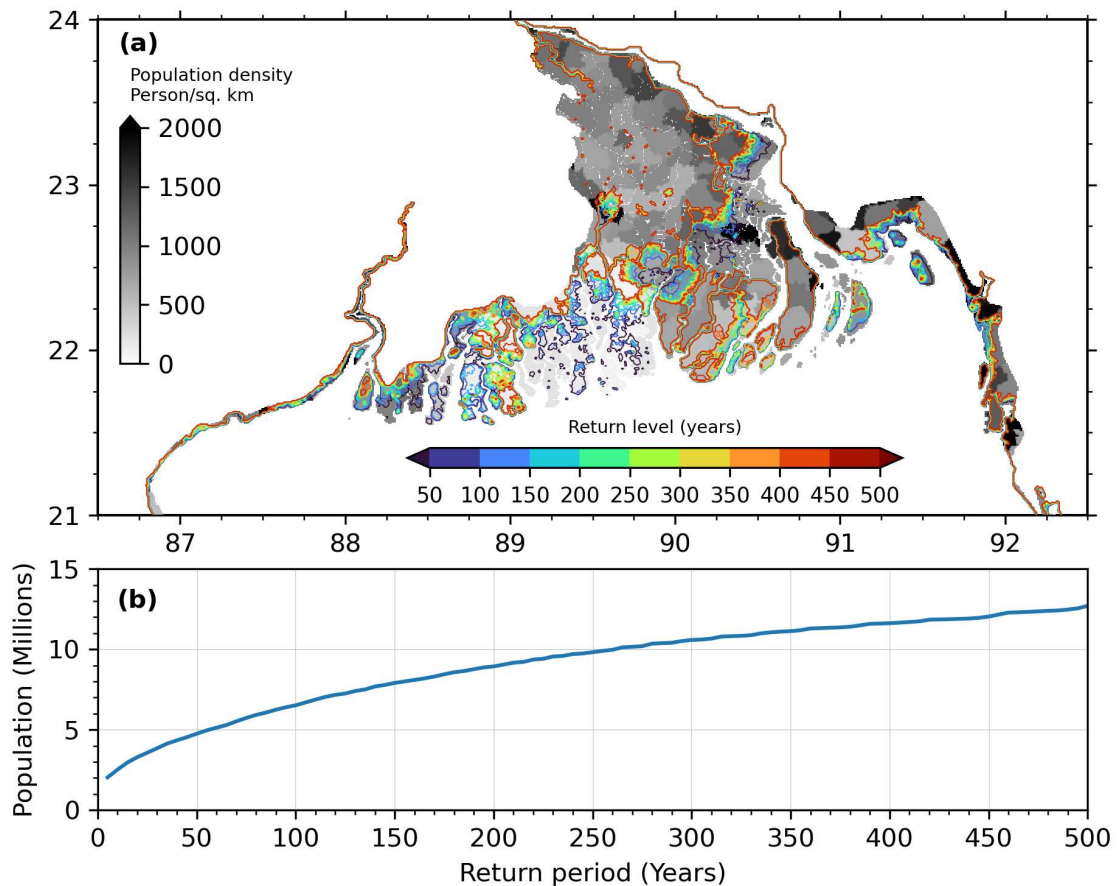


Figure 6.8: (a) Spatial coverage of flooding at various n-year return period estimated from the model. Gray colorbar shows the population density per square kilometre. (b) Number of people affected at various n-year water level return period.

elevation 5 m or less. The count of the exposed population at various return level of inundation is shown in Figure 6.8b. Our estimate shows that about 2 Million people live in a 5-year return period flood level area. Even if the embankments were to work without failure during a cyclone, about 3 Million more people get exposed to flooding going from 5-year to 50-year return period. This additional count of the population is about 10% of the total population living inside the study area. At a 100-year return level, this amounts to about 21% of the total population inside the modelled domain.

A refined estimation of the exposed population requires further refinement of the population spatial distribution, which is out of the scope of this work, and not pursued further. In this assessment, we did not consider the probable existence of city protection embankments around Barisal (90.36°E, 22.69°N) as discussed in Chapter 5, the potential degradation of the dikes, and possible dike breaching during an intense cyclonic event (Chapter 5). Knowledge of these factors will surely change the anticipated exposure of the population to flooding. Instead, our focus was mainly on the physical mechanism of the flooding from storm surges. Our preliminary assessment shows that the inundation estimates produced in our study provide useful information at relevant spatial scales to understand the vulnerability and exposure to storm surge for the vast population living in the Bengal delta continuum.

6.6 Conclusions and perspective

In this study, we present a robust estimate of the return period of water level over the whole Bengal delta shoreline under the current climate. We based our estimates on a large ensemble of statistically and physically consistent cyclones and high-resolution coupled hydrodynamic modelling. For the first time, we estimated the extreme water levels associated with storm surge for a broad range of return periods (5-500 years) at sub-kilometric spatial resolution over the Bengal delta. We show a diverse range of extreme water level variability both along the shorelines and the estuaries. Compared to previous studies, we estimate a lower storm surge water level. We show that embankments play a significant role in determining the flooding pattern. Our estimate suggests that about 10% of the coastal population is exposed to storm surge inundation at 50-year return period. The return period water level derived here could provide valuable information for robust engineering, social, economic assessment and future policy decisions. The information should also be a valuable tool for zoning the risky areas, and for more efficient resource allocation for pre-cyclone preparedness. The diverse range of extreme water levels and their evolution also should guide future research directions to understand better the extreme water level dynamics over the continuum of the Bengal delta. We are conscious of a potential drawback in our model set-up resulting from our inaccurate knowledge of the actual height of the embankments and potential existence of non-documented city protection embankments (Chapter 5), so the flooding extent seen in Figure 6.5 may be considered with caution. One may revisit the same question once a more reliable and consolidated database of dikes heights becomes available across the delta region.

The utility of such large ensemble is very high for modelling-based process analysis, particularly for a data-poor region like the Bengal delta. Various configuration of model physics could be adopted to study the interplay between various components of tide, surge, wave, and seasonal

sea level. This implies that, for each model configurations, the whole set of 3600 cyclones are to be computed again. While such in-depth analysis remains for the future perspective, one such example is shown in Figure 6.9. Including a tide-free ensemble (not shown), this figure amounts to simulating 18000 ($=5 \times 3600$) individual cyclones. These further perspectives are discussed in Chapter 7.

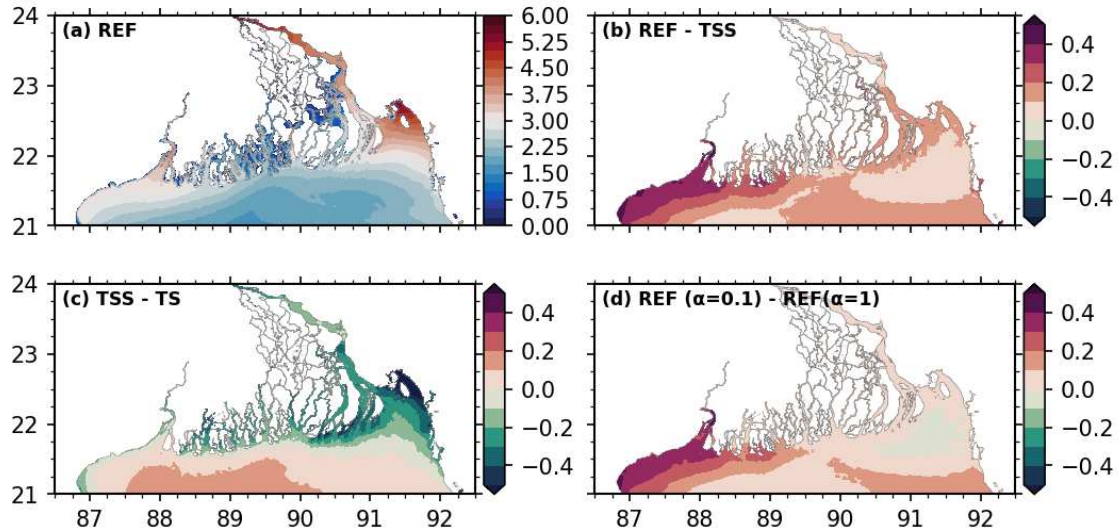


Figure 6.9: (a) Inundation extent and corresponding water level at 50-year return period (REF) computed with coupled tide-surge-wave model and $\alpha = 0.1$. This is same as Figure 6.5. (b) Difference in 50-year return period water level between REF and the ensemble computed with simulations from only tide-surge coupled model including seasonal variability of sea level and without wave coupling (TSS). (c) Difference in 50-year return period water level between TSS and the ensemble computed with simulations from only tide-surge coupled model without seasonal variability of sea level (TS). (d) Difference in 50-year return period water level between REF as shown in (a) and REF but $\alpha = 1$ (typically used value).

Epilogue

The Bengal delta continuum is well-known for its exposure to storm surge hazard. From the numerical modelling of large ensembles of statistically and physically consistent storms, it was possible to acquire a synoptic outlook on the flooding hazard under the current climate. The flooding hazard is spatially diverse, with a strong dependency on the local tide. The sensitivity of water level to the return period considered is substantial along the estuaries. At least 10% of the coastal population, amounting to 5 M people, may be affected by a 1-in-50 year return-period flood. Throughout the delta, the flooding is strongly controlled by the embankment system. Its failure, not considered in the present study, but seen during cyclone Amphan for instance, can expose an even larger fraction of the population to the same level of flooding hazard. Assuming the storm statistics remain the same, the change in coastal tide combined with sea level rise and land subsidence will potentially further exacerbate the exposure to flooding under a changing climate.

CHAPTER 7

CONCLUSIONS AND PERSPECTIVES FOR FUTURE WORK

“What the caterpillar calls the end, the rest of the world calls a butterfly.” – Lao Tzu

7.1 Conclusion

Cette thèse a porté sur la dynamique d'inondation du continuum rivières-estuaire-océan du delta du Bengale, et en particulier sur la façon dont la marée, les ondes de tempête et les vagues entraînent l'inondation. Il est très important de comprendre la dynamique des inondations et ses processus pertinents sur le continuum du delta du Bengale, car plus de 30 millions de personnes vivent à seulement 5 m ou moins au-dessus du niveau de la mer. Pour un delta aussi complexe et pauvre en données que le delta du Bengale, le fossé des connaissances est objectivement profond. Parmi une pléthore de questions scientifiques passionnantes et pertinentes, seul un certain nombre de directions de recherche ont pu être explorées dans le cadre de cette thèse de doctorat. Finalement, ce travail de recherche a permis d'ouvrir vers d'autres questions fondamentales et des directions de recherche diverses. En gardant à l'esprit cette abondance de questions de recherche et les perspectives scientifiques associées, le grand objectif de la thèse est divisé en quatre questions -

1. Comment la synergie entre la télédétection et la modélisation hydrodynamique peut-elle nous fournir des informations pertinentes sur la topographie de la zone intertidale littorale ?
2. Quelle est la sensibilité des constituants harmoniques de la marée à l'élévation du niveau de la mer dans le delta du Bengale, de sa partie côtière à son réseau estuarien ?
3. Quels sont les mécanismes nécessaires à prendre en compte pour modéliser les ondes de tempête et quels sont les principaux défis qui restent à relever pour modéliser le processus d'inondation ?
4. Quelle est la cartographie du risque d'inondation dû aux ondes de tempête le long du littoral du delta du Bengale dans le climat actuel ?

Ces questions sont abordées à l'aide d'une approche de modélisation numérique, complétée et contrainte par des observations in situ et de télédétection spatiale. L'apport de la modélisation numérique pour l'étude d'un système hydrodynamique complexe sous-observé comme celui du delta du Bengale, sur des échelles de temps allant de quelques heures à plusieurs décennies, a

été démontré au cours de cette thèse et constitue en lui-même un message important de cette thèse.

La première question qui concerne la topographie intertidale a été abordée dans le chapitre 3 en exploitant la capacité d'observation des images multispectrales acquises par la constellation de satellites Sentinel-2 et les prédictions de hauteur d'eau liées à la marée provenant du modèle hydrodynamique. Un résultat important a été la production d'un MNT intertidal à une résolution horizontale de 10 m couvrant une zone de 1134 km². Comparé à deux ensembles de données indépendants in situ, la précision verticale du MNT s'élève à environ 1,5 m, ce qui correspond à la barre d'erreur typique des ensembles de données de validation utilisés. Cette méthodologie est conforme aux contraintes de monitoring en temps quasi-réel car elle est automatique et numériquement efficace. Cela ouvre également des perspectives de recherche future pour des images spatiales à haute résolution, par exemple la future mission CO3D (<https://co3d.cnes.fr>). La combinaison de cette technique de récupération de la bathymétrie dans la zone intertidale avec l'inversion des vagues provenant des acquisitions satellitaires dans la zone littorale pourrait permettre une surveillance complète de la topographie et de la bathymétrie littorale.

La deuxième question a été explorée au chapitre 4 en expérimentant le modèle de marée basé sur une série de projections de l'élévation du niveau de la mer. Les observations in situ ont permis de compléter notre recherche sur cette question. Il s'avère que l'effet de l'élévation du niveau de la mer sur la marée est significatif et qu'il dépend de la région. Sur les régions sud-ouest et sud-est du delta, l'amplitude de la marée devrait augmenter lorsque le niveau de la mer sera plus élevé, ce qui ne manquera pas d'aggraver le risque d'inondation par la marée. En revanche, la partie centrale du delta pourrait connaître une inondation massive des berges des rivières et des plaines d'inondation adjacentes dans les scénarios dépassant 0,5 m de hausse du niveau de la mer ; en conséquence, cette inondation induira une diminution de l'amplitude des marées dans cette zone. Notre étude montre ainsi que la modulation des marées est un élément important dont il faut tenir compte dans l'évolution de l'hydrodynamique future du delta du Bengale. Le mécanisme d'amortissement et d'amplification dominé par la friction et contrasté au niveau régional souligne également la nécessité d'examiner l'application potentielle d'une stratégie de dé-poldérisation pour la gestion durable du delta à l'avenir.

La troisième question a été examinée au chapitre 5 en couplant le modèle de marée à un modèle de vagues et en l'appliquant ensuite à une étude de cas d'un cyclone récent. Une poignée d'enregistrements d'observations in situ, d'observations altimétriques par satellite et une enquête a posteriori des inondations observées, basée sur des articles de journaux, ont complété les résultats. L'importance des ingrédients-clés qui sont nécessaires à une prévision fiable de l'onde de tempête, comme une bonne bathymétrie, une bonne topographie, le couplage marée-surcote-vagues, la connaissance précise des hauteurs de digues, a été réaffirmée le long de cette région côtière active et complexe. Ce chapitre a aussi démontré la maturité de notre système de modélisation et notamment sa capacité de mise en œuvre opérationnelle en temps réel, qui devrait pouvoir améliorer considérablement la qualité des prévisions locales et aider à des prises de décision plus efficaces.

La quatrième question a été abordée au chapitre 6 en utilisant notre système de modélisation sur un ensemble de 3600 événements cycloniques synthétiques, statistiquement et physiquement

cohérents avec le climat actuel. Une analyse statistique sur ce grand échantillon de surcotes cycloniques a été effectuée. Les résultats montrent qu’il existe une gamme variée de niveaux extrêmes le long de la côte et dans les estuaires du delta du Bengale, avec des caractéristiques régionales bien définies. Le risque d’inondation lié à des surcotes avec une période de retour donnée s’avère être étroitement contrôlé par la présence de digues côtières et leur hauteur. On estime qu’environ 10% de la population côtière vit actuellement sous l’exposition d’une inondation cinquantennale. Ces cartes d’inondation devraient fournir des informations pertinentes pour l’ingénierie des infrastructures côtières, le zonage des risques, l’allocation des ressources, ainsi que pour la planification des recherches futures. Le vaste ensemble de données générées au cours de cette partie de l’étude ouvre également la possibilité de cartographier la contribution de divers processus individuels dans la dynamique des niveaux extrêmes.

7.2 Overview

The focus of this thesis has been on the inundation dynamics of the rivers-estuaries-ocean continuum of the Bengal delta, and in particular how tide, storm surges and waves drive the inundation. Understanding the inundation dynamics and its relevant processes over the continuum of Bengal delta is of high importance as more than 30 million people live only 5 m or less above MSL. For a data-poor, complex delta like the Bengal delta, the extent of the knowledge gap is objectively deep. Among a plethora of exciting and relevant scientific questions, only so much could be explored under the framework of a doctorate thesis. Eventually, this effort opened up even more profound questions and diverse research directions. Keeping in mind this abundance of research questions and associated future perspectives, I split the grand thesis objective into four questions –

1. How can the synergy between remote sensing and hydrodynamic modelling provide us with relevant information about the topography of the nearshore intertidal zone?
2. How sensitive are the tidal harmonic constituents to sea level rise over the Bengal delta, from its coastal part to and its estuarine network?
3. What mechanisms are necessary to model storm surge events, and what are the main remaining challenges to model the inundation process?
4. What is the pattern of the inundation hazard from storm surges along the shoreline of the Bengal delta under current climate?

I tackled these questions using a numerical modelling approach, complemented by in situ and satellite observations. A consistent important message pointed throughout the thesis has been the utility of numerical modelling to study a complex under-monitored hydrodynamic system like that of Bengal delta, across a range of timescales from hours to decades.

The first question was tackled in Chapter 3 by exploiting the observational capacity of the spaceborne multispectral imageries acquired by Sentinel-2 satellites (Sentinel 2A and 2B) and the predictability of tidal water level from the hydrodynamic model.

The second question was explored in Chapter 4 by experimenting with the tidal model based on a range of projections of sea level rise. Some insights from the situ observations complemented the study.

The third question was examined in Chapter 5 by first extending the tidal model to a coupled tide-surge-waves model and then applying it to a case study of a recently observed storm event. A handful of in situ observational records, satellite altimeter observations, and a secondary survey of observed flooding based on newspaper reports further complemented the findings.

The fourth question was tackled in Chapter 6 by combining the extended tide-surge-waves model with a large ensemble of cyclones climatology. I used large-sample statistical analysis on the storm surges climatology. The analysis provided a synoptic view of the storm surge hazard over the Bengal delta continuum region.

The objective of this chapter is first to summarize the conclusions we reached based on these four thesis questions, then to present the potential impacts of these findings as well as their limitations (Section 7.3). This summary is then continued to cover the future challenges ahead, based on the current state-of-the-art knowledge about the environmental dynamics of the Bengal delta (Section 7.4). Finally, the chapter ends with brief concluding remarks in Section 7.5.

7.3 Summary of conclusions and impacts

7.3.1 The synergy between the remote sensing and hydrodynamic modelling

Spaceborne remote sensing is one of those technologies which has revolutionized our ability to monitor the Earth and its environment. Spaceborne remote sensing platforms are now collecting Earth observations at an unprecedented rate and at unprecedented resolution. Increase in resolution inevitably increases the size of the datasets, the processing of which could seem a daunting task. In Chapter 3, we took a step towards extracting high-resolution mapping of the water bodies from a moderately high resolution (10 m) spaceborne image platform, viz. Sentinel 2 constellation. For the Bengal delta, our particular interest was the position of the shorelines and their temporal evolution. The method developed and presented in Chapter 3 was found to be generic enough to be routinely applied over the whole delta, without any modification. At the same time, the method was found to be light enough to be operated with a consumer-grade computing device, e.g. typically a laptop computer.

The combination of this observed shoreline positions from the satellite images with the corresponding tidal water level revealed a topographic map of the intertidal region. Around the world coastlines, the intertidal region is the most active landform due to the erosion and accretion processes. These intertidal regions are also poorly mapped due to the very high cost of in situ surveys, particularly so for the remote regions. Reduced accessibility to these locations makes the problem even more complicated. Satellite monitoring provides a relatively cheap method for repeated monitoring of these biodiverse coastal regions. From our analysis, we mapped more than 1134 km² area over the northern Bay of Bengal region. Our analysis revealed a well-defined intertidal zone along the Chittagong and Hooghly estuary (with width of order ~km). At the mouth of GBM estuary and the islands inside the estuary, a strong morphological evolution is observed. Along the central part of GBM estuary, the intertidal zone appears to

be thin (<100 m), essentially controlled by the embankments. The presented waterbody and shoreline extraction method is lightweight and automatic. These characteristics make it a good candidate for application with even higher resolution current and future spaceborne imageries – e.g., Pleiades, CO3D. The use of this method to monitor water bodies and inundations, and to study the shoreline and morpho-dynamics could provide valuable information to the coastal engineering and research community.

The knowledge of the intertidal topography complements the bathymetric dataset we worked out in the offshore domain (Chapter 3), which sets the path forward for high-resolution modelling of the nearshore processes in a data-poor region like Bengal delta. Indeed, the water-line approach can be extended to other shoreline monitoring approaches, e.g, SAR observations from Sentinel-1. Combination with other complementary approaches to extract the nearshore bathymetry from satellite observations, e.g., wave inversion (Almar et al., 2020; Poupardin et al., 2016) can provide a comprehensive bathymetric knowledge extending from the intertidal flats to the offshore ocean, to push forward the understanding of nearshore processes (Salameh et al., 2019).

7.3.2 Impact of sea level rise on the coastal tide

The impact of sea level rise on tidal properties along the shoreline and the estuaries of the Bengal delta reveals an interesting pattern of response. We found that the tide has a considerable sensitivity to sea level rise. This effect appears to be prominently dependent on the coastal morphology. In the regions where the tide can freely inundate and extend landward, the tidal properties are found to respond to sea level rise as a damping: the higher the mean sea level, the less the tidal amplitude. On the other hand, where the shoreline is rigid, without overflowing through the tidal cycle, tidal range shows an amplification as the mean sea level rises. For the Bengal delta, the tidal amplification with sea level rise is particularly strong along the Meghna estuary, with a typical increase of the tidal range of order 30% of the mean sea level rise. The shorelines along this part of the delta are mostly protected and do not allow the free intrusion of tidal water. The estuary inside Sundarbans mangrove behaves the opposite way. In this free-flooded natural zone, the tidal range shows a typical damping of order 10 to 30% of the sea level rise, associated with an increase of the area of the intertidal and permanently flooded zones.

The impact of sea level rise on the characteristics of the coastal tide is regionally-dependent, mostly non-linear and most importantly, of first to zeroth order compared to the magnitude of sea level rise, over vast areas of the delta. For most of the delta, the coastal tide amplifies with sea level rise, which further aggravates the potential exposure to future flooding. In other words, the analysis of future hydrodynamics, flooding hazard assessment, and delta management policy should consider the impact of such a mechanism.

The results here have particular insights for the delta management policy. As we saw, enough intertidal flooding can dampen the tide and reduce the tidal range. Over the Bengal delta, the coastal embankment system was developed without any coastal buffer zone. Our results suggest that introducing such buffer zones with artificial mangroves and vegetation can be a potential nature-based engineering solution to adapt to the sea level rise (Thorslund et al., 2017).

7.3.3 Modelling and forecasting of storm surge inundation

Storm surges are the primary source of extreme water level variability over the Bengal delta region. The sea level rise-induced inundation process is a slow-onset hazard. On the other hand, storm surges are relatively rapid-onset hazards. Historically, cyclonic storms and associated surges have been responsible for a massive loss of lives and economic damages. For such rapid onset hazards, efficient and accurate forecasting is of paramount importance. We show that with an efficient ocean-wave coupled storm surge modelling system, forced by publicly available storm forecasts, it is feasible to forecast in real time the evolution of a storm surge along the Bengal delta coastline.

We also demonstrate the necessity of considering a coupled hydrodynamic tide-surge-wave modelling framework for effective forecasting or hindcasting of storm surges over the head Bay of Bengal. For our case study of cyclone Amphan, the contribution from the tide-surge interaction and wave setup typically amounts to 10% and 10-15% of the total water level, respectively. Thanks to the numerical efficiency of our modelling framework, the coupled storm surge model was shown to be tractable in a real-time manner with consumer-grade desktop hardware.

Our modelling experiment and post-disaster news-survey of flooding report revealed the prominent control of embankments on coastal flooding. In the cyclone Amphan case study, inland inundation was induced by embankments failures that occurred at many places. Thus, for an efficient inland inundation forecasting capacity, routine monitoring of embankments topography and their structural conditions across the Bengal delta appears of vital importance. Such an effort appears urgently needed, in the current context of growing flooding hazard of the nearshore part of the delta.

The complexity of hydrodynamics and computational challenges with coupled hydrodynamic-waves model retarded the development of a reliable storm surge forecasting system over the Bengal delta. With the improvement of both storm forecasting and tide-surge modelling, it is one more step towards a real-time storm surge forecast system. Cyclone and storm surge warning has always been a communication and trust issue in the Bay of Bengal. Communicating a well-grounded storm and surge forecast to the community thus have a substantial impact on pre-disaster preparedness, evacuation effort, and informed decision-making during a storm surge.

In Chapter 5, I showed the maturity of the modelling framework to simulate storm surges. With publicly available storm forecast and advisories, a proof-of-concept for a forecast system is also presented there. Our pro-active forecast activity is currently giving birth to a new collaboration with the operational forecasting agency of Bangladesh – Flood Forecasting and Warning Center (FFWC) of Bangladesh Water Development Board (BWDB). The objective of this collaboration is to transfer the know-how of storm surge modelling and the modelling framework. This collaboration allows further testing the forecasting capability in an operational setting, as well as accessing a sizeable operational monitoring network of BWDB for further exploration of the water level dynamics in the delta.

7.3.4 Mapping the risk of inundation from storm surge under current climate

Over the vast coastal region of the Bengal delta, the impact of any landfalling storm and of its associated surge obviously depends on the landfall location, on the tide vs. surge phasing and interaction, and on swell characteristics. The inundation, being a threshold value problem, directly depends on the coastal topography. We show that a robust estimate of the inundation hazard, considering tide-surges-waves and their interactions, can be estimated through explicit hydrodynamic modelling of climatic storm surge activity. From a synthetic database representing 5000-year activity of storms under the current climate, we estimate that about 10% of the coastal population is currently exposed to storm surge flooding at 50-year return period.

We could also map the level of flooding at a broad range of return periods (from 5 to 500 years) over the delta at a sub-kilometric resolution. Such estimates may prove impactful for engineering planning of coastal structures, social and economic assessment of risk and vulnerability, identification of hotspots, and pre-cyclone disaster preparedness.

The utility of the ensemble modelling does not end with the mapping of the flooding hazard. It also gives a unique opportunity to understand the regional sensitivity of hydrodynamic processes during cyclonic storms. An example of that capabilities is presented in the Epilogue of Chapter 6.

The large ensemble of cyclone surges I built also opens up other applications – for example, machine learning. In recent years data-driven methods for environmental processes have gained much interest. A major requirement for the data-driven method is a large, curated dataset of the forcing and outputs of the process to be modelled – which fits within the characteristics of the large ensemble. Once trained, the machine learning methods are computationally very cheap to apply to a new storm to forecast or to study the sensitivity of the various input parameters.

7.4 Future Research Perspectives

Throughout the chapters presented in this thesis, it is clear that the water level dynamics in the low-lying Bengal delta continuum is markedly complex. The complexity in water level dynamics is driven by a strong tide, large river discharge, and exposure to storms and cyclones (Becker et al., 2020; Idier et al., 2019). The water level and inundation dynamics are further complicated by the man-made water control structures and the rapid change in land use pattern due to urbanization and population growth (Adnan, Haque, & Hall, 2019). Furthermore, the understanding of the flooding hazard and vulnerability depends on the understanding of individual components of the delta dynamics in an interdisciplinary fashion. Keeping in mind this inter-disciplinary dependency for a densely populated flood-prone delta, here I will focus on the hydrodynamics related future research perspectives, with hints of social and economic perspectives.

7.4.1 Modelling tidal dynamics

Tide is the primary source of water level variability along the coast of the Bengal delta. As shown in this thesis, state-of-the-art tidal models can reproduce the tidal water level with complex errors ranging from 5-20 cm (Chapter 3). While it is a significant improvement over the global

atlases available (e.g., FES, GOT, TPXO), further improvement is warranted. As seen in the successive chapters presented here, tide and storm surges penetrate far inside the delta and can cause large-scale inundation.

Inside the delta, the tidal influence is felt as far as the north-eastern part of Bangladesh (300 kilometres upstream, in the Meghna catchment). The large continental discharge strongly modulates the tidal propagation inside the delta. While long-term evolution of the water level is observed throughout the delta (Becker et al., 2020), no synoptic view on the tidal properties is currently present over this region. The change in water level inside the delta at seasonal timescale is of particular interest as it modulates the sea level along the estuary and in the coastal ocean (Durand et al., 2019). On the other hand, the impact of tides, particularly the spring tide, on controlling and modulating the monsoon flood and associated flooding hazard on the intermediate-to-upper part of the delta is not yet quantified.

In the nearshore coastal zone, altimetry-based observations can guide the calibration and validation of the hydrodynamical models. Particularly the recent processing schemes for altimetry in coastal water (e.g., ALES) seems promising (The Climate Change Initiative Coastal Sea Level Team et al., 2020). The upcoming altimetric missions like SWOT (2022) are also expected to provide a synoptic view of the global water surface, including inside the delta regions.

To better understand these inundations in the upstream part of the delta demands further refining our understanding of the tidal propagation inside the delta. This improvement of tidal modelling demands further improvement of the knowledge of bathymetry and topography as well as of the bottom roughness distribution. Variation of bottom roughness inland due to land cover appears to have a significant impact on coastal flooding too. The tidal modelling framework presented in Chapter 3 and 4 relies on a rather crude and fairly uniform parameterization of the bottom friction along the rivers and estuaries. A more distributed bottom friction parameterization, such as shown in Figure 7.1, could be a next step forward. The performance of this distribution of the bottom friction is currently under investigation and our model is to be benchmarked over the delta against a new extended dataset of water level records. At current benchmark locations (5 tide gauge stations) the error estimates seem promising (Table 7.1). This calls for further investigations on the representation of bottom roughness over the delta.

7.4.2 Salinity and steric sea level

In the Bay of Bengal, the sea level evolves seasonally mostly due to monsoon wind-driven variability of thermohaline stratification of the ocean (Benshila et al., 2014; Shankar & Shetye, 2001). This evolution is well-observed and documented over the region. Expectedly, this evolution of sea level affects the water level inside the delta. The dynamics of this seasonal picture, the evolution of the freshwater plume, and the interaction of the freshwater discharge with saline seawater, with the tide and with the frequent surges are interesting open-ended questions. In the current modelling framework, I followed a depth-average (2DH) formulation. The ocean steric variability is parameterized through a seasonally-changing barotropic sea level, based on the empirical knowledge of the steric sea level variability. To introduce the necessary physics to capture this steric variability requires both introduction of a varying density with active thermodynamics in a 3D framework. These features are already implemented in the SCHISM model

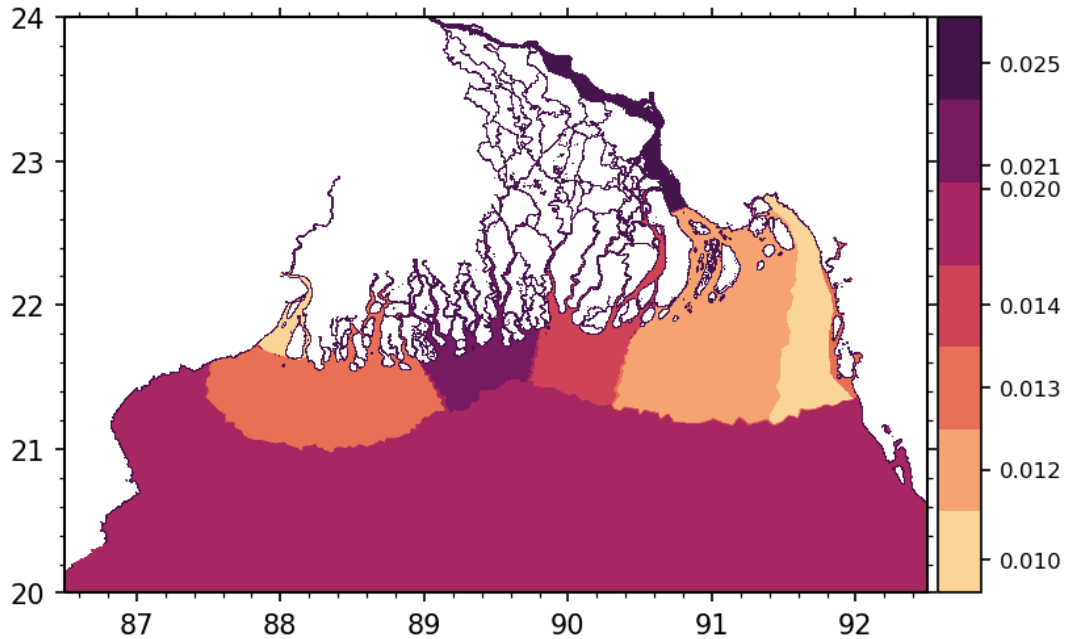


Figure 7.1: Regionally distributed Manning parameter. A constant value of $n = 0.07$ is imposed over land (not shown).

code, and the current 2D configuration gives a solid starting point for incorporating the 3D physics. Moreover, SCHISM is capable of discretizing the depth in unstructured fashion with LSC2 (Localized Sigma Coordinate with Shaved Cell) vertical grid, which is necessary for an efficient cross-scale modelling in a river-estuary-ocean continuum setting.

This interaction of tide and freshwater is also vital to understand the salinity intrusion inside the delta. A recent analysis of a moderate database of in situ observations suggests that the salinity front in the southern part of the delta shows a diverse rate of change (Sherin et al., 2020). Interestingly these changes have sudden but spatially consistent spikes in them advancing the salinity front by tens of kilometres. Change in freshwater discharges, rise in sea level, depletion of groundwater levels was proposed as some probable reasons. However, these mechanisms are still inconclusive and warrant further investigation with hydrodynamic modelling. Understanding of the salinization patterns has strong societal implications, being one of the major stressors for human migration and agricultural income over the Bengal delta (Chen & Mueller, 2018).

7.4.3 Role of embankments and mangroves

The understanding of storm surge inundation hazard will also benefit from up-to-date, accurate databases of embankments elevation and embankment conditions, where still a large knowledge gap exists (Chapter 5). The knowledge of the embankments geometry is of significant importance in many respects. Embankments control flooding, sediment distribution, and salinity intrusions (Adnan, Haque, & Hall, 2019). However, the overall impact of the embankments on the hydrodynamics over the Bengal delta is not well understood. While embankments are found to protect the inland areas from fluvial-tidal flooding, their failure is both poorly documented and a major cause of flooding and associated damage.

Table 7.1: Estimated complex error with regionally distributed Manning shown in Figure 7.1 (New Manning) compared to the one presented in this thesis (Current Model).

Station	Observation		Current Model			New Manning			
	A_0	ϕ_0	A_m	ϕ_m	Error	A_m	ϕ_m	Error	
Sagar Roads (88.0300°E, 21.6500°N)	M2	140.0	115.6	144.5	114.9	4.8	141.3	116.2	1.7
	S2	66.0	150.0	62.4	153.3	5.2	60.7	154.9	7.6
	K1	15.0	262.3	15.6	265.4	1.1	15.6	266.0	1.1
	O1	5.0	250.3	5.7	251.6	0.8	5.8	252.3	0.8
	σ_s					5.1			5.6
Diamond Harbour (88.1733°E, 22.1928°N)	M2	157.4	167.6	142.3	165.6	15.9	138.9	166.7	18.6
	S2	68.0	210.0	57.6	208.6	10.5	56.0	210.3	12.0
	K1	15.3	285.3	13.2	286.3	2.1	13.2	287.5	2.1
	O1	6.9	258.3	5.4	257.7	1.5	5.4	259.9	1.5
	σ_s					13.6			15.7
Hiron Point (89.4780°E, 21.8169°N)	M2	80.7	126.9	99.9	115.0	26.7	79.8	119.9	9.8
	S2	34.3	159.1	41.6	150.5	9.2	32.4	154.7	3.2
	K1	13.0	268.0	15.0	265.7	2.1	13.9	271.5	1.2
	O1	5.1	257.8	5.7	255.0	0.7	5.5	259.4	0.4
	σ_s					20.0			7.3
Dhulasar (90.2700°E, 21.8500°N)	M2	73.0	157.6	67.6	143.3	18.3	59.1	147.6	18.0
	S2	35.0	193.0	28.5	179.6	9.8	24.7	184.2	11.2
	K1	13.0	286.3	13.3	287.8	0.5	13.1	291.5	1.2
	O1	4	278.3	5.6	273.8	1.6	5.6	276.7	1.6
	σ_s					14.7			15.0
Charchanga (91.0500°E, 22.2188°N)	M2	96.0	233.8	95.8	216.9	28.2	91.6	218.7	25.0
	S2	37.5	264.9	36.6	250.3	9.5	34.9	250.2	9.6
	K1	12.7	304.2	16.8	308.7	4.3	17.1	306.7	4.4
	O1	7.6	285.2	8.1	293.1	1.2	8.5	291.7	1.3
	σ_s					21.3			19.2
Chittagong (91.8274 °E, 22.2434°N)	M2	171.7	196.1	149.2	194.8	22.8	163.1	195.5	8.8
	S2	62.4	228.9	55.0	225.8	8.1	61.0	226.7	2.8
	K1	18.8	277.8	19.1	284.9	2.4	20.5	281.1	2.0
	O1	8.2	264.2	7.9	267.3	0.5	8.3	263.7	0.1
	σ_s					17.2			6.7
Chandpur (90.6385°E, 23.2344°N)	M2	29.7	31.4	33.6	333.7	30.7	34.5	355.9	20.1
	S2	10.5	62.3	11.2	6.4	10.2	11.2	29.7	6.1
	K1	5.6	28.6	5.4	21.9	0.7	7.1	24.0	1.6
	O1	3.4	12.9	3.6	357.4	1	4.5	1.18	1.4
	σ_s					22.9			14.9

Additionally, the embankments may restrict the sediments pathways, infilling the channels, inducing land subsidence inside the polders and subsequently increasing the flooding hazard (Auerbach et al., 2015; Wilson et al., 2017). We also saw that in embanked regions of the delta, the tide amplifies with sea level rise. A similar amplification of water level could occur during storm surges too (Huguet, Bertin, & Arnaud, 2018). These interconnected mechanisms are still open-ended questions, however with broad implications for structuring the future management of the delta.

The Sundarbans mangrove forest sits over the central part of the shoreline. Its impact on

the modulation of water level, particularly on storm surges, remains relatively unknown (Deb & Ferreira, 2017). It is hypothesized that the damage from the cyclones that made landfall there is significantly reduced due to the attenuation of the surges by this large, dense, rough mangrove forest. The bathymetry, topography and roughness of the dense channel network are all missing pieces in this puzzle. Recent atlases of spaceborne vegetation thickness may be useful in refining roughness there (e.g., Global Mangrove Distribution, Aboveground Biomass, and Canopy Height, (Simard et al., 2019)). Moreover, these mangroves are also expected to change the wind direction and intensity, which is generally not considered during hydrodynamic modelling. The mangroves are under threat from human invasion and rapid deforestation. The assessment of ecosystem services of these natural systems comprising their hydrodynamical function, both in current and future sea level can provide a significant incentive on the governments effort to protect these.

7.4.4 Storm surge flooding mechanisms

As noted earlier, the ensemble approach can significantly help in the understanding of tide-surge interaction, and particularly the contribution of waves in flooding dynamics. The coupled tide-surge-wave modelling frameworks still suffer from limitations in resolutions (Gu erin et al., 2018; Lavaud et al., 2020). It is particularly so for our model grid over the nearshore region, where tens of meters resolution are ideal (Gu erin et al., 2018). Generation of infragravity waves during cyclonic storms in the Bengal delta region has been hypothesized but not yet evidenced. For example, during cyclone Sidr, large bore-like waves were reported by local witnesses during post-cyclone survey (Shibayama et al., 2008), which are yet to be confirmed and assessed from dedicated modelling.

Recent investigations of the nearshore waves breaking suggest that over flat seabeds the default parameterization for wave breaking is not correct and can cause an underestimation of the wave setup estimation by a factor of two (Pezerat et al., Accepted). In the current experiment setup, I used a reduced value for the breaking coefficient (0.1 instead of 1) to account for this potential error. A new adaptive formulation of the breaking coefficient has emerged (Pezerat et al., Accepted). The default parameterization appears to have a substantial underestimation of the flooding during cyclone Sidr (Figure 7.2) compared to reduced breaking coefficient or the adaptive method of Pezerat et al. (Accepted).

To further assess these parameterizations, so as to further improve the overall modelling of sea states, we recently conducted a dedicated near-shore sub-tidal bathymetry survey, and bottom-pressure moorings were deployed over the location of the large surge of cyclone Sidr shown in Figure 7.2. The bottom pressure recorders have been running for more than a year and are expected to have recorded the recent cyclone Amphan (presented in Chapter 5). Once these observations are recovered, it will allow the calibration of spectral wave models for the very low bed-slope conditions seen over the Bengal delta coastline. Once calibrated, it will allow, for the first time, a more reliable estimate of sea state, wave setup as well as assessment of the infragravity waves generation along this coastline. Additionally, recent estimate of directional wind and wave fields from spaceborne rotating scatterometer (e.g., CFOSAT) are also expected to provide useful publicly available information (J. Liu et al., 2020).

For further investigation of inland flooding, the contribution of rainfall is also of potential

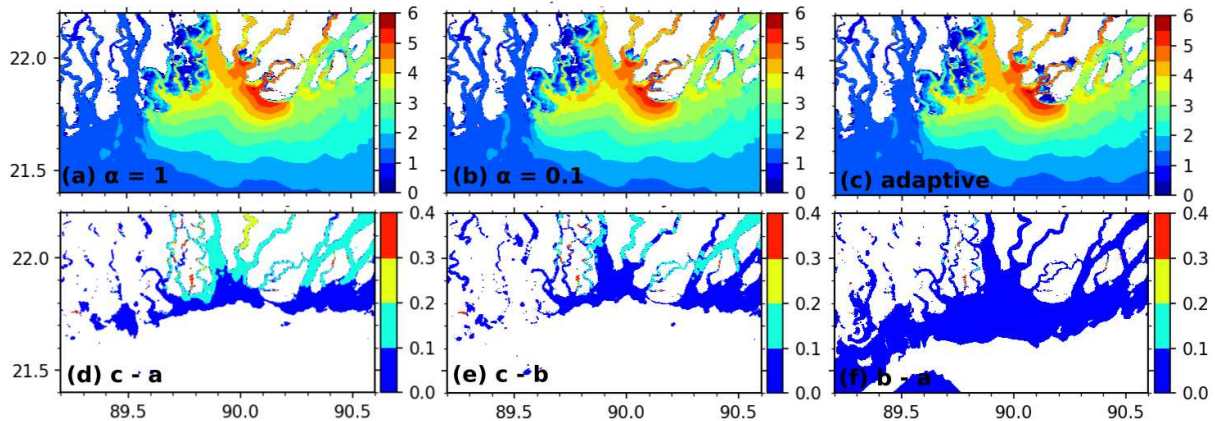


Figure 7.2: Maximum modelled water level during cyclone Sidr with (a) default wave breaking parameterization ($\alpha=1$), (b) the parameterization used in this study ($\alpha=0.1$), and (c) adaptive parameterization proposed by (Pezerat et al., Accepted). (d) and (e) shows the maximum water level difference between adaptive and $\alpha = 1$ and $\alpha = 0.1$ respectively. (f) shows the maximum water level difference between $\alpha = 0.1$ and $\alpha = 1$.

interest. During cyclones, Bengal delta also receives a large volume of rainfall. This rainfall can introduce local waterlogging, particularly inside a closed system like the polders. How much this cyclonic rainfall contribute to inland flooding in the coastal region is mostly unknown. SCHISM is capable of accounting for precipitation flux in the hydrodynamics. This flexibility allows extending the storm surge model further, even in conjunction with the 3D configuration to study the resulting compound flooding phenomenon (Ye et al., 2020).

7.4.5 Future storm surge hazard

Global warming and associated sea level rise pose a significant threat to this vast low-lying community of more than 150 million people (Oppenheimer et al., 2019). Sea level rise combined with land subsidence will shape the future exposure to inundation in the course of 21st century and beyond. Under sea level rise, how the tide and waves will shape the human-influenced shorelines is mostly unknown. Sea level rise, upstream tidal amplification, combined with riverine floods, can aggravate the inundation in the delta. The inundation from storm surges is expected to aggravate under sea level rise conditions, which is yet to be quantified. The statistical-deterministic approach we used in Chapter 6 may prove a well-formulated tool to pave the way for such future endeavours. One example of such an approach is shown in Figure 7.3, with the same 50-year return period water level as shown in Figure 6.5 of Chapter 6 but in a context of sea level 1 m higher than today. It was estimated from the same ensemble of 3600 cyclones, through systematic simulations of the ensemble with our hydrodynamic model. It is seen that the area subject to flooding hazard changes vastly compared to the current situation. The sensitivity of the flooding hazard under other sea level scenarios (0.5 m, 1.5 m, and 2 m) is currently under analysis.

Beyond sea level rise, global warming poses another question in terms of changes in the characteristics of future storms. The long-term changes in the characteristics and properties of cyclonic storms generation and intensification in the Bay of Bengal under global warming re-

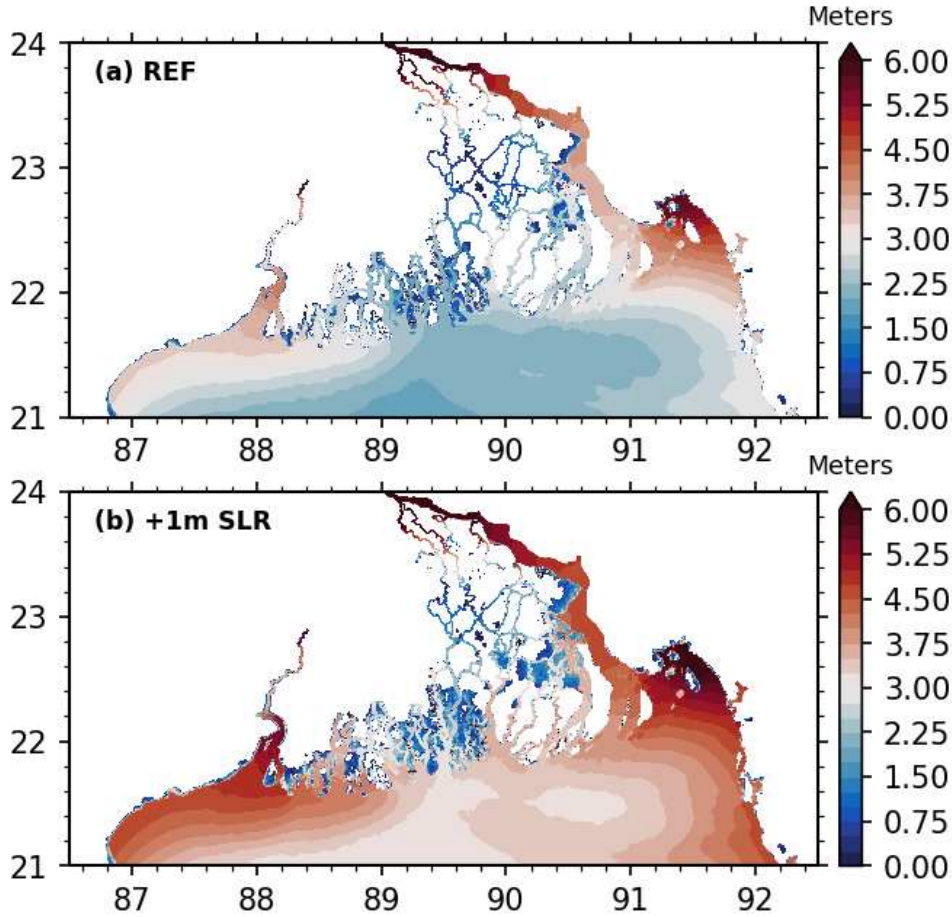


Figure 7.3: 50-year return period water level obtained from the statistical-deterministic analysis of our large ensemble of simulations for (a) current mean sea level conditions and (b) in a 1 m sea level rise scenario (+1m SLR).

mains controversial. Global-scale studies on this topic suggest opposite trends (Emanuel, 2013; Gettelman et al., 2017; Knutson et al., 2020). Sensitivity experiments based on past cyclones in the Bay of Bengal suggest that an increase in sea surface temperature could greatly intensify the magnitude and frequency of intense cyclones (Tasnim et al., 2014). Any increase in intense cyclones intensity and count combined with sea level rise is expected to impact the coastal region of the Bengal delta significantly. Future research is needed in this regard to understand the storms dynamics and the flooding hazard it imposes. The aforementioned analysis of ensemble cyclones under SLR scenarios however provides a way forward to statistically analyse the sensitivity of change in cyclone distribution. For example, one could think of utilizing subsets of our large ensembles of explicit surges simulations, varying the relative distribution of the cyclone category and selectively sampling from the large ensemble to assess how the exposure to flooding changes with such hypothetical changes in the cyclone intensity distribution.

7.4.6 Relative sea level rise

As in several other tropical deltas, land subsidence and relative sea level rise is a major issue over the Bengal delta (Becker, Karpytchev, & Papa, 2019; Brown & Nicholls, 2015). In our

general understanding, subsidence of a delta plain enhances the vulnerability of its inhabitants to flooding and waterlogging (Becker et al., 2020). The diverse physical processes that induce subsidence can be of natural or anthropogenic origin. From the natural origin, the involved processes include glacial or sedimentary isostatic adjustment, tectonics, and/or sediment compaction (Krien et al., 2019). On the other hand, human-induced processes include land use, groundwater extraction, and constrained sediment transport (Syvitski et al., 2009). The most recent estimated regional rate of land subsidence ranges from 1 to 7 mm/year (Becker et al., 2020), making it commensurate with the rate of eustatic sea level rise. However, locally the subsidence rate can be much different from the regional rate (Auerbach et al., 2015). It is particularly true for the embanked polders of the southern Bengal delta. Reportedly, some polders are subsiding while the outside of the polder is gaining height (Auerbach et al., 2015). These regional and local-scale mechanisms indeed need further investigation to understand the inundation dynamics over the Bengal delta and its evolution in the course of the next decades.

7.4.7 Other relevant environmental processes

Annually about 1 Gt sediment is discharged through GBM (Goodbred & Kuehl, 1999). Recent estimates extrapolate it to half Gt, but with a large error bar (M. Rahman et al., 2018). The pathway of the distribution of this massive sediment discharge is relatively unresolved. While the common understanding is that the major sediment distribution path is through the GBM river system, far away region like Sundarbans mangrove forest is reportedly gaining sediments (Bomer et al., 2020). Widespread infilling of the distributary channels is also observed (Wilson et al., 2017). Large-scale observation and modelling studies may reveal relevant information regarding morpho- and sediment dynamics. Understanding of these dynamics is of particular importance as the sediment distribution mechanisms dictate the morphodynamics, which in turns modulates the inundation. It is also of much importance to device future management policies of subsiding deltas like Bengal delta (Ouillon, 2018).

The morphodynamics of the Bengal delta, particularly along the GBM rivers and estuary, is another area of knowledge gap. From the analysis of Sentinel-2 imagery, we observed a strong temporal variation of intertidal morphology around the Meghna estuary. The associated erosion processes are putting the coastal community at risk by damaging coastal buffers and embankments. On the other hand, due to population pressure, people are moving to newly accreted lands, which increases the exposure of these people to the flooding hazard. The monitoring and understanding of the morphodynamics is obviously necessary to manage land use, as well as, natural or man-made coastal protection systems. These research directions perhaps will benefit from the better understanding of continuum hydrodynamics and associated modelling that were pursued here.

7.5 Transferrable lessons and concluding remarks

Inundation mechanisms in the Bengal delta result in a complex interaction between hydrodynamic factors like the tide, surges, waves, river discharges and topographic processes like erosion-accretion and subsidence. Combined with human modifications (e.g., embankments, polders), the flooding process integrates diverse sources. The findings of this research underline

this complexity and illustrate the importance of joint observations and modelling techniques to study such complex interdependent systems – particularly from the viewpoint of hydrodynamics.

This thesis is solely focused on the flooding mechanisms of Bengal delta at a regional scale. The knowledge obtained from this thesis can be transferred in two ways – inward to local scale and outward to other deltas. From the presented analyses and modelling experiments, it is clear that there is a broad diversity of flooding mechanisms at local scale inside the delta. The modelling methodologies developed here can be focused on a particular region with localized inundation issues in mind. On the other hand, the deltas around the world coastlines share all or some of the hydrodynamic forcing factors. For example, in the Bay of Bengal itself, the Irrawaddy delta in Myanmar and the Mahanadi Delta in India are two such examples of similar deltaic environments. The Mekong delta in the South China Sea is another example of the large low-lying tropical deltas with exposure to storm-surge in a fluvio-tidal environment. Similarly, the methodologies can be transferred to deltas like Niger which is impacted by vigorous wave activity, or Amazon where the continental flow is the primary source of water level variability and associated inundation.

Finally, many deltas are densely populated, heavily managed, and going through both natural and anthropogenic changes. The flooding mechanisms in these deltas are diverse across broad ranges of spatial and temporal scales. Therefore, understanding of the inundation events and their future evolutions in the deltas requires the understanding of the associated mechanisms and managements at both regional and local scales.

BIBLIOGRAPHY

- Adnan, M. S. G., Haque, A., & Hall, J. W. (2019). Have coastal embankments reduced flooding in bangladesh? *Science of The Total Environment*, *682*, 405–416. <https://doi.org/10.1016/j.scitotenv.2019.05.048> (cit. on pp. 95, 122, 124)
- Alam, E., & Dominey-Howes, D. (2014). A new catalogue of tropical cyclones of the northern bay of bengal and the distribution and effects of selected landfalling events in bangladesh. *International Journal of Climatology*, *35*(6), 801–835. <https://doi.org/10.1002/joc.4035> (cit. on pp. 1, 2, 6–8, 71, 72, 94, 104)
- Ali, A. (1996). Vulnerability of bangladesh to climate change and sea level rise through tropical cyclones and storm surges. *Climate change vulnerability and adaptation in asia and the pacific* (pp. 171–179). Springer Netherlands. https://doi.org/10.1007/978-94-017-1053-4_16. (Cit. on pp. 1, 7, 110)
- Ali, A. (1999). Climate change impacts and adaptation assessment in bangladesh. *Climate Research*, *12*, 109–116. <https://doi.org/10.3354/cr012109> (cit. on pp. 2, 7, 30, 71, 94)
- Allain, D. J. (2016). TUGOm tidal toolbox. <ftp://ftp.%20legos.%20obs>. (Cit. on pp. 25, 42, 55, 90)
- Almar, R., Bergsma, E. W., Gawehn, M., Aarninkhof, S., & Benschila, R. (2020). High-frequency temporal wave-pattern reconstruction from a few satellite images: A new method towards estimating regional bathymetry. *Journal of Coastal Research*, *95*(sp1), 996. <https://doi.org/10.2112/si95-194.1> (cit. on p. 120)
- Andersen, O. B., Woodworth, P. L., & Flather, R. A. (1995). Intercomparison of recent ocean tide models. *Journal of Geophysical Research*, *100*(C12), 25261. <https://doi.org/10.1029/95jc02642> (cit. on p. 25)
- Anthony, E. J., Brunier, G., Besset, M., Goichot, M., Dussouillez, P., & Nguyen, V. L. (2015). Linking rapid erosion of the mekong river delta to human activities. *Scientific Reports*, *5*(1). <https://doi.org/10.1038/srep14745> (cit. on p. 3)
- Antony, C., & Unnikrishnan, A. (2013). Observed characteristics of tide-surge interaction along the east coast of india and the head of bay of bengal. *Estuarine, Coastal and Shelf Science*, *131*, 6–11. <https://doi.org/10.1016/j.ecss.2013.08.004> (cit. on pp. 19, 75, 97)
- Antony, C., Unnikrishnan, A., & Woodworth, P. L. (2016). Evolution of extreme high waters along the east coast of india and at the head of the bay of bengal. *Global and Planetary Change*, *140*, 59–67. <https://doi.org/10.1016/j.gloplacha.2016.03.008> (cit. on pp. 1, 6, 13, 19, 95, 96)
- Ardhuin, F., Rogers, E., Babanin, A. V., Filipot, J.-F., Magne, R., Roland, A., van der Westhuysen, A., Queffelec, P., Lefevre, J.-M., Aouf, L., & Collard, F. (2010). Semiempirical dissipation source functions for ocean waves. part i: Definition, calibration, and validation. *Journal of Physical Oceanography*, *40*(9), 1917–1941. <https://doi.org/10.1175/2010jpo4324.1> (cit. on pp. 78, 101)
- As-Salek, J. A., & Yasuda, T. (2001). Tide–surge interaction in the meghna estuary: Most severe conditions. *Journal of Physical Oceanography*, *31*(10), 3059–3072. [https://doi.org/10.1175/1520-0485\(2001\)031<3059:tsitm>2.0.co;2](https://doi.org/10.1175/1520-0485(2001)031<3059:tsitm>2.0.co;2) (cit. on pp. 19, 74, 75, 85)
- Athanasiou, P., van Dongeren, A., Giardino, A., Vousdoukas, M., Gaytan-Aguilar, S., & Ranasinghe, R. (2019). Global distribution of nearshore slopes with implications for coastal

- retreat. *Earth System Science Data*, 11(4), 1515–1529. <https://doi.org/10.5194/essd-11-1515-2019> (cit. on p. 48)
- Auerbach, L. W., Jr, S. L. G., Mondal, D. R., Wilson, C. A., Ahmed, K. R., Roy, K., Steckler, M. S., Small, C., Gilligan, J. M., & Ackerly, B. A. (2015). Flood risk of natural and embanked landscapes on the ganges–brahmaputra tidal delta plain. *Nature Climate Change*, 5(2), 153–157. <https://doi.org/10.1038/nclimate2472> (cit. on pp. 9, 13, 51, 59, 75, 88, 125, 129)
- Bacmeister, J. T., Reed, K. A., Hannay, C., Lawrence, P., Bates, S., Truesdale, J. E., Rosenbloom, N., & Levy, M. (2016). Projected changes in tropical cyclone activity under future warming scenarios using a high-resolution climate model. *Climatic Change*, 146(3-4), 547–560. <https://doi.org/10.1007/s10584-016-1750-x> (cit. on p. 9)
- Bamber, J. L., Oppenheimer, M., Kopp, R. E., Aspinall, W. P., & Cooke, R. M. (2019). Ice sheet contributions to future sea-level rise from structured expert judgment. *Proceedings of the National Academy of Sciences*, 116(23), 11195–11200. <https://doi.org/10.1073/pnas.1817205116> (cit. on p. 50)
- Battjes, J. A., & Janssen, J. P. F. M. (1978). Energy loss and set-up due to breaking of random waves. <https://doi.org/10.1061/9780872621909.034> (cit. on pp. 21, 78, 101)
- Becker, M., Karpytchev, M., & Papa, F. (2019). Hotspots of relative sea level rise in the tropics. *Tropical extremes* (pp. 203–262). Elsevier. <https://doi.org/10.1016/b978-0-12-809248-4.00007-8>. (Cit. on pp. 1–3, 9, 128)
- Becker, M., Papa, F., Karpytchev, M., Delebecque, C., Krien, Y., Khan, J. U., Ballu, V., Durand, F., Cozannet, G. L., Islam, A. K. M. S., Calmant, S., & Shum, C. K. (2020). Water level changes, subsidence, and sea level rise in the ganges–brahmaputra–meghna delta. *Proceedings of the National Academy of Sciences*, 201912921. <https://doi.org/10.1073/pnas.1912921117> (cit. on pp. 1, 3, 8, 13, 50, 51, 94–96, 122, 123, 129)
- Benshila, R., Durand, F., Masson, S., Bourdallé-Badie, R., de Boyer Montégut, C., Papa, F., & Madec, G. (2014). The upper bay of bengal salinity structure in a high-resolution model. *Ocean Modelling*, 74, 36–52. <https://doi.org/10.1016/j.ocemod.2013.12.001> (cit. on pp. 53, 123)
- Bergmann, M., Durand, F., Krien, Y., Khan, M. J. U., Ishaque, M., Testut, L., Calmant, S., Maisongrande, P., Islam, A. S., Papa, F., & Ouillon, S. (2018). Topography of the intertidal zone along the shoreline of chittagong (bangladesh) using PROBA-v imagery. *International Journal of Remote Sensing*, 1–21. <https://doi.org/10.1080/01431161.2018.1504341> (cit. on pp. 27, 30, 32, 35, 37, 40, 43, 45)
- Bernier, N. B., & Thompson, K. R. (2015). Deterministic and ensemble storm surge prediction for atlantic canada with lead times of hours to ten days. *Ocean Modelling*, 86, 114–127. <https://doi.org/10.1016/j.ocemod.2014.12.002> (cit. on p. 73)
- Bertin, X., Li, K., Roland, A., & Bidlot, J.-R. (2015). The contribution of short-waves in storm surges: Two case studies in the bay of biscay. *Continental Shelf Research*, 96, 1–15. <https://doi.org/10.1016/j.csr.2015.01.005> (cit. on pp. 81, 83)
- Bertin, X., Li, K., Roland, A., Zhang, Y. J., Breilh, J. F., & Chaumillon, E. (2014). A modeling-based analysis of the flooding associated with xynthia, central bay of biscay. *Coastal Engineering*, 94, 80–89. <https://doi.org/10.1016/j.coastaleng.2014.08.013> (cit. on pp. 40, 54, 77, 81)
- Bhardwaj, P., & Singh, O. (2019). Climatological characteristics of bay of bengal tropical cyclones: 1972–2017. *Theoretical and Applied Climatology*, 139(1-2), 615–629. <https://doi.org/10.1007/s00704-019-02989-4> (cit. on p. 71)
- Bianchi, T. S. (2016). *Deltas and humans: A long relationship now threatened by global change*. Oxford University Press. (Cit. on p. 2).
- Bidlot, J. (2012). Present status of wave forecasting at ecmwf. *Workshop on ocean waves*, 25–27 (cit. on p. 21).

- Bidlot, J., Janssen, P., Abdalla, S., & Hersbach, H. (2007). *A revised formulation of ocean wave dissipation and its model impact*. ECMWF Reading, UK. (Cit. on p. 21).
- Birol, F., Fuller, N., Lyard, F., Cancet, M., Niño, F., Delebecque, C., Fleury, S., Toubanc, F., Melet, A., Saraceno, M., & Léger, F. (2017). Coastal applications from nadir altimetry: Example of the x-TRACK regional products. *Advances in Space Research*, 59(4), 936–953. <https://doi.org/10.1016/j.asr.2016.11.005> (cit. on p. 27)
- Bishop-Taylor, R., Sagar, S., Lymburner, L., & Beaman, R. J. (2019). Between the tides: Modelling the elevation of australia’s exposed intertidal zone at continental scale. *Estuarine, Coastal and Shelf Science*, 223, 115–128. <https://doi.org/10.1016/j.ecss.2019.03.006> (cit. on pp. 29, 45)
- Bomer, E. J., Wilson, C. A., Hale, R. P., Hossain, A. N. M., & Rahman, F. A. (2020). Surface elevation and sedimentation dynamics in the ganges-brahmaputra tidal delta plain, bangladesh: Evidence for mangrove adaptation to human-induced tidal amplification. *CATENA*, 187, 104312. <https://doi.org/10.1016/j.catena.2019.104312> (cit. on pp. 51, 59, 129)
- Bouwer, L. M., & Jonkman, S. N. (2018). Global mortality from storm surges is decreasing. *Environmental Research Letters*, 13(1), 014008. <https://doi.org/10.1088/1748-9326/aa98a3> (cit. on p. 71)
- Brammer, H. (1990). Floods in bangladesh: Geographical background to the 1987 and 1988 floods. *The Geographical Journal*, 156(1), 12. <https://doi.org/10.2307/635431> (cit. on pp. 1, 4–6, 13)
- Brammer, H. (2014). Bangladesh’s dynamic coastal regions and sea-level rise. *Climate Risk Management*, 1, 51–62. <https://doi.org/10.1016/j.crm.2013.10.001> (cit. on p. 13)
- Brammer, H. (2016). Floods, cyclones, drought and climate change in bangladesh: A reality check. *International Journal of Environmental Studies*, 73(6), 865–886. <https://doi.org/10.1080/00207233.2016.1220713> (cit. on p. 6)
- Brown, S., & Nicholls, R. (2015). Subsidence and human influences in mega deltas: The case of the ganges–brahmaputra–meghna. *Science of The Total Environment*, 527–528, 362–374. <https://doi.org/10.1016/j.scitotenv.2015.04.124> (cit. on p. 128)
- Bunya, S., Dietrich, J. C., Westerink, J. J., Ebersole, B. A., Smith, J. M., Atkinson, J. H., Jensen, R., Resio, D. T., Luettich, R. A., Dawson, C., Cardone, V. J., Cox, A. T., Powell, M. D., Westerink, H. J., & Roberts, H. J. (2010). A high-resolution coupled riverine flow, tide, wind, wind wave, and storm surge model for southern louisiana and mississippi. part i: Model development and validation. *Monthly Weather Review*, 138(2), 345–377. <https://doi.org/10.1175/2009mwr2906.1> (cit. on pp. 20, 23, 100)
- Carrère, L., Lyard, F., Cancet, M., Guillot, A., & Roblou, L. (2013). FES 2012: A new global tidal model taking advantage of nearly 20 years of altimetry. *20 Years of Progress in Radar Altimetry*, 710 (cit. on pp. 22, 27, 42, 55, 78).
- Center For International Earth Science Information Network-CIESIN-Columbia University. (2016). Documentation for gridded population of the world, version 4 (gpwv4). <https://doi.org/10.7927/H4D50JX4>. (Cit. on pp. 31, 112)
- Chen, J., & Mueller, V. (2018). Coastal climate change, soil salinity and human migration in bangladesh. *Nature Climate Change*, 8(11), 981–985. <https://doi.org/10.1038/s41558-018-0313-8> (cit. on p. 124)
- Chittibabu, P., Dube, S. K., Macnabb, J. B., Murty, T. S., Rao, A. D., Mohanty, U. C., & Sinha, P. C. (2004). Mitigation of flooding and cyclone hazard in orissa, india. *Natural Hazards*, 31(2), 455–485. <https://doi.org/10.1023/b:nhaz.0000023362.26409.22> (cit. on pp. 96–98)
- Chiu, S., & Small, C. (2016). Observations of cyclone-induced storm surge in coastal bangladesh. *Journal of Coastal Research*, 321, 1149–1161. <https://doi.org/10.2112/jcoastres-d-15-00030.1> (cit. on pp. 1, 6, 13, 96)

- Chowdhury, J. U., Watkins, D. W., Rahman, M. R., & Karim, M. F. (1998). Models for cyclone shelter planning in bangladesh. *Water International*, 23(3), 155–163. <https://doi.org/10.1080/02508069808686762> (cit. on pp. 95–97)
- Chowdhury, M. A. M., & Al Rahim, M. (2012). A proposal on new scheduling of turbine discharge at kaptai hydro-electric power plant to avoid the wastage of water due to overflow in the dam. *2012 7th International Conference on Electrical and Computer Engineering*, 758–762 (cit. on pp. 23, 42, 55, 105).
- Church, J. A., Clark, P. U., Cazenave, A., Gregory, J. M., Jevrejeva, S., Levermann, A., Merrifield, M. A., Milne, G. A., Nerem, R. S., Nunn, P. D., Payne, A. J., Pfeffer, W. T., Stammer, D., & Unnikrishnan, A. S. (2013). Sea level change. *Climate change 2013: The physical science basis. contribution of working group i to the fifth assessment report of the intergovernmental panel on climate change*. (Cit. on p. 50).
- Condon, A. J., Sheng, Y. P., & Paramygin, V. A. (2013). Toward high-resolution, rapid, probabilistic forecasting of the inundation threat from landfalling hurricanes. *Monthly Weather Review*, 141(4), 1304–1323. <https://doi.org/10.1175/mwr-d-12-00149.1> (cit. on p. 73)
- Dangendorf, S., Marcos, M., Wöppelmann, G., Conrad, C. P., Frederikse, T., & Riva, R. (2017). Reassessment of 20th century global mean sea level rise. *Proceedings of the National Academy of Sciences*, 114(23), 5946–5951. <https://doi.org/10.1073/pnas.1616007114> (cit. on p. 50)
- Daniel, P., Haie, B., & Aubail, X. (2009). Operational forecasting of tropical cyclones storm surges at meteo-france. *Marine Geodesy*, 32(2), 233–242. <https://doi.org/10.1080/01490410902869649> (cit. on p. 73)
- Das, M. K., Islam, A. K. M. S., Karmakar, S., Khan, M. J. U., Mohammed, K., Islam, G. M. T., Bala, S. K., & Hopson, T. M. (2019). Synoptic flow patterns and large-scale characteristics of flash flood-producing rainstorms over northeast bangladesh. *Meteorology and Atmospheric Physics*. <https://doi.org/10.1007/s00703-019-00709-1> (cit. on p. 5)
- Das, P. K. (1972). Prediction model for storm surges in the bay of bengal. *Nature*, 239(5369), 211–213. <https://doi.org/10.1038/239211a0> (cit. on p. 73)
- Deb, M., & Ferreira, C. (2016). Simulation of cyclone-induced storm surges in the low-lying delta of bangladesh using coupled hydrodynamic and wave model (SWAN + ADCIRC). *Journal of Flood Risk Management*, 11, S750–S765. <https://doi.org/10.1111/jfr3.12254> (cit. on pp. 74, 85)
- Deb, M., & Ferreira, C. M. (2017). Potential impacts of the sunderban mangrove degradation on future coastal flooding in bangladesh. *Journal of Hydro-environment Research*, 17, 30–46. <https://doi.org/10.1016/j.jher.2016.11.005> (cit. on p. 126)
- Dominicis, M. D., Wolf, J., Jevrejeva, S., Zheng, P., & Hu, Z. (2020). Future interactions between sea level rise, tides, and storm surges in the world’s largest urban area. *Geophysical Research Letters*, 47(4), nil. <https://doi.org/10.1029/2020gl087002> (cit. on pp. 50, 59)
- Dronkers, J. J. (1964). *Tidal computations in rivers and coastal waters*. North-holland publishing company Amsterdam. (Cit. on p. 63).
- Du, J., Shen, J., Zhang, Y. J., Ye, F., Liu, Z., Wang, Z., Wang, Y. P., Yu, X., Sisson, M., & Wang, H. V. (2018). Tidal response to sea-level rise in different types of estuaries: The importance of length, bathymetry, and geometry. *Geophysical Research Letters*, 45(1), 227–235. <https://doi.org/10.1002/2017gl075963> (cit. on pp. 63–65)
- Dube, S. K., Chittibabu, P., Sinha, P. C., Rao, A. D., & Murty, T. S. (2004). Numerical modelling of storm surge in the head bay of bengal using location specific model. *Natural Hazards*, 31(2), 437–453. <https://doi.org/10.1023/b:nhaz.0000023361.94609.4a> (cit. on pp. 73, 87)
- Dube, S. K., Jain, I., Rao, A. D., & Murty, T. S. (2009). Storm surge modelling for the bay of bengal and arabian sea. *Natural Hazards*, 51(1), 3–27. <https://doi.org/10.1007/s11069-009-9397-9> (cit. on pp. 73, 74)

- Durand, F., Piecuch, C. G., Becker, M., Papa, F., Raju, S. V., Khan, J. U., & Ponte, R. M. (2019). Impact of continental freshwater runoff on coastal sea level. *Surveys in Geophysics*. <https://doi.org/10.1007/s10712-019-09536-w> (cit. on pp. 42, 75, 123)
- Eakins, B. W., & Grothe, P. R. (2014). Challenges in building coastal digital elevation models. *Journal of Coastal Research*, 297, 942–953. <https://doi.org/10.2112/jcoastres-d-13-00192.1> (cit. on p. 28)
- Edmonds, D. A., Caldwell, R. L., Brondizio, E. S., & Siani, S. M. O. (2020). Coastal flooding will disproportionately impact people on river deltas. *Nature Communications*, 11(1). <https://doi.org/10.1038/s41467-020-18531-4> (cit. on pp. 1–3)
- Egbert, G. D., & Erofeeva, S. Y. (2002). Efficient inverse modeling of barotropic ocean tides. *Journal of Atmospheric and Oceanic Technology*, 19(2), 183–204 (cit. on pp. 55, 78).
- Eldeberky, Y. (1996). *Nonlinear transformation of wave spectra in the nearshore zone* (PhD Thesis). Delft University of Technology, The Netherlands. Delft. (Cit. on p. 21).
- Emanuel, K. (2013). Downscaling CMIP5 climate models shows increased tropical cyclone activity over the 21st century. *Proceedings of the National Academy of Sciences*, 110(30), 12219–12224. <https://doi.org/10.1073/pnas.1301293110> (cit. on pp. 9, 128)
- Emanuel, K. (2005). Increasing destructiveness of tropical cyclones over the past 30 years. *Nature*, 436(7051), 686–688. <https://doi.org/10.1038/nature03906> (cit. on p. 72)
- Emanuel, K., DesAutels, C., Holloway, C., & Korty, R. (2004). Environmental control of tropical cyclone intensity. *Journal of the Atmospheric Sciences*, 61(7), 843–858. [https://doi.org/10.1175/1520-0469\(2004\)061<0843:ecotci>2.0.co;2](https://doi.org/10.1175/1520-0469(2004)061<0843:ecotci>2.0.co;2) (cit. on pp. 24, 104)
- Emanuel, K., Ravela, S., Vivant, E., & Risi, C. (2006). A statistical deterministic approach to hurricane risk assessment. *Bulletin of the American Meteorological Society*, 87(3), 299–314. <https://doi.org/10.1175/bams-87-3-299> (cit. on pp. 11, 98, 103, 104)
- Emanuel, K., & Rotunno, R. (2011). Self-stratification of tropical cyclone outflow. part i: Implications for storm structure. *Journal of the Atmospheric Sciences*, 68(10), 2236–2249. <https://doi.org/10.1175/jas-d-10-05024.1> (cit. on pp. 24, 79, 101, 104)
- Ericson, J., Vorosmarty, C., Dingman, S., Ward, L., & Meybeck, M. (2006). Effective sea-level rise and deltas: Causes of change and human dimension implications. *Global and Planetary Change*, 50(1-2), 63–82. <https://doi.org/10.1016/j.gloplacha.2005.07.004> (cit. on pp. 1–3)
- Esteves, L. S. (2014). *Managed realignment : A viable long-term coastal management strategy?* Springer Netherlands. <https://doi.org/10.1007/978-94-017-9029-1>. (Cit. on p. 67)
- Feng, X., Wan, W., Liu, Q., Yin, B., Yang, D., & Gao, G. (2019). Study of the tide and tidal currents in the bay of bengal based on refined simulations. *Journal of Coastal Research*, 35(1), 33. <https://doi.org/10.2112/jcoastres-d-18-00048.1> (cit. on pp. 59, 60)
- Fernández-Montblanc, T., Vousdoukas, M., Ciavola, P., Voukouvalas, E., Mentaschi, L., Breyianis, G., Feyen, L., & Salamon, P. (2019). Towards robust pan-European storm surge forecasting. *Ocean Modelling*, 133, 129–144. <https://doi.org/10.1016/j.ocemod.2018.12.001> (cit. on pp. 77, 83)
- Flather, R. (1987). A tidal model of the northeast pacific. *Atmosphere-Ocean*, 25(1), 22–45. <https://doi.org/10.1080/07055900.1987.9649262> (cit. on pp. 42, 55)
- Flather, R. (1994). A storm surge prediction model for the northern bay of bengal with application to the cyclone disaster in april 1991. *Journal of Physical Oceanography*, 24(1), 172–190. [https://doi.org/10.1175/1520-0485\(1994\)024<0172:asspmf>2.0.co;2](https://doi.org/10.1175/1520-0485(1994)024<0172:asspmf>2.0.co;2) (cit. on p. 73)
- Flowerdew, J., Mylne, K., Jones, C., & Titley, H. (2012). Extending the forecast range of the UK storm surge ensemble. *Quarterly Journal of the Royal Meteorological Society*, 139(670), 184–197. <https://doi.org/10.1002/qj.1950> (cit. on p. 73)
- Fortunato, A. B., Oliveira, A., Rogeiro, J., Tavares da Costa, R., Gomes, J. L., Li, K., de Jesus, G., Freire, P., Rilo, A., Mendes, A., Rodrigues, M., & Azevedo, A. (2017). Operational

- forecast framework applied to extreme sea levels at regional and local scales. *Journal of Operational Oceanography*, 10(1), 1–15. <https://doi.org/10.1080/1755876X.2016.1255471> (cit. on pp. 81, 89)
- Frank, N. L., & Husain, S. (1971). The deadliest tropical cyclone in history? *Bulletin of the American Meteorological Society*, 52(6), 438–445 (cit. on pp. 7, 72).
- Frazier, P. S., Page, K. J. et al. (2000). Water body detection and delineation with landsat tm data. *Photogrammetric engineering and remote sensing*, 66(12), 1461–1468 (cit. on p. 29).
- Gettelman, A., Bresch, D. N., Chen, C. C., Truesdale, J. E., & Bacmeister, J. T. (2017). Projections of future tropical cyclone damage with a high-resolution global climate model. *Climatic Change*, 146(3-4), 575–585. <https://doi.org/10.1007/s10584-017-1902-7> (cit. on pp. 9, 128)
- Glahn, B., Taylor, A., Kurkowski, N., & Shaffer, W. (2009). The role of the slosh model in national weather service storm surge forecasting. *National Weather Digest*, 33(1), 3–14 (cit. on p. 73).
- Goodbred, S. L., & Kuehl, S. A. (1998). Floodplain processes in the bengal basin and the storage of ganges–brahmaputra river sediment: An accretion study using 137cs and 210pb geochronology. *Sedimentary Geology*, 121(3-4), 239–258. [https://doi.org/10.1016/s0037-0738\(98\)00082-7](https://doi.org/10.1016/s0037-0738(98)00082-7) (cit. on p. 13)
- Goodbred, S. L., & Kuehl, S. A. (1999). Holocene and modern sediment budgets for the ganges–brahmaputra river system: Evidence for highstand dispersal to flood-plain, shelf, and deep-sea depocenters. *Geology*, 27(6), 559. [https://doi.org/10.1130/0091-7613\(1999\)027<0559:hamsbf>2.3.co;2](https://doi.org/10.1130/0091-7613(1999)027<0559:hamsbf>2.3.co;2) (cit. on pp. 5, 13, 51, 129)
- Gregory, J. M., Griffies, S. M., Hughes, C. W., Lowe, J. A., Church, J. A., Fukimori, I., Gomez, N., Kopp, R. E., Landerer, F., Cozannet, G. L., Ponte, R. M., Stammer, D., Tamisiea, M. E., & van de Wal, R. S. W. (2019). Concepts and terminology for sea level: Mean, variability and change, both local and global. *Surveys in Geophysics*, 40(6), 1251–1289. <https://doi.org/10.1007/s10712-019-09525-z> (cit. on p. 52)
- Guérin, T., Bertin, X., Coulombier, T., & de Bakker, A. (2018). Impacts of wave-induced circulation in the surf zone on wave setup. *Ocean Modelling*, 123, 86–97. <https://doi.org/10.1016/j.ocemod.2018.01.006> (cit. on pp. 40, 77, 81, 126)
- Haigh, I. D., MacPherson, L. R., Mason, M. S., Wijeratne, E. M. S., Pattiaratchi, C. B., Crompton, R. P., & George, S. (2013). Estimating present day extreme water level exceedance probabilities around the coastline of australia: Tropical cyclone-induced storm surges. *Climate Dynamics*, 42(1-2), 139–157. <https://doi.org/10.1007/s00382-012-1653-0> (cit. on p. 98)
- Haigh, I. D., Pickering, M. D., Green, J. A. M., Arbic, B. K., Arns, A., Dangendorf, S., Hill, D. F., Horsburgh, K., Howard, T., Idier, D., Jay, D. A., Jänicke, L., Lee, S. B., Müller, M., Schindelegger, M., Talke, S. A., Wilmes, S.-B., & Woodworth, P. L. (2020). The tides they are a-changin’: A comprehensive review of past and future nonastronomical changes in tides, their driving mechanisms, and future implications. *Reviews of Geophysics*, 58(1). <https://doi.org/10.1029/2018rg000636> (cit. on pp. 51, 52)
- Hallegatte, S., Green, C., Nicholls, R. J., & Corfee-Morlot, J. (2013). Future flood losses in major coastal cities. *Nature Climate Change*, 3(9), 802–806. <https://doi.org/10.1038/nclimate1979> (cit. on p. 28)
- Hasselmann, K., Barnett, T., Bouws, E., Carlson, H., Cartwright, D., Enke, K., Ewing, J., Gienapp, H., Hasselmann, D., Kruseman, P., et al. (1973). Measurements of wind-wave growth and swell decay during the joint north sea wave project (jonswap). *Ergänzungsheft 8-12* (cit. on p. 21).
- Hasselmann, S., Hasselmann, K., Allender, J. H., & Barnett, T. P. (1985). Computations and parameterizations of the nonlinear energy transfer in a gravity-wave spectrum. part II:

- Parameterizations of the nonlinear energy transfer for application in wave models. *Journal of Physical Oceanography*, 15(11), 1378–1391. [https://doi.org/10.1175/1520-0485\(1985\)015<1378:capotn>2.0.co;2](https://doi.org/10.1175/1520-0485(1985)015<1378:capotn>2.0.co;2) (cit. on p. 21)
- Heygster, G., Dannenberg, J., & Notholt, J. (2010). Topographic mapping of the german tidal flats analyzing SAR images with the waterline method. *IEEE Transactions on Geoscience and Remote Sensing*, 48(3), 1019–1030. <https://doi.org/10.1109/tgrs.2009.2031843> (cit. on p. 29)
- Hipel, K. W., & McLeod, A. I. (1994). *Time series modelling of water resources and environmental systems*. Elsevier. (Cit. on p. 53).
- Hirsch, R. M., Slack, J. R., & Smith, R. A. (1982). Techniques of trend analysis for monthly water quality data. *Water Resources Research*, 18(1), 107–121. <https://doi.org/10.1029/wr018i001p00107> (cit. on p. 53)
- Holland, G. J. (1980). An analytic model of the wind and pressure profiles in hurricanes. *Monthly Weather Review*, 108(8), 1212–1218. [https://doi.org/10.1175/1520-0493\(1980\)108<1212:aamotw>2.0.co;2](https://doi.org/10.1175/1520-0493(1980)108<1212:aamotw>2.0.co;2) (cit. on pp. 24, 79, 101, 104)
- Holleman, R. C., & Stacey, M. T. (2014). Coupling of sea level rise, tidal amplification, and inundation. *Journal of Physical Oceanography*, 44(5), 1439–1455. <https://doi.org/10.1175/jpo-d-13-0214.1> (cit. on p. 66)
- Hoornweg, D., & Pope, K. (2017). Population predictions for the world’s largest cities in the 21st century. *Environment and Urbanization*, 29(1), 195–216. <https://doi.org/10.1177/0956247816663557> (cit. on p. 67)
- Huguet, J.-R., Bertin, X., & Arnaud, G. (2018). Managed realignment to mitigate storm-induced flooding: A case study in la faute-sur-mer, france. *Coastal Engineering*, 134, 168–176. <https://doi.org/10.1016/j.coastaleng.2017.08.010> (cit. on p. 125)
- Hussain, M., Tajima, Y., Hossain, M., & Das, P. (2017). Impact of cyclone track features and tidal phase shift upon surge characteristics in the bay of bengal along the bangladesh coast. *Journal of Marine Science and Engineering*, 5(4), 52. <https://doi.org/10.3390/jmse5040052> (cit. on pp. 97, 98, 101)
- Ibáñez, C., Alcaraz, C., Caiola, N., Prado, P., Trobajo, R., Benito, X., Day, J., Reyes, E., & Syvitski, J. (2019). Basin-scale land use impacts on world deltas: Human vs natural forcings. *Global and Planetary Change*, 173, 24–32. <https://doi.org/10.1016/j.gloplacha.2018.12.003> (cit. on p. 2)
- Idier, D., Bertin, X., Thompson, P., & Pickering, M. D. (2019). Interactions between mean sea level, tide, surge, waves and flooding: Mechanisms and contributions to sea level variations at the coast. *Surveys in Geophysics*, 40(6), 1603–1630. <https://doi.org/10.1007/s10712-019-09549-5> (cit. on pp. 20, 51, 67, 75, 122)
- Idier, D., Paris, F., Cozannet, G. L., Boulahya, F., & Dumas, F. (2017). Sea-level rise impacts on the tides of the European Shelf. *Continental Shelf Research*, 137, 56–71. <https://doi.org/10.1016/j.csr.2017.01.007> (cit. on p. 51)
- IFRC. (2020). Operation Update Report. Retrieved September 10, 2020, from <http://adore.ifrc.org/Download.aspx?FileId=329843>. (Cit. on p. 74)
- Islam, A. S., Bala, S. K., Hussain, M. A., Hossain, M. A., & Rahman, M. M. (2011). Performance of coastal structures during cyclone sidr. *Natural Hazards Review*, 12(3), 111–116. [https://doi.org/10.1061/\(asce\)nh.1527-6996.0000031](https://doi.org/10.1061/(asce)nh.1527-6996.0000031) (cit. on pp. 75, 112)
- Jain, I., Rao, A. D., Jitendra, V., & Dube, S. K. (2010). Computation of expected total water levels along the east coast of india. *Journal of Coastal Research*, 264, 681–687. <https://doi.org/10.2112/08-1170.1> (cit. on pp. 96–98)
- Jain, S. K., Singh, R. D., Jain, M. K., & Lohani, A. K. (2005). Delineation of flood-prone areas using remote sensing techniques. *Water Resources Management*, 19(4), 333–347. <https://doi.org/10.1007/s11269-005-3281-5> (cit. on p. 29)

- Jakobsen, F., Azam, M. H., Ahmed, M. M. Z., & Mahboob-ul-Kabir, M. (2006). Cyclone storm surge levels along the bangladeshi coastline in 1876 and 1960–2000. *Coastal Engineering Journal*, 48(3), 295–307. <https://doi.org/10.1142/s057856340600143x> (cit. on pp. 96, 97, 111)
- Jelesnianski, C. P. (1992). *Slosh: Sea, lake, and overland surges from hurricanes* (Vol. 48). US Department of Commerce, National Oceanic; Atmospheric Administration. (Cit. on p. 24).
- Ji, M., Aikman, F., & Lozano, C. (2009). Toward improved operational surge and inundation forecasts and coastal warnings. *Natural Hazards*, 53(1), 195–203. <https://doi.org/10.1007/s11069-009-9414-z> (cit. on p. 73)
- Jian, J., Webster, P. J., & Hoyos, C. D. (2009). Large-scale controls on ganges and brahmaputra river discharge on intraseasonal and seasonal time-scales. *Quarterly Journal of the Royal Meteorological Society*, 135(639), 353–370. <https://doi.org/10.1002/qj.384> (cit. on p. 23)
- Johns, B., & Ali, M. A. (1980). The numerical modelling of storm surges in the bay of bengal. *Quarterly Journal of the Royal Meteorological Society*, 106(447), 1–18. <https://doi.org/10.1002/qj.49710644702> (cit. on pp. 73, 74, 85)
- Kalnay, E., Kanamitsu, M., Kistler, R., Collins, W., Deaven, D., Gandin, L., Iredell, M., Saha, S., White, G., Woollen, J., Zhu, Y., Leetmaa, A., Reynolds, R., Chelliah, M., Ebisuzaki, W., Higgins, W., Janowiak, J., Mo, K. C., Ropelewski, C., ... Joseph, D. (1996). The NCEP/NCAR 40-year reanalysis project. *Bulletin of the American Meteorological Society*, 77(3), 437–471. [https://doi.org/10.1175/1520-0477\(1996\)077<0437:tnyrp>2.0.co;2](https://doi.org/10.1175/1520-0477(1996)077<0437:tnyrp>2.0.co;2) (cit. on p. 103)
- Kapoor, D. C. (1981). General bathymetric chart of the oceans (GEBCO). *Marine Geodesy*, 5(1), 73–80. <https://doi.org/10.1080/15210608109379408> (cit. on p. 14)
- Kendall, M. G. (1975). *Rank correlation measures*. Charles Griffin. (Cit. on p. 53).
- Kennett, D. J., & Kennett, J. P. (2006). Early state formation in southern mesopotamia: Sea levels, shorelines, and climate change. *The Journal of Island and Coastal Archaeology*, 1(1), 67–99. <https://doi.org/10.1080/15564890600586283> (cit. on p. 2)
- Khalid, A., & Ferreira, C. (2020). Advancing real-time flood prediction in large estuaries: iFLOOD a fully coupled surge-wave automated web-based guidance system. *Environmental Modelling & Software*, 104748. <https://doi.org/10.1016/j.envsoft.2020.104748> (cit. on p. 73)
- Khalil, G. M. (1993). The catastrophic cyclone of april 1991: Its impact on the economy of bangladesh. *Natural Hazards*, 8(3), 263–281. <https://doi.org/10.1007/bf00690911> (cit. on pp. 7, 72)
- Khan, M. J. U., Ansary, M. N., Durand, F., Testut, L., Ishaque, M., Calmant, S., Krien, Y., Islam, A. S., & Papa, F. (2019). High-resolution intertidal topography from sentinel-2 multi-spectral imagery: Synergy between remote sensing and numerical modeling. *Remote Sensing*, 11(24), 2888. <https://doi.org/10.3390/rs11242888> (cit. on pp. 77, 78, 81, 101)
- Khan, M. J. U., Durand, F., Testut, L., Krien, Y., & Islam, A. S. (2020). Sea level rise inducing tidal modulation along the coasts of bengal delta. *Continental Shelf Research*, 211, 104289. <https://doi.org/10.1016/j.csr.2020.104289> (cit. on pp. 94, 101)
- Khan, M. J. U., Islam, A. K. M. S., Bala, S. K., & Islam, G. M. T. (2020). Changes in climate extremes over bangladesh at 1.5 °c, 2 °c, and 4 °c of global warming with high-resolution regional climate modeling. *Theoretical and Applied Climatology*. <https://doi.org/10.1007/s00704-020-03164-w> (cit. on p. 9)
- Khan, M. J. U., Islam, A. S., Das, M. K., Mohammed, K., Bala, S. K., & Islam, G. T. (2019). Observed trends in climate extremes over bangladesh from 1981 to 2010. *Climate Research*, 77(1), 45–61. <https://doi.org/10.3354/cr01539> (cit. on p. 9)

- Knapp, K. R., Diamond, H. J., Kossin, J. P., Kruk, M. C., & Schreck, C. J. (2018). International best track archive for climate stewardship (ibtracs) project, version 4. <https://doi.org/10.25921/82TY-9E16>. (Cit. on p. 7)
- Knutson, T., Camargo, S. J., Chan, J. C. L., Emanuel, K., Ho, C.-H., Kossin, J., Mohapatra, M., Satoh, M., Sugi, M., Walsh, K., & Wu, L. (2020). Tropical cyclones and climate change assessment: Part II: Projected response to anthropogenic warming. *Bulletin of the American Meteorological Society*, *101*(3), E303–E322. <https://doi.org/10.1175/bams-d-18-0194.1> (cit. on p. 128)
- Kossin, J. P., Olander, T. L., & Knapp, K. R. (2013). Trend analysis with a new global record of tropical cyclone intensity. *Journal of Climate*, *26*(24), 9960–9976. <https://doi.org/10.1175/jcli-d-13-00262.1> (cit. on p. 93)
- Krien, Y., Dudon, B., Roger, J., & Zahibo, N. (2015). Probabilistic hurricane-induced storm surge hazard assessment in guadeloupe, lesser antilles. *Natural Hazards and Earth System Science*, *15*(8), 1711–1720. <https://doi.org/10.5194/nhess-15-1711-2015> (cit. on pp. 98, 104)
- Krien, Y., Karpytchev, M., Ballu, V., Becker, M., Grall, C., Goodbred, S., Calmant, S., Shum, C. K., & Khan, Z. (2019). Present-day subsidence in the ganges-brahmaputra-meghna delta: Eastern amplification of the holocene sediment loading contribution. *Geophysical Research Letters*, *46*(19), 10764–10772. <https://doi.org/10.1029/2019gl083601> (cit. on pp. 9, 51, 129)
- Krien, Y., Mayet, C., Testut, L., Durand, F., Tazkia, A. R., Islam, A. K. M. S., Gopalakrishna, V. V., Becker, M., Calmant, S., Shum, C. K., Khan, Z. H., Papa, F., & Ballu, V. (2016). Improved bathymetric dataset and tidal model for the northern bay of bengal. *Marine Geodesy*, *39*(6), 422–438. <https://doi.org/10.1080/01490419.2016.1227405> (cit. on pp. 2, 8–10, 13–16, 18–20, 25, 27, 30, 40–42, 50, 51, 54–58, 65, 73, 74, 77, 91, 94, 98–100, 102)
- Krien, Y., Testut, L., Islam, A., Bertin, X., Durand, F., Mayet, C., Tazkia, A., Becker, M., Calmant, S., Papa, F., Ballu, V., Shum, C., & Khan, Z. (2017). Towards improved storm surge models in the northern bay of bengal. *Continental Shelf Research*, *135*, 58–73. <https://doi.org/10.1016/j.csr.2017.01.014> (cit. on pp. 2, 9, 13, 16, 18–20, 24, 30, 40, 47, 50, 51, 70, 73–75, 79, 85–87, 94, 96–98, 101, 102)
- Krien, Y., Arnaud, G., Cécé, R., Ruf, C., Belmadani, A., Khan, J., Bernard, D., Islam, A., Durand, F., Testut, L., Palany, P., & Zahibo, N. (2018). Can we improve parametric cyclonic wind fields using recent satellite remote sensing data? *Remote Sensing*, *10*(12), 1963. <https://doi.org/10.3390/rs10121963> (cit. on pp. 24, 79, 81, 86, 101)
- Krien, Y., Dudon, B., Roger, J., Arnaud, G., & Zahibo, N. (2017). Assessing storm surge hazard and impact of sea level rise in the lesser antilles case study of martinique. *Natural Hazards and Earth System Sciences*, *17*(9), 1559–1571. <https://doi.org/10.5194/nhess-17-1559-2017> (cit. on pp. 59, 77, 98, 101, 104)
- Kuroda, T., Saito, K., Kunii, M., & Kohno, N. (2010). Numerical simulations of myanmar cyclone nargis and the associated storm surge part i: Forecast experiment with a nonhydrostatic model and simulation of storm surge. *Journal of the Meteorological Society of Japan*, *88*(3), 521–545. <https://doi.org/10.2151/jmsj.2010-315> (cit. on pp. 73, 74)
- Lakshmi, D. D., Murty, P., Bhaskaran, P. K., Sahoo, B., Kumar, T. S., Shenoi, S., & Srikanth, A. (2017). Performance of WRF-ARW winds on computed storm surge using hydrodynamic model for phailin and hudhud cyclones. *Ocean Engineering*, *131*, 135–148. <https://doi.org/10.1016/j.oceaneng.2017.01.005> (cit. on p. 23)
- Lane, E., Walters, R., Gillibrand, P., & Uddstrom, M. (2009). Operational forecasting of sea level height using an unstructured grid ocean model. *Ocean Modelling*, *28*(1-3), 88–96. <https://doi.org/10.1016/j.ocemod.2008.11.004> (cit. on p. 73)

- Lavaud, L., Bertin, X., Martins, K., Arnaud, G., & Bouin, M.-N. (2020). The contribution of short-wave breaking to storm surges: The case klaus in the southern bay of biscay. *Ocean Modelling*, *156*, 101710. <https://doi.org/10.1016/j.ocemod.2020.101710> (cit. on p. 126)
- Lazo, J. K., & Waldman, D. M. (2011). Valuing improved hurricane forecasts. *Economics Letters*, *111*(1), 43–46. <https://doi.org/10.1016/j.econlet.2010.12.012> (cit. on p. 73)
- Lee, H. S. (2013). Estimation of extreme sea levels along the bangladesh coast due to storm surge and sea level rise using EEMD and EVA. *Journal of Geophysical Research: Oceans*, *118*(9), 4273–4285. <https://doi.org/10.1002/jgrc.20310> (cit. on pp. 96, 111)
- Lewis, M., Bates, P., Horsburgh, K., Neal, J., & Schumann, G. (2013). A storm surge inundation model of the northern bay of bengal using publicly available data. *Quarterly Journal of the Royal Meteorological Society*, *139*(671), 358–369. <https://doi.org/10.1002/qj.2040> (cit. on p. 87)
- Lewis, M., Horsburgh, K., & Bates, P. (2014). Bay of bengal cyclone extreme water level estimate uncertainty. *Natural Hazards*, *72*(2), 983–996. <https://doi.org/10.1007/s11069-014-1046-2> (cit. on p. 98)
- Li, Z., Heygster, G., & Notholt, J. (2014). Intertidal topographic maps and morphological changes in the german wadden sea between 1996–1999 and 2006–2009 from the waterline method and SAR images. *IEEE Journal of Selected Topics in Applied Earth Observations and Remote Sensing*, *7*(8), 3210–3224. <https://doi.org/10.1109/jstars.2014.2313062> (cit. on p. 29)
- Lin, N., Emanuel, K. A., Smith, J. A., & Vanmarcke, E. (2010). Risk assessment of hurricane storm surge for new york city. *Journal of Geophysical Research*, *115*(18). <https://doi.org/10.1029/2009jd013630> (cit. on pp. 98, 104)
- Lin, N., & Chavas, D. (2012). On hurricane parametric wind and applications in storm surge modeling. *Journal of Geophysical Research: Atmospheres*, *117*(D9), n/a–n/a. <https://doi.org/10.1029/2011jd017126> (cit. on pp. 23–25, 79, 87, 101)
- Liu, J., Lin, W., Dong, X., Lang, S., Yun, R., Zhu, D., Zhang, K., Sun, C., Mu, B., Ma, J., He, Y., Wang, Z., Li, X., Zhao, X., & Jiang, X. (2020). First results from the rotating fan beam scatterometer onboard CFOSAT. *IEEE Transactions on Geoscience and Remote Sensing*, *58*(12), 8793–8806. <https://doi.org/10.1109/tgrs.2020.2990708> (cit. on p. 126)
- Liu, Y., Huang, H., Qiu, Z., & Fan, J. (2013). Detecting coastline change from satellite images based on beach slope estimation in a tidal flat. *International Journal of Applied Earth Observation and Geoinformation*, *23*, 165–176. <https://doi.org/10.1016/j.jag.2012.12.005> (cit. on p. 29)
- Longuet-Higgins, M., & Stewart, R. (1962). Radiation stresses in water waves: A physical discussion with applications. *Deep Sea Research and Oceanographic Abstracts*, *11*(4), 529–562. [https://doi.org/10.1016/0011-7471\(64\)90001-4](https://doi.org/10.1016/0011-7471(64)90001-4) (cit. on pp. 21, 75, 105)
- Lyard, F., Lefevre, F., Letellier, T., & Francis, O. (2006). Modelling the global ocean tides: Modern insights from FES2004. *Ocean Dynamics*, *56*(5-6), 394–415. <https://doi.org/10.1007/s10236-006-0086-x> (cit. on pp. 19, 96)
- Madsen, H., & Jakobsen, F. (2004). Cyclone induced storm surge and flood forecasting in the northern bay of bengal. *Coastal Engineering*, *51*(4), 277–296. <https://doi.org/10.1016/j.coastaleng.2004.03.001> (cit. on p. 74)
- Magnusson, L., Bidlot, J.-R., Bonavita, M., Brown, A. R., Browne, P. A., Chiara, G. D., Dahoui, M., Lang, S. T. K., McNally, T., Mogensen, K. S., Pappenberger, F., Prates, F., Rabier, F., Richardson, D. S., Vitart, F., & Malardel, S. (2019). ECMWF activities for improved hurricane forecasts. *Bulletin of the American Meteorological Society*, *100*(3), 445–458. <https://doi.org/10.1175/bams-d-18-0044.1> (cit. on p. 73)
- Mann, H. B. (1945). Nonparametric tests against trend. *Econometrica*, *13*(3), 245. <https://doi.org/10.2307/1907187> (cit. on p. 53)

- Mason, D. C., Davenport, I. J., Robinson, G. J., Flather, R. A., & McCartney, B. S. (1995). Construction of an inter-tidal digital elevation model by the ‘water-line’ method. *Geophysical Research Letters*, *22*(23), 3187–3190. <https://doi.org/10.1029/95gl03168> (cit. on pp. 27–29, 45)
- Mason, D. C., & Garg, P. K. (2001). Morphodynamic modelling of intertidal sediment transport in morecambe bay. *Estuarine, Coastal and Shelf Science*, *53*(1), 79–92. <https://doi.org/10.1006/ecss.2000.0618> (cit. on p. 29)
- Mason, D. C., Gurney, C., & Kennett, M. (2000). Beach topography mapping—a comparison of techniques. *Journal of Coastal Conservation*, *6*(1), 113–124. <https://doi.org/10.1007/bf02730475> (cit. on p. 28)
- Mason, D. C., Hill, D., Davenport, I., Flather, R., & Robinson, G. (1997). Improving inter-tidal digital elevation models constructed by the waterline technique. *European Space Agency-Publications-Esa SP*, *414*, 1079–1082. <https://earth.esa.int/workshops/ers97/papers/mason/> (cit. on pp. 28, 30)
- Mayet, C., Testut, L., Legresy, B., Lescarmonier, L., & Lyard, F. (2013). High-resolution barotropic modeling and the calving of the mertz glacier, east antarctica. *Journal of Geophysical Research: Oceans*, *118*(10), 5267–5279. <https://doi.org/10.1002/jgrc.20339> (cit. on p. 90)
- McCreary, J. P., Han, W., Shankar, D., & Shetye, S. R. (1996). Dynamics of the east india coastal current: 2. numerical solutions. *Journal of Geophysical Research: Oceans*, *101*(C6), 13993–14010. <https://doi.org/10.1029/96jc00560> (cit. on p. 53)
- McFeeters, S. K. (1996). The use of the normalized difference water index (NDWI) in the delineation of open water features. *International Journal of Remote Sensing*, *17*(7), 1425–1432. <https://doi.org/10.1080/01431169608948714> (cit. on p. 29)
- Melton, G., Gall, M., Mitchell, J. T., & Cutter, S. L. (2009). Hurricane katrina storm surge delineation: Implications for future storm surge forecasts and warnings. *Natural Hazards*, *54*(2), 519–536. <https://doi.org/10.1007/s11069-009-9483-z> (cit. on p. 73)
- Minderhoud, P. S. J., Coumou, L., Erkens, G., Middelkoop, H., & Stouthamer, E. (2019). Mekong delta much lower than previously assumed in sea-level rise impact assessments. *Nature Communications*, *10*(1). <https://doi.org/10.1038/s41467-019-11602-1> (cit. on p. 8)
- Mirza, M. M. Q. (2002). Global warming and changes in the probability of occurrence of floods in bangladesh and implications. *Global Environmental Change*, *12*(2), 127–138. [https://doi.org/10.1016/s0959-3780\(02\)00002-x](https://doi.org/10.1016/s0959-3780(02)00002-x) (cit. on pp. 13, 67)
- Mirza, M. M. Q., Warrick, R. A., & Ericksen, N. J. (2003). The implications of climate change on floods of the ganges, brahmaputra and meghna rivers. *Climatic Change*, *57*(3), 287–318. <https://doi.org/10.1023/a:1022825915791> (cit. on pp. 5, 6)
- Mittal, R., Tewari, M., Radhakrishnan, C., Ray, P., Singh, T., & Nickerson, A. K. (2019). Response of tropical cyclone phailin (2013) in the bay of bengal to climate perturbations. *Climate Dynamics*. <https://doi.org/10.1007/s00382-019-04761-w> (cit. on p. 9)
- Mohammed, K., Islam, A. K. M. S., Islam, G. M. T., Alfieri, L., Khan, M. J. U., Bala, S. K., & Das, M. K. (2018). Future floods in bangladesh under 1.5°C, 2°C, and 4°C global warming scenarios. *Journal of Hydrologic Engineering*, *23*(12), 04018050. [https://doi.org/10.1061/\(asce\)he.1943-5584.0001705](https://doi.org/10.1061/(asce)he.1943-5584.0001705) (cit. on pp. 4, 9)
- Morss, R. E., Cuite, C. L., Demuth, J. L., Hallman, W. K., & Shwom, R. L. (2018). Is storm surge scary? the influence of hazard, impact, and fear-based messages and individual differences on responses to hurricane risks in the USA. *International Journal of Disaster Risk Reduction*, *30*, 44–58. <https://doi.org/10.1016/j.ijdrr.2018.01.023> (cit. on p. 90)
- Mukhopadhyay, S., Biswas, H., De, T., & Jana, T. (2006). Fluxes of nutrients from the tropical river hooghly at the land–ocean boundary of sundarbans, NE coast of bay of bengal, india. *Journal of Marine Systems*, *62*(1-2), 9–21. <https://doi.org/10.1016/j.jmarsys.2006.03.004> (cit. on pp. 23, 42, 55, 105)

- Murray, N. J., Phinn, S. R., DeWitt, M., Ferrari, R., Johnston, R., Lyons, M. B., Clinton, N., Thau, D., & Fuller, R. A. (2018). The global distribution and trajectory of tidal flats. *Nature*, *565*(7738), 222–225. <https://doi.org/10.1038/s41586-018-0805-8> (cit. on p. 28)
- Murty, P., Bhaskaran, P. K., Gayathri, R., Sahoo, B., Kumar, T. S., & SubbaReddy, B. (2016). Numerical study of coastal hydrodynamics using a coupled model for hudhud cyclone in the bay of bengal. *Estuarine, Coastal and Shelf Science*, *183*, 13–27. <https://doi.org/10.1016/j.ecss.2016.10.013> (cit. on pp. 18, 19, 75, 85)
- Murty, P., Padmanabham, J., Kumar, T. S., Kumar, N. K., Chandra, V. R., Shenoi, S., & Mohapatra, M. (2017). Real-time storm surge and inundation forecast for very severe cyclonic storm ‘hudhud’. *Ocean Engineering*, *131*, 25–35. <https://doi.org/10.1016/j.oceaneng.2016.12.026> (cit. on pp. 73, 74, 86)
- Murty, P., Sandhya, K., Bhaskaran, P. K., Jose, F., Gayathri, R., Nair, T. B., Kumar, T. S., & Shenoi, S. (2014). A coupled hydrodynamic modeling system for PHAILIN cyclone in the bay of bengal. *Coastal Engineering*, *93*, 71–81. <https://doi.org/10.1016/j.coastaleng.2014.08.006> (cit. on pp. 20, 73, 75, 85, 87)
- Murty, T., Flather, R., & Henry, R. (1986). The storm surge problem in the bay of bengal. *Progress in Oceanography*, *16*(4), 195–233. [https://doi.org/10.1016/0079-6611\(86\)90039-x](https://doi.org/10.1016/0079-6611(86)90039-x) (cit. on pp. 13, 70, 71, 73, 74, 85, 94)
- National Centers for Environmental Prediction, National Weather Service, NOAA, U.S. Department of Commerce. (2015). NCEP GDAS/FNL 0.25 Degree Global Tropospheric Analyses and Forecast Grids. <https://doi.org/10.5065/D65Q4T4Z>. (Cit. on p. 78)
- Needham, H. F., Keim, B. D., & Sathiaraj, D. (2015). A review of tropical cyclone-generated storm surges: Global data sources, observations, and impacts. *Reviews of Geophysics*, *53*(2), 545–591. <https://doi.org/10.1002/2014rg000477> (cit. on pp. 7, 71, 94)
- Neumann, B., Vafeidis, A. T., Zimmermann, J., & Nicholls, R. J. (2015). Future coastal population growth and exposure to sea-level rise and coastal flooding - a global assessment (L. Kumar, Ed.). *PLOS ONE*, *10*(3), e0118571. <https://doi.org/10.1371/journal.pone.0118571> (cit. on p. 50)
- Nicholls, R. J., Adger, W. N., Hutton, C. W., & Hanson, S. E. (2019). Delta challenges and trade-offs from the holocene to the anthropocene. *Deltas in the anthropocene* (pp. 1–22). Springer International Publishing. https://doi.org/10.1007/978-3-030-23517-8_1. (Cit. on p. 2)
- Niedermeier, A., Romaneessen, E., & Lehner, S. (2000). Detection of coastlines in SAR images using wavelet methods. *IEEE Transactions on Geoscience and Remote Sensing*, *38*(5), 2270–2281. <https://doi.org/10.1109/36.868884> (cit. on p. 29)
- Nowreen, S., Jalal, M. R., & Khan, M. S. A. (2013). Historical analysis of rationalizing south west coastal polders of bangladesh. *Water Policy*, *16*(2), 264–279. <https://doi.org/10.2166/wp.2013.172> (cit. on pp. 6, 9, 16, 75, 88, 95)
- Oliveira, A., Fortunato, A., Rogeiro, J., Teixeira, J., Azevedo, A., Lavaud, L., Bertin, X., Gomes, J., David, M., Pina, J., Rodrigues, M., & Lopes, P. (2020). OPENCoastS: An open-access service for the automatic generation of coastal forecast systems. *Environmental Modelling & Software*, *124*, 104585. <https://doi.org/10.1016/j.envsoft.2019.104585> (cit. on pp. 73, 89)
- Oppenheimer, M., Glavovic, B., Hinkel, J., van de Wal, R., Magnan, A. K., Abd-Elgawad, A., Cai, R., Cifuentes-Jara, M., DeConto, R. M., Ghosh, T., Hay, J., Isla, F., Marzeion, B., Meyssignac, B., & Sebesvari, Z. (2019). Sea Level Rise and Implications for Low Lying Islands, Coasts and Communities. *Ipc special report on the ocean and cryosphere in a changing climate*. (Cit. on pp. 2, 9, 50, 127).
- Ouillon, S. (2018). Why and how do we study sediment transport? focus on coastal zones and ongoing methods. *Water*, *10*(4), 390. <https://doi.org/10.3390/w10040390> (cit. on p. 129)

- Paul, B. K., & Dutt, S. (2010). Hazard warnings and responses to evacuation orders: The case of bangladesh's cyclone sidr. *Geographical Review*, *100*(3), 336–355. <https://doi.org/10.1111/j.1931-0846.2010.00040.x> (cit. on pp. 8, 72, 89, 90)
- Paul, B. K. (2009). Why relatively fewer people died? the case of bangladesh's cyclone sidr. *Natural Hazards*, *50*(2), 289–304. <https://doi.org/10.1007/s11069-008-9340-5> (cit. on pp. 8, 72, 94)
- Pekel, J.-F., Vancutsem, C., Bastin, L., Clerici, M., Vanbogaert, E., Bartholomé, E., & Defourny, P. (2014). A near real-time water surface detection method based on HSV transformation of MODIS multi-spectral time series data. *Remote Sensing of Environment*, *140*, 704–716. <https://doi.org/10.1016/j.rse.2013.10.008> (cit. on pp. 30, 35)
- Penning-Rowsell, E. C., Sultana, P., & Thompson, P. M. (2013). The 'last resort'? population movement in response to climate-related hazards in bangladesh. *Environmental Science & Policy*, *27*, S44–S59. <https://doi.org/10.1016/j.envsci.2012.03.009> (cit. on p. 8)
- Pethick, J., & Orford, J. D. (2013). Rapid rise in effective sea-level in southwest bangladesh: Its causes and contemporary rates. *Global and Planetary Change*, *111*, 237–245. <https://doi.org/10.1016/j.gloplacha.2013.09.019> (cit. on pp. 52, 54)
- Petrucci, B., Huc, M., Feuvrier, T., Ruffel, C., Hagolle, O., Lonjou, V., & Desjardins, C. (2015). Maccs: Multi-mission atmospheric correction and cloud screening tool for high-frequency revisit data processing. *Image and Signal Processing for Remote Sensing XXI*, *9643*, 964307 (cit. on p. 32).
- Pezerat, M., Bertin, X., Martins, K., Mengual, B., & Hamm, L. (Accepted). Simulating storm waves in the nearshore area using spectral model: Current issues and a pragmatic solution. *Ocean Modelling* (cit. on pp. 126, 127).
- Pezerat, M., Martins, K., & Bertin, X. (2020). Modelling Storm Waves in the Nearshore Area Using Spectral Models. *Journal of Coastal Research*, *95*(sp1), 1240. <https://doi.org/10.2112/SI95-240.1> (cit. on pp. 75, 78, 101, 105)
- Philip, S., Sparrow, S., Kew, S. F., van der Wiel, K., Wanders, N., Singh, R., Hassan, A., Mohammed, K., Javid, H., Haustein, K., Otto, F. E., Hirpa, F., Rimi, R. H., Islam, A. S., Wallom, D. C., & van Oldenborgh, G. J. (2018). Attributing the 2017 bangladesh floods from meteorological and hydrological perspectives. *Hydrology and Earth System Sciences Discussions*, 1–32. <https://doi.org/10.5194/hess-2018-379> (cit. on p. 8)
- Pickering, M., Horsburgh, K., Blundell, J., Hirschi, J.-M., Nicholls, R., Verlaan, M., & Wells, N. (2017). The impact of future sea-level rise on the global tides. *Continental Shelf Research*, *142*, 50–68. <https://doi.org/10.1016/j.csr.2017.02.004> (cit. on pp. 52, 55, 59, 60, 66)
- Poupardin, A., Idier, D., de Michele, M., & Raucoules, D. (2016). Water depth inversion from a single SPOT-5 dataset. *IEEE Transactions on Geoscience and Remote Sensing*, *54*(4), 2329–2342. <https://doi.org/10.1109/tgrs.2015.2499379> (cit. on p. 120)
- Priest, G. R., Zhang, Y., Witter, R. C., Wang, K., Goldfinger, C., & Stimely, L. (2014). Tsunami impact to washington and northern oregon from segment ruptures on the southern cascadia subduction zone. *Natural Hazards*, *72*(2), 849–870. <https://doi.org/10.1007/s11069-014-1041-7> (cit. on p. 40)
- Provost, C. L., & Vincent, P. (1986). Some tests of precision for a finite element model of ocean tides. *Journal of Computational Physics*, *65*(2), 273–291. [https://doi.org/10.1016/0021-9991\(86\)90209-3](https://doi.org/10.1016/0021-9991(86)90209-3) (cit. on p. 19)
- Rahman, A. F., Dragoni, D., & El-Masri, B. (2011). Response of the sundarbans coastline to sea level rise and decreased sediment flow: A remote sensing assessment. *Remote Sensing of Environment*, *115*(12), 3121–3128. <https://doi.org/10.1016/j.rse.2011.06.019> (cit. on p. 31)
- Rahman, M., Dustegir, M., Karim, R., Haque, A., Nicholls, R. J., Darby, S. E., Nakagawa, H., Hossain, M., Dunn, F. E., & Akter, M. (2018). Recent sediment flux to the ganges-

- brahmaputra-meghna delta system. *Science of The Total Environment*, 643, 1054–1064. <https://doi.org/10.1016/j.scitotenv.2018.06.147> (cit. on pp. 51, 129)
- Rahman, S., Islam, A. K. M. S., Saha, P., Tazkia, A. R., Krien, Y., Durand, F., Testut, L., Islam, G. M. T., & Bala, S. K. (2019). Projected changes of inundation of cyclonic storms in the ganges–brahmaputra–meghna delta of bangladesh due to SLR by 2100. *Journal of Earth System Science*, 128(6). <https://doi.org/10.1007/s12040-019-1184-8> (cit. on pp. 9, 59)
- Ray, R. D. (1999). *A global ocean tide model from TOPEX/POSEIDON altimetry: GOT99*. 2. National Aeronautics; Space Administration, Goddard Space Flight Center. (Cit. on pp. 55, 78).
- Ray, R. D. (2013). Precise comparisons of bottom-pressure and altimetric ocean tides. *Journal of Geophysical Research: Oceans*, 118(9), 4570–4584. <https://doi.org/10.1002/jgrc.20336> (cit. on p. 55)
- Reading, H. G. (2009). *Sedimentary environments: Processes, facies and stratigraphy*. John Wiley & Sons. (Cit. on p. 2).
- Roland, A., Zhang, Y. J., Wang, H. V., Meng, Y., Teng, Y.-C., Maderich, V., Brovchenko, I., Dutour-Sikiric, M., & Zanke, U. (2012). A fully coupled 3d wave-current interaction model on unstructured grids. *Journal of Geophysical Research: Oceans*, 117(C11), n/a–n/a. <https://doi.org/10.1029/2012jc007952> (cit. on pp. 21, 78, 101)
- Rose, L., & Bhaskaran, P. K. (2017). Tidal propagation and its non-linear characteristics in the head bay of bengal. *Estuarine, Coastal and Shelf Science*, 188, 181–198. <https://doi.org/10.1016/j.ecss.2017.02.024> (cit. on pp. 30, 47)
- Roy, B., Islam, A. K. M. S., Islam, G. M. T., Khan, M. J. U., Bhattacharya, B., Ali, M. H., Khan, A. S., Hossain, M. S., Sarker, G. C., & Pieu, N. M. (2019). Frequency analysis of flash floods for establishing new danger levels for the rivers in the northeast haor region of bangladesh. *Journal of Hydrologic Engineering*, 24(4), 05019004. [https://doi.org/10.1061/\(asce\)he.1943-5584.0001760](https://doi.org/10.1061/(asce)he.1943-5584.0001760) (cit. on p. 5)
- Roy, C., Sarkar, S. K., Åberg, J., & Kovordanyi, R. (2015). The current cyclone early warning system in bangladesh: Providers' and receivers' views. *International Journal of Disaster Risk Reduction*, 12, 285–299. <https://doi.org/10.1016/j.ijdr.2015.02.004> (cit. on pp. 74, 89, 90)
- RSMC. (2020). *Super Cyclonic Storm “AMPHAN” over the southeast Bay of Bengal (16th – 21st May 2020): Summary* (tech. rep.). Regional Specialised Meteorological Centre - Tropical Cyclones. New Delhi. Retrieved July 30, 2020, from www.rsmcnewdelhi.imd.gov.in/images/pdf/publications/preliminary-report/amphan.pdf. (Cit. on p. 76)
- Rumpf, J., Weindl, H., Höpfe, P., Rauch, E., & Schmidt, V. (2007). Stochastic modelling of tropical cyclone tracks. *Mathematical Methods of Operations Research*, 66(3), 475–490. <https://doi.org/10.1007/s00186-007-0168-7> (cit. on p. 98)
- Rundquist, D. C., Lawson, M. P., Queen, L. P., & Cervený, R. S. (1987). The relationship between summer-season rainfall events and lake-surface area. *JAWRA Journal of the American Water Resources Association*, 23(3), 493–508. <https://doi.org/10.1111/j.1752-1688.1987.tb00828.x> (cit. on p. 29)
- Sagar, S., Roberts, D., Bala, B., & Lymburner, L. (2017). Extracting the intertidal extent and topography of the australian coastline from a 28 year time series of landsat observations. *Remote Sensing of Environment*, 195, 153–169. <https://doi.org/10.1016/j.rse.2017.04.009> (cit. on p. 29)
- Salameh, E., Frappart, F., Almar, R., Baptista, P., Heygster, G., Lubac, B., Raucoules, D., Almeida, L. P., Bergsma, E. W. J., Capo, S., Michele, M. D., Idier, D., Li, Z., Marieu, V., Poupardin, A., Silva, P. A., Turki, I., & Laignel, B. (2019). Monitoring beach topography and nearshore bathymetry using spaceborne remote sensing: A review. *Remote Sensing*, 11(19), 2212. <https://doi.org/10.3390/rs11192212> (cit. on pp. 28, 29, 45, 48, 120)

- Schmidt, S., Kemfert, C., & Hölpe, P. (2009). Tropical cyclone losses in the USA and the impact of climate change — A trend analysis based on data from a new approach to adjusting storm losses. *Environmental Impact Assessment Review*, 29(6), 359–369. <https://doi.org/10.1016/j.eiar.2009.03.003> (cit. on p. 72)
- Sciortino, J. A. et al. (2010). *Fishing harbour planning, construction and management*. Food; Agriculture Organization of the United Nations. (Cit. on p. 45).
- Scott, T., & Mason, D. (2007). Data assimilation for a coastal area morphodynamic model: Morecambe bay. *Coastal Engineering*, 54(2), 91–109. <https://doi.org/10.1016/j.coastaleng.2006.08.008> (cit. on p. 29)
- Sen, P. K. (1968). Estimates of the regression coefficient based on kendall's tau. *Journal of the American Statistical Association*, 63(324), 1379–1389. <https://doi.org/10.1080/01621459.1968.10480934> (cit. on p. 53)
- Seo, S. N., & Bakkensen, L. A. (2017). Is tropical cyclone surge, not intensity, what kills so many people in south asia? *Weather, Climate, and Society*, 9(2), 171–181. <https://doi.org/10.1175/wcas-d-16-0059.1> (cit. on pp. 71, 94)
- Shankar, D., McCreary, J. P., Han, W., & Shetye, S. R. (1996). Dynamics of the east india coastal current: 1. analytic solutions forced by interior ekman pumping and local alongshore winds. *Journal of Geophysical Research: Oceans*, 101(C6), 13975–13991. <https://doi.org/10.1029/96jc00559> (cit. on p. 53)
- Shankar, D., & Shetye, S. R. (2001). Why is mean sea level along the indian coast higher in the bay of bengal than in the arabian sea? *Geophysical Research Letters*, 28(4), 563–565. <https://doi.org/10.1029/2000gl012001> (cit. on pp. 22, 123)
- Sherin, V., Durand, F., Papa, F., Islam, A. S., Gopalakrishna, V., Khaki, M., & Suneel, V. (2020). Recent salinity intrusion in the bengal delta: Observations and possible causes. *Continental Shelf Research*, 202, 104142. <https://doi.org/10.1016/j.csr.2020.104142> (cit. on p. 124)
- Shibayama, T., Tajima, Y., Kakinuma, T., Nobuoka, H., Yasuda, T., Ahsan, R., Rahman, M., & Islam, M. S. (2008). Field survey of storm surge disaster due to cyclone sidr in bangladesh. *Proceedings of Coastal Engineering, JSCE*, 55, 1396–1400. <https://doi.org/10.2208/proceed1989.55.1396> (cit. on p. 126)
- Simard, M., Fatoyinbo, T., Smetanka, C., Rivera-Monroy, V., Castaneda-Mova, E., Thomas, N., & Van Der Stocken, T. (2019). Global mangrove distribution, aboveground biomass, and canopy height. <https://doi.org/10.3334/ORNLDAAAC/1665>. (Cit. on p. 126)
- Sindhu, B., & Unnikrishnan, A. S. (2011). Return period estimates of extreme sea level along the east coast of india from numerical simulations. *Natural Hazards*, 61(3), 1007–1028. <https://doi.org/10.1007/s11069-011-9948-8> (cit. on pp. 96, 97, 111)
- Sindhu, B., & Unnikrishnan, A. S. (2013). Characteristics of tides in the bay of bengal. *Marine Geodesy*, 36(4), 377–407. <https://doi.org/10.1080/01490419.2013.781088> (cit. on pp. 1, 6, 9, 13, 18, 25, 58, 59, 90, 94)
- Singh, K., Panda, J., & Mohapatra, M. (2020). Robustness of best track data and associated cyclone activity over the north indian ocean region during and prior to satellite era. *Journal of Earth System Science*, 129(1). <https://doi.org/10.1007/s12040-020-1344-x> (cit. on pp. 93, 97, 98)
- Small, C., & Nicholls, R. J. (2003). A global analysis of human settlement in coastal zones. *Journal of coastal research*, 584–599 (cit. on p. 2).
- Stammer, D., Ray, R. D., Andersen, O. B., Arbic, B. K., Bosch, W., Carrère, L., Cheng, Y., Chinn, D. S., Dushaw, B. D., Egbert, G. D., Erofeeva, S. Y., Fok, H. S., Green, J. A. M., Griffiths, S., King, M. A., Lapin, V., Lemoine, F. G., Luthcke, S. B., Lyard, F., ... Yi, Y. (2014). Accuracy assessment of global barotropic ocean tide models. *Reviews of Geophysics*, 52(3), 243–282. <https://doi.org/10.1002/2014rg000450> (cit. on p. 42)

- Stanley, D. J. (1996). Nile delta: Extreme case of sediment entrapment on a delta plain and consequent coastal land loss. *Marine Geology*, 129(3-4), 189–195. [https://doi.org/10.1016/0025-3227\(96\)83344-5](https://doi.org/10.1016/0025-3227(96)83344-5) (cit. on p. 3)
- Stockdon, H. F., Holman, R. A., Howd, P. A., & Sallenger, A. H. (2006). Empirical parameterization of setup, swash, and runup. *Coastal Engineering*, 53(7), 573–588. <https://doi.org/10.1016/j.coastaleng.2005.12.005> (cit. on pp. 31, 43)
- Suh, S. W., Lee, H. Y., Kim, H. J., & Fleming, J. G. (2015). An efficient early warning system for typhoon storm surge based on time-varying advisories by coupled ADCIRC and SWAN. *Ocean Dynamics*, 65(5), 617–646. <https://doi.org/10.1007/s10236-015-0820-3> (cit. on pp. 73, 83)
- Sweet, W. W. V., Kopp, R., Weaver, C. P., Obeysekera, J., Horton, R. M., Thieler, E. R., Zervas, C. E., et al. (2017). *Global and regional sea level rise scenarios for the united states* (Technical Report). National Oceanic and Atmospheric Administration. (Cit. on p. 50).
- Swenson, J. B. (2005). Fluvial and marine controls on combined subaerial and subaqueous delta progradation: Morphodynamic modeling of compound-cliniform development. *Journal of Geophysical Research*, 110(F2). <https://doi.org/10.1029/2004jf000265> (cit. on p. 2)
- Syvitski, J. P. M. (2005). Impact of humans on the flux of terrestrial sediment to the global coastal ocean. *Science*, 308(5720), 376–380. <https://doi.org/10.1126/science.1109454> (cit. on p. 2)
- Syvitski, J. P. M. (2008). Deltas at risk. *Sustainability Science*, 3(1), 23–32. <https://doi.org/10.1007/s11625-008-0043-3> (cit. on p. 2)
- Syvitski, J. P. M., Kettner, A. J., Overeem, I., Hutton, E. W. H., Hannon, M. T., Brakenridge, G. R., Day, J., Vörösmarty, C., Saito, Y., Giosan, L., & Nicholls, R. J. (2009). Sinking deltas due to human activities. *Nature Geoscience*, 2(10), 681–686. <https://doi.org/10.1038/ngeo629> (cit. on pp. 3, 129)
- Tajima, Y., Hamada, Y., & Hussain, M. A. (2015). Impact of dynamic morphology change on storm surge disaster risks along the meghna estuary. *Procedia Engineering*, 116, 947–954. <https://doi.org/10.1016/j.proeng.2015.08.385> (cit. on p. 31)
- Talke, S. A., & Jay, D. A. (2020). Changing tides: The role of natural and anthropogenic factors. *Annual Review of Marine Science*, 12(1), 121–151. <https://doi.org/10.1146/annurev-marine-010419-010727> (cit. on pp. 51, 52, 65, 66)
- Tallapragada, V., Kieu, C., Kwon, Y., Trahan, S., Liu, Q., Zhang, Z., & Kwon, I.-H. (2014). Evaluation of storm structure from the operational HWRF during 2012 implementation. *Monthly Weather Review*, 142(11), 4308–4325. <https://doi.org/10.1175/mwr-d-13-0001.0.1> (cit. on pp. 73, 87)
- Tasnim, K. M., Shibayama, T., Esteban, M., Takagi, H., Ohira, K., & Nakamura, R. (2014). Field observation and numerical simulation of past and future storm surges in the bay of bengal: Case study of cyclone nargis. *Natural Hazards*, 75(2), 1619–1647. <https://doi.org/10.1007/s11069-014-1387-x> (cit. on pp. 9, 128)
- Tazkia, A., Krien, Y., Durand, F., Testut, L., Islam, A. S., Papa, F., & Bertin, X. (2017). Seasonal modulation of m2 tide in the northern bay of bengal. *Continental Shelf Research*, 137, 154–162. <https://doi.org/10.1016/j.csr.2016.12.008> (cit. on pp. 1, 6, 13, 22, 40, 42, 50, 53, 54, 58, 66, 74, 75, 95, 99)
- Tessler, Z. D., Vorosmarty, C. J., Grossberg, M., Gladkova, I., Aizenman, H., Syvitski, J. P. M., & Foufoula-Georgiou, E. (2015). Profiling risk and sustainability in coastal deltas of the world. *Science*, 349(6248), 638–643. <https://doi.org/10.1126/science.aab3574> (cit. on p. 50)
- The Climate Change Initiative Coastal Sea Level Team, Benveniste, J., Birol, F., Mir Calafat, F., Cazenave, A., Dieng, H., Gouzenes, Y., Legeais, J. F., Léger, F., Niño, F., Passaro, M., et al. (2020). Coastal sea level anomalies and associated trends from Jason satellite

- altimetry over 2002–2018. *Scientific Data*, 7(1). <https://doi.org/10.1038/s41597-020-00694-w> (cit. on p. 123)
- Thorslund, J., Jarsjo, J., Jaramillo, F., Jawitz, J. W., Manzoni, S., Basu, N. B., Chalov, S. R., Cohen, M. J., Creed, I. F., Goldenberg, R., Hylin, A., Kalantari, Z., Koussis, A. D., Lyon, S. W., Mazi, K., Mard, J., Persson, K., Pietro, J., Prieto, C., ... Destouni, G. (2017). Wetlands as large-scale nature-based solutions: Status and challenges for research, engineering and management. *Ecological Engineering*, 108, 489–497. <https://doi.org/10.1016/j.ecoleng.2017.07.012> (cit. on p. 120)
- Toro, G. R., Resio, D. T., Divoky, D., Niedoroda, A. W., & Reed, C. (2010). Efficient joint-probability methods for hurricane surge frequency analysis. *Ocean Engineering*, 37(1), 125–134. <https://doi.org/10.1016/j.oceaneng.2009.09.004> (cit. on p. 98)
- Tribune, D. (2020). Govt: Cyclone caused damage worth Tk1,100 crore. Retrieved September 10, 2020, from <https://www.dhakatribune.com/bangladesh/crisis/2020/05/21/govt-estimated-damages-from-amphan-worth-1-100-crore>. (Cit. on p. 74)
- Tseng, K.-H., Kuo, C.-Y., Lin, T.-H., Huang, Z.-C., Lin, Y.-C., Liao, W.-H., & Chen, C.-F. (2017). Reconstruction of time-varying tidal flat topography using optical remote sensing imageries. *ISPRS Journal of Photogrammetry and Remote Sensing*, 131, 92–103. <https://doi.org/10.1016/j.isprsjprs.2017.07.008> (cit. on pp. 28, 29)
- Tucker, C. J., & Sellers, P. J. (1986). Satellite remote sensing of primary production. *International Journal of Remote Sensing*, 7(11), 1395–1416. <https://doi.org/10.1080/01431168608948944> (cit. on p. 29)
- Unnikrishnan, A. S., & Sundar, D. (2004). Analysis of extreme sea level along the east coast of india. *Journal of Geophysical Research*, 109(6). <https://doi.org/10.1029/2003jc002217> (cit. on p. 96)
- Velden, C., Harper, B., Wells, F., Beven, J. L., Zehr, R., Olander, T., Mayfield, M., Guard, C. “., Lander, M., Edson, R., Avila, L., Burton, A., Turk, M., Kikuchi, A., Christian, A., Caroff, P., & McCrone, P. (2006). The dvorak tropical cyclone intensity estimation technique: A satellite-based method that has endured for over 30 years. *Bulletin of the American Meteorological Society*, 87(9), 1195–1210. <https://doi.org/10.1175/bams-87-9-1195> (cit. on p. 24)
- Verlaan, M., Zijderfeld, A., de Vries, H., & Kroos, J. (2005). Operational storm surge forecasting in the netherlands: Developments in the last decade. *Philosophical Transactions of the Royal Society A: Mathematical, Physical and Engineering Sciences*, 363(1831), 1441–1453. <https://doi.org/10.1098/rsta.2005.1578> (cit. on p. 73)
- Vishnu, S., Sanjay, J., & Krishnan, R. (2019). Assessment of climatological tropical cyclone activity over the north indian ocean in the CORDEX-south asia regional climate models. *Climate Dynamics*, 53(7-8), 5101–5118. <https://doi.org/10.1007/s00382-019-04852-8> (cit. on p. 9)
- Warner, J. F., van Staveren, M. F., & van Tatenhove, J. (2018). Cutting dikes, cutting ties? reintroducing flood dynamics in coastal polders in bangladesh and the netherlands. *International Journal of Disaster Risk Reduction*, 32, 106–112. <https://doi.org/10.1016/j.ijdr.2018.03.020> (cit. on p. 88)
- Westerink, J. J., Luettich, R. A., Feyen, J. C., Atkinson, J. H., Dawson, C., Roberts, H. J., Powell, M. D., Dunion, J. P., Kubatko, E. J., & Pourtaheri, H. (2008). A basin- to channel-scale unstructured grid hurricane storm surge model applied to southern louisiana. *Monthly Weather Review*, 136(3), 833–864. <https://doi.org/10.1175/2007mwr1946.1> (cit. on p. 23)
- Wilson, C., Goodbred, S., Small, C., Gilligan, J., Sams, S., Mallick, B., & Hale, R. (2017). Widespread infilling of tidal channels and navigable waterways in human-modified tidal deltaplain of southwest bangladesh. *Elem Sci Anth*, 5(0), 78. <https://doi.org/10.1525/elementa.263> (cit. on pp. 9, 125, 129)

- Woodruff, J. D., Irish, J. L., & Camargo, S. J. (2013). Coastal flooding by tropical cyclones and sea-level rise. *Nature*, *504*(7478), 44–52. <https://doi.org/10.1038/nature12855> (cit. on pp. 1, 3)
- Woodworth, P. (2012). A note on the nodal tide in sea level records. *Journal of Coastal Research*, *280*(nil), 316–323. <https://doi.org/10.2112/jcoastres-d-11a-00023.1> (cit. on p. 52)
- Woodworth, P. (2010). A survey of recent changes in the main components of the ocean tide. *Continental Shelf Research*, *30*(15), 1680–1691. <https://doi.org/10.1016/j.csr.2010.07.002> (cit. on p. 51)
- Work, E., & Gilmer, D. S. (1976). Utilization of satellite data for inventorying prairie ponds and lakes. *Photogrammetric Engineering and Remote Sensing*, *42*(5), 685–694 (cit. on p. 29).
- World Bank. (2005). *Project Performance Assessment Report - Coastal Embankment Rehabilitation Project* (Technical report). World Bank. Washington 31565. https://ieg.worldbankgroup.org/sites/default/files/Data/reports/ppar%7B%5C_%7D31565.pdf. (Cit. on pp. 6, 51)
- WW3DG, T. W. I. D. G. (2019). User manual and system documentation of WAVEWATCH III TM. (Cit. on p. 78).
- Xu, H. (2006). Modification of normalised difference water index (NDWI) to enhance open water features in remotely sensed imagery. *International Journal of Remote Sensing*, *27*(14), 3025–3033. <https://doi.org/10.1080/01431160600589179> (cit. on p. 29)
- Xu, Z., Kim, D.-j., Kim, S. H., Cho, Y.-K., & Lee, S.-G. (2016). Estimation of seasonal topographic variation in tidal flats using waterline method: A case study in gomso and hampyeong bay, south korea. *Estuarine, Coastal and Shelf Science*, *183*, 213–220. <https://doi.org/10.1016/j.ecss.2016.10.026> (cit. on p. 29)
- Xu, Z. (2017). A note on interpreting tidal harmonic constants. *Ocean Dynamics*, *68*(2), 211–222. <https://doi.org/10.1007/s10236-017-1122-8> (cit. on p. 22)
- Yang, K., Paramygin, V. A., & Sheng, Y. P. (2020). A rapid forecasting and mapping system of storm surge and coastal flooding. *Weather and Forecasting*, *35*(4), 1663–1681. <https://doi.org/10.1175/waf-d-19-0150.1> (cit. on p. 73)
- Ye, F., Zhang, Y. J., Yu, H., Sun, W., Moghimi, S., Myers, E., Nunez, K., Zhang, R., Wang, H. V., Roland, A., Martins, K., Bertin, X., Du, J., & Liu, Z. (2020). Simulating storm surge and compound flooding events with a creek-to-ocean model: Importance of baroclinic effects. *Ocean Modelling*, *145*, 101526. <https://doi.org/10.1016/j.ocemod.2019.101526> (cit. on pp. 77, 127)
- Zhang, Y. J., & Baptista, A. M. (2008). SELFE: A semi-implicit eulerian–lagrangian finite-element model for cross-scale ocean circulation. *Ocean Modelling*, *21*(3-4), 71–96. <https://doi.org/10.1016/j.ocemod.2007.11.005> (cit. on pp. 30, 40, 54, 77, 99)
- Zhang, Y. J., Stanev, E., & Grashorn, S. (2016). Unstructured-grid model for the north sea and baltic sea: Validation against observations. *Ocean Modelling*, *97*, 91–108. <https://doi.org/10.1016/j.ocemod.2015.11.009> (cit. on p. 77)
- Zhang, Y. J., Ye, F., Stanev, E. V., & Grashorn, S. (2016). Seamless cross-scale modeling with SCHISM. *Ocean Modelling*, *102*, 64–81. <https://doi.org/10.1016/j.ocemod.2016.05.002> (cit. on pp. 17, 27, 40, 54, 77, 99)
- Zhang, Y. J., Ye, F., Yu, H., Sun, W., Moghimi, S., Myers, E., Nunez, K., Zhang, R., Wang, H., Roland, A., Du, J., & Liu, Z. (2020). Simulating compound flooding events in a hurricane. *Ocean Dynamics*. <https://doi.org/10.1007/s10236-020-01351-x> (cit. on p. 77)
- Zhao, B., Guo, H., Yan, Y., Wang, Q., & Li, B. (2008). A simple waterline approach for tidelands using multi-temporal satellite images: A case study in the yangtze delta. *Estuarine, Coastal and Shelf Science*, *77*(1), 134–142. <https://doi.org/10.1016/j.ecss.2007.09.022> (cit. on pp. 28, 29)

Résumé. Le delta du Bengale est le plus vaste au monde. Il est formé par la confluence des trois rivières transfrontalières que sont le Gange, le Brahmapoutre et la Meghna. Des inondations massives frappent régulièrement cette région côtière très densément peuplée, située à seulement quelques mètres au-dessus du niveau moyen de la mer. Elles résultent du puissant cycle saisonnier des débits fluviaux, de la marée océanique très ample, et des cyclones tropicaux fréquents. Au cours des cinquante dernières années, les inondations de la partie littorale du delta ont fait plus de 500'000 victimes. La montée du niveau moyen de la mer ne va faire qu'aggraver la vulnérabilité de cette région où le taux de pauvreté est très élevé. Le long du littoral, les estrans sont les zones alternativement inondées à marée haute et découvertes à marée basse. Leur topographie joue un rôle important dans l'hydrodynamique littorale et dans les submersions qui surviennent lors des événements extrêmes. En mettant en œuvre une synergie entre l'imagerie par télédétection spatiale de la constellation Sentinel-2 et la modélisation numérique de la marée, nous avons cartographié la topographie de l'estran du delta du Bengale sur une superficie de 1134 km², avec une résolution de 10 m. Les marées, qui sont le facteur dominant de la variabilité du niveau de la mer côtier, sont apparues comme sensibles à la montée du niveau de la mer. Dans une hiérarchie de scénarios de montée du niveau de la mer représentatifs de l'évolution attendue au 21^{ème} siècle, nous avons conclu que l'amplitude de marée devrait augmenter significativement avec la montée du niveau de la mer, à la fois dans le Sud-Ouest et dans le Sud-Est du delta. Au contraire, l'extension graduelle et massive de la superficie des estrans dans la partie centrale du delta devrait induire une nette atténuation de la marée, dans ces scénarios futurs. La marée joue par ailleurs un rôle central dans l'évolution des surcotes cycloniques. Un exercice de prévision du dernier super-cyclone ayant frappé le delta du Bengale avec notre plate-forme de modélisation hydrodynamique couplée marée-surcote-vagues a révélé la nécessité du couplage dynamique entre ces trois composantes de la submersion, et nous avons pu confirmer le rôle-clé de la topographie côtière dans le succès des prévisions numériques. Grâce à une approche ensembliste basée sur la simulation numérique hydrodynamique de plusieurs milliers de cyclones synthétiques, cohérents tant du point de vue de la physique que de la statistique, nous avons pu conclure qu'il y a à l'heure actuelle de l'ordre de 10% de la population côtière du delta, soit trois millions de personnes, résidant dans la zone exposée à la submersion cinquantennale. La compréhension et la quantification des mécanismes de l'inondation exposés dans cette thèse constituent une information pertinente pour contribuer à l'ingénierie des infrastructures côtières, à la gestion du risque, ainsi qu'à l'élaboration de l'agenda de la recherche en hydrodynamique côtière sur le delta du Bengale.

Abstract. The Bengal delta is the largest in the world. It is formed by the confluence of three transboundary rivers - Ganges, Brahmaputra, and Meghna. Flooding induced by large seasonal continental discharge, strong tide, and frequent deadly storm surges, regularly strikes this densely populated (density > 1000 person/km²), low-lying coastal region (<5 m above mean sea level). In the last five decades, coastal flooding took more than half a million lives. Ongoing global sea level rise (SLR) will only further aggravate the vulnerability of this impoverished region. Along the shoreline, intertidal zones are the first landmass that gets flooded, periodically between each high- and low-tide. Their topography plays an important role in the coastal hydrodynamics and associated flooding during extremes. A synergy between remote sensing from Sentinel-2 constellation and tidal numerical modelling allowed us to map an intertidal area of 1134 km² and its topography at 10 m resolution. Tides, that prominently drive the variability of coastal sea level, are shown to be sensitive to SLR. In future SLR scenarios in line with the 21st century forecasts, we found that the tidal amplitude will significantly increase with SLR over both the south-western and south-eastern parts of the delta. In contrast, the central part of the delta will potentially experience massive free-flooding of river banks, hereby inducing a decay of the tidal amplitude. Tide plays a vital role in the evolution of storm surges also. Hindcast simulation of a recent super cyclone with our coupled tide-surge-wave model reveals the necessity of the coupling between tide, surge and wave modelling, and confirmed the crucial role played by the coastal topography for effective inundation modelling and forecast. With an ensemble forecast of thousands of physically and statistically consistent synthetic cyclones, we could conclude that about 10% of the coastal population of the Bengal delta, amounting to 3 million people, currently lives exposed to the 50-year return period flooding. The understanding and quantification of the inundation mechanisms extended in this study is expected to help with coastal infrastructure engineering, risk zoning, resource allocation and future adaptation to coastal flood across the Bengal delta.
